MODELING OF OPERATOR ACTION FOR INTELLIGENT CONTROL OF HAPTIC HUMAN-ROBOT INTERFACES

A Thesis
Presented to
The Academic Faculty

by

William John Gallagher

In Partial Fulfillment
of the Requirements for the Degree
Doctor of Philosophy in
Robotics

Daniel Guggenheim School of Aerospace Engineering
Georgia Institute of Technology
December 2013

MODELING OF OPERATOR ACTION FOR INTELLIGENT CONTROL OF HAPTIC HUMAN-ROBOT INTERFACES

Approved by:

Dr. Jun Ueda, Advisor
George W Woodruff School of
Mechanical Engineering
Georgia Institute of Technology

Dr. Minoru Shinohara
School of Applied Physiology
Georgia Institute of Technology

Dr. Karen Feigh
Daniel Guggenheim School of
Aerospace Engineering
Georgia Institute of Technology

Dr. Andrea Thomaz
School of Interactive Computing
Georgia Institute of Technology

Dr. Wayne Book
George W Woodruff School of
Mechanical Engineering
Georgia Institute of Technology

Date Approved: July 22, 2013

ACKNOWLEDGEMENTS

I would like to begin by thanking my advisor, Dr. Jun Ueda, for all of his guidance and advice during my time at Georgia Tech. His support has been invaluable as I endeavoured to research new and challenging things. Also, my co-advisor, Dr. Karen Feigh, provided help and assistance time and again, and I greatly appreciate that. I owe her with the success of my human subjects experiments, especially. Additionally, I would like to thank my committee members, Dr. Wayne Book, Dr. Minoru Shinohara, and Dr. Andrea Thomaz, for their helpful suggestions and insight into useful additions to my research. This work could not have been completed without them.

I owe a special thanks to JD Huggins for his help in designing and building the testbed device used for much of this research. Thank you, also, to Timothy McPherson for his assistance with measuring the human muscles using EMGs. Similarly, the prior work of Dr. Ming Ding with Dr. Ueda in modeling of the human upper arm has proved extremely helpful for completing this work.

Thank you to Dalong Gao and General Motors for their support of getting this research started. They have provided valuable insight into real world systems related to this work and financial support, along with continued collaboration as the project progressed.

My fellow lab mates in the Bio-Robotics and Human Modeling Lab, along with those of the neighboring labs, have become good friends and provided imeasurable assistance, and I would like to thank them for this: David MacNair, Joshua Schultz, Ellenor Brown, Melih Turkseven, Greg Henderson, Timothy McPherson, Lauren Lacey, Efrain Teran, Michael Kim, Heather Humphreys, Brian Post, and Hannes Daepp. Thank you to you all for being volunteers in my experiments! Also, I'd like

to thank Jake Huckaby, Tiffany Chen, Carlos Neito, Rahul Chipalkatty, and the rest of the RoboGrads crew for their support of myself and of the robotics program.

I need to additionally thank all of my friends both in Atlanta and afar. You all mean so much to me, and I will be forever grateful for all the support. Thanks to Tanner Freeman and Jen Smith; thanks to Greg Ortiz, Lauren La Bella, and Justin Dobies; thanks to Shahin Mehrabanzad, Jenn Telling, Manny Diaz, Akshay Pendharkar, and the rest of the YJFC; and thanks to everybody else that I've gotten to know along the way!

Finally, and most importantly, I would like to thank my family for their unending love and encouragement. Thanks to my mom for always telling me to reach out and grab the brass ring and for teaching me to always strive for the best. My brother, Deny, has always been there, and has been the best little brother I could ask for! Lastly, I thank God for all of the wonderful blessings and opportunities He's provided and the strength and wisdom to follow them.

TABLE OF CONTENTS

LIST OF TABLES

LIST OF FIGURES

LIST OF SYMBOLS

Variables

α	Angle of antagonism between two muscles
$\boldsymbol{A}$	System matrix
$1-\beta$	Statistical power of an experiment
$\boldsymbol{B}$	Input matrix
BM	Box's test metric
b	Damping
$\boldsymbol{C}$	Output matrix
$CC(t)$	Cocontraction of a muscle pair
c	Weighting factor for muscle force optimization
d	Distance
ϵ	Transformed allowable error in muscle force
ε	Maximum muscle force factor
$E(s)$	Error from target position (Laplace domain)
$EMG(t)$	Raw EMG signal
$EMG^{\%}(t)$	Percent activation of a muscle
$EMG^{*}(t)$	Processed and rectified EMG signal
EMG^{MVF}	Maximum voluntary force EMG value
e	Allowable error in muscle force
$F_m(s)$	Measured force (Laplace domain)

$F_o(s)$	Force applied on device by operator (Laplace domain)
F	F-ratio in an ANOVA analysis or regression
f	Force
$\boldsymbol{\Gamma}$	Solution to Ricatti equation for Kalman Filter
$\boldsymbol{g}$	Gravity force vector
γ	Force control gain
h	Target width
$\boldsymbol{I}$	Identity matrix
$j_{accuracy}$	Score of the accuracy-based task
j_{speed}	Score of the speed-based task
J	Optimal control cost function
$\boldsymbol{K}$	Kalman filter gain
κ	Probability normalizing constant
D_1	PD controller derivative gain
D_2	PD controller proportional gain
k	Stiffness
$\boldsymbol{L}$	Control gain matrix
ℓ	Stiffness classification threshold
λ	Lagrange multipliers for the KKT condition
μ	Mean of a distribution
m	Mass

η	Target muscle change ratio
n	Exponent for muscle force optimization
$\boldsymbol{O}$	HMM sensor output model
$\boldsymbol{\Phi}$	Solution to Ricatti equation
$\boldsymbol{\phi}$	Joint Angles
$\boldsymbol{\Pi}$	Solution to Ricatti-like equation for a stochastically varying system
$\boldsymbol{\Psi}$	Muscle moment arm matrix
$\boldsymbol{\psi}$	Moment arm vector of a muscle
$\boldsymbol{P}$	HMM probability vector for all states
ψ	Moment arm of a muscle on a joint
$PCSA$	Physiological cross sectional area
PV	Pillai's trace metric
p	Significance of a statistical test
$\boldsymbol{Q}_1$	Optimal control weighting matrix for x
$\boldsymbol{Q}_2$	Optimal control weighting matrix for u
$\boldsymbol{Q}_3$	Optimal control weighting matrix for covariance of x
q	Transformed muscle force
ρ	Optimization principle cost function
R^2	Correlation coefficient of a regression
r_p^2	Zero-order correlation coefficient for predictor p of a regression
$RMSE$	Root mean square error

$\boldsymbol{\Sigma}$	Covariance for a stochastically varying system
σ	Standard deviation of a distribution
s	Laplace domain parameter (Laplace domain)
τ	Torque
θ	Angular position of haptic device
$T(s)$	Torque (Laplace domain)
t	Time
$\boldsymbol{U}$	HMM transition model
u	Control input
$\boldsymbol{V}$	Process noise covariance matrix
v	System process noise
$\boldsymbol{\Omega}$	Jacobian from joints to arm end-point
$\boldsymbol{W}$	Sensor noise covariance matrix
ω	Transformed joint torque
w	Output sensor noise
$\boldsymbol{\xi}$	Muscle control solution parameter of redundancy
$\hat{x}$	State estimate
$X(s)$	Position (Laplace domain)
$X_d(s)$	Target position (Laplace domain)
x	Position
Y	Observed sensor value

y	System output
$\boldsymbol{\zeta}$	Muscle control solution
Z	Estimated stiffness state
z	A specific stiffness state

Constants

BB	Biceps Brachii muscle
ECR	Extensor Carpi Radialis muscle
ECU	Extensor Carpi Ulnaris muscle
E	Elbow joint
FCR	Flexor Carpi Radialis muscle
FCU	Flexor Carpi Ulnaris muscle
H	Number of stiffness state classifications
M	Number of joints
$\tilde{N}$	Number of active muscles
N	Number of muscles
TB	Triceps Brachii muscle
W	Wrist joint

Subscripts

0	Indicates values for the nominal case
a	Indicates values as generated by the exoskeleton
b	Indicates values at the target

d	Indicates desired values
ex	Indicates values as externally applied
e	Indicates values at arm end-point
h	Indicates values for haptic device
i	Indicates joint, $i = 1, \ldots, M$
j	Indicates muscle, $j = 1, \ldots, N$
k	Indicates classification state, $k = 1, \ldots, H$
l	Indicates values at the lower bound of the KKT condition
m	Indicates values measured by sensors
n	Indicates values for non-target active muscles
o	Indicates values for human operator
s	Indicates values for overshooting the target
t	Indicates values for target muscles
u	Indicates values at the upper bound of the KKT condition
v	Indicates values for inactive muscles
w	Indicates values as generated by the wearer

SUMMARY

Control of systems requiring direct physical human-robot interaction (pHRI) requires special consideration of the motion, dynamics, and control of both the human and the robot. Humans actively change their dynamic characteristics during motion, and robots should be designed with this in mind. Both the case of humans trying to control haptic robots using physical contact and the case of using wearable robots that must work with human muscles are pHRI systems.

Force feedback haptic devices require physical contact between the operator and the machine, which creates a coupled system. This human contact creates a situation in which the stiffness of the system changes based on how the operator modulates the stiffness of their arm. The natural human tendency is to increase arm stiffness to attempt to stabilize motion. However, this increases the overall stiffness of the system, making it more difficult to control and reducing stability. Instability poses a threat of injury or load damage for large assistive haptic devices with heavy loads. Controllers do not typically account for this, as operator stiffness is often not directly measurable. The common solution of using a controller with significantly increased controller damping has the disadvantage of slowing the device and decreasing operator efficiency. By expanding the information available to the controller, it can be designed to adjust a robot's motion based on the how the operator is interacting with it and allow for faster movement in low stiffness situations. This research explored the utility of a system that can estimate operator arm stiffness and compensate accordingly. By measuring muscle activity, a model of the human arm was utilized to estimate the stiffness level of the operator, and then adjust the gains of an impedance-based

controller to stabilize the device. This achieved the goal of reducing oscillations and increasing device performance, as demonstrated through a series of user trials with the device. Through the design of this system, the effectiveness of a variety of operator models were analyzed and several different controllers were explored. The final device has the potential to increase the performance of operators and reduce fatigue due to usage, which in industrial settings could translate into better efficiency and higher productivity.

Similarly, wearable robots must consider human muscle activity. Wearable robots, often called exoskeleton robots, are used for a variety of tasks, including force amplification, rehabilitation, and medical diagnosis. Force amplification exoskeletons operate much like haptic assist devices, and could leverage the same adaptive control system. The latter two types, however, are designed with the purpose of modulating human muscles, in which case the wearer's muscles must adapt to the way the robot moves, the reverse of the robot adapting to how the human moves. In this case, the robot controller must apply a force to the arm to cause the arm muscles to adapt and generate a specific muscle activity pattern. This related problem is explored and a muscle control algorithm is designed that allows a wearable robot to induce a specified muscle pattern in the wearer's arm.

The two problems, in which the robot must adapt to the human's motion and in which the robot must induce the human to adapt its motion, are related critical problems that must be solved to enable simple and natural physical human robot interaction.

CHAPTER I

INTRODUCTION

1.1 Motivation

As robotics technology advances, the area of human-robot interaction (HRI) is expanding rapidly. Robots can no longer be designed in isolation from the people that will use them, as typical industrial systems have been. HRI systems must consider that the human is an integral part of the system. This applies especially to physical human-robot interaction (pHRI) systems, where the the operator must make physical contact with the robot. For pHRI systems, the contact between the robot and the human gives a coupled system, so the robot must be designed based on an understanding of how the human will move and what the intended purpose of the system is.

Industrial settings are increasingly utilizing robotics and automation to streamline difficult jobs. However, some situations make the use of automated robots difficult due to the usually strict tolerances required for repetitive tasks. Vehicle assembly lines are one example of this situation, where the placement of a vehicle component, such as a door, must be done within tolerances, but the location of the vehicle itself may vary slightly. In this case, it is still more efficient to have a human accomplish the task. In addition, often the task requires a cautious force sensitivity that is best accomplished through human touch. However, components such as a car door can be heavier than a worker can lift. For this reason, assistive robotic devices can be useful in aiding the completion of this and other similar tasks through force amplification. While teleoperated systems could also be used, this removes the operator from directly participating in the task and uses remote sensing methods, introducing room for errors

and forcing users to move more slowly and cautiously. Therefore, a system that the operator could directly interact with is preferred.

Haptics is a popular control method, because operators find touch to be a very intuitive way for controlling a robotic device. Force feedback and haptic controllers are now common in areas from gaming to industrial machines. However, requiring physical contact between the operator and the robot introduces force feedback and creates a coupled operator-robot system. Various studies have shown that such a coupled system can result in reduced stability if not properly controlled. This instability can increase task completion time and decrease performance, making the job of the robot operator more difficult. In addition, it can be dangerous and creates an opportunity for injury to the robot operator or damage to the load of the device. The natural response of a human to unsteady or oscillatory motion is to increase stiffness in an attempt to control it. Unfortunately, this actually creates a stiffer coupled system, leading to more instability rather than less. Since generic robot controllers cannot directly measure the level of operator stiffness, most cannot adjust to such changes. A system that could access information about the operator and their method for interacting with the robot could adjust accordingly, and thereby increase stability, bolster operator and load safety, and make the task of the operator easier. This would enable increased operator performance, which in industrial settings can result in increased efficiency.

Another type of pHRI system involves the situation where a robot is attempting to modulate the fashion in which the user is moving. This is most often seen with wearable robots, or exoskeleton robots, which are often used also for force amplification, as well as for medical diagnosis or rehabilitation. In these systems, the robot is designed to change the way the wearer would normally move. Rehabilitation or diagnosis systems attempt to specifically generate a desired motion or force level. To do this, they must apply very specific forces to induce the desired muscle forces and

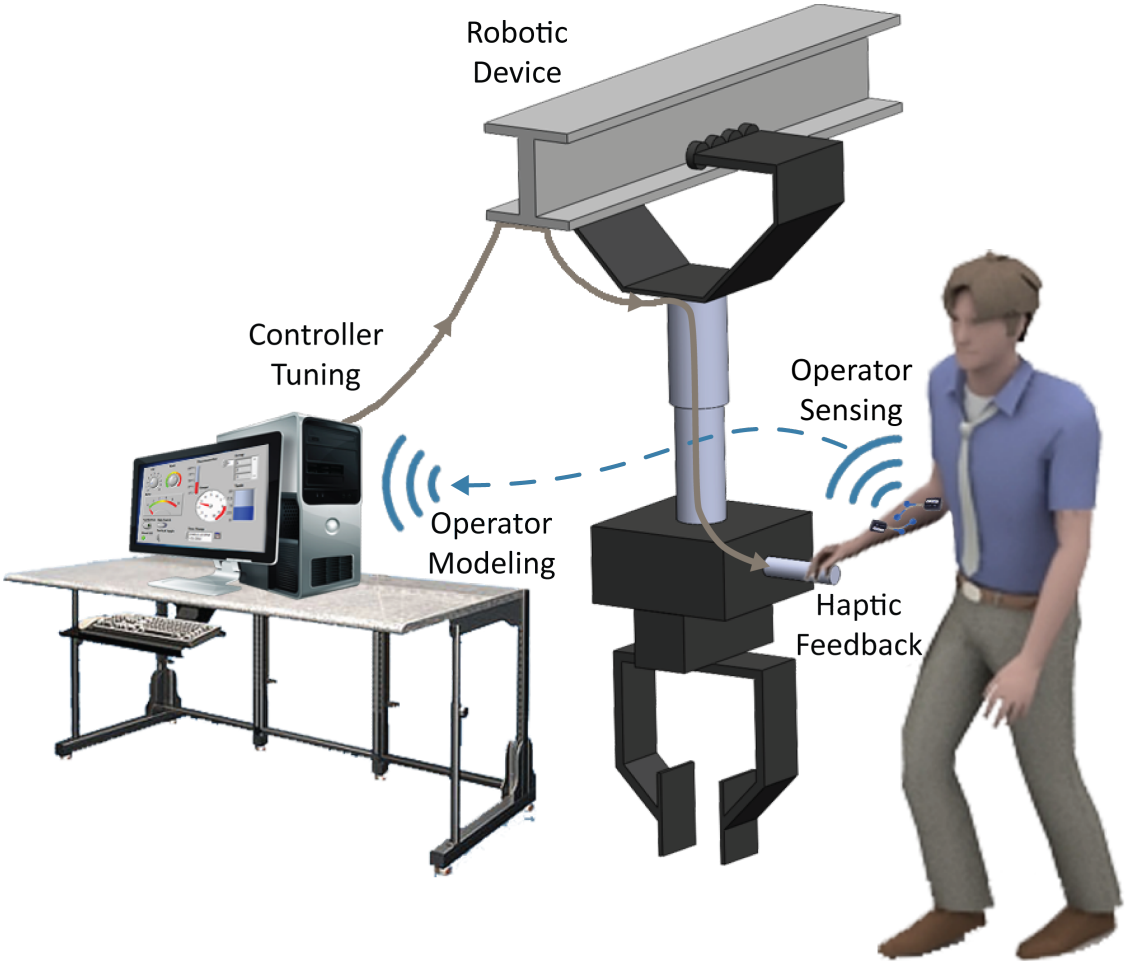

Figure 1: Conceptual drawing of a haptically controlled robotic device with a controller that adjusts based on estimated operator model

motion. Therefore, a control system must be designed that can predict the necessary joint torques to be applied to generate this desired muscle activity pattern.

1.2 Overview

As a proposed solution to the problem of a pHRI robot that must account for modulations in the way a human operator moves, this research developed a method that will allow a haptic robot controller to adjust to changes in the manner in which the operator is interacting with the robot by expanding the information available about the operator to the controller. Figure 1 shows a conceptual illustration of how the system should operate. The designed system will measure metrics that have been shown

to be indicative of how the operator is intending to move the device, and incorporate them into a model of the operator. This model will then estimate the operator's current motion, which can be used to adjust the gains of the robot's controller to assist the operator. Modeling the operator in this way allows the robot to actively adjust to changes in the way the operator moves, ensuring stability and ease of use. It may also be possible to design a more robust system that can accommodate a wider range of operator parameters, but these systems tend to result in lower performance in general, and higher performance and efficiency is beneficial in industrial settings.

Haptic systems, which require physical human robot interaction, create a coupled and bilateral system in which the device responds to the force applied by the operator and the operator adjusts the applied force based on the device's motion. Many haptic systems are designed to resist the motion of the operator so as to provide a virtual environment for them to feel [25, 62, 79, 92]. These systems enable people to receive force feedback from an environment they may not actually be located in, such as when controlling a teleoperated robot or maneuvering a virtual end effector in a digital environment. For the case of assisting the operator, many attempt to amplify their motion so as to enable increased capabilities [88–90, 104]. Some of the early ground work for such devices was laid by Kazerooni [91], which ultimately led to the design of a force amplifying exoskeleton system for human amplification [88, 89]. Li has also investigated force amplification control for industrial type robots, which allow an operator to lift objects heavier than what they would typically be capable of [103, 104]. Force assisting devices are the primary concern for this research, but some studies relative to other types of haptic devices may also be applicable. In all cases, the device is controlled based on the measured force applied by the operator.

The recognition of the difficulty of the contact induced instability in haptic devices has led to a number of recent advances in haptic interfaces. Early work by researchers such as Salisbury and Hogan established that impedance based control

methods that can modulate the device's impedance can be effective [78, 136]. This work also showed that there are some limitations on how operators can adapt to rapidly changing dynamics. It has been shown that there is a trade off between designing a system capable of high performance versus designing one with the requisite stability for safe operation [175]. Investigations into how humans handle the stable and unstable dynamics of such devices have revealed that people modulate their arm motion to help control unstable dynamics [50]. This has led to endeavors to find new and useful ways to measure the dynamic characteristics of the arm during interaction with haptic interfaces [72, 97], lessons from which can be used to determine the most effective way to estimate stiffness and enable the design of a control system that can adapt to them. Such compensating systems have recently been demonstrated to be capable of increased stability without sacrificing performance [115]

In industrial settings, there are several common tasks which operators perform often and which can be used to test the performance of haptic devices. The simplest is a basic point-to-point motion, where the operator must hold the device at one position, then move it to another position, then hold the device at the final position. From this basic task comes two more advanced motions. In a pick-and-place task, the goal is to use the device to pick up an object, then move it to another location, and place it down with some precision. This requires steadying the device to both align with the object to be picked up, then again to align the object with the location where it is to be set down. An example of such a task is picking up a part that must be placed in a certain location on an assembly. Similarly, in a peg-in-hole task, the operator must take the device, and align some object or end effector with a small target, typically a hole. This requires steadying the device during motion to insert the object or end effector into the hole. An example of such a motion is drilling or screwing parts together. For all these tasks, it is desirable that the motion phase allow smooth and easy motion, while the steadying phase allows the operator to easily

stabilize the device and avoid excessive oscillations.

The goal of a more responsive yet equally stable system requires investigating a variety of topics related to both human physiology and robot mechanics and controls. Therefore, this research began by considering human muscles and the causes of arm stiffness, along with the effect on the stability of haptic force assist devices. It was then necessary to develop a model of the human arm which can accurately provide a haptic controller with information about the mechanical properties of the operator. Subsequently, a robust controller that can dynamically vary its control parameters based on this information was needed. The final goal was to demonstrate both improved stability and higher performance with such an integrated human model and controller on a haptic force assist device [56–58].

To achieve these objectives, a system was designed and tested as a proof of concept that modeled the operator's arm stiffness, and adjusted the characteristics of an impedance controller accordingly. The sequence of tasks for this system is represented by Figure 2. Since stiffness is not directly measurable in typical control situations, it recorded muscle activity using electromyogram (EMG) signals, which provided an estimate of stiffness from. The muscles used were justified based on a musculoskeletal model of the human arm. The system was tested experimentally with human subjects to ensure its feasibility and measure its effect on stability and performance. Based on the results of initial trials, several methods were developed that could adapt to the observed non-deterministic nature of operator force and stiffness generation. These relied on advance probabilistic models and optimal controllers designed to handle varying system parameters to achieve further increases in performance. Ultimately, this research should lead to an industrially viable system for making robot operation easier. The results could be used in the design and control of various human-machine interfaces with applications to many areas of robotics, such as industrial assembly lines robots or space robots.

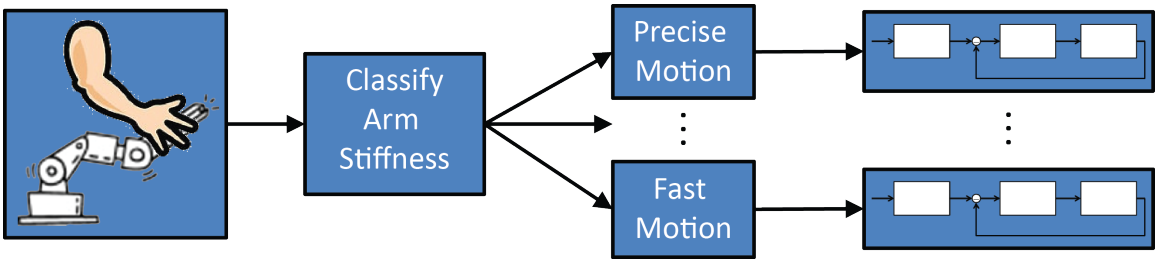

Figure 2: Basic tasks of compensating system

The problem of exoskeleton robotics is a related pHRI concern, and force assisting exoskeletons would benefit from the use of such an adapting system as well. However, rehabilitation or diagnosis exoskeleton systems must deal with the reverse problem. Rather than the robot adapting to the desired motion of the human, the goal is to have the wearer adapt to the desired motion of the robot. Therefore, the inverse system must be designed. However, targeting a specific muscle or group of muscles can be difficult, due to the large number of muscles compared to the relatively small number of joints where torque may be applied. With a mathematical formulation for a muscle activation pattern for a given applied loading, it should be possible to perform the inverse calculation and find the required applied loading to achieve a certain activation pattern for some target muscles. To accomplish this objective, the mechanisms of redundant muscle coordination during human-robot physical interaction need to be rigorously formulated and understood. Such a method has been developed by [35, 149, 150, 152], wherein it is possible to provide target forces for a certain subset of arm muscles. However, the developed method has limitations and works only if certain feasibility criteria are met. Therefore, it is advantageous to develop a relaxed formulation that is more widely applicable [55].

To thoroughly discuss the challenges associated with the problem posed in this chapter, this thesis will explore each topic individually, then present the integrated system. Chapter 2 will discuss the topic of human muscle and arm stiffness and the challenges associated with measuring it. It will look at a detailed muscle model of the

arm to understand how muscle cocontraction leads to increased arm stiffness. Based on this information, Chapter 3 will describe methodologies for estimating operator motion. It will introduce a simplified arm model that is usable in a real time controller, then present two different methods for informing the controller of the system state. Chapter 4 will examine haptic control methods and ways to account for non-deterministic system parameters. It will present three different methods which were proposed for handling the fact that human arm stiffness is an inherently stochastic quantity. A prototype integrated system will be presented in Chapter 5. The results of a series of user studies performed to evaluate its effectiveness will also be discussed. The related pHRI problem of controlling the muscle forces of a person using a wearable exoskeleton robot will be discussed in Chapter 6. An existing but restrictive method will be presented, and a more versatile methodology will be developed. Finally, the research will be summarized and its implications will be discussed in Chapter 7, which will also propose potential future enhancements.

1.3 Testbed Devices

To enable to the design of the systems discussed in Section 1.2, devices were used that enabled easy implementation and testing.

1.3.1 1-DOF Haptic Paddle

For testing of the force feedback adapting system, a small robotic device was desired that would simulate large force assisting robotic devices. Therefore, a simple 1 degree of freedom (1-DOF) device was produced that could create haptic feedback by means of a force either impeding or assisting the user's motion. The design chosen was that of a haptic paddle and was influenced by small haptic feedback devices such as the Phantom devices manufactured by Sensable [110] and several other haptic paddle designs [14, 63, 65, 133, 164]. This design was chosen for its versatility and low cost, but was modified and scaled up for increased force capability. This research

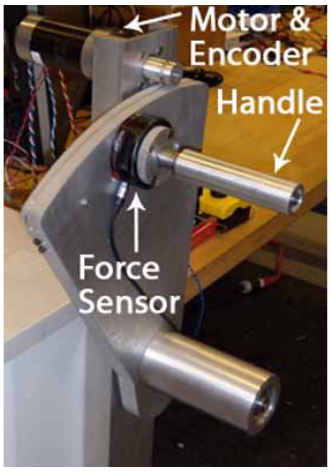

(a) One degree of freedom haptic paddle

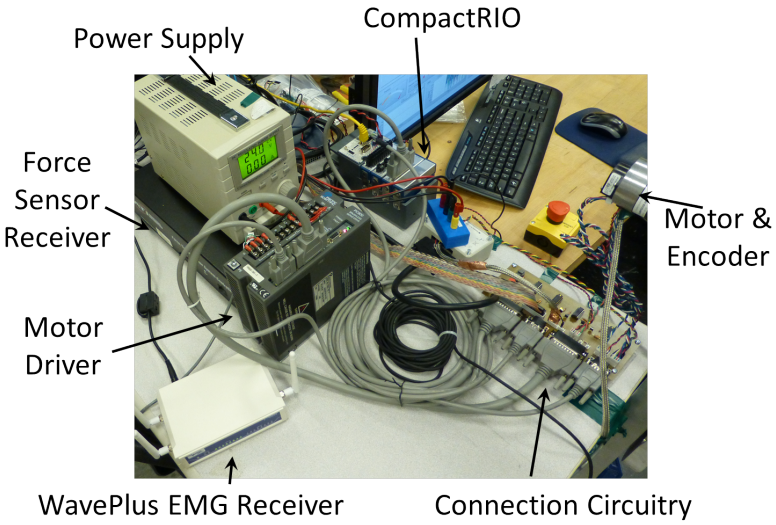

(b) Components to operate the haptic device

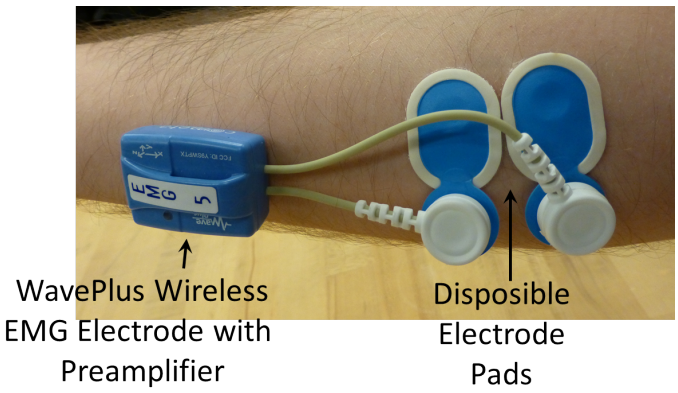

(c) Wireless EMG electrode

Figure 3: The one degree of freedom haptic device and control system

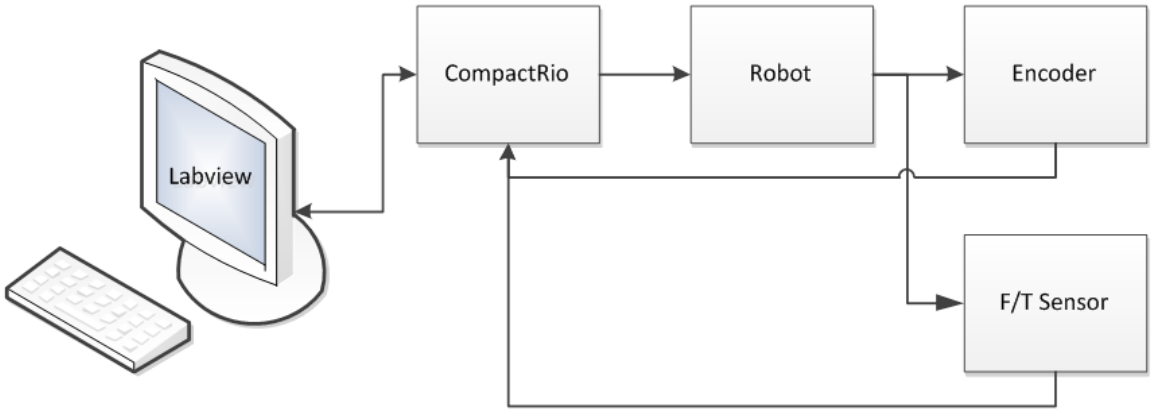

Figure 4: Diagram of system connections

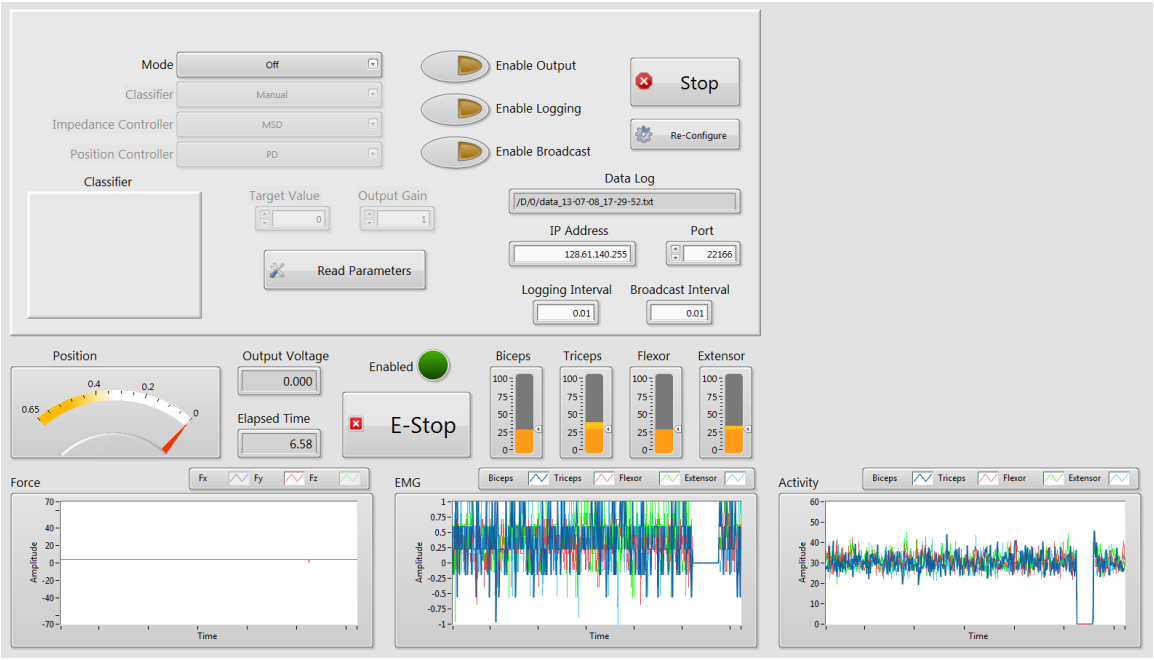

Figure 5: LabView interface for controlling device

also required testing with human subjects, so the robotic device was designed using a cable drive system. This ensured that the device was still compliant to the forces applied by the user while also amplifying the force produced to the motor.

The final design is shown in Figure 3(a). The position of the device is measured as an angle, θ, in the clockwise direction when looking at the device from the front, as shown by Figure 6. The device can generate up to 100 N of force at the handle and gives a frequency response of up to 10 Hz, shown in Figure 7, utilizing a brushless DC

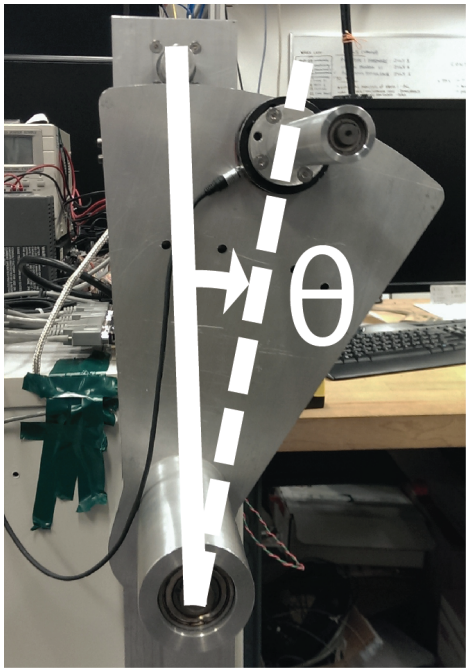

Figure 6: Schematic showing how device position is measured

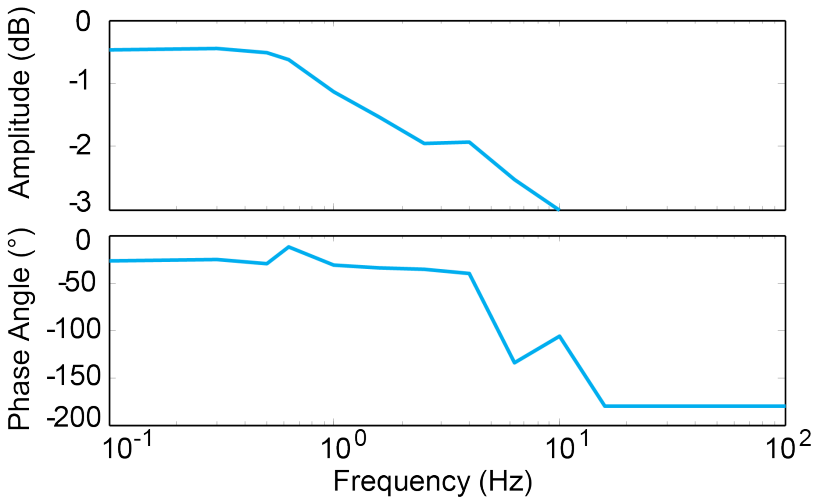

Figure 7: Frequency response of haptic device

motor from Anaheim Automation and Pacific Scientific motor driver capable of output at up to 16 kHz. A CompactRIO real-time controller with an embedded FPGA was used in combination with LabView to run the device, with the LabView user interface shown in Figure 5. This allowed the control logic to run at up 1 kHz, though to match speed of the sensor processing, it was limited to 250 Hz. The device incorporated a

six-axis force and torque sensor by ATI Industrial Automation capable of measuring up to 67 N of force and 5.6 Nm of torque down to a resolution of 14 mN and 0.17 mNm, respectively. It was also equipped with an optical quadrature encoder by US Digital capable of 1000 counts per rotation. Factoring in the gearing of the motor and cable drive, this yields a resolution for the device's position of approximately 4.5×10^{-6} rad. These are all shown in Figure 3(b), and Figure 4 shows how the various system components were connected. This research utilized two different EMG measurement systems. Early work incorporated a Myopac Jr. system by RUN Technologies. Later work utilized a more advance wireless WavePlus system from Cometa Systems, shown in Figure 3(c). Further images and details can be found in Appendix A.1.

1.3.2 Upper Body Exoskeleton

The muscle control system was designed with wearable exoskeletons in mind. Therefore, it utilized a wearable robotic device that used pneumatic actuators for some testing [149, 151]. The exoskeleton, shown in Figure 8, was developed to control the muscle forces of the human right arm. Figure 9 shows the structure of the 4-DOF robot, which uses 8 actuators to apply torques to the right arm: *a*) 1-DOF for the flexion/extension of the elbow joint, *b*) 1-DOF for the supination/pronation of the forearm, and *c*) 2 DOF for the flexion/extension and adduction/abduction of the wrist joint. The one of the pneumatic actuators used is shown in Figure 10, which has a 20 mm diameter, a maximum pressure of 0.4 MPa, and a maximum force of 60 N. Each of the actuators is equipped with a force transducer and controlled by a combination of feed forward and PI force feedback control so that it will contract when pressurized by a compressor controlled by an electropneumatic regulator. The actuators are also modeled as wires, which will apply forces to the joints when they contract, as shown in Figure 11. Both ends of each actuator are attached to plastic frames, which are then attached to a wearable jacket by Velcro tapes, which allows

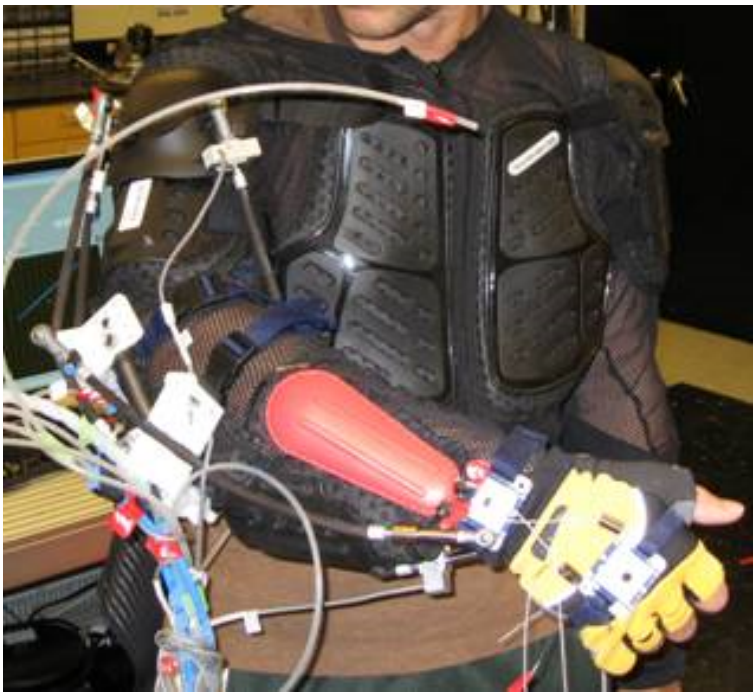

Figure 8: The complete exoskeleton device

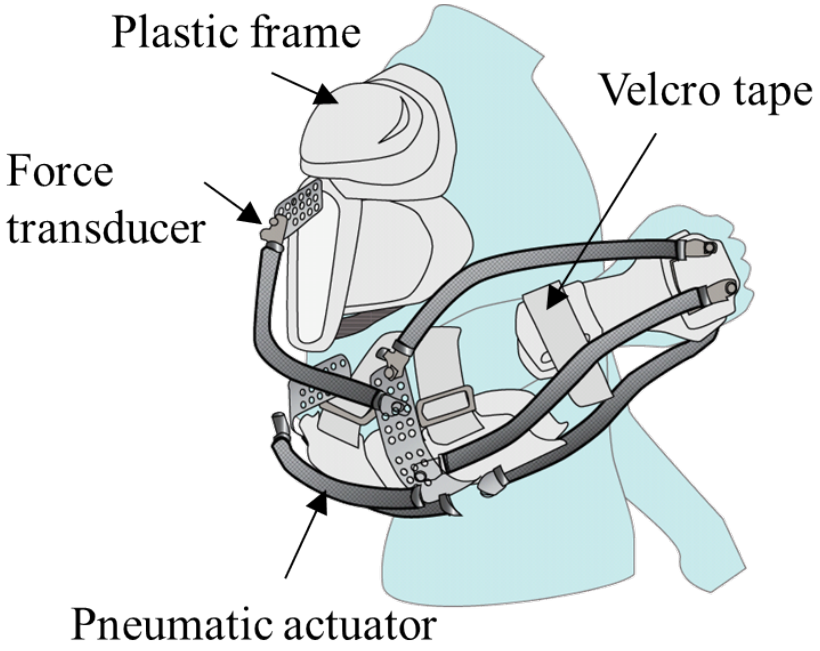

Figure 9: Schematic showing the components of the exoskeleton

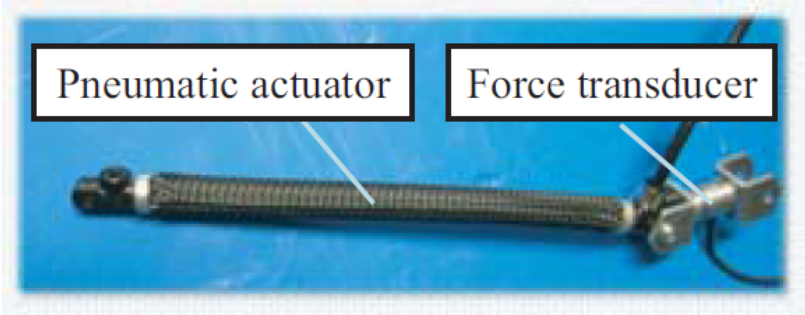

Figure 10: Pneumatic actuator used in the exoskeleton

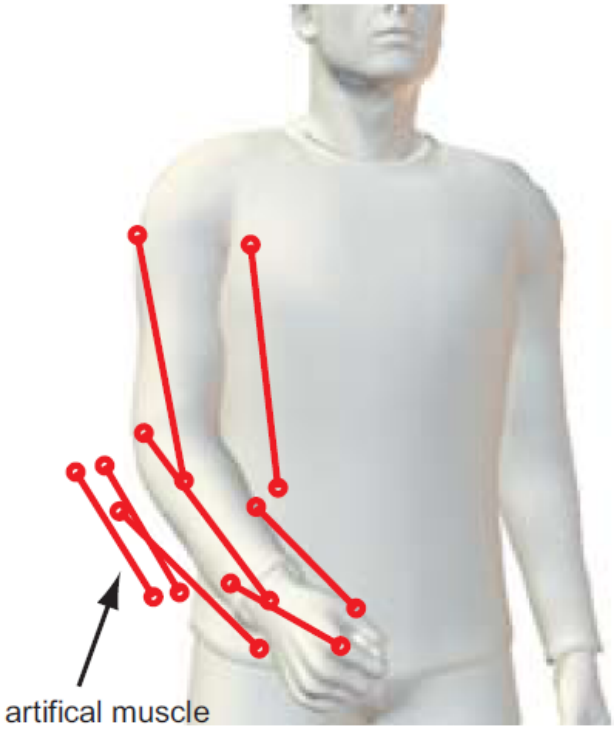

Figure 11: Exoskeleton actuator locations on the arm

the device to be adjustable to various body sizes. The total weight of the exoskeleton including the 8 pneumatic actuators, 8 force transducers, attachment frames, and tubings is 2.5 kg, which excludes pneumatic servo valves and a compressor.

Unlike many exoskeleton mechanisms, this device does not have any rigid link mechanisms, but only compliant pneumatic actuators for safety reasons. The maximum pressure of the compressor is limited so that the maximum force generated by a single actuator does not exceed 60 N. This force reduces as an actuator contracts

and becomes 0 N for around 12% of contraction. Therefore, the torques applied by the exoskeleton will reduce if the subject moves his/her joints along the directions of the applied forces, leading to weaker application of torques. The actuators are made from compliant rubber that does not require protective covers. In addition, no rigid member connects a joint to another, with only actuators connecting the joints, so the movement of a wearer is not kinematically constrained. Even though all the actuators exert their maximum forces, the aggregate joint torque generated by the robot is not strong so that a subject can move his or her joints by resisting the exoskeleton robot. This design ensures that the device is safe for wearers while still capable of applying forces to the joints for testing of the muscle force control algorithm. Further images and details can be found in Appendix A.2.

CHAPTER II

HUMAN ARM MUSCLES AND STIFFNESS

In order to design a system that can adapt based on the motion of an operator, it is necessary to establish a relationship between the arm muscles and the dynamic characteristics of the arm. Arm stiffness is an important factor in the stability of a haptic device, so the causes of arm stiffness were investigated. By utilizing the fact that muscle cocontraction contributes to increased arm stiffness, it was determined that stiffness could be estimated by measuring the activity level of antagonistic muscles. Using a model of the upper body, candidate muscle pairs were identified and a methodology for measuring cocontraction was designed.

2.1 Muscles and Stiffness

Under typical control situations, an operator's arm stiffness is not directly measurable. Stiffness is defined as the change in force over a change in distance from a given neutral point, and while the applied force is readily measurable with sensors, the change in distance is not. This is because as the operator moves, the neutral point moves as well. In addition, there are several different stiffnesses related to the motion of the human arm: *a*) muscle stiffness - the resistance of a single muscle to changes in length; *b*) joint stiffness - the resistance of a joint to changes in joint angle; and *c*) end-point stiffness - the resistance of the entire arm to changes in end-point location. End-point stiffness is of most interest for the design of the robotic controller, but it is affected by both individual muscle stiffnesses and joint stiffnesses.

The basis of much of our understanding of human muscles comes from Hill's work, which models muscles primarily as springs with a force generation component [54, 71], which is shown in Figure 12, as well as Bernstein's discussion of human motor control

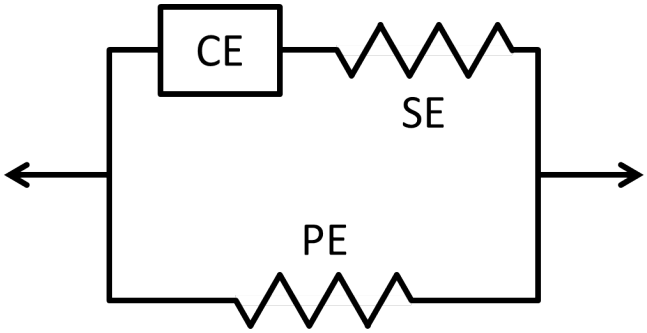

Figure 12: Hill model of a muscle, with a contractile element (CE) in series with a spring element (SE), which are together in parallel with another spring element (PE)

[10]. Muscles accomplish a variety of functions, acting as force generators and brakes to allow human locomotion [34], but their spring properties are of particular interest in understanding arm stiffness. It has been well established that muscles resist a change in length when contracting [68, 81]. Studies on their elastic properties have found that the spring constant of muscles is a nonlinear function of both generated force and length [116]. In addition, muscle stiffness can be separated into an intrinsic static component and a reflex-based component [94, 105, 140, 172]. The static component acts much like a traditional spring under a displacement, instantly supplying a force tending towards returning to the pre-displacement length. The reflex component of stiffness comes from the nervous system's reaction to an unintended change in muscle length, causing the muscle to generate more force to return to the pre-displacement length. This component is not instantaneous, but takes a small amount of time to respond. Under dynamic situations, large velocities can further change the intrinsic stiffness of the muscle [109]. In general, however, a muscle generating a larger force will exhibit a higher stiffness.

Since muscles can only provide contractive force, joints in the body normally have two or more opposing antagonistic muscles. Increases in joint stiffness have been linked to simultaneous activation of these muscles, or cocontraction [77, 142]. This leads to an increase in both force and stiffness of each muscle without a net change

in torque on the joint. Since a change in joint angle would lead to a change in the length of both muscles, this thereby increases the stiffness of the joint. This has been experimentally verified on many joints, including, the ankle, wrist, and trunk [30, 59, 64, 102, 114, 120, 155].

From a mechanical point of view, arm end-point stiffness is simply the result of several springs in series, since the stiffness of each joint affects the overall stiffness of the end-point [78, 112]. Therefore, any increase in joint stiffness will cause an increase in end-point stiffness. For this reason, cocontraction of antagonistic muscles in the arm will lead to higher end-point stiffness. An important consideration, however, is that the moment arm of a particular muscle on a given joint changes as the arm posture changes, so the stiffness of a joint will vary based on posture [117], affecting the end-point stiffness of the entire arm [46]. Several studies have shown that people generally can not control end-point stiffness independently of force and position [112, 128, 129], which implies that an estimate of end-point stiffness is indicative of either involuntary reactions to the environment or an intended voluntary applied force and motion. In general, these studies found a roughly linear increase in end-point stiffness with voluntary force.

The nonlinear effects of muscle activity on the motion and stiffness of a muscle are demonstrated in Hatze's thorough model of muscular motion [69, 70]. In his work, a complete force model of a muscle is developed as a function of muscle activity and activation rate, in which the the length and force of a muscle vary in a complex nonlinear fashion based on these two parameters. Similarly, the model presented by Zajac illustrates this nonlinearity [171]. Both authors show how the elastic properties of a muscle are influenced by the dynamic motion of the muscle. Since force and length vary based on muscle activity, and stiffness has been shown to be a nonlinear function of these two [116], it might be questioned how a linear approximation of muscle stiffness could be useful. However, both Hatze and Zajac go on to discuss

a simplified model which can linearly approximate a muscle's motion for a specific region away from the extremes of length and force, which corresponds to muscle activations of up to approximately one third of the maximum activation. In this region, therefore, it is reasonable to approximate a muscle with a linear spring.

Numerous studies have evaluated the response of humans to unexpected perturbations or instability when trying to control an object. It has been demonstrated that the brain attempts to correct for an inability to maintain a desired target by increasing arm stiffness, which is a result of increased cocontraction [8, 17, 30, 48, 49, 113, 114], and has a similar response when trying to resist movement [99, 147]. Also, the reverse has been demonstrated during smooth movements or when not trying to resist motion, which result in lower stiffness with less cocontraction [8, 30]. Therefore, for the purpose of designing a system to detect the body's reaction to unstable situations, it should be possible to measure the level of cocontraction in the operator's arm and use it as an indication of stiffness level.

2.2 Upper Body Musculoskeletal Model

Prior work by Ueda and Ding [35–37, 149–153] involved developing a computer model of the human musculoskeletal system in the upper body and arms. Figures 13 and 14 show the complete model of the arm. Due to the large difference between the number of muscles and the number joints, the problem has a large null space, within which the level of cocontraction can be varied without changing end-point force. As indicated by the literature presented in Section 2.1, this will lead to an overall increase in arm end-point stiffness. Together, this provides a thorough model of how arm muscle activity is modulated to lead to increased stiffness, and contributes useful information on how to estimate stiffness based on muscle activity.

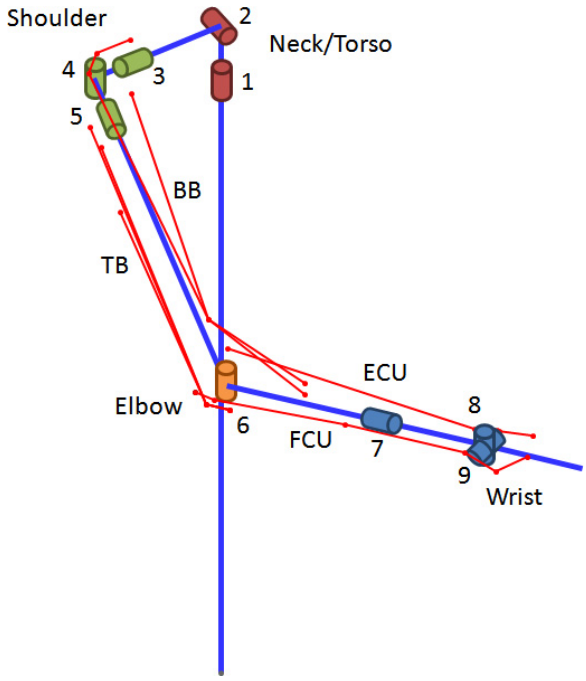

Figure 13: The 9 arm joints included in the musculoskeletal model with important muscles [149]

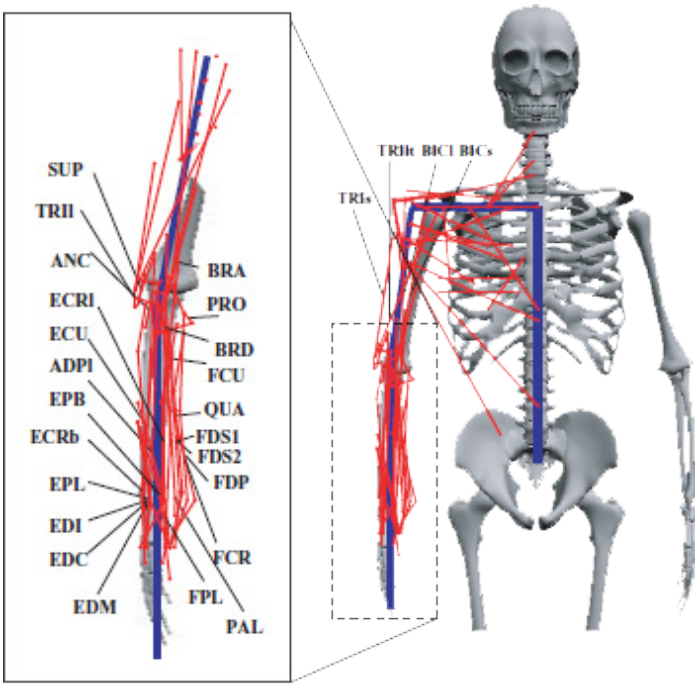

Figure 14: The 51 arm muscles included in the musculoskeletal model [149]

2.3 Level of Antagonism of Arm Muscles

Several candidate muscle groups that could provide the necessary cocontraction information were identified using the model by comparing the effect of various muscles on the wrist and elbow joints to determine the best antagonistic pairs to use. Each muscle's contribution to the torque on the arm joints can be represented using the moment arm matrix, $\boldsymbol{\Psi}$, such that the joint torques, $\boldsymbol{\tau}$, may be calculated if the muscle forces, $\boldsymbol{f}$, are known. The element at the ith row and jth column, ψ_{ij} gives the moment arm of muscle j on joint i. (1) gives this relationship, where $\boldsymbol{\Psi}$ is $M \times N$, $\boldsymbol{\tau}$ is of length M, and $\boldsymbol{f}$ is of length N for a human musculoskeletal model that has M joints and N muscles.

$$\boldsymbol{\tau} = \boldsymbol{\Psi} \boldsymbol{f} \tag{1}$$

For this model, $M = 9$ and $N = 51$. The contribution of a single muscle, j, is given by its moment arm vector, $\boldsymbol{\psi}_j$, which is the corresponding (jth) column of $\boldsymbol{\Psi}$. The angle between the moment arm vectors of two muscles, j_1 and j_2, can be found by taking the inner product as shown in (2).

$$\alpha = \cos^{-1} \frac{\langle \boldsymbol{\psi}_{j_1}, \boldsymbol{\psi}_{j_2} \rangle}{||\boldsymbol{\psi}_{j_1}|| \, ||\boldsymbol{\psi}_{j_2}||} = \cos^{-1} \frac{\boldsymbol{\psi}_{j_1}^{\mathsf{T}} \boldsymbol{\psi}_{j_2}}{||\boldsymbol{\psi}_{j_1}|| \, ||\boldsymbol{\psi}_{j_2}||} \tag{2}$$

Two completely antagonistic muscles would directly oppose one another, resulting in an angle of 180°.

In reality, each muscle contributes to the torque on multiple joints, so very few muscle pairs yield such direct antagonism. However, several good candidate pairs emerge from the primary muscles of the wrist (W) and elbow (E). Ultimately, one pair from each was chosen, with the first being the Biceps Brachii (BB) and Triceps

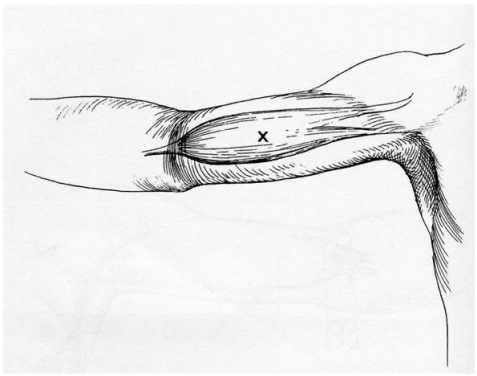

(a) Biceps Brachii (BB) muscle

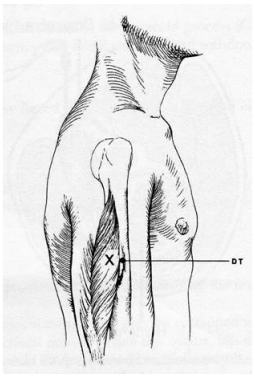

(b) Triceps Brachii (TB) muscle

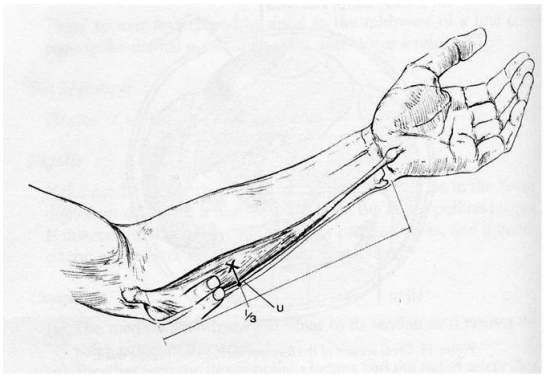

(c) Flexor Carpi Ulnaris (FCU) muscle

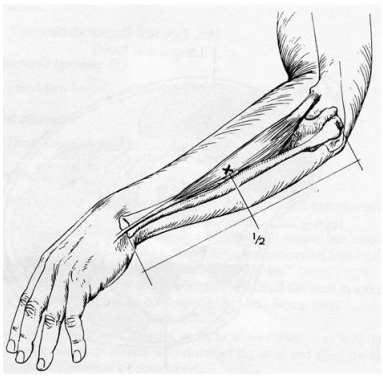

(d) Extensor Carpi Ulnaris (ECU) muscle

Figure 15: Locations of the muscles chosen [127, 131]

Brachii (TB) in the upper arm for the elbow and the second being the Flexor Carpi Ulnaris (FCU) and Extensor Carpi Ulnaris (ECU) in the lower arm for the wrist. Each of these is shown in the schematic in Figure 13, and their anatomical locations are shown in Figure 15. The moment arms of the BB/TB pair are compared visually in Figure 16(a) and yield an angle of 163°. It can be seen that these two muscles primarily affects joint 6, while also significantly affecting joint 3. In both cases, the effect of TB is opposite and nearly equal to that of BB. BB also has some effects on joints 4, 5, and 7, which explains why the angle is not a perfect 180°. Conveniently, both BB and TB are close to the skin and easily measured using non-invasive techniques. Similarly, the FCU/ECU pair are compared in Figure 16(b) and yield an angle of 100°. This pair does not exhibit the same level of perfect antagonism as TB and BB, but it is still clear that they act in opposite direction from each other.

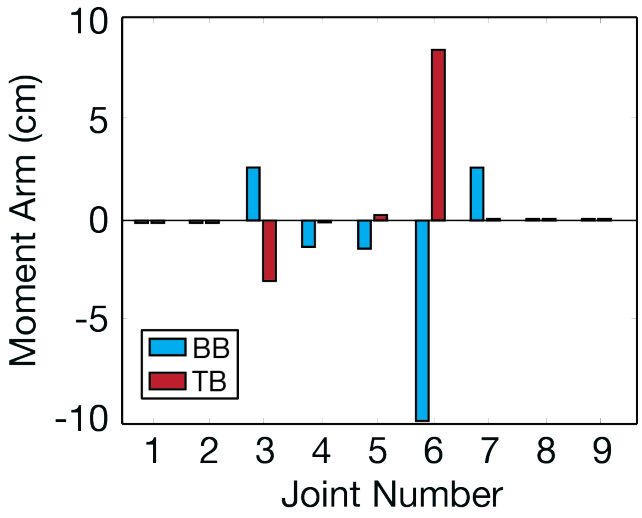

(a) BB & TB muscles

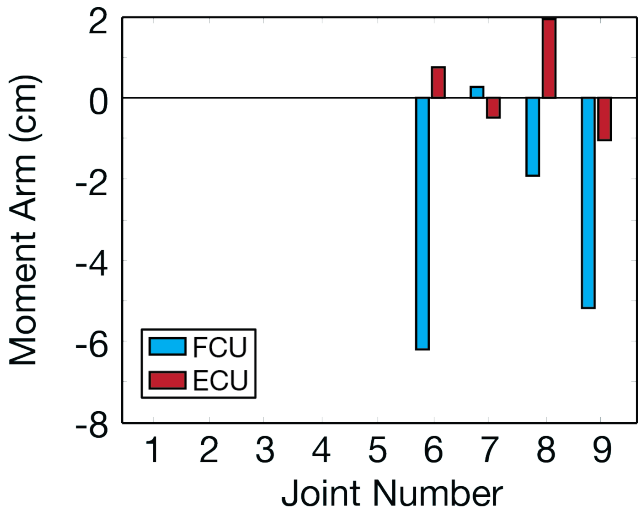

(b) FCU & ECU muscles

Figure 16: Comparison of moment arms on each arm joint for antagonistic pairs (See Figure 13 for joint numbers)

Both muscles have the same not insignificant effect on joint 9, which leads to an angle that is farther from 180° than the previous pair. However, neglecting this joint and considering only the first eight, an assumption that is justified by the testing hardware described in Section 1.3.1, in which the handle of the device is designed such that there should be little to no motion in joints 8 and 9, the muscles give an angle of 127°, which is a significant improvement. An alternative antagonistic pair in the wrist, the Flexor Carpi Radialis (FCR) and Extensor Carpi Radialis (ECR) provides an angle

of only 96°, which improves to only 114° when neglecting joint 9, and any other candidate muscles are not close enough to the skin to easily obtain accurate readings with non-invasive techniques [127, 131].

2.4 Measuring Cocontraction

While there exist a variety of methods for measuring muscle activity, electromyogram (EMG) measurements are an established technology that have frequently been used, and have been used for stiffness estimates [123, 124]. Alternatives such as ultrasound or mechanical vibration measurements either require larger, more bulky equipment or are less established in the literature, so EMG was used for all measurements in this research. To measure the level of cocontraction, one pair of electrodes was placed on each of the four muscles chosen, TB, BB, FCU, ECU. The EMG signals were used to calculate a measure of cocontraction for each antagonistic pair, E, W. EMG measurements are highly amplified because of the very small voltages that are measured in human muscles, which causes a high level of noise. Also, a raw EMG signal is an oscillatory signal with a mean value of zero, with muscle activity being a positive value given by the amplitude of the EMG signal. For this reason, it was necessary to process and filter the signals to acquire the desired value for muscle activity. The raw EMG signal for a given muscle, $EMG(t)$, $j = TB, BB, FCU, ECU$, was filtered by passing it through a 2 Hz low pass filter after being rectified to removing the DC component, resulting in the processed signal $EMG_j^*(t)$. To calibrate this, the maximum voluntary force (MVF) of each muscle, EMG_j^{MVF}, was measured by having the user generate the maximum force in their arm through a series of isometric contraction, and then was processed in the same manner. The processed signal was then normalized by its MVF as given by (3) to give the percent effort of a muscle, $EMG_j^{\%}(t)$.

$$EMG_j^{\%}(t) = \frac{EMG_j^*(t)}{EMG_j^{MVF}} \tag{3}$$

Finally, the cocontraction of each muscle pair, $CC_i(t)$, $i = E, W$, was found by taking the minimum level that both muscles of the pair were contracted to, as shown by (4).

$$\begin{aligned} CC_W(t) &= \min EMG_{FCU}^{\%}(t), EMG_{ECU}^{\%}(t) \\ CC_E(t) &= \min EMG_{BB}^{\%}(t), EMG_{TB}^{\%}(t) \end{aligned} \tag{4}$$

2.5 Cocontraction as Indicator of Stiffness

2.5.1 Concept

The use of EMG signals was experimentally validated to ensure this methodology, which is simplified from what previous studies have done, is justified. The stiffness of the operator, k_o, can be calculated from (5) if the base of a spring was fixed and the position, x_e and applied force, f_e, of the end were known.

$$f_e = k_o x_e \tag{5}$$

By controlling these values, only the EMG signal must be measured. This procedure was developed based on that used by several other studies [18, 118, 123, 124, 147].

Participants held the handle of a one degree of freedom (1-DOF) haptic paddle device discussed in Section 1.3.1 while the position and force were controlled as the two independent experimental variables. The stiffness, the desired independent variable, was then directly calculated from these values by recording their difference from the control inputs and modeled as an intermediate variable. The EMG signal for each muscle was recorded as the dependent variables. It was expected that the EMG

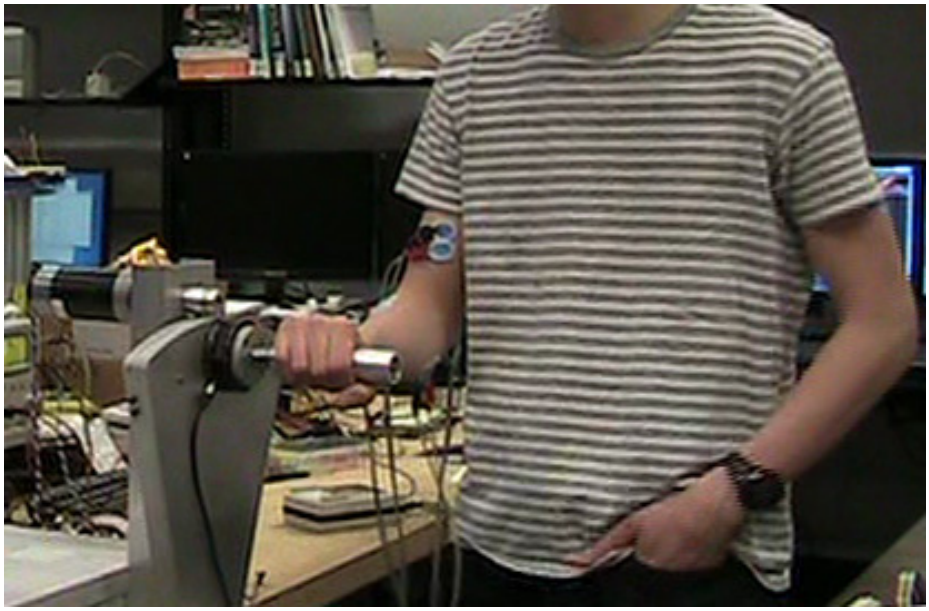

Figure 17: A participant performing the experiment

signals and stiffness value would covary throughout the experiment. To verify this as exhaustively as possible, this was done for a variety of stiffness values. Therefore, the force was tested at twenty levels evenly spaced from $f_h = 5\,\mathrm{N}, \ldots, 100\,\mathrm{N}$, and the handle position at three levels of $\theta = -20°, 0°, 20°$.

Since stiffness was the main value of interest, the individual combinations of force and position were not expected to influence the results significantly. However, the human arm is not necessarily a linear system, and it is possible that human muscles could exhibit other unexpected tendencies. The most exhaustive design that fully crossed the levels of force and position was used, leading to sixty cases. Each person's size and strength varied, introducing extraneous variables that complicated comparisons between individuals. For this reason, each experiment participant was asked to perform multiple trials of the experiment, covering all of the sixty cases. It was expected that each participant's results would follow the same general trend.

2.5.2 Method

Participants held device comfortably as shown in Figure 17. For each case, they were asked to hold the device stationary in the given position, then it applied a force against them. This required them to stiffen their arm to continue to hold the device in place, and the EMG signals for each of the four muscles were recorded. Learning effects associated with the task were expected to be insignificant due to its simple nature. The data was then analyzed to look for correlations between stiffness and EMG signal.

This experiment was performed following an approved Georgia Institute of Technology Institutional Review Board (IRB) protocol.

2.5.3 Analysis

A multiple regression/correlation (MRC) technique was used as in Cohen [21] to look for a relationship between the cocontraction values and arm stiffness. Another MRC was calculated using all four EMG signals as predictors instead of the two cocontractions for completeness. For both, the nominal values of device position and generated force were included to measure their influence on the relationship. For each regression, the values of the multiple correlation coefficient, R^2, (indicating the quality of the fit) and the zero-order correlation coefficients for each predictor, r_n^2's, (indicating predictor n's influence on the predicted variable's variance) were found. The results were expected to indicate a statistically significant relationship between cocontraction and stiffness and comparable results between EMG signals and stiffness, with no significant contribution to the variance of stiffness from position or force. The data from all participants was anonymized and processed using MATLAB software, while SPSS and G*Power 3.1 [43] were used for statistical analysis.

The number of participants was chosen based on the desired power, $1 - \beta$, of the resulting statistical analysis, which indicates the chance of statistical errors, β. Often

Table 1: Stiffness Correlation Experiment Participant Data

Total	Male	Female	Ages
4	4	0	20 - 26

chosen as $1-\beta = 0.95$, leaving a 5% chance of statistical errors, a higher desired power had to be chosen for this experiment due to the very large amount of data collected, which was well in excess of 200 points. For simplicity, trial data was filtered down to 10 points, which reduced noise without masking the main effects in the signal, giving 600 data points per subject. Using $1 - \beta = 0.9999$ required approximately 1,500 data points, which resulted in a 1 in approximately 10,000 chance of error and required at least three participants to obtain. A total of four trials of the experiment were completed, with Table 1 summarizing the participant demographics, resulting in roughly 2,000 data points. Due to the limits of the force sensor on the device, trials with very high forces could not be accurately read, reducing the number of usable data points to approximately 1,200, resulting in $1-\beta = 0.9976$ and a required critical $F = 4.69$ for statistical significance of the regression.

2.5.4 Results

The MRC method resulted in a cocontraction/stiffness relationship utilizing a logarithmic transformation that achieved $R^2 = 0.338$. Table 2 lists the variance of the stiffness partitioned amongst the predictor variables, indicating the degree to which each predictor contributed to a change in stiffness. The regression resulted in $F = 75.8$. The EMG/stiffness relationship with a similar transformation resulted in $R^2 = 0.377$ and $F = 59.8$, and the corresponding partitioning of the variance of the stiffness is shown in Table 3. Both regressions were statistically significant. Initial results not utilizing a logarithmic transformation provided a poorer fit, and since the fundamental form of the relationship between muscle activity and arm stiffness was unknown, data transformations such exponential and logarithmic were tested,

Table 2: Variance Partitioning for Cocontraction

Variable	r_n^2
Cocontraction (E)	11.7%
Cocontraction (W)	11.1%
Nominal Angle	0.2%
Nominal Force	28.7%

Table 3: Variance Partitioning for EMG

Variable	r_n^2
EMG (BB)	11.6%
EMG (TB)	16.0%
EMG (ECU)	8.0%
EMG (FCU)	12.9%
Nominal Angle	0.2%
Nominal Force	28.7%

with logarithmic providing the best fit. The stiffness data had a mean value of $k_o = 2.231\,{}^{\text{kN}}/_{\text{rad}}$ and the range $0.402\,{}^{\text{kN}}/_{\text{rad}} \leq k_o \leq 7.966\,{}^{\text{kN}}/_{\text{rad}}$ encompassing 95% of the data and was not characterized by a normal distribution, as shown in Figure 19(a). More detailed results can be found in Appendix B.1.

2.5.5 Discussion

The results indicated a statistically significant relationship exists that allows the use of measured EMG signals as a predictor of the operator's arm stiffness. The starting position of the device accounted for only 0.2% of the variance, as expected. However, the nominal force of each trial had a much larger effect on the regression than anticipated. The correlations would likely be insufficiently accurate for calculating exact values of end-point stiffness. However, the proposed system relies only on detecting changes in stiffness. Therefore, since an increase in cocontraction will always correlate to an increase in stiffness, the statistically significant results demonstrate the viability of using EMG signals in the controller design, and are consistent with published literature [123, 124].

2.6 Enabling Stiffness Estimation

The results of this chapter demonstrate that it is possible to estimate the end-point stiffness level of the human arm using EMG measurements. This is promising, as it ensures that the concept of an adjusting controller is plausible. Before designing the controller, however, it will be necessary to first analyze the stiffness information and determine how it relates to the motion of the operator.

CHAPTER III

CLASSIFICATION OF OPERATOR STIFFNESS

Using the cocontraction data, it was possible to design a system that could estimate the intended motion of the operator to be fed into the controller. Two types of systems were designed, which tackled the problem from different angles. First, a threshold based system was designed that could directly provide a controller with information about the user's arm stiffness level. This could be beneficial, as the controller would have an estimate of the actual level of stiffness and could modulate its parameters for this. However, it might be more useful to have an estimate of the actual phase of the motion that the operator is performing. A probabilistic model was designed that could accomplish this task. The two designs will be compared experimentally in later chapters.

3.1 Estimates of Stiffness

A variety of studies have endeavored to measure the dynamic characteristics of human joints [93, 97], and often the human arm can be modeled as a mass-spring-damper system for the purposes of haptic control interfaces and human robot interaction [41, 145, 148]. This allows for a useful and significant simplification from the previously developed detailed model, which was valid for only static situations. Measuring stiffness directly, however, requires a controlled situation that is not possible in the normal use of a haptic device, with most literature using specifically design setups that constrain the user's motion [18, 118, 123, 124, 147]. Therefore, it is desirable to use some correlated metric that is more easily measured to provide a rough estimate of arm stiffness level. Based on the discussion and analysis in Chapter 2, it should be possible to measure muscle activity so that cocontraction levels can be calculated and

provide an estimate of stiffness [18, 118, 147]. Alternatives have been proposed, such as introducing small vibrations into the motion of the device to obtain an indirect measure of arm stiffness [72]. This technique shows promise, but has some drawbacks for the types of systems this research is looking to control. Most importantly, introducing additional vibrations into a force amplifying system is undesirable.

3.2 Threshold-based Classification

Using the cocontraction level calculated, the estimated stiffness level, Z, of the operator's arm could be classified into H discrete levels, $z_1, z_2, \ldots, z_H$, using a simple threshold based approach. This method was chosen because the noise in the EMG readings made a continuous stiffness scale difficult to implement. This was done using a set $H-1$ adjustable thresholds, $\ell_{i1}, \ell_{i2}, \ldots, \ell_{i(H-1)}$, for each pair of muscles, $i = E, W$, based on (6), allowing the system to be tuned to the differences in each user.

$$Z = \begin{cases} z_K & \text{if } C_W(t) \geq \ell_{W(H-1)} \text{ or } C_E(t) \geq \ell_{E(H-1)} \\ z_{K-1} & \text{if } C_W(t) \geq \ell_{W(H-2)} \text{ or } C_E(t) \geq \ell_{E(H-2)} \\ \vdots & \\ z_2 & \text{if } C_W(t) \geq \ell_{W1} \text{ or } C_E(t) \geq \ell_{E1} \\ z_1 & \text{if } C_W(t) < \ell_{W1} \text{ and } C_E(t) < \ell_{E1} \end{cases} \tag{6}$$

To avoid excessive oscillation between states, the state only changed when the cocontraction level crossed the threshold for some finite amount of time. In addition, the signals were filtered as described in Section 2.4 to reduce noise, adding to the time that the signal must exceed the threshold to be registered and helping with this issue.

Figure 18 shows the distribution of stiffness points collected from the experiment

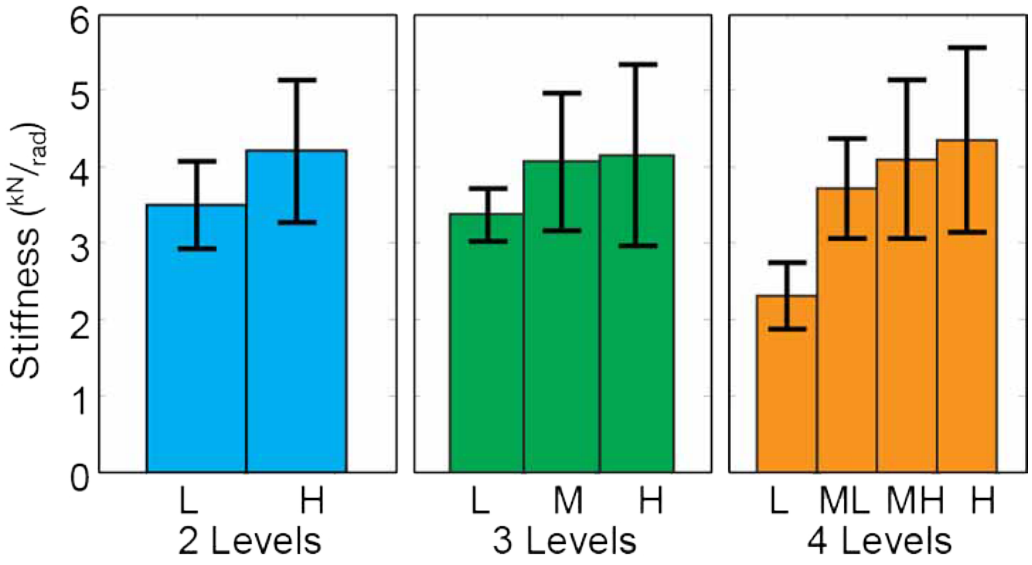

Figure 18: Average of classified stiffness levels for experimental data, error bars show standard deviation of classified points.

of Section 2.5 as classified using the threshold based method on the measured cocontraction. Classifying with more than two levels using evenly distributed thresholds gave little significant difference between the higher levels, and the best performance was obtained with only two levels. While a finer discretization could likely provide smoother adjustments in the final system, it would require more accurate measurements of cocontraction than what is possible currently.

Further analysis of the collected data indicated that the operator's strategy for choosing the appropriate stiffness level for a given situation was not straightforward. It would be expected for a person to choose a stiffness level that is just high enough for the applied force, but the data showed that the stiffness level for a given applied force was inconsistent. While the strategy that a human uses to choose the appropriate stiffness level is unknown, it is clearly more complicated than balancing the applied force with minimum effort. Figure 19 shows that the data is neither normally nor uniformly distributed. While it does show a Poisson type shape, Figure 19(b) shows that such a fit is not ideal with an R^2 of only 0.780, as it poorly represents the higher stiffness levels recorded. Figure 19(c) shows a better candidate distribution,

the gamma distribution, with an improved R^2 of 0.872, which can more accurately represent these levels, but with the sacrifice of less accurately representing the drop off in the occurrences of stiffness levels above $2\,{}^{\mathrm{kN}}/_{\mathrm{rad}}$. Since Figure 18 demonstrates that classification into two levels worked well, the data was also fit to the sum of two Gaussian normal distributions. As shown by Figure 19(d), this provided a very close fit, with an even better R^2 of only 0.917. This gave a low stiffness distribution having a mean of $\mu_{k_o} = 1.067\,{}^{\mathrm{kN}}/_{\mathrm{rad}}$ and a standard deviation of $\sigma_{k_o} = 0.485\,{}^{\mathrm{kN}}/_{\mathrm{rad}}$ and a high stiffness distribution having a mean of $\mu_{k_o} = 2.734\,{}^{\mathrm{kN}}/_{\mathrm{rad}}$ and a standard deviation of $\sigma_{k_o} = 1.513\,{}^{\mathrm{kN}}/_{\mathrm{rad}}$.

3.3 Operator Intent Model Classification

3.3.1 Operator Intention

A threshold based classifier can provide only a rudimentary estimate of stiffness that essentially amounts to whether the stiffness is high or low. In reality, as shown by the variety of poor fits in Figure 19, it is difficult to fit the range of operator cocontraction levels into a small finite number of fixed bins. A model which can provide insight into what motion the operator is performing would be much more useful. A more advanced model should more accurately give the controller information not just about the estimated stiffness range, but about what the operator is intending to do with the device. In this way, the controller can adapt more specifically to the task at hand. For example, as discussed in Section 1.2, industrial devices are often used for pick-and-place tasks, in which an item must be picked up from one location, moved to another location, and placed down. In it's simplest form, this amounts to three distinct subtasks: an operator holding the device steady, moving to a target position, then holding the device steady at the target again, and finally relaxing to prepare for the next task. A classifier which could identify the intention of the human operator for each of the subtasks of this task, such as holding steady, moving, and relaxed, would

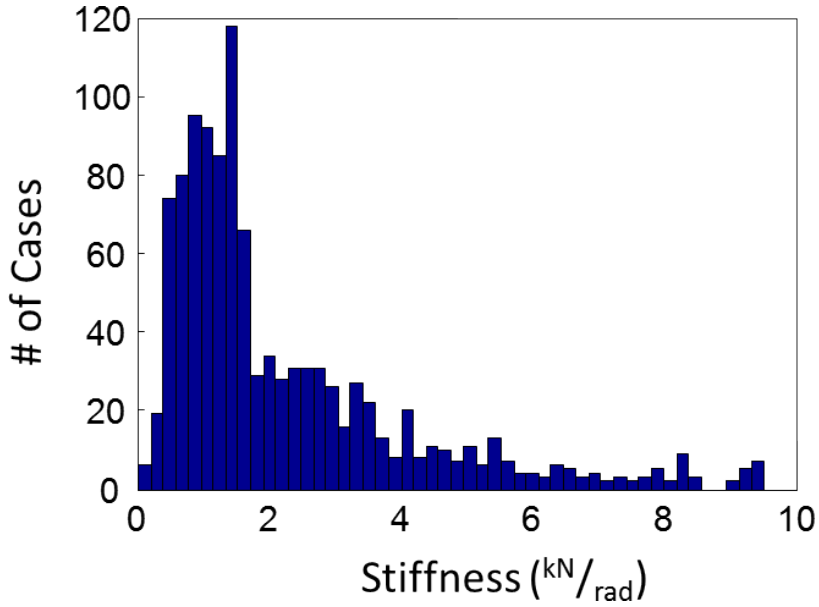

(a) Data demonstrates neither normal nor uniform distribution

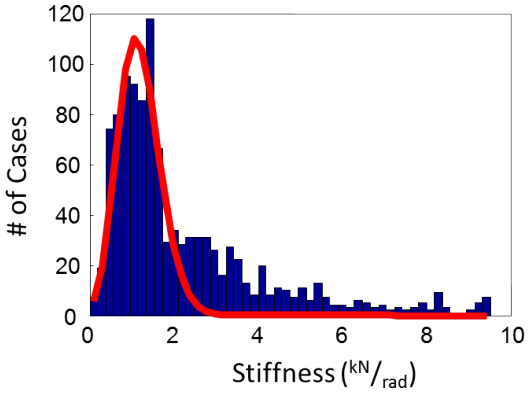

(b) Poisson distribution, $R^2 = 0.780$

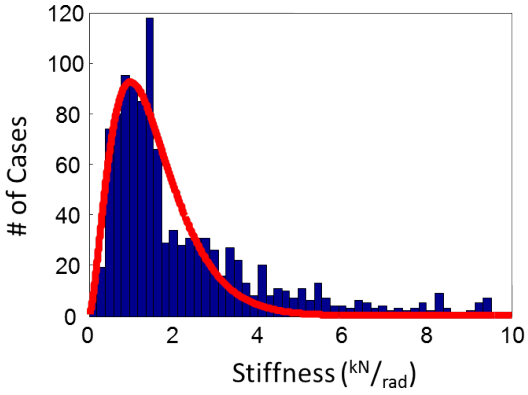

(c) Gamma distribution, $R^2 = 0.872$

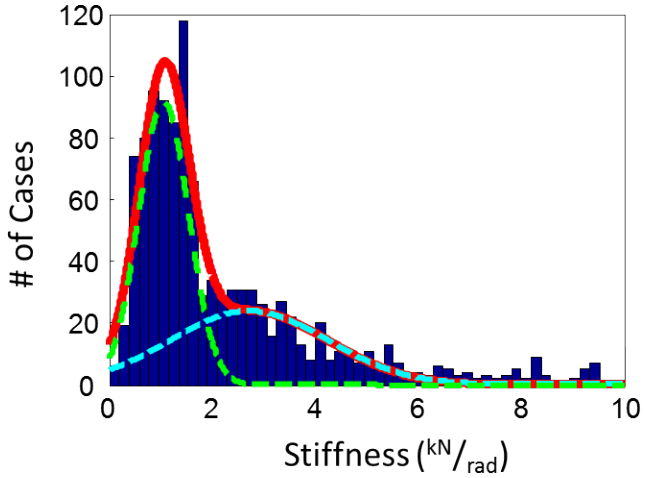

(d) Sum of two normal distributions, $R^2 = 0.917$

Figure 19: Histogram of stiffness data fit to various distributions

be much more useful than a simple threshold based system, allowing the controller to have multiple sets of gains tuned optimally for each phase of the task. Additionally, it would help overcome the limitations of a fixed threshold based system, including hysteresis and chatter between states when near the threshold.

The operator's intended subtask is not directly observable or measurable, but can often be estimated based on measurements that are known to correlate with certain intentions. Numerous studies exist about intention estimation and human-robot interaction, covering a variety of areas. Some perform a purely theoretical analysis of human intention [6], while others analyze methods for enabling human-robot interaction in both static and dynamic tasks. In general these studies relate to the cognitive side of human-robot interaction, where a robot is attempting to help a human accomplish a task [3, 74–76, 80, 95, 137]. There are several, however, that are concerned with predicting human motion for physical human-robot interaction [33, 87, 144, 156, 167]. The methods applied in those cases can be used here. For example, it has been demonstrated the when a person thinks about an object they want to move, they generally look at it [135]. Therefore, studies have used gaze following to estimate the most likely object a person is focusing on. In the same way, metrics such as muscle activity, body pose, and end point force are indicative to how a person is attempting to move a haptic robot. If a task can be divided into a finite number of unique subtasks, then a robot could use these metrics to estimate the most likely subtask that the operator is attempting to perform at the current time.

3.3.2 Hidden Markov Models

The subtask is a hidden state that is not directly observable by a robot, so it must be estimated based on observable metrics. For the purposes of the tasks associated with the industrial haptic devices considered previously, it can be assumed that the operator is only attempting to complete one subtask at a time, and therefore has

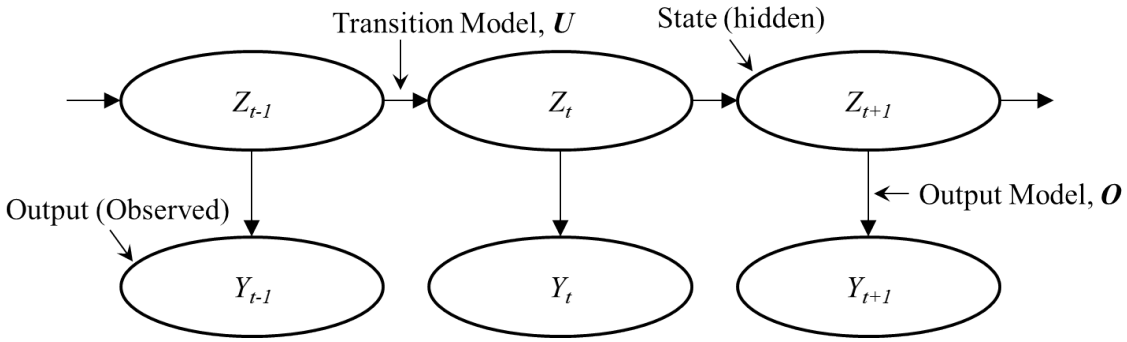

Figure 20: Representation of a Hidden Markov Model [134]

a single intention at any given time. Given these conditions, it is reasonable to use a probabilistic estimate of the current state of the operator's intention based on measurements of relevant metrics. Further, while the current intention depends on which part of the task was completed previously, and therefore on the most recent previous intention, it is reasonable to assume that intentional states beyond the most recent will have little to no effect on the current state, as the operator will likely only be concerned with which subtask comes next. Based on these assumptions, Hidden Markov Models (HMMs) are a natural choice for modeling the operator to estimate intention. Several studies have demonstrated the use of HMMs or related methods for estimating which of a finite number of intentions is most likely [33, 75, 76, 137, 144, 167]. Alternatives to HMMs exist, but are not as well suited to this problem. Deterministic classifiers, such as Artificial Neural Networks (ANNs) or Support Vector Machines (SVMs) would be applicable, but HMMs are more suited to detecting state transitions with temporal dynamics, and there is a significant body of existing work relating to their use for activity recognition. Also, the probabilistic parameters of an HMM can be estimated if initially unknown, and then can be fine tuned using experimental data if necessary.

A Hidden Markov Model, represented in Figure 20, is a probabilistic model relying on Bayesian probabilities that can estimate some current, unknown, hidden state, Z_t, from a finite list of possible states, $z_1, z_2, \ldots, z_H$, of a system based on the prior state,

Z_{t-1}, and current measurement of related metrics, Y_t. HMMs rely on the assumption that a system satisfies the criteria for a Markov process, mainly that the next state transition is dependent on only the current state, and not past history. In the case of the human-haptic device, this is reasonable, as it expected that a person will decide their next motion based on their current situation, not on the sequence of motions they had previously made. An HMM uses two models to do this: The transition model, $\boldsymbol{U} = P\left(Z_t|Z_{t-1}\right)$, which gives the probability of the each state following each other state, and is a $H \times H$ matrix; and the sensor model, $\boldsymbol{O} = P\left(Y_t|Z_t\right)$, which gives the probability of the the measured evidence value given each state. Given the two models, the current measurements, and the previous state, the probability of the system being in the current state can be found with Equation 7, where κ is a normalizing constant.

$$\mathrm{P}\left(Z_t|Y_1,\ldots,Y_t\right) = \kappa \mathrm{P}\left(Y_t|Z_t\right) \sum_{z_k} \mathrm{P}\left(Z_t|Z_{t-1}=z_k\right) \mathrm{P}\left(Z_{t-1}=z_k|Y_1,\ldots,Y_{t-1}\right) \quad (7)$$

Putting this equation in matrix form to obtain a vector of the probabilities for all states, $\boldsymbol{P}_t$, given the $H \times H$ transition probability matrix, $\boldsymbol{U}$, giving the chance of transition from each state to each other state, the diagonal $H \times H$ sensor likelihood matrix, $\boldsymbol{O}_t$ where the terms on the diagonal give the likelihood of each state given the current sensor measurement, and the previous likelihood vector, $\boldsymbol{P}_{t-1}$, yields (8).

$$\boldsymbol{P}_t = \kappa \boldsymbol{O}_t \boldsymbol{U} \boldsymbol{P}_{t-1} \quad (8)$$

This can be applied recursively to find the current state given the starting state, $\boldsymbol{P}_0$, and a sequence of sensor measurements, $\boldsymbol{O}_t$'s. Using this approach, called filtering, the most likely current state is the one with the highest probability [134]. The

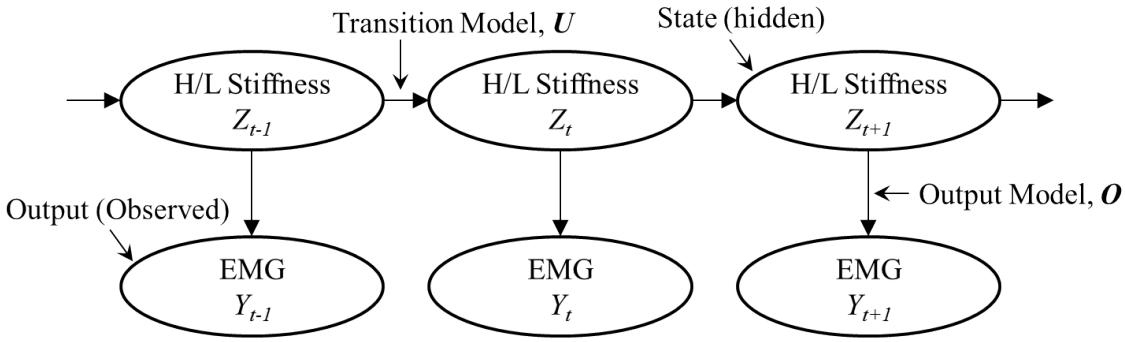

Figure 21: Representation of stiffness HMM

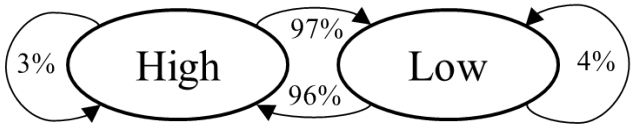

Figure 22: Transition model of stiffness HMM

controller would then use the parameters tuned for that state until the estimated state changes. The challenge then becomes determining $\boldsymbol{U}$ and $\boldsymbol{O}_t$ so as to provide accurate estimates. In addition, additional sensor readings can be omitted and the filtering propagated forward in time to predict future states. While this will only provide useful predictions for a small, finite time into the future, this can be useful for anticipating an operator's next motion and smoothing unnecessary state transitions.

3.3.3 HMM Stiffness Level Model

As a proof of concept, a simple HMM was developed to replicate the results of the threshold based stiffness classifier, which is shown in the diagram in Figure 21. It was trained using some of the experimental data collected from experimental volunteers while testing the prototype adjusting system, as described in Chapter 5. The sequence of states was identified manuall based on whether the stiffness exceeded the threshold or not, allowing calculation an estimated sensor model and transition model. An HMM is most commonly utilized in a discrete form, so the sensor data was discretized and binned. The HMM was then validated using the remaining data

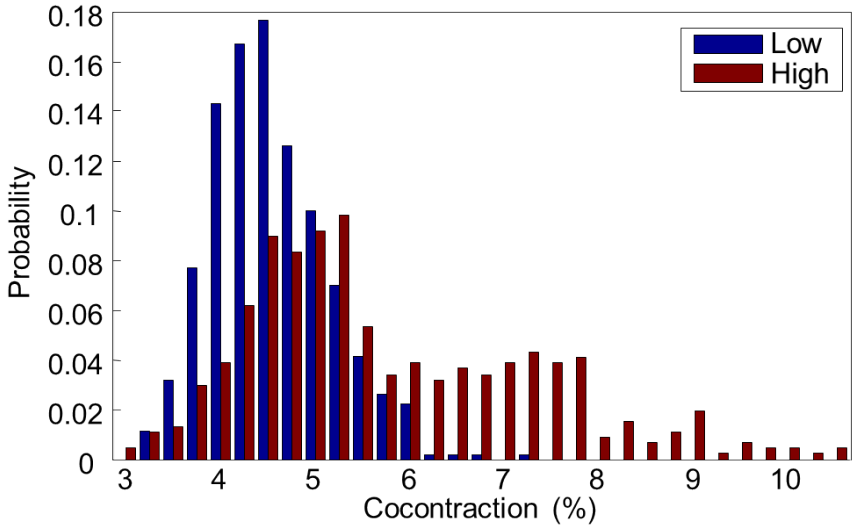

Figure 23: Sensor model of stiffness HMM showing probability of low (blue) and high (red) states for each level of cocontraction

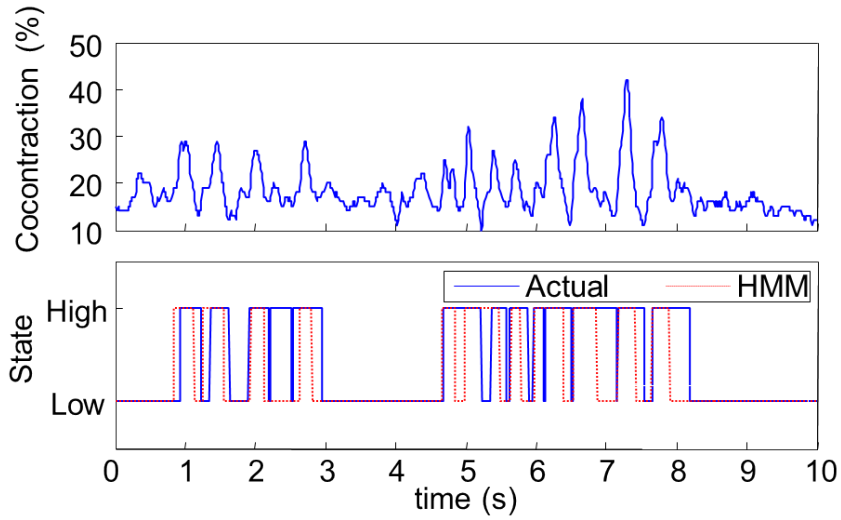

Figure 24: Results of stiffness HMM in simulation: Top - cocontraction data; Bottom - actual state identified with threshold classifier (solid blue) & estimated state (dashed red)

collected to find its accuracy. Figure 22 shows the estimated transition model, while Figure 23 shows the resultant sensor model. As expected, lower cocontraction gives a much higher probability of lower stiffness than higher stiffness. In addition, the

low stiffness case gives an approximately Gaussian distribution with a mean of of approximately 4% cocontraction. The high stiffness case is much more likely at higher cocontractions and gives a much wider distribution. This matches the results discussed in Section 2.5.5. The model was validated using a simulation which was fed actual recorded cocontraction data from testing, ensuring that the validation cocontraction data was different from that used for training the model. Figure 24 shows the results of the validation simulation along with the cocontraction data. The HMM generally reproduces the results of the threshold based stiffness classifier, providing 77% accuracy. While this is somewhat low, it is not unexpected. HMMs work best when classifying unique states rather than trying to identify whether a value is above or below a threshold.

3.3.4 HMM Intent Model

A more useful approach to using an HMM as a human operator model is to focus on intended subtask instead of stiffness level. While stiffness level is indicative of the operators motion, estimating the phase of motion itself will help eliminate some of the problems with the stochasticity and wide variability of human arm stiffness. Therefore, the HMM model was refined to be able to estimate which subtask of a given task an operator was performing. This gives the updated representation given in Figure 25, where the hidden state is no longer high or low stiffness, but is now one of a finite set of subtasks which the current task can be decomposed into.

As a concrete example, the pick-and-place task, discussed in Section 1.2, has the three distinct subtasks listed in Section 3.3.1: holding steady, moving, and relaxed. Using a similar process, the HMM was trained with actual cocontraction data collected during testing, in which the three states were known and identified, then validated using other cocontraction data. Figure 26 shows the resultant transition model between the three states, and Figure 27 gives the sensor model. Based on this,

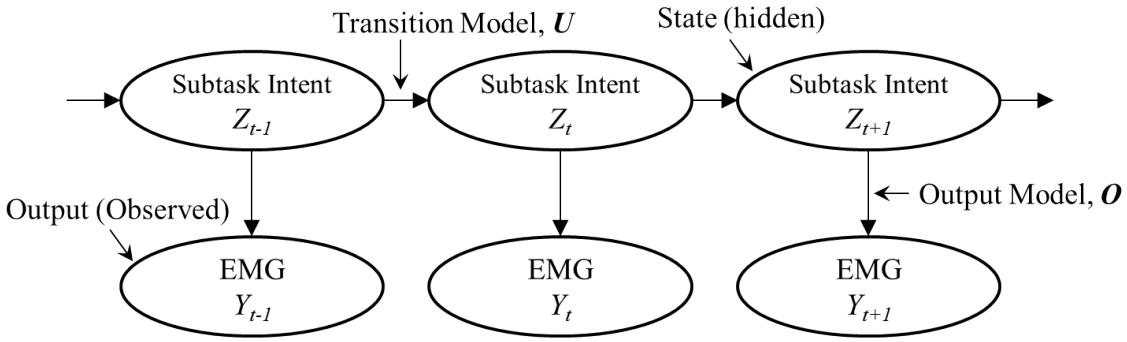

Figure 25: Representation of intended subtask HMM

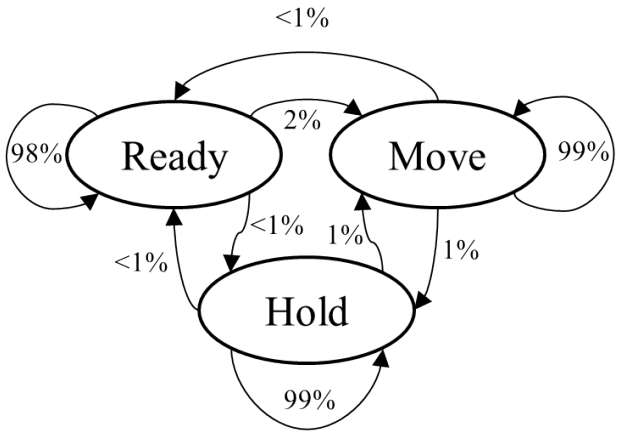

Figure 26: Transition model of intended subtask HMM

the simulation results, shown in Figure 28, provided a much higher accuracy of 87%.

3.4 Classification Enables Adaptive Control

This chapter established two methodologies for classifying the cocontraction data read from EMG signals into useful information to be fed to a device controller. The threshold based classifier performed best with two levels, and can enable an adaptive controller that is aware of the stiffness level of the user. The disadvantage, however, is its simplistic design, which may result in suboptimal performance. Alternatively, the probabilistic HMM can estimate the phase of motion of the user, though it requires more thorough training. If not trained properly, the accuracy of the classification may suffer. The next step in the process is the design of the adapting control system.

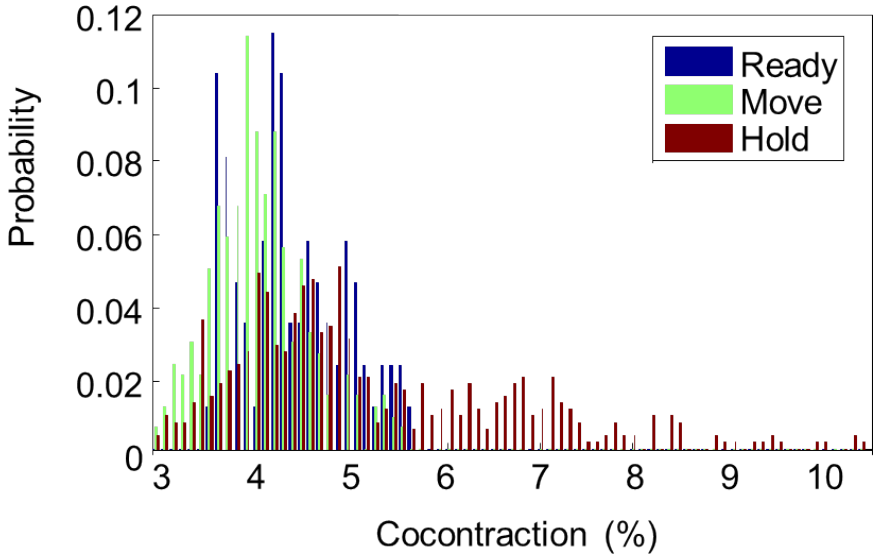

Figure 27: Sensor model of intended subtask HMM showing probability of each state for each level of cocontraction

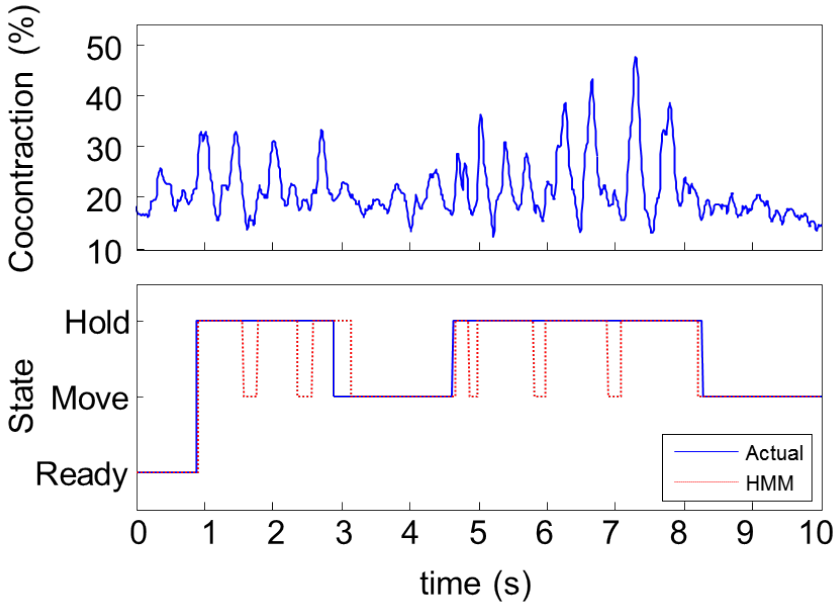

Figure 28: Results of intended subtask HMM in simulation: Top - cocontraction data; Bottom - actual state identified manually (solid blue) & estimated state (dashed red)

CHAPTER IV

FORCE AMPLIFYING HAPTIC CONTROL

Using the classifications provided by either the threshold system or the HMM system, an assistive controller can adjust its gains based on the current operator state. There are a variety of assistive control methods, but an impedance controller has been proven to be a reliable and simple way to control haptic devices. The impedance controller can estimate the motion of some desired system and feed this to a position controller that will track it. There is some flexibility, however, in the choice of the impedance controller, from simple methods such as a PD based control system, to more advanced optimal controllers. Since the human arm stiffness is inherently non-deterministic, some controllers capable of optimal control of stochastic systems were explored.

4.1 Assistive Control Methods

For the case of force assisting devices, the simplest control method is pure force amplification, where the force generated by the device is simply a gain multiplied by the applied force [138], as shown by Figure 29. This simple system, which requires no feedback, will scale up the measured operator's force, f_y, to generate an applied force, f_h, as given by (11), where γ is the control gain. The controller block in Figure 29 has the relatively simple transfer function given by (13), where $X(s)$, $T(s)$, $F_m(s)$ correspond to the position, motor torque, and measured force, respectively, in the s domain. Modeling the operator as a system with mass, m_o, damping, b_o, and stiffness, k_o, as discussed in Chapter 2 and the haptic device as having mass, m_h, damping, b_h, and stiffness, k_h, then (9) is the equation of motion of the contact point of the operator with the device and (10) is the equation of motion of the device itself. From these follows the derivation of (12), which is the equation of motion of a force

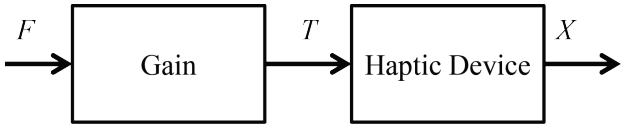

Figure 29: Control system to provide force assistance [138]

amplifying system, where f_o is felt by the operator. This demonstrates how the load on the operator is lessened by a factor of $1 + \gamma$ by the assistance of the controller. However, for large gains, this can be difficult and unnatural to control. Alternatively, an impedance controller is often used, as discussed in Section 4.2.

$$f_o - f_m = m_o\ddot{x} + b_o\dot{x} + k_o x \tag{9}$$

$$f_h + f_m = m_h\ddot{x} + b_h\dot{x} + k_h x \tag{10}$$

$$f_h = \gamma f_m \tag{11}$$

$$f_o = \left(m_o + \frac{m_h}{1+\gamma}\right)\ddot{x} + \left(b_o + \frac{b_h}{1+\gamma}\right)\dot{x} + \left(k_o + \frac{k_h}{1+\gamma}\right)x \tag{12}$$

$$\frac{T(s)}{F_m(s)} = \gamma \tag{13}$$

4.2 Impedance Control

Many haptic systems use impedance control, which, rather than simply scaling the applied force, generates an assistive force so as to mask the actual system dynamics

and allow the operator to feel a desired system with an arbitrary set of dynamic characteristics [138]. The control force is determined based on the desired mass, m_d, damping, b_d, and stiffness, k_d, as given by (14). When used on a robot, this can mask the device's dynamics, as shown by the equation of motion in (15). This makes the load on the user lighter and allows easier operation, which, when combined with haptic feedback, can give a very natural feeling to operating the robot. An impedance controller incorporates an outer force controller that finds the change in position, x_d, that the desired system would exhibit under the applied loading, with an inner position controller loop that attempts to drive the error, e, between this and the device position, x, to zero. Figure 30 shows the block diagram for such a system, which yields the transfer function for the outer block as given by (16), with X_d giving the desired position in the s domain, while the inner block can be any position controller, whose transfer function is assumed to be given by some function $G(s)$ as in (17), where E gives the error in position from X_d in the s domain. Using an impedance controller with an inner PD position controller with proportional gain K_p and derivative gain K_d provides the most basic impedance masking control scheme, with $G(s)$ given by (18).

$$f_h = (m_d - m_h)\,\ddot{x} + (b_d - b_h)\,\dot{x} + (k_d - k_h)\,x \tag{14}$$

$$f_o = (m_o + m_d)\,\ddot{x} + (b_o + b_d)\,\dot{x} + (k_o + k_d)\,x \tag{15}$$

$$\frac{X_d(s)}{F_m(s)} = \frac{1}{m_d s^2 + b_d s + k_d} \tag{16}$$

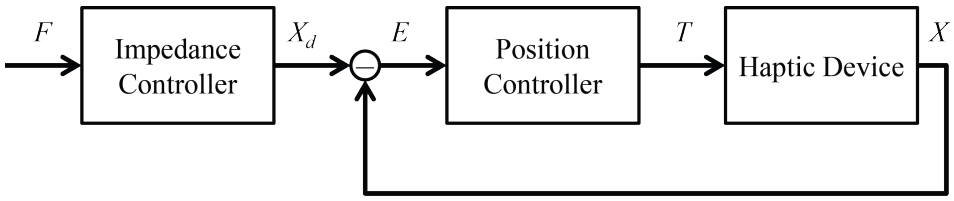

Figure 30: Block diagram of an impedance controlled system [138]

$$\frac{T(s)}{E(s)} = G(s) \tag{17}$$

$$\frac{T(s)}{E(s)} = D_1 s + D_2 \tag{18}$$

The actual desired position output from the impedance controller, x_d, can be calculated by integrating the standard equation of motion of an isolated mass-spring-damper system with the desired characteristics, given in (19). In most cases, it is desirable to eliminate stiffness from the model, otherwise the controller will naturally return to a set neutral point, which gives the differential equation in (20). Integrating and solving for x_d and $\dot{x}_d$, gives the desired motion to be passed to the position controller, shown in (21) and (22), where x_0 and $\dot{x}_0$ are the measured position and velocity of the system and δt is some time span that the motion is being predicted over. When converted to a discrete system, this will become the period of the control loop.

$$f_m = m_d \ddot{x}_d + b_d \dot{x}_d + k_d x_d \tag{19}$$

$$\ddot{x}_d = \frac{b_d \dot{x}_d - f_y}{m_d} \tag{20}$$

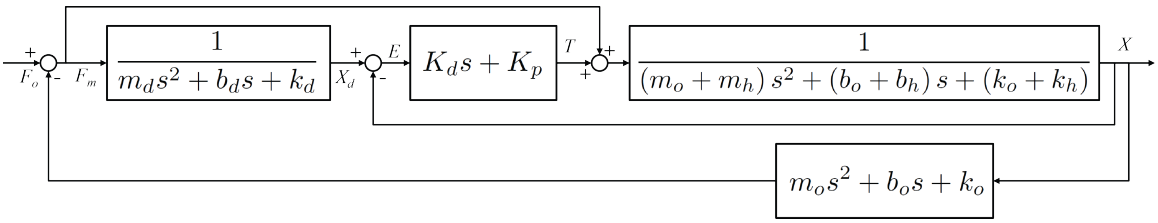

Figure 31: s domain block diagram of impedance controller utilizing PD inner position control and operator system

$$x_d = x_0 + \dot{x}_0 \frac{m_d}{b_d}\left(1 - e^{-\frac{b_d}{m_d}\delta t}\right) + f_m \frac{m_d}{b_d^2}\left(\frac{b_d}{m_d}\delta t - \left(1 - e^{-\frac{b_d}{m_d}\delta t}\right)\right) \tag{21}$$

$$\dot{x}_d = \dot{x}_0 e^{-\frac{b_d}{m_d}\delta t} + f_m \frac{1}{b_d}\left(1 - e^{-\frac{b_d}{m_d}\delta t}\right) \tag{22}$$

4.3 System Equations

Figure 31 shows the complete system, including an impedance controller with a PD inner position controller, device, and operator characteristics, in the s domain. To account for the fact that the measured force may not exactly equal the actual force applied to the handle, a feed forward element is included to transmit the applied force to the device. The impedance controller takes the measured force to calculate the desired motion, x_d, which is passed to the position controller. The position controller then passes the appropriate torqeu to the haptic device. The motion of the device and operator are a coupled system, incorporateing the dynamics of both. Finally, the operator dynamics close the force loop, creating additional feedback and adding to the conscious applied force of the operator, f_o. Based on Figure 31, the characteristic equation of the system can be derived, which gives a full transfer function from operator applied force to device position. This transfer function is shown by (23), where F_o is the operator's applied force in the s domain. Note that in this equation, it is assumed that the desired stiffness, k_d, and the device stiffness, k_h are zero or negligible.

$$\frac{X(s)}{F_o(s)} = \frac{G_1(s)}{G_2(s)G_3(s) + k_o G_4(s)} \tag{23}$$

where

$$G_1(s) = m_d s^2 + (b_d + K_d)\, s + K_p$$

$$G_2(s) = m_d s^2 + b_d s$$

$$G_3(s) = m_h s^2 + (b_h + K_d)\, s + K_p$$

$$G_4(s) = 2m_d s^2 + (2b_d + K_d)\, s + K_p$$

4.4 Human Contact Induced Instability

Devices using force control have been shown to become unstable under contact with stiff environments or the presence of a time delay, both of which are often present under contact with a human operator [24, 41, 148]. Human reaction times can be orders of magnitude larger than the typical period of a single control loop, and the demonstrated human reaction under instability is to increase contact stiffness. Introducing compliance into the robotic system can mitigate this issue, but this inherently decreases performance of the system, a trade off which has been well documented [23, 24, 41, 148]. Since the goal of the designed system is to increase performance, introducing a measure of compliance to the robot system would not be beneficial. Hogan has shown that users actively adapt to the changes in the way a device moves [78]. Studies have also shown that despite the induced unstable dynamics, operators can learn to control the device's trajectory [50], but that increased effort is required.

Stability of human-robot interaction using haptic systems has been analyzed using both root-locus methods [148] and Lyapunov theory [41]. These studies provided useful stability bounds, which were highly dependent on the stiffness of the human operator. However, these studies do not account for deliberate stiffening of the human operator's arm, and therefore are not sufficient for this design, which requires further

stability analysis. The stability of teleoperation systems is often viewed from the perspective of passivity, and this has been extended to haptic devices as well [24, 25, 66, 100, 103, 170]. While this could provide a useful condition for the stability of a system, force assisting devices are by nature not strictly passive. Several more recent studies have combined these two methods in a way that could be applicable to analyzing haptic force assistive systems [62, 79]. Studies have explored the design of robust controllers for interacting systems and teleoperation [2, 22, 23, 101, 170], but require a priori knowledge of the range of the system parameters.

4.5 System Stability

Due to the nature of the contribution of the operator stiffness, k_o, it cannot be isolated to be the loop gain of a unity-feedback system. Therefore, the stability analysis that follows is based on the closed-loop poles and zeros of the system, with k_o varied to determine its effect on stability. The characteristic equation gives Figure 32, which shows theses poles and zeros using two different set of desired impedance characteristics with zero operator stiffness. The trajectories indicate the movement of the poles as stiffness increases. When the operator stiffness is zero, all poles and zeros lie in the left half plane. As stiffness increases, the two real poles lying close to zero move leftward towards the zeros lying on the real axis. However, the two complex poles move into the right half plane and approach infinity, demonstrating the destabilizing effect of increased operator arm stiffness. The second set of poles shown in Figure 32 demonstrates the effect of varying the impedance controller characteristics. Increasing the damping, b_d, moves the complex poles to the left, while increasing the mass, m_d, slows the rate at which they move, keeping the system stable for higher stiffness values. The square in Figure 32 show this for a fixed $k_o = 4.0\,{}^{\mathrm{kN}}/_{\mathrm{rad}}$, which based on the data collected, is a typical value for high stiffness. In addition, force sensor data must be filtered, introducing a delay into the controller when converting to a discrete

time system for implementation, adding an additional destabilizing influence.

Using a 1-DOF haptic device of Section 1.3.1 as a testbed it was possible to reproduce the conditions under which the system grew unstable as operator arm stiffness increased. Figure 33 plots the magnitude of device oscillation while the operator attempts to hold the device steady, where ther color scale ranges from blue for little to no oscillation through yellow to red for large oscillations. The time delay for the force feedback and the stiffness of the operator's arm were independently varied to characterize the stability of the device. As either variable increased, the magnitude of the uncontrollable oscillation grew, as indicated by the red bars near the back of the plot. With no time delay and minimal stiffness, the device was much more stable, as indicated by the dark blue bars near the origin. This shows that the increased stiffness and time delay combine to prevent the system from remaining stable.

This simple pole-zero analysis, using the operator stiffness as the variable gain, demonstrates the contact instability in such devices, which is corroborated by experimental results. Passivity based analysis could provide sufficient criteria for stability, but tend to be very conservative, whereas the traditional pole-zero method is not. It is possible for a system to fail to meet passivity criteria and still remain stable. In addition, since force assistive devices are not strictly passive, such an analysis may break down for situations with contact induced instabilities that are not well modeled, as has been demonstrated by Li in his work with passivity and force assisting devices [103, 104]. Therefore, satisfying these conservative criteria or implementing a robust controller would result in a compromise in the desired performance of the system.

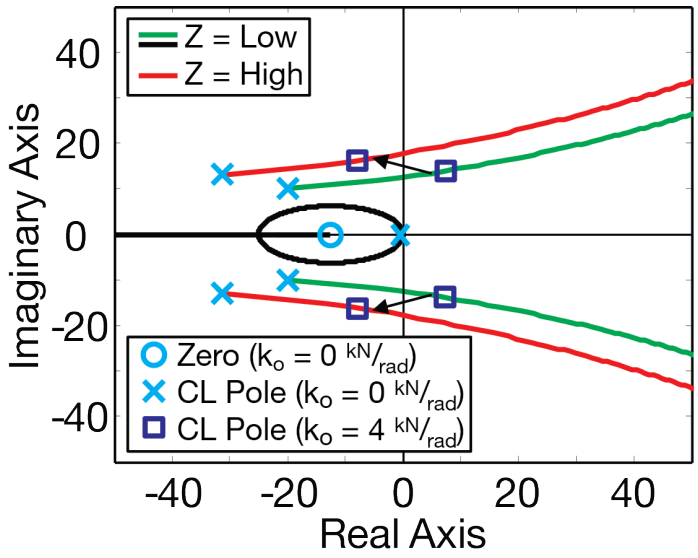

Figure 32: Controller-operator system root locus: 4 poles and 2 zeros shown for zero stiffness; as stiffness increases, 2 poles near zero move left towards 2 zeros (one is off left side of plot) and 2 complex poles move into right half plane towards infinity (Note that only the two unstable poles are shown for both low and high damping gains)

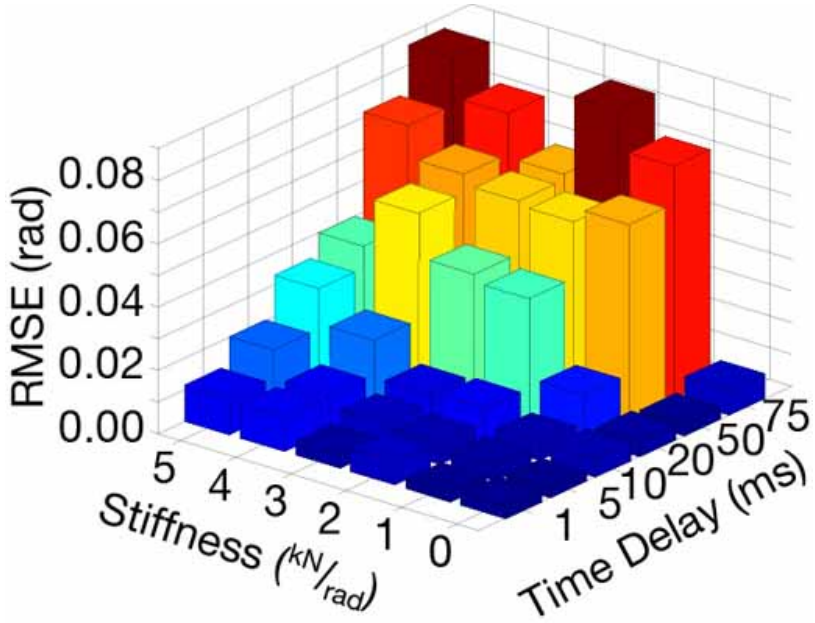

Figure 33: Larger oscillations (higher RMS error) as time delay and stiffness increase (red - large oscillations, blue - no oscillation)

4.6 Control of Stochastically Varying Systems

4.6.1 System Parameter Variation

As discussed in Chapter 3, human arm stiffness is an inherently stochastic value that is best modeled probabilistically. Humans do not deterministically generate force or stiffness based on any discernible criteria of the task they are performing. Since the complete system is coupled between the human and the device, this means that the overall system dynamics are changing in an unknown and stochastic manner from the controller's point of view. Therefore, it is desirable for the controller to be tolerant of these variances in the system parameters.

A typical mass-spring-damper system has the equation of motion given by (24), where the system input, u is the applied force [122].

$$\begin{aligned} \dot{x} &= \boldsymbol{A}x + \boldsymbol{B}u \qquad (24) \\ \text{where} \qquad \boldsymbol{A} &= \begin{bmatrix} 0 & 1 \\ -\frac{k}{m} & -\frac{b}{m} \end{bmatrix} \\ \boldsymbol{B} &= \begin{bmatrix} 0 \\ \frac{1}{m} \end{bmatrix} \end{aligned}$$

If the stiffness, k, and in the most general situation, the damping, b, is changing, then the $\boldsymbol{A}$ matrix is not constant. When its value with time is known, a control law can be designed around it. However, in the case of the coupled operator-robot system, this value is changing stochastically based on the response of the human. Therefore, it is desirable to utilize a controller designed for such a case of uncertain system parameters, which can be substituted for inner position controller in the impedance control scheme. This will ensure that even as the actual system parameters vary, the device can still maintain the motion of the desired system model. Since the range of

stiffness the operator generates can be found experimentally, an expected distribution can be found, allowing the design of a controller than is optimal for the expected range of values.

4.6.2 Linear Quadratic Gaussian Control

The Linear Quadratic Regulator (LQR) is a very common type of optimal controller that is designed to stabilize a system with a minimum amount of control effort [51, 82, 173, 174]. However, the design of an LQR controller requires full knowledge of the system parameters, and assumes they are time-invariant. The focus of early attempts to control stochastic systems involved modeling the variation as additive or multiplicative noise. Fleming and Dreyfus both provided a detailed look at early approaches to the problem [40, 47]. To further this foundation, De Koning generalized the concepts to stabilizability and observability to systems with stochastic parameters, allowing sufficient conditions regarding the stability of stochastic system controllers [28, 29]. The work of Kalman became a cornerstone of these efforts, as they provided a reliable way to estimate the state of a system under uncertainty and noise [82, 83]. Based on the resulting Kalman filter, an optimal controller was developed with a control law based that utilized the resulting model of the expected system state rather than the actual, potentially erroneous, sensor measurements [4, 5, 125]. This resulted in the Linear Quadratic Gaussian (LQG) control method, which combined a Kalman filter for state estimation with a LQR optimal controller, which has become one of the fundamental techniques for control under uncertainty.

Consider a discrete linear system given by (25), where the system matrices $\boldsymbol{A}$ and $\boldsymbol{B}$ are assumed time-invariant.

$$x_{t+1} = \boldsymbol{A}x_t + \boldsymbol{B}u_t \tag{25}$$

The standard LQR control input, given by (26), is derived from the goal of using the

optimal control input, $u_0, u_1, ..., u_t$, via the minimization of the cost function, J, shown in (27) for all t, where $\boldsymbol{Q}$ and $\boldsymbol{R}$ are weighting matrices to emphasize minimization or error or control effort, respectively, and are positive semi-definite.

$$u_t = -\boldsymbol{L}x_t \tag{26}$$

$$J = \sum_{t=0}^{\infty} \left(x_t^\top \boldsymbol{Q}_1 x_t + u_t^\top \boldsymbol{Q}_2 u_t \right) \tag{27}$$

This problem can be solved using dynamic programming, which gives that the optimal control law can be found from the solution of the Ricatti equation shown in (28), and is given by (29).

$$\boldsymbol{\Phi} = \boldsymbol{Q}_1 + \boldsymbol{A}^\top \boldsymbol{\Phi} \boldsymbol{A} - \boldsymbol{A}^\top \boldsymbol{\Phi} \boldsymbol{B} \left(\boldsymbol{Q}_2 + \boldsymbol{B}^\top \boldsymbol{\Phi} \boldsymbol{B} \right)^{-1} \boldsymbol{B}^\top \boldsymbol{\Phi} \boldsymbol{A} \tag{28}$$

$$\boldsymbol{L} = \left(\boldsymbol{Q}_2 + \boldsymbol{B}^\top \boldsymbol{\Phi} \boldsymbol{B} \right)^{-1} \boldsymbol{B}^\top \boldsymbol{\Phi} \boldsymbol{A} \tag{29}$$

This solution provides an optimal controller that minimizes the required control effort. However, it relies on the accuracy of the system model and the assumption of time invariance. Consider, instead, the system given by (30) measured by sensors which provide the output in (31), where v_t is some process noise in the system, and w_t is sensor noise.

$$x_{t+1} = \boldsymbol{A}x_t + \boldsymbol{B}u_t + v_t \tag{30}$$

$$y_t = \boldsymbol{C}x_t + w_t \tag{31}$$

In this case, the process and sensor noise is unknowable a priori and not directly measurable. Therefore, rather than control based on the measured system state, which may be inaccurate, it is better to control based on a model of the system that can account for this unknown noise. This leads to utilizing a Kalman filter to perform state estimation as in (32), where $\boldsymbol{K}$ is the Kalman gain, then applying the control law in (33).

$$\hat{x}_{t+1} = \boldsymbol{A}\hat{x}_t + \boldsymbol{B}u_t + \boldsymbol{K}\left(y_{t+1} - \boldsymbol{C}\left(\boldsymbol{A}\hat{x}_t + \boldsymbol{B}u_t\right)\right) \tag{32}$$

$$u_t = -\boldsymbol{L}\hat{x}_t \tag{33}$$

The task then becomes determining $\boldsymbol{K}$ and $\boldsymbol{L}$ to minimize J, which remains unchanged. Again using dynamic programming techniques, these values are derived from the solution to the Ricatti equation. L remains as in the LQR case, with the addition of the equation shown in (34), which allows calculating the optimal $\boldsymbol{K}$ using (35), where the diagonals of $\boldsymbol{W}$ and $\boldsymbol{V}$ give the expected range of the elements of w_t and v_t, respectively.

$$\boldsymbol{\Gamma} = \boldsymbol{V} + \boldsymbol{A}\boldsymbol{\Gamma}\boldsymbol{A}^\top - \boldsymbol{A}\boldsymbol{\Gamma}\boldsymbol{C}^\top\left(\boldsymbol{W} + \boldsymbol{C}\boldsymbol{P}\boldsymbol{C}^\top\right)^{-1}\boldsymbol{C}\boldsymbol{\Gamma}\boldsymbol{A}^\top \tag{34}$$

$$\boldsymbol{K} = \boldsymbol{\Gamma}\boldsymbol{C}^\top\left(\boldsymbol{W} + \boldsymbol{C}\boldsymbol{\Gamma}\boldsymbol{C}\right)^{-1} \tag{35}$$

4.6.3 Control of Stochastically Varying Parameters

While the LQG controller holds promise for stabilizing uncertain systems, it is not designed specifically for systems with parameters that vary stochastically, but rather for time invariant systems disturbed by white noise. It has been demonstrated that the standard LQG controller, while optimal for a known linear system, is not robust to large variations in system parameters due to its reliance on the standard Kalman filter [1, 39]. As shown in Section 2.5.5, the stiffness generated by the human operator can be approximated using a series of Gaussian distributions, so it should be possible to determine a priori an expected value for $\boldsymbol{A}$ and an estimated variance. Therefore, the ideal controller would be designed to accept a distribution for the system parameters and calculate an optimal control law that will be well conditioned over most of that distribution.

Recent work in control of stochastic systems has made numerous advances and provided a variety of robust and optimal controllers that are effective. There have been several efforts to extend the standard LQG controller using a more robust model than a simple Kalman Filter, which assumes only white process and sensor noise. Siljak provides a survey of some of these earlier efforts [139]. A variety of controllers classified as Minimax LQG developed to handle more complex uncertainty [130, 168]. These approaches are improved, but still rely on the assumption that the disturbance to the system is a form of bounded noise rather than a direct change in system parameters, which it assumes may be known with uncertainty, but remain constant. Early work to design optimal and robust controllers stems from Kullback and Leibler's work to characterize the amount of information available about a system [98], and controllers have been designed around minimizing the resulting Kullback-Leibler distance [85, 86]. Alternatively, some authors have focused on H_∞ control, which aims to minimize the H_∞ norm of the system rather than a control cost function [60, 61, 158, 160–162]. Even open loop feedforward controllers [9, 143] and sliding mode

controllers [121] have been designed to handle the issue. However, a large portion of the literature regarding on uncertain systems has focused on systems with fixed dynamics but unknown time delays [106, 166, 169]. While these methods are innovative, they are less applicable to the problem of control of systems with uncertain parameters, as the uncertainty present cannot be attributed purely to a time delay in the dynamics. Adaptive systems have proven useful [20], but tend to work best with the assumption of small perturbations. Insight can even be found from outside of the domain of engineering by looking at work in economics, in which it is often desired to control highly uncertain and sometimes chaotic systems [38, 67]. Several other novel techniques have attempted to replace the Kalman filter with more advanced models, such as particle filters [12, 13], Markov based models [73, 96], neural networks, [157], and other state estimation techniques [159]. Ultimately, the most promising of these approaches for this research incorporated an assumed distribution for the system parameters directly into the derivation of the optimal control law, ensuring that the controller would optimal for their expected value, but still perform well as they varied [42], with Fujimoto providing such a system that was designed to minimize the variance of the control signal [52, 53].

Consider again the system of (25), except where $\boldsymbol{A}$ and $\boldsymbol{B}$ are stochastically varying parameters given by some distribution that does not change with time with expected values $\mathrm{E}[\boldsymbol{A}]$ and $\mathrm{E}[\boldsymbol{B}]$. In this case, it is desirable to not only minimize the control effort, but also the variance of the system's tracking error, so the cost function is modified as in (36), with the additional weight parameter, $\boldsymbol{S}$, which must also be positive semi-definite.

$$J = \mathrm{E}\left[\sum_{t=0}^{\infty}\left(x_t^\top \boldsymbol{Q}_1 x_t + u_t^\top \boldsymbol{Q}_2 u_t + \mathrm{tr}\left[\boldsymbol{Q}_3 \mathrm{cov}\left[x_{t+1}, x_t\right]\right]\right)\right] \tag{36}$$

Following the methodology of Fujimoto [52, 53], the optimal control gain can be found

via (39), with the parameter $\mathbf{\Pi}$ given by (37) and the covariances $\mathbf{\Sigma}_{XY}$ are given by (38).

$$\begin{aligned}\mathbf{\Pi} &= \boldsymbol{Q}_1 + \mathbf{\Sigma}_{AA} + \mathrm{E}\left[\boldsymbol{A}^\top \mathbf{\Pi} \boldsymbol{A}\right] - \left(\mathrm{E}\left[\boldsymbol{A}^\top \mathbf{\Pi} \boldsymbol{B}\right] + \mathbf{\Sigma}_{AB}\right) \\ &\quad \left(\mathrm{E}\left[\boldsymbol{B}^\top \mathbf{\Pi} \boldsymbol{B}\right] + \mathbf{\Sigma}_{BB} + \boldsymbol{Q}_2\right)^{-1} \left(\mathrm{E}\left[\boldsymbol{B}^\top \mathbf{\Pi} \boldsymbol{A}\right] + \mathbf{\Sigma}_{BA}\right) \end{aligned} \tag{37}$$

$$\mathbf{\Sigma}_{XY} = \mathrm{E}\left[\boldsymbol{X}^\top \boldsymbol{Q}_3 \boldsymbol{Y}\right] - \mathrm{E}\left[\boldsymbol{X}\right]^\top \boldsymbol{Q}_3 \mathrm{E}\left[\boldsymbol{Y}\right] \tag{38}$$

$$\boldsymbol{L} = \left(\mathrm{E}\left[\boldsymbol{B}^\top \mathbf{\Pi} \boldsymbol{B}\right] + \mathbf{\Sigma}_{BB} + \boldsymbol{Q}_2\right)^{-1} \left(\mathrm{E}\left[\boldsymbol{B}^\top \mathbf{\Pi} \boldsymbol{A}\right] + \mathbf{\Sigma}_{BA}\right) \tag{39}$$

Note that (39) is a Ricatti like equation, but due to the expected value operator, is not a true Ricatti equation. It can instead be solved numerically, using the solution of the similar Ricatti equation (40) as an initial guess.

$$\begin{aligned}\mathbf{\Pi}_0 &= \boldsymbol{Q}_1 + \mathbf{\Sigma}_{AA} + \mathrm{E}\left[\boldsymbol{A}\right]^\top \mathbf{\Pi}_0 \mathrm{E}\left[\boldsymbol{A}\right] - \left(\mathrm{E}\left[\boldsymbol{A}\right]^\top \mathbf{\Pi}_0 \mathrm{E}\left[\boldsymbol{B}\right] + \mathbf{\Sigma}_{AB}\right) \\ &\quad \left(\mathrm{E}\left[\boldsymbol{B}\right]^\top \mathbf{\Pi}_0 \mathrm{E}\left[\boldsymbol{B}\right] + \mathbf{\Sigma}_{BB} + \boldsymbol{Q}_2\right)^{-1} \left(\mathrm{E}\left[\boldsymbol{B}\right]^\top \mathbf{\Pi}_0 \mathrm{E}\left[\boldsymbol{A}\right] + \mathbf{\Sigma}_{BA}\right) \end{aligned} \tag{40}$$

Using this methodology, an optimal controller, which will be referred to as a Stochastic Linear Quadratic Regulator (SLQR), can be designed if the expected value and covariance matrix of the $\boldsymbol{A}$ and $\boldsymbol{B}$ matrices are known that will minimize the control effort and variance of the output. The emphasis on each of these can be varied by choosing appropriate values for the $\boldsymbol{Q}$'s.

4.7 System Integration

The basic impedance control is expected to be sufficient for solving the problem posed in earlier chapters. However, as human arm stiffness varies stochastically, it is

expected that the control systems specifically designed for probabilistically varying systems will perform better. The classifiers and controllers can be integrated to test this theory using the 1-DOF haptic device. This testing should be thorough, testing the device's stability along with the effect of the compensating system on performance.

CHAPTER V

COMPENSATING SYSTEM DESIGN AND EVALUATION

Integrating the complete system involves combining the output of the classifier system with the controller, enabling it to adjust its gains with the operator's motion. To understand how this system compares to fixed gain systems, its stability and performance must be tested. Using the 1-DOF haptic device, several experiments were devised. By testing the system in a situation that haptic devices typically have difficulty with, it was shown that the compensating device can increase stability over devices without high damping while still allowing more rapid motion than systems with high damping. Experiments also demonstrated that the compensating system provides improved performance over such fixed gain systems. As expected, the stochastically tolerant controllers demonstrated better results.

5.1 Integrated Stiffness Adjusting Controller

Literature has demonstrated that adjusting the impedance of a system is an effective method for adapting to the motion of an operator [78, 115, 136]. Integrating the stiffness estimating classifier with the impedance controller utilizing one of the inner position controllers yields the complete system shown in the block diagram in Figure 34. In the final system, the position of the device is controlled solely by the force applied to the device as with a standard impedance controller. However, additional data in the form of the arm stiffness is used to adjust the way in which the controller performs this task. The classifier model is updated at the same rate as the controller, but EMG data does not directly affect the output of the device, as that would cause a bilateral interaction, with a change in force of the device affecting the muscle activity that is used to calculate that force.

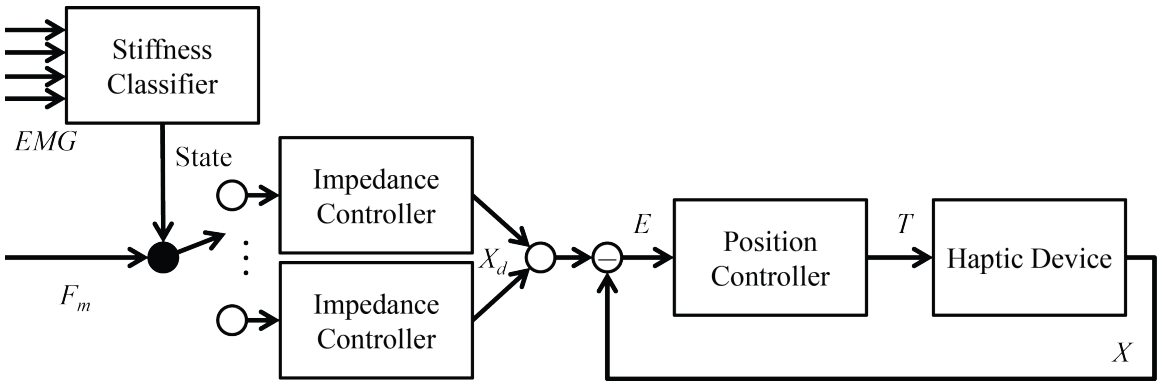

Figure 34: Block diagram of the complete control system

5.2 Controller Parameters

To incorporate the stiffness classifier with the impedance controller, two sets of impedance characteristics were experimentally determined based on the desired motion of an industrial force assisting robot for each stiffness case. For low stiffness situations, the system should move quickly and easily with little resistance, so the mass and damping were set to be small. In the case of high stiffness, the system should have less oscillation and be easier to hold steady, allowing the operator to more precisely control, so a higher damping and mass were used. The threshold based system of Section 3.2 provided two states, one for low arm stiffness and one for high, so these mapped directly to the low damping and high damping gains, respectively. The HMM classifier of Section 3.3.4, however, classifies muscle activity into one of three task phases. Since both the relaxed and moving phase would typically correspond to low stiffness, these were mapped to the low damping case, whereas the holding steady phase was mapped to the high damping gains. Keeping the sets of gains consistent between the two classifiers ensured that they could be compared on even ground without concern that different sets of gains may have inadvertently altered the results. The gains of the PD position controller did not change based on the stiffness classification. However, the two stochastically capable controllers, the LQG and SLQR controllers, incorporated the estimated stiffness distributions found

Table 4: Integrated System Parameters

Module		Parameter	value
Threshold Classifier		ℓ_W	(Varies)
		ℓ_E	(Varies)
HMM Classifier		$\boldsymbol{O}$	(Varies)
		$\boldsymbol{U}$	(Varies)
		$\boldsymbol{P}_0$	$\left[\frac{1}{3} \quad \frac{1}{3} \quad \frac{1}{3}\right]^\top$
Impedance Controller	Low	m_d	$10^{-4}\,\mathrm{kg}$
		b_d	$3\,{}^{\mathrm{Ns}}/_{\mathrm{m}}$
		k_d	$0\,{}^{\mathrm{N}}/_{\mathrm{m}}$
	High	m_d	$10^{-4}\,\mathrm{kg}$
		b_d	$100\,{}^{\mathrm{Ns}}/_{\mathrm{m}}$
		k_d	$0\,{}^{\mathrm{N}}/_{\mathrm{m}}$
PD Controller		D_1	$200\,{}^{\mathrm{Nms}}/_{\mathrm{rad}}$
		D_2	$2500\,{}^{\mathrm{Nm}}/_{\mathrm{rad}}$
LQG Controller	Low	$\boldsymbol{L}$	$[632 \quad 61.8]$
		$\boldsymbol{K}$	$[1.00 \quad 218]^\top$
	High	$\boldsymbol{L}$	$[1660 \quad 61.8]$
		$\boldsymbol{K}$	$[1.00 \quad 217]^\top$
SLQR Controller	Low	$\boldsymbol{L}$	$[18.8 \quad 0.303]$
	High	$\boldsymbol{L}$	$[66.6 \quad 1.09]$

in Section 4.6.2 and Section 4.6.3. These controllers used different gain matrices for each state. The final values are shown in Table 4. The parameters for the two classifiers are user dependent, and therefore values are not given. These must be determined based on training data from a particular operator and are valid only for that operator.

5.3 Improvement with Compensation

To demonstrate the usefulness of the compensating controller, it was run through a series of basic tests with volunteers operating the device. These were performed using the threshold-based classifier from Section 3.2 and with the impedance controller using a basic PD inner position controller from Section 4.2. In Figures 35(a) and 35(b), the top graph shows the motion of the device using a standard impedance controller, and the bottom graph shows the same motion with the new system, with the yellow

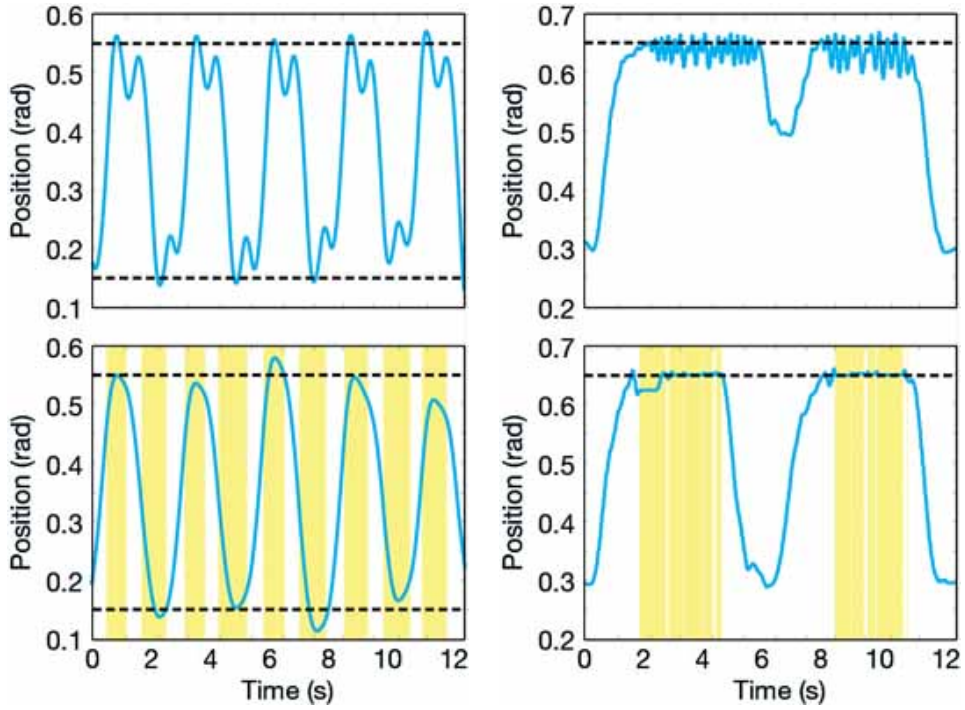

(a) Movement between two targets (b) Contact with rigid surface

Figure 35: Comparison of response without compensation, top, and with compensation, bottom (highlight indicates high stiffness)

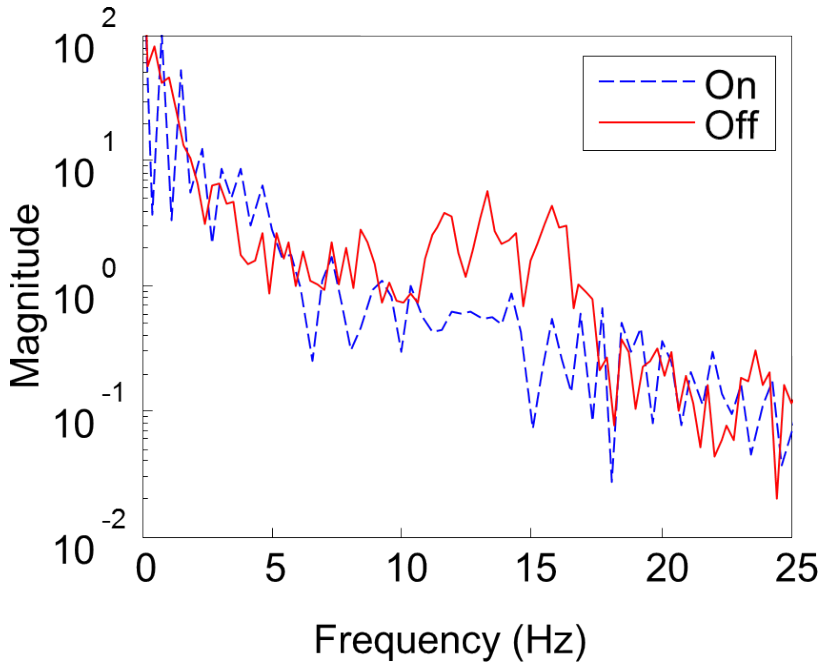

Figure 36: Rigid surface contact has smaller oscillation magnitude in frequency spectrum between 10-20 Hz with compensation (blue) than without (red)

Table 5: RMS of Distance From Rigid Surface During Contact

Compensation	RMSE
Off	2.22×10^{-2} rad
On	0.99×10^{-2} rad
Decrease of	60 %

highlight indicating the system has detected higher operator arm stiffness and is compensating for it. First, the haptic device was moved back and forth between two target positions. The graph showing the compensating controller illustrates the increased stability and smoother motion without sacrificing the ability to move the handle rapidly over long distances, whereas without compensation, stopping at the target and reversing directions smoothly was more difficult. Next, the device was held against a rigid surface. Without compensation, the device oscillates rapidly under the stiff conditions. However, with the compensation, the device can be easily held against the rigid surface. The root mean square error (RMSE) of the distance from the surface decreased by 60% with the compensation, as shown in Table 5. To further demonstrate this improvement, Figure 36 shows the frequency spectrum of both signals. The range between 10 and 20 Hz shows a clear decrease in the magnitude of oscillations with the compensation on.

5.4 Contact with Rigid Surface

To validate the theoretical stability analysis, it was necessary to test the stability of the device under real world conditions. Therefore, the first experiment was designed to create a situation which is usually unstable for haptic devices and evaluate how well the compensating system could stabilize the device as compared to a low damping fixed gain system.

5.4.1 Concept

Haptic devices are typically difficult to hold against a rigid surface due to the reaction force of contact between the two. When an operator attempts to do so, the device repeatedly bounces off the surface as they attempt to push it back towards the surface and becomes unstable. It was expected that the operator would stiffen their arm to hold the device against the surface, so the damping coefficient would increase when the compensation was on, stabilizing the system when needed. For this experiment, all variables, such as the position of the surface, were held constant, with the compensation state being the only independent variable, and the device position was recorded over time. To measure the stability of the system, the root mean square error (RMSE) of the distance to the surface was calculated for the duration the operator was attempting to hold the device against the surface, which was expected to be minimal for a goal of maintaining contact with the surface

5.4.2 Method

Each participant was oriented with the EMG measurement system and haptic device before performing the experiment. They had the EMG measurement system connected to their right arm and stood aside the device in a similar posture to the previous experiment described in Section 2.5. They were allowed to use the device unconstrained for two to three minutes and become accustomed to it, but with the compensation off, which helped minimize learning effects that might be present.

Participants were then asked to place the handle of the device against a rigid surface and hold it in contact for five seconds until instructed to move the handle away. This was repeated several times with the compensation both on and off. The first several trials were used to allow the experimenter to adjust the cocontraction threshold to the participant's individual requirements identify their particular transition point between low stiffness for easy motion and high stiffness for steadiness, which also

Table 6: Rigid Surface and Simulated Lifting Task Participant Data

Total	Male	Female	Ages
20	12	8	19 - 37

helped to minimize learning effects in the task. Each participant performed between 4 and 8 trials of the task, with 2 used for data collection: one with the compensation off and one with the compensation on and properly tuned. The compensation on case utilized the threshold classifier and PD position controller.

This experiment was conducted following an approved IRB protocol.

5.4.3 Analysis

The ANOVA analysis was performed after the data from all participants was anonymized. Processing was done using MATLAB software, while SPSS and G*Power 3.1 [43] were used for statistical analysis.

A power analysis was performed beforehand to calculate the required number of participants, based on the desired power, 1 , of the resulting statistical analysis, which indicates the chance of statistical errors, . A typical value power $1 - \beta = 0.95$ was chosen, which required a minimum of 16 participants to obtain statistically significant results. The experiment included 20 participants, whose distribution is shown in Table 6, resulting in $1-\beta = 0.965$ and a required critical $F = 1.29$ for statistical significance.

5.4.4 Results

The experiment yielded 80 data points, as there were 2 with the compensation on and 2 with the compensation off per subject. As demonstrated by Figure 37, the participants were able to reduce their average RMSE with the compensation on. The ANOVA analysis resulted in $F = 35.75$ and $p \leq 0.001$, demonstrating statistical significance. More detailed results can be found in Appendix B.2.

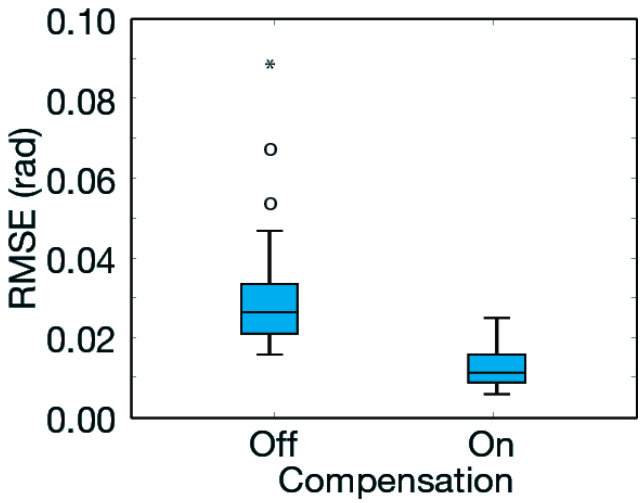

Figure 37: Significant decrease in RMSE with compensation on

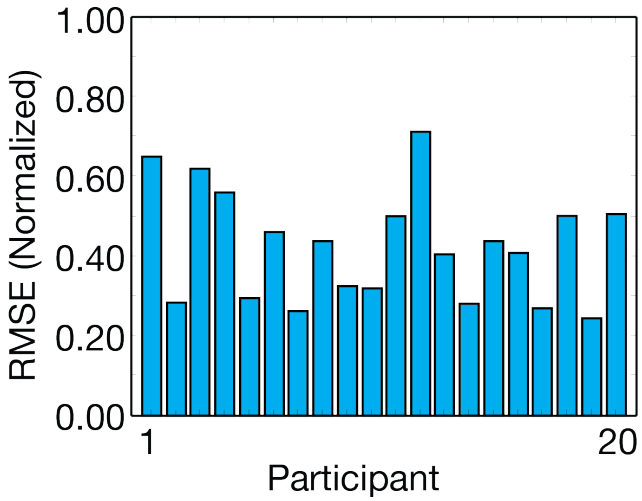

Figure 38: Compensation on RMSE as fraction of compensation off shows decrease for all participants

5.4.5 Discussion

The compensating controller provided significantly increased stability during rigid surface contact, decreasing the magnitude of oscillations. On average, the magnitude was decreased by more than 50%, with the best case showing a decrease of 75%, as demonstrated in Figure 38. Most participants showed an RMSE of less than half the compensation off case.

5.5 Simulated Lifting Task

Having established that the compensating system could improve stability, the next task was to evaluate its effect on the system's performance. By asking users to perform a task similar to the types of industrial tasks the system would be used for, a measure of the change in speed and accuracy of the system could be obtained.

5.5.1 Concept

An additional experiment was designed to mimic a real-world usage scenario involving the large force assisting devices that this system was designed for, which are typically used to move objects from one point to another. Participants were asked to accomplish a pick-and-place task by using the haptic device to control a simulated lifting arm. The operator pressed a button to lower the arm and pick up an object, then moved the arm to a target and put the object down. Figure 39 shows the simulation. The task was performed for both controller states, and the distance of the object's initial location to the target was varied, therefore independent variables were the state of the controller and the distance of the object's initial location to the target. Objectively measuring performance can be difficult, so the dependent variables, the speed and accuracy of the operator's object placement, were chosen based on industrial applications, such as a factory or assembly line, which try to produce as many products with the best quality possible. It was expected that this experiment would show an improvement in both with the compensation on.

5.5.2 Method

Participants were introduced to the simulation of the task and given the goal of picking up the object and placing it as close to the center of the target as possible. After being given free time to use the device and become accustomed to the simulation, a similar tuning method was used as described in Section 5.4.2 to ensure that the thresholds were appropriate to each participant and minimize learning effects. The

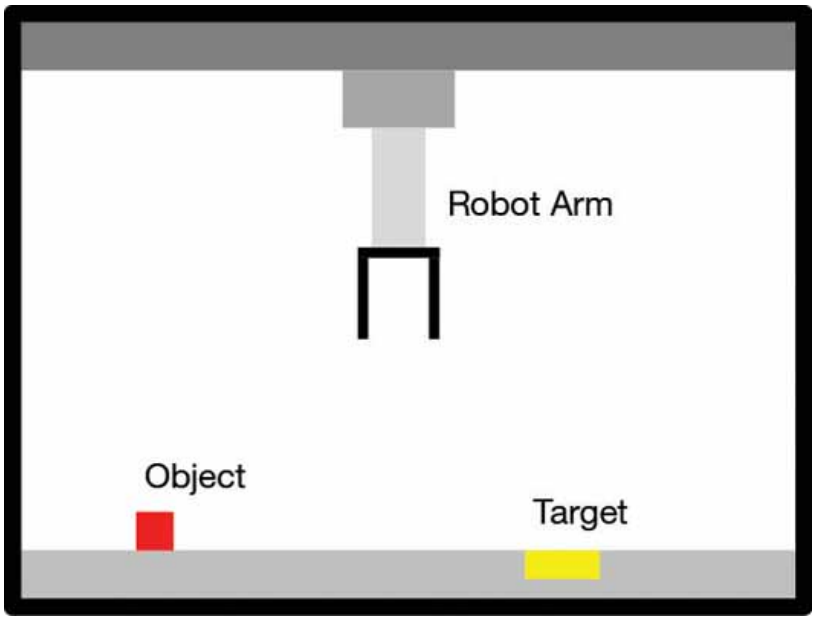

(a) Simulation parts

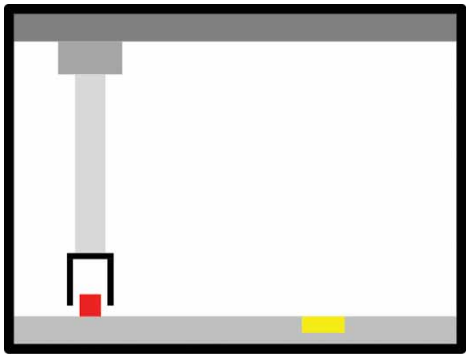

(b) Pick

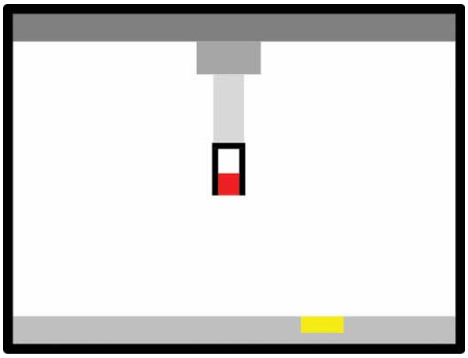

(c) Move

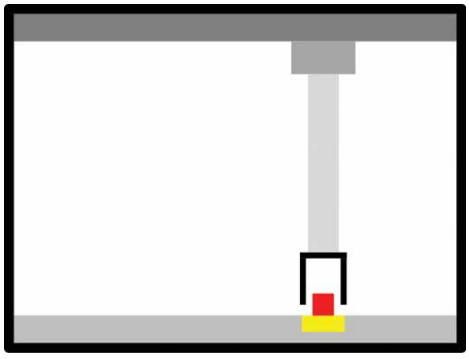

(d) Place

Figure 39: The simulated lifting device, shown in each phase of the task

participant performed the task several times for each trial, with only two of the trials used for data analysis similar to the previous task. The compensation on case again utilized the threshold classifier and PD position controller.

This experiment was conducted following an approved IRB protocol.

5.5.3 Analysis

This experiment was performed in conjunction with the rigid surface experiment described in Section 5.4, and therefore used the same participant pool. Analysis was performed similarly, also using ANOVA as in Section 5.4.3.

5.5.4 Results

Due to the variations in each person's interpretation of the provided instructions, participants' execution of the task varied widely. All participants were given the same instructions but interpreted them differently and executed the task to different tolerances, which made comparing speed and accuracy between subjects difficult. Therefore, statistical significance was not obtained. However, a less rigorous analysis was used on each participant individually, which provided only 10 data points per analysis. While less than the amount required for statistical significance, it showed helpful trends in the data. The individual results of several participants were supportive of the hypothesis that the compensation would lead to increased performance. Figure 40 shows the results for one such participant, showing faster and more accurate placement. More detailed results can be found in Appendix B.3.

5.5.5 Discussion

The performance task results did not provide statistical significance due to the variations in each person's execution of the task. Some participants placed the object quickly as best as they could, but others more carefully positioned the object before releasing it. Despite the lack of statistical significance in the results, numerous helpful

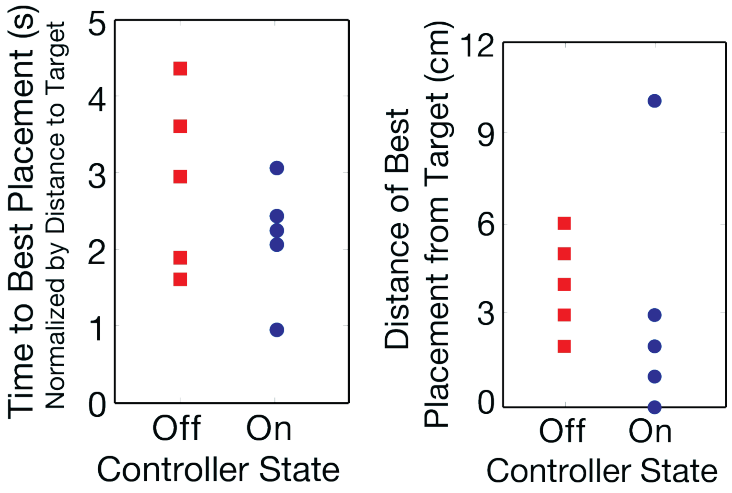

(a) Quicker placement (b) More accurate placement

Figure 40: General comparison of results of simulation with compensation on and off

observations were made during the experiment, and trends were observed for participants individually. In addition to generally faster and more accurate placement, the experiment demonstrated the usefulness of the system and also made evident several concerns with the basic system, which utilized the threshold classifier and PD position controller.

Several participants made observations that when the compensation was turned off, the device became more difficult to stabilize. One participant observed that the experiment "was getting harder" after this occurred. Another participant commented with compensation on that the device was "moving more smoothly." In general, most participants noticed the difference between the two cases. Therefore, despite the lack of statistical significance, the visible trends and operator observations demonstrate an improvement.

The speed and accuracy of object placement were calculated for each trial, and most participants took less time to place the object and had less error with the compensation on. Some participants showed somewhat more noticeable increases in performance, while a few showed little to no performance gain. In one trial, the

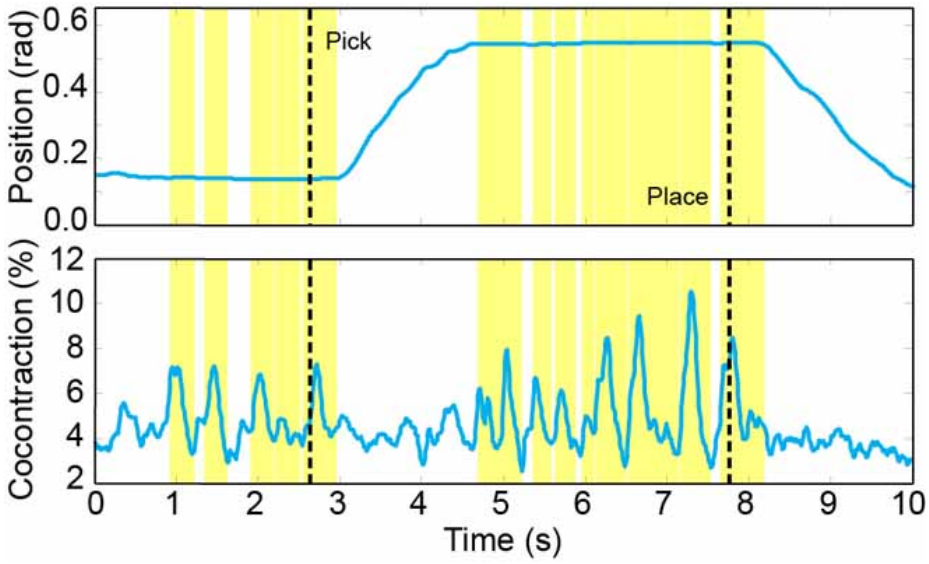

Figure 41: Cocontraction increased while the participant steadied the robot during the task (Highlight indicates compensation effect)

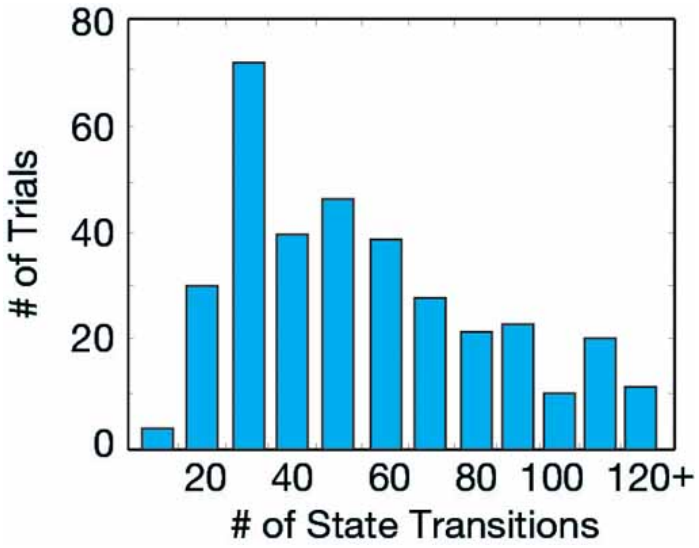

Figure 42: Histogram of number of state transitions in simulation task trials showing excessive transitions indicative of chatter in most trials

participant shown in Figure 40 was able to place the object exactly on the target. While the error is very high, the analysis supports the fact that an overall performance increase results from use of the designed system.

Figure 41 shows that the cocontraction clearly increased while the participant held

the device steady to pick up the object or place the object down. However, it demonstrates a flaw in the system where the operator, sensing the increased stability, relaxed when the compensation turned on, causing the compensation to turn off, resulting in the operator stiffening again. This chatter is undesired and made accomplishing the task more difficult. Figure 42 shows the number of state transitions across all trials of all subjects of the simulation task. An ideal task would have less than 10 transitions, with ideally one transition at the beginning and end of both pick and place. However, only 10% of all trials have less than 20 transitions, with some exhibiting more than 120 transitions in an approximately 10 second span. Eliminating this chatter should be possible by utilizing the more advanced operator model to identify phases of the task from the time history of stiffness estimates and incorporating one of the stochastically tolerant inner position controllers. In addition, Figure 41 also shows that the operator tends to break down the task into multiple subtasks to complete it, each of which is characterized by a different purpose, as well as different types of movement and levels of cocontraction, which supports the use of a classifier such as the HMM described in Section 3.3

5.6 Performance Evaluation

Despite the lack of statistical significance, the initial performance testing was promising. Therefore, the various classifiers and controllers were tested to see which had the best results. Using more tightly controlled tasks ensured a higher chance of statistically significant results.

5.6.1 Concept

The results of the experiments of Section 5.4 and Section 5.5 demonstrated the effectiveness of the compensating system, but did not evaluate the various classifiers and controllers to determine which provided the best improvement. In addition, the lifting simulation proved to be too unrestricted of a task to obtain statistical significance.

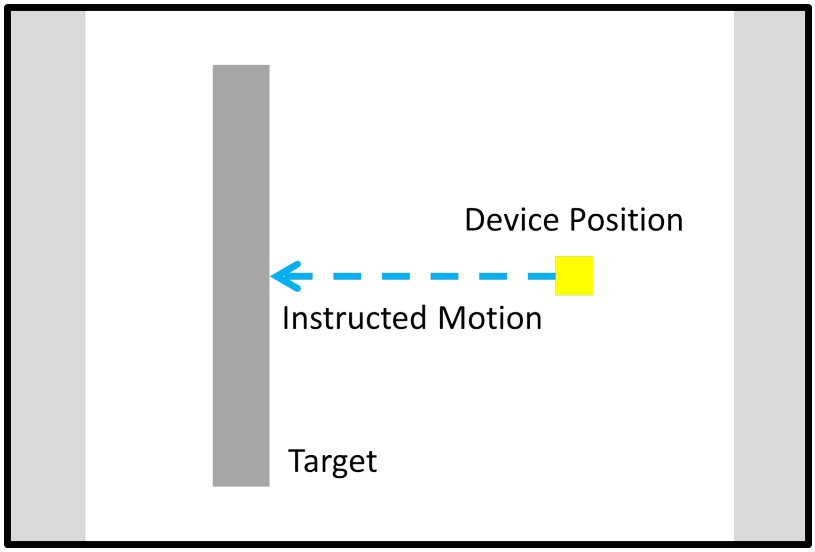

Figure 43: Experimental simulation - The yellow box moved with the device as participants moved the handle; Participants were instructed to move to the gray target with an emphasis on either speed or accuracy

Therefore, a further experiment was performed which compared the performance of the compensating system utilizing both the threshold based classifier of Section 3.2 and the Hidden Markov Model (HMM) classifier of Section 3.3 as well as the PD inner position controller of Section 4.3, the Linear Quadratic Gaussian (LQG) inner position controller of Section 4.6.2, and the Stochastic Linear Quadratic Regulator (SLQR) of Section 4.6.3. In addition, each controller was tested with a non-compensating system utilizing low damping to allow fast motion or high damping to allow for stability. This allowed both the comparison of a standard non-compensating system with the compensating system as well as the determination of which modules worked best in the compensating system.

Based on the results of the simulated lifting task in Figure 39, two new tasks were designed which would allow more targeted testing of speed and accuracy. In each task, the participant was given a series of targets to reach on a computer screen in front of the device, and the instructions were varied based on whether speed or accuracy was to be measured. Figure 43 shows the simulation, which was much simplified

over the previous experiment. In this way, accuracy and speed improvements were characterized independently in a much more rigorous fashion, significantly increasing the likelihood of getting statistically significant results.

5.6.2 Method

After obtaining informed consent, participants were first introduced to the haptic device and were provided with an explanation of the experiment. After having the EMG measurement system affixed to their right arm, they stood next to the device using the same posture as in previous experiments, first described in Section 2.5. The simulation was then introduced, and the instructions for the two tasks were given. For the speed-based task, participants were told to move their marker to the target as quickly as possible. It was explained that overshooting the target was acceptable, since accuracy was not of importance, but they were told that they should end at the target and hold on the target as best as possible. For the accuracy-based task, the instructions were to move their marker to the target as accurately as possible and to avoid overshooting the target as much as possible. For both tasks, the operator was given a score for each target that was displayed once they had reached the target. The calculation of the scores will be further explained in Section 5.6.3. Participants were then allowed to run practice trials of both tasks as many times as they needed until they felt comfortable with the device and the two tasks. Figure 44 shows a participant using the device with the simulation displayed on the screen in front of them.

Once the practice trials were completed, participants performed a similar trial that recorded their muscle activity for calibration of the various classifiers and controllers. In this trial, the participants were told that they were not scored for their motions to the targets on either speed or accuracy. Instead, they were given one of three instructions that corresponded to the three subtasks identified in Section 3.3.1:

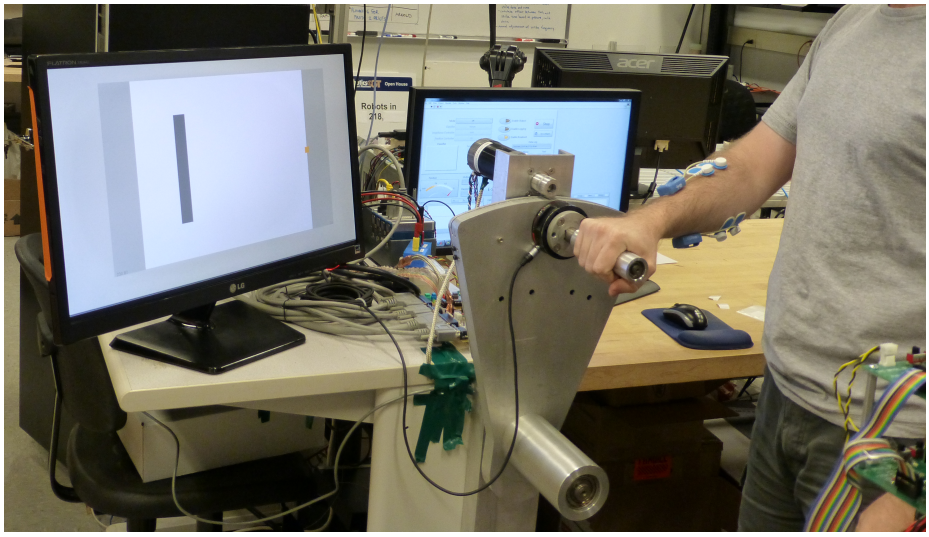

Figure 44: A participant performing the experiment with the simulation displayed on the screen in front of the device

a) "Ready" - participants were instructed to relax and not attempt to move the device; *b*) "Move" - participants were instructed to move the device towards the target; and "Hold" - participants were instructed to hold the device steady on the target. After the completion of the trial, the parameters for the threshold and HMM classifiers were calculated based on the measured EMG levels recorded for each command. After this, the calibration trial was repeated to verify to accuracy of the classifications.

Finally, once the preliminary trials were completed, the experimental trials were started. Each participant performed a full factorial of available options, with four classifiers: *A*) Fixed low damping, *B*) Fixed high damping, *C*) Threshold, *D*) HMM; three controllers: *a*) PD, *b*) LQG, *c*) SLQR; and two tasks: *1*) Accuracy, *2*) Speed. This gave a total of 24 trials, each of which consisted of 24 scored targets. After each trial, participants filled out a short survey asking them how that controller performed various scales. They were asked to rate it from 1 to 10 based on the amount of effort required (1 = no effort, 10 = too much effort), how much the controller seemed to be helping or fighting their motion (1 = helping, 10 = fighting), and how stable it felt (1 = extremely, 10 = extremely unstable). They were also allowed to provide

Table 7: Performance Comparison Participant Data

Total	Male	Female	Ages
24	16	8	19 - 42

additional comments of interest. The complete survey is given in Appendix B.4. The trials were ordered based on a Latin Squares design to esnure that each participant saw the tasks in a unique order and to minimize the effects of learning and fatigue.

This experiment was conducted following an approved IRB protocol.

5.6.3 Analysis

To eliminate any learning effects or other confounding factors, a Latin Squares design of experiments was utilized. The 24 trials were organized such that there were 24 unique sequences designed to ensure every trial was seen in a different position by each participant, and no participant performed the same two trials consecutively. For this reason, 24 participants were targeted, which would allow each participant to follow a unique sequence of trials. The order of the 24 target positions in the simulations was organized using a similar methodology.

In total, 29 volunteers participated in the experiment, with 5 participants' data being excluded due to equipment malfunctions, incomplete trials, or poor EMG electrode contact. This led to the participant distribution given in Table 7. Each participant ran 24 trials with 24 targets, giving 576 data points per participant, for a total of over 13,000 data points. This led to an actual power of $1 - \beta > 0.999$, which will ensure the any statistically significant results will be very strong. The analysis utilized a generalized linear model to perform a repeated-measures multivariate ANOVA, following the methodologies presented by Warner and Field [44, 163].

The scores for the two tasks were calculated based on the targeted metric for the task, and were devised before running the experiment. For the speed-based task, the score, j_{speed}, was the amount of time for the user to move to the target, t_b, normalized

by the distance to the target, d_b. To differentiate between two identical times in which one user reached the target closely and another significantly overshot the target, a fraction of the overshoot time, t_o, was also added to the score, which scored motions that were both fast and accurately slightly better than motions which were only fast. This resulted in the equation for the score given by (41), in which a lower score is a better performance.

$$j_{speed} = \frac{t_b}{d_b} + c_s t_s \tag{41}$$

For the accuracy task, the score, $j_{accuracy}$ was based on the point of closest approach to the center of the target, d_{min}, or the maximum overshoot, d_s if the participant overshot the target. This was normalized by the width of the target, h, then squared to more strongly penalize poor accuracy. Also, if the participant overshot the target, an additional penalizing factor was added. Finally, if two users had the same accuracy, it would be preferable to obtain it with a faster motion, so a small factor that accounted for the velocity to reach the target, $\dot{x}_z$, was added to differentiate between the two. The equation for the score is given by (42), with a lower score again indicating better performance.

$$j_{accuracy} = \begin{cases} \left(\frac{d_{min}}{h}\right)^2 - \frac{\dot{x}_b}{\dot{x}_{max}} & \text{if no overshoot} \\ \left(\frac{d_s}{h}\right)^2 + \frac{d_s}{w} + \frac{\dot{x}_b}{\dot{x}_{max}} & \text{if overshoot} \end{cases} \tag{42}$$

5.6.4 Results

Figure 45 shows the distribution of the data for the accuracy, separated by classifier in Figure 45(b) and by controller in Figure 45(c), while Figure 46 shows the results of the speed tasks in a similar fashion. Outliers outside of two standard deviations, or most extreme 5% of the data, are not shown on these figures. The mean and its 95%

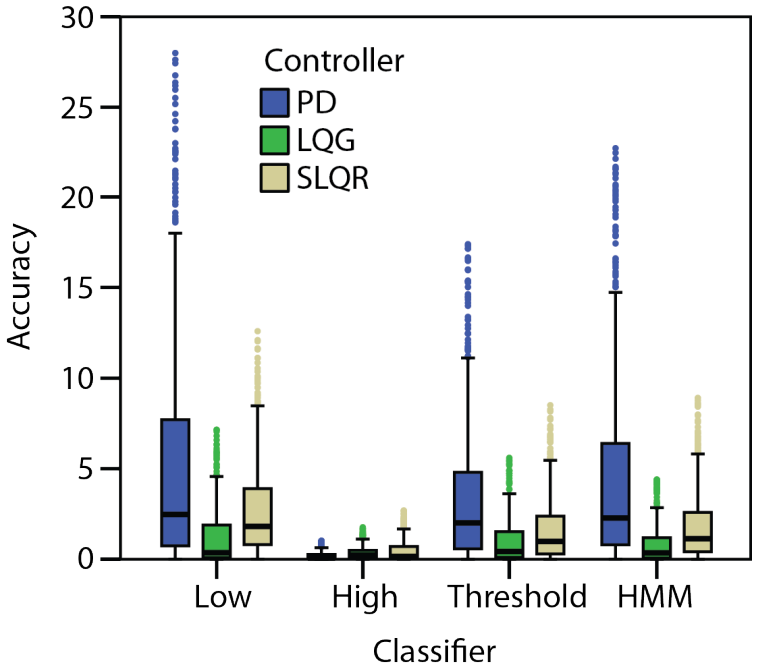

(a) All cases

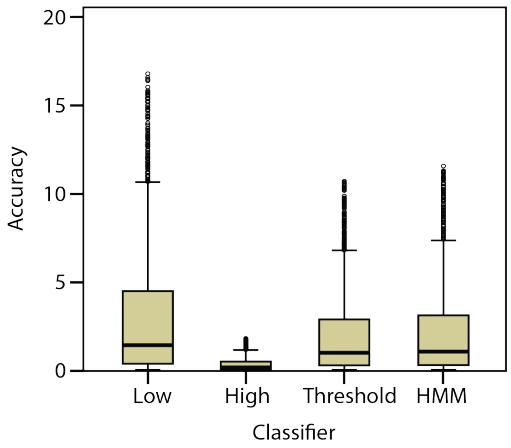

(b) Separated by classifier

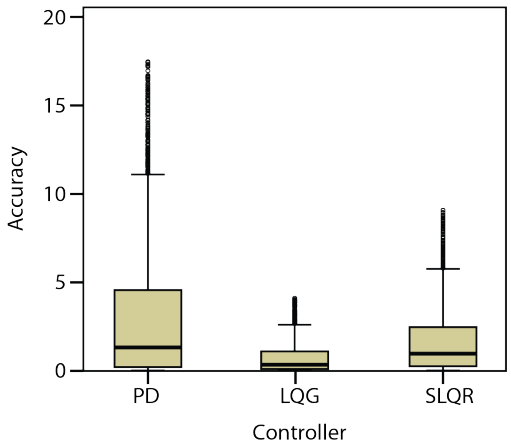

(c) Separated by controller

Figure 45: Performance comparison experiment accuracy task results (Lower score = better performance)

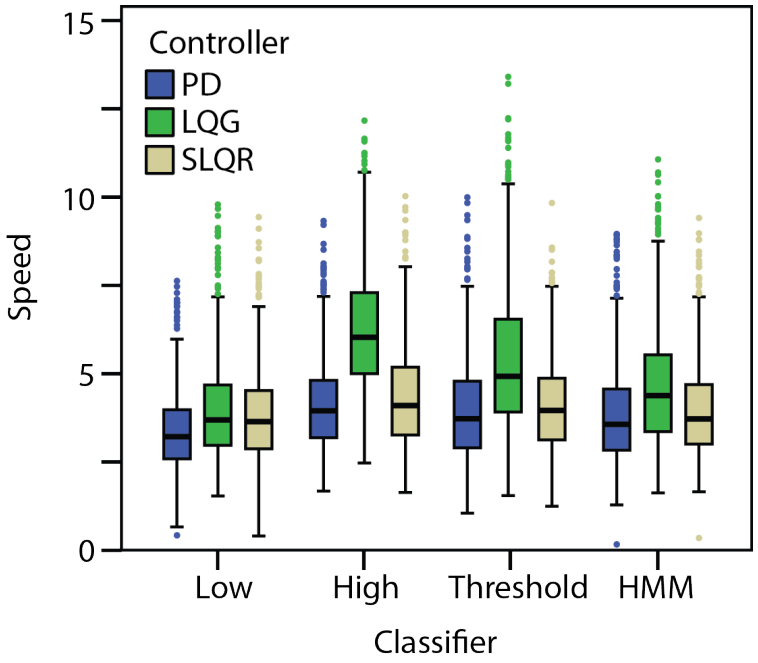

(a) All cases

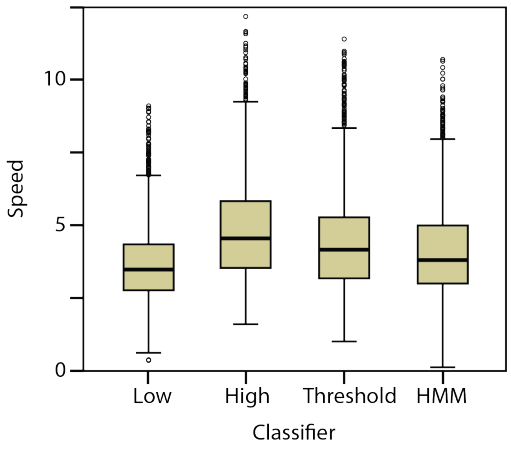

(b) Separated by classifier

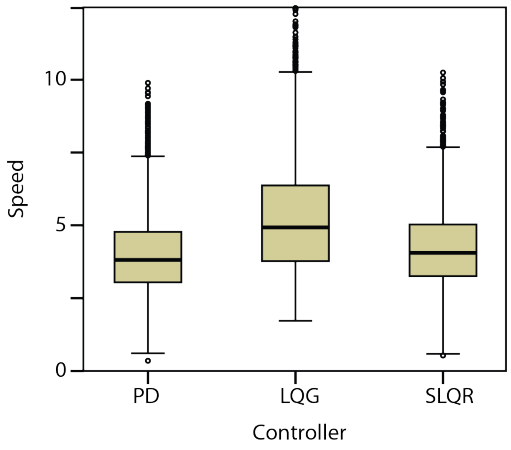

(c) Separated by controller

Figure 46: Performance comparison experiment speed task results (Lower score = better performance)

Table 8: Performance Comparison Results

Classifier	Controller	Accuracy		Speed	
		Mean	95% Interval	Mean	95% Interval
Low Damping	PD	5.848	5.461 - 6.235	3.498	3.377 - 3.618
	LQG	2.625	2.238 - 3.013	4.098	3.978 - 4.218
	SLQR	3.356	2.968 - 3.743	3.965	3.845 - 4.085
High Damping	PD	0.503	0.115 - 0.890	4.259	4.139 - 4.379
	LQG	0.527	0.140 - 0.915	6.248	6.228 - 6.468
	SLQR	0.793	0.405 - 1.180	4.434	4.314 - 4.554
Threshold	PD	3.869	3.479 - 4.240	4.060	3.942 - 4.178
	LQG	2.201	1.820 - 2.581	5.498	5.380 - 5.616
	SLQR	2.142	1.761 - 2.522	4.186	4.068 - 4.304
HMM	PD	5.029	4.649 - 5.410	4.002	3.884 - 4.120
	LQG	1.844	1.464 - 2.225	4.757	4.639 - 4.875
	SLQR	2.442	2.061 - 2.822	4.085	3.967 - 4.203

Table 9: Performance Comparison Results

Item	Accuracy		Speed	
	Mean	95% Interval	Mean	95% Interval
Low Damping	3.943	3.719 - 4.167	3.853	3.784 - 3.923
High Damping	0.608	0.384 - 0.831	5.014	4.945 - 5.083
Threshold	2.734	2.514 - 2.954	4.581	4.513 - 4.649
HMM	3.105	2.885 - 3.325	4.281	4.213 - 4.350
PD	3.810	3.618 - 4.002	3.955	3.895 - 4.014
LQG	1.799	1.607 - 1.991	5.175	5.116 - 5.235
SLQR	2.183	1.991 - 2.375	4.168	4.108 - 4.227

confidence interval of each combination are shown in Table 8, and the overall mean and confidence interval for each controller and classifier are shown in Table 9.

The results of the performance comparison experiments proved to be statistically significant. The assumption of equal variances was not valid, with Box's M test giving $BM = 4.721 \times 10^3$, $F = 142.9$, and $p < 0.001$ and Levene's giving $F = 96.75$ for the accuracy task, $F = 33.51$ for the speed task, and $p < 0.001$. To account for this, all statistics presented will present a corrected F value using Pillai's trace. Also, unless otherwise stated, $p < 0.001$ may be assumed.

For the variation of classifier, the results demonstrated that the change of the classifier had a statistically significant effect on both tests, with $PV = 0.112$ and

$F = 162.0$. For the variation of the controller, the results were also statistically significant, with $PV = 0.125$ and $F = 273.9$. Also, testing for interactions between the two independent variables showed that the combination of classifier and controller variation has a statistically significant effect on the results, with $PV = 0.48$ and $F = 33.52$.

Pairwise comparisons between each of the classifiers showed statistically significance differences with $p < 0.001$, except for between the HMM and Threshold, which did not demonstrate a statistically significant difference with $p = 0.116$. Between the controllers, all pairs were significantly different with $p < 0.001$, except for between the LQG and SLQR, which showed significance with $p = 0.017$.

The survey results proved to be too varied to obatin statistical significance. More detailed results, including the results of the user surveys, can be found in Appendix B.4.

5.6.5 Discussion

The results of the experiment very strongly suggest a statistically significant difference between the non-compensating system and the compensating one. There are several very clear and positive results. First, the trade-off between the speed and accuracy of a device is clearly demonstrated, as for all controllers, the high damping case consistently yielded higher speed scores and lower accuracy scores. It is important to remember that a lower speed score indicated reaching the target faster and that a lower accuracy score similarly indicated reaching the target more accurately. Both the threshold classifier and HMM classifier achieved a balance between the two. The graphs in Figure 47 display the means for each case, compared so as to more easily discern the differences between the cases.

For the accuracy task results, the low damping case provided the worst scores and the high damping case provided the best. It is evident from Figure 47(a), however,

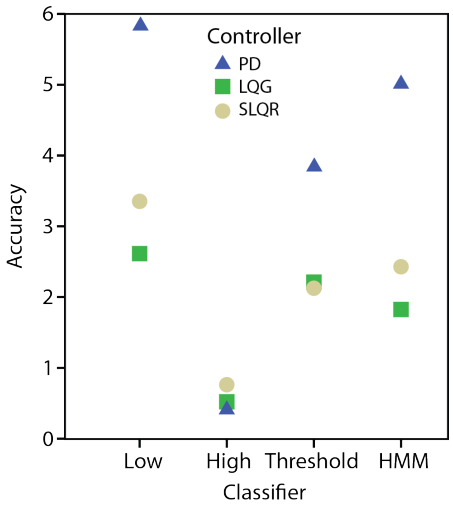

(a) Accuracy task trends by classifier

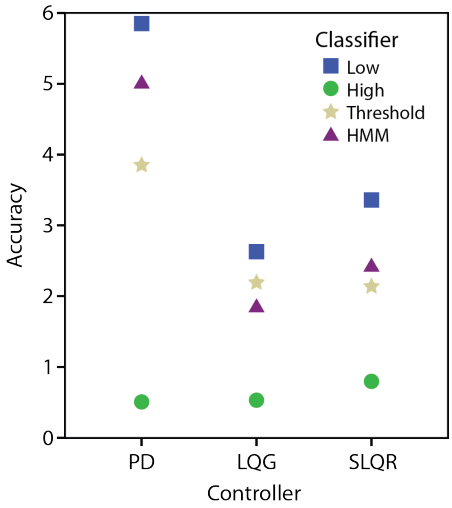

(b) Accuracy task trends by controller

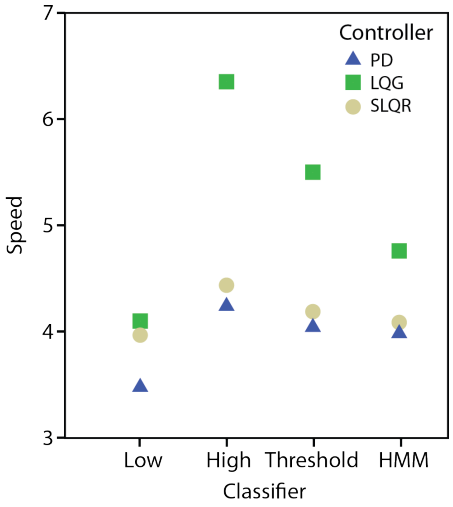

(c) Speed task trends by classifier

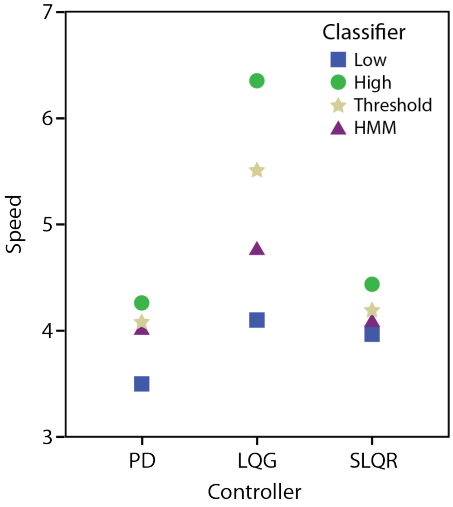

(d) Speed task trends by controller

Figure 47: Performance comparison experiment marginal means

that the compensating system provided improved accuracy over the low damping case, especially when one of the controllers designed for stochastic systems was used. Statistically, there is little difference between the results using the LQG and SLQR controllers, and Figure 47(b) shows that which of the two performed better depending on which classifier was used. In all cases except for the high damping case, however, the two stochastic controllers clearly outperformed the basic PD controller. For the high damping case, there's little difference between any of the controllers, indicating that the effect of changing controllers on accuracy becomes negligible as the damping is increased.

The results of the speed task can be similarly broken down, with non-compensating low damping giving the best scores and the high damping giving the worst. As expected, this is exactly opposite of the accuracy results. Figure 47(c) shows that generally, the HMM provided slightly better performance than the threshold classifier, especially in the case of the LQG controller. For the controllers, the SLQR and PD are consistently better performing than the LQG, though between the former two, there's little statistically significant difference.

Overall, the results confirm the initial hypothesis that the compensating system would outperform the current state-of-the-art, which utilizes increased damping, with regards to speed while obtaining better accuracy than a non-compensating system with less damping. Further, better results were obtained using a stochastically tolerant inner position controller than a standard PD inner position controller. Based on the speed results, the SLQR controller provides the better overall performance, as the LQG controller had much worse speed scores. This is likely due to the model-based nature of the LQG controller, which will actively resist the motion of the user if they attempt to move the device faster than the model impedance system will allow, whereas the other two controllers do not do this.

The results also indicate that, contrary to expectations, the HMM classifier performed no better than the threshold based classifier, with no statistical significance between the two except in limited cases. To further understand this, the data from the verification trials was analyzed. Section 3.3.4 demonstrated an HMM that could achieve accuracy of at least 87% in simulations using prerecorded EMG data sequences. Unfortunately, under real world circumstances, this proved unobtainable with this model. Figure 48 shows the distribution of classification accuracy for the participants, which had a mean of $\mu_{hmm} = 57.0\%$ and a standard deviation of $\sigma_{hmm} = 5.75\%$. The distribution was skewed towards the upper end of the range, with the highest accuracy equal to 64.8%. Because of the lower than expected classification accuracy, the HMM was unable to eliminate the chatter observed in previous experiments with the threshold based classifier, as shown by the comparison of number of state transitions shown in Figure 49, in which the two classifiers gave nearly identical results. One of the most likely causes of this was the method in which the training data was utilized. States were manually identified, and the HMM was trained to match those results. Additionally, the speed at which the operator moves was not included in the model, but would probably be useful in identify the current state. Another factor could be the time scale on which the model runs, which matches that of the controller. In reality, the human state changes much more slowly, and so may not be best modeled at that time scale. While the results were not as anticipated, the use of a probabilistic classifier still hold promise, as there are several alterations to the model that may yet provide a better system, which will be discussed further in Section 7.3.2.

5.7 Enabling Advanced Physical Human-Robot Interaction

The results of these experiments are promising, as they demonstrate that the envisioned compensating control system does, in fact, provide the performance gains

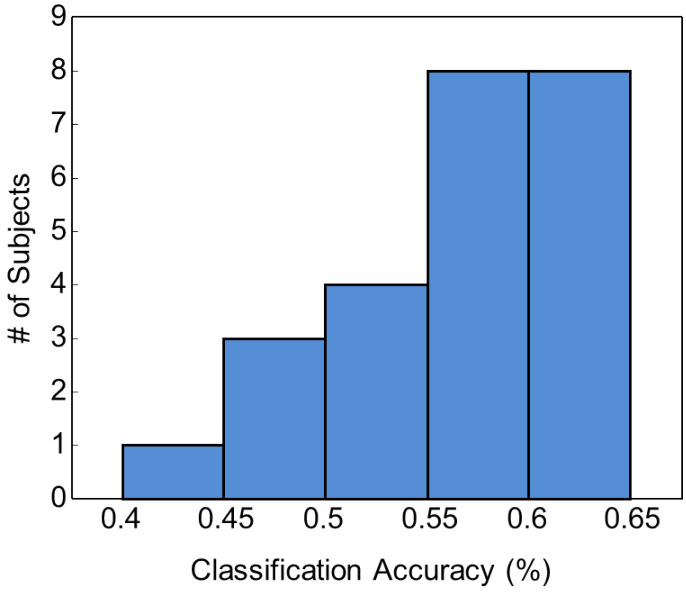

Figure 48: Histogram showing the distribution of HMM classification accuracy

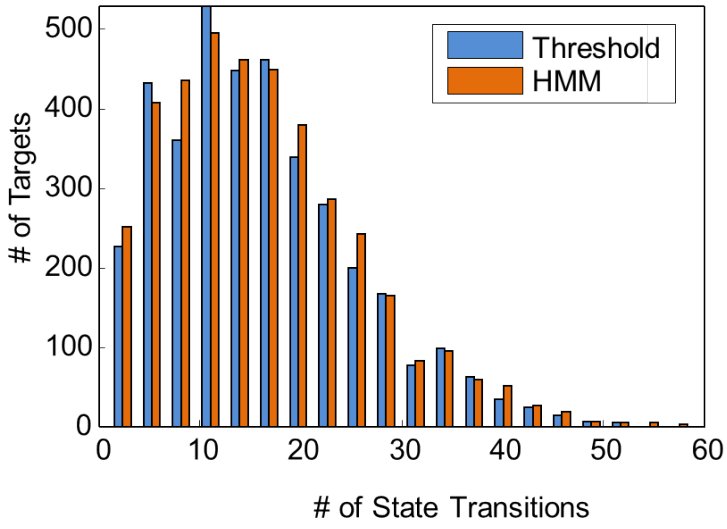

Figure 49: Histogram comparing the amount of chatter for the two classifiers

hoped for. While there are still some issues which must be overcome, such a system could have wide applicability in a number of pHRI settings. One such setting involves the use of exoskeleton robots, which must be designed with the safety of the wearer in mind. As a related pHRI problem, these systems must be able to adapt to the way humans move, but they have the added advantage of being able to apply torques

directly to human joints. This allows advanced control methods which can directly modulate the muscle activity of the wearer and the way in which the wearer moves.

CHAPTER VI

MUSCLE CONTROL WITH HAPTIC DEVICES

Control of pHRI systems in not limited to point contacts, such as with the haptic device. Wearable exoskeleton devices have extensive contact with the wearer, which amplifies the problem of contact induced instability. For this reason, these systems are often very compliant, and so could benefit from a controller capable of gathering information about the user's arm dynamics. This could even enable methods for controlling the wearer directly through application of forces and torques directly to the human joints, which would be useful for rehabilitation and diagnosis devices.

6.1 Background

The compensating control system developed by this research has alternative applications, especially in the area of exoskeleton robotics. Coupled with an understanding of the integrated structure of the human musculoskeletal system of the arm and the manner in which the central nervous system (CNS) modulates muscle activity, an intelligent control that can measure muscle activity could be safer for wearers. Also, rehabilitation and diagnosis exoskeleton robots could utilize the information to induce specific desired muscle activity patterns. Such systems would benefit from a more detailed analysis of muscle activity and how it is generated. A variety of studies have investigated methods for predicting the activation pattern of human muscles under some applied loading [15, 26, 84]. These typically make use of the expected optimality principle in the nervous system, which assumes that the CNS attempts to minimize some performance criteria of the muscles involved. Published literature has developed a mathematical formulation for this criteria based on empirical data about the way in which the CNS optimizes muscle activation patterns [32, 84, 111, 146].

Building on this understanding, detailed models of the human arm under static loading have been developed by Ueda, Ding, et al, for the purpose of developing an exoskeleton based robot for diagnosis and rehabilitation purposes [35, 149, 150, 152]. The model, discussed in Section 2.2, includes 9 joints and 51 muscles of the arm. This work utilized the mathematical formulation for a muscle activation pattern for a given applied loading to perform the inverse calculation and find the required applied loading to achieve a certain activation pattern for some target muscles. This methodology could exactly achieve the desired target muscle forces without inducing activity in otherwise inactive muscles. Thus, the algorithm was able to calculate the necessary joint torques to be applied by an exoskeleton, an overview of which will be presented in Section 6.2. However, this method had several key limitations. It included several feasibility criteria that had to be met in order for the muscle activation pattern to be physically feasible [149]. These criteria required that target muscle forces be achieved exactly, which may not always be possible or necessary. For many exercise or rehabilitation situations, approximate forces may be acceptable. In addition, it required that inactive muscles be maintained as inactive, another requirement that may not be strictly necessary. Finally, the formulation did not address the upper limit of muscle forces, requiring only that the calculated forces be non-negative. In reality, using such a system on a person could result in excess applied force, causing muscle strain. These limitations were accepted to simplify the resultant formulation, but are of concern for safe usage and the generalizability of the method, so Section 6.3 will present further advancements of the model. This study will relax the requirements and reframe the feasibility criteria as optimization problems to achieve the target muscle pattern with as little error as possible, as well as account for the upper limit of muscle forces [55].

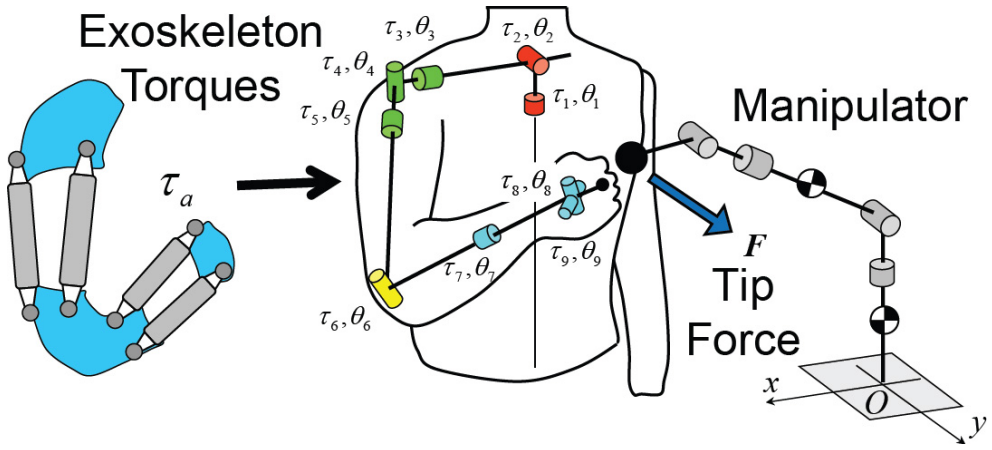

Figure 50: Human operator performs a motor task against a manipulator while wearing an exoskeleton

6.2 Problem Formulation

6.2.1 System Equation

Consider the individual muscle force generation for static tasks, where it is assumed that a subject does not change his or her posture during a task and all muscle contractions are isometric. The dynamics of the body and robot are neglected. Figure 50 shows a schematic diagram where a human operator is performing a motor task, which requires the human to exert their muscles to accomplish some target force or motion, while interacting with a robotic manipulator and wearing an exoskeleton device. The robot is capable of applying force to the human's hand in three dimensions, while the exoskeleton is assumed to be ideal and designed such that it is capable of applying torques to all nine of the human's arm joints. The goal is to modulate the muscle forces applied by the human through these forces and torques applied by the manipulator and exoskeleton. For a human musculoskeletal model that has M joints and N muscles, the net torques in the human joints is given by (43).

$$\boldsymbol{\tau}_w = \boldsymbol{g}(\boldsymbol{\theta}) + \boldsymbol{\Omega}(\boldsymbol{\phi})^\top \boldsymbol{f}_e - \boldsymbol{\tau}_a \tag{43}$$

Here, $\boldsymbol{\tau}_w \in \Re^M$ is a vector of human joint torques, $\boldsymbol{\phi} = [\phi_1, \cdots, \phi_M]^\top \in \Re^M$ is a vector of joint angles, $\boldsymbol{f}_e = [f_x, f_y, f_z]^\top$ is the translational force at the tip (i.e., the force the human applies to the environment or the force applied by the manipulator to the human), $\boldsymbol{\Omega}(\boldsymbol{\phi})$ is the Jacobian between the joints and end-point, $\boldsymbol{g}(\boldsymbol{\phi})$ is the gravity force, and $\boldsymbol{\tau}_a \in \Re^M$ is the joint torque applied by the exoskeleton. The static equation of the musculoskeletal system is then given by (44). In order to achieve the desired muscle control, the muscle forces should be induced such that the joint torques are those applied externally by (43).

$$\boldsymbol{\tau}_w = \boldsymbol{\Psi}(\boldsymbol{\phi})\boldsymbol{f} = \begin{bmatrix} \psi_{11} & \cdots & \psi_{1N} \\ \vdots & \ddots & \vdots \\ \psi_{M1} & \cdots & \psi_{MN} \end{bmatrix} \begin{bmatrix} f_1 \\ \vdots \\ f_N \end{bmatrix} \tag{44}$$

In this relation, $\boldsymbol{\Psi} \in \Re^{M \times N}$ is the moment-arm matrix of the muscles and $\boldsymbol{f} = [f_1, \cdots, f_N]^\top \in \Re^N$ is the human muscle force vector. The element a_{ij} of $\boldsymbol{\Psi}$ represents the moment arm of muscle j for joint i, so $a_{ij} = 0$ is given if f_j does not affect joint i. Note $f_j \geq 0$ $(j = 1, \cdots, N)$ because muscle contraction cannot generate negative forces. $\boldsymbol{g}(\boldsymbol{\phi})$, $\boldsymbol{\Omega}(\boldsymbol{\phi})$, and $\boldsymbol{\Psi}(\boldsymbol{\phi})$ for a given posture $\boldsymbol{\phi}$ can be calculated by the musculoskeletal model developed in [149, 150, 152]. This model of the upper-right limb with 51 muscles has been developed to analyze the physical interaction between the exoskeleton and the wearer at the level of individual muscles. This model consists of 5 rigid links and 9 joints. For more detail, see [149]. To simplify the problem, no upper-bound is given for $\boldsymbol{\tau}_a$.

6.2.2 Optimization Principle in the Neuromuscular System and Muscle Force Prediction

The human body has a much larger number of muscles than the number of joints, i.e., $N \gg M$, leading to muscle redundancy. This fact makes the prediction of muscle forces $\boldsymbol{f}$ by knowing joint torques $\boldsymbol{\tau}_w$ an ill-posed problem. Various optimization

approaches have been proposed to model the Optimization Principle in the neuromuscular system [15, 26, 132, 154] and to solve this problem by minimizing a cost function. The main difference among the approaches is the structure of cost functions that represent performance criteria on which the neuromuscular system optimizes the activation of muscle forces. In the literature that deals with isometric or relatively slow motions, the cost functions have a general form comprised of the sum of muscular stress or force raised to a power. The static optimization method can be formulated as follows.

$$\text{Minimize} \quad \rho(\boldsymbol{f}) = \sum_{j=1}^{N} c_j f_j^n \tag{45}$$

$$\text{subject to} \begin{cases} \boldsymbol{\tau}_w = \boldsymbol{\Psi} \boldsymbol{f} \\ 0 \leq f_j \leq f_{\max j} (j = 1, \ldots, N) \end{cases} \tag{46}$$

The cost function $\rho(\boldsymbol{f})$ is determined by the weighting factors c_j's, which are determined based on the physical characteristics of each muscle, and the integer power n. Crowninshield determined that the optimal weights are given by (47) and the max force is given by (48).

$$c_j = \left(\frac{1}{PCSA_j} \right) \tag{47}$$

$$f_{\max j} = \varepsilon PCSA_j \tag{48}$$

In these equations, $PCSA_j$ is the physiological cross sectional area (PCSA) each muscle, as given in the model used by [149]. Also, as given by [84], $\varepsilon = 0.7 \times 10^6 \, \mathrm{N/m^2}$. Typically, $n = 2$ is often used, though it should be noted that arguments still exist

on the choice of the weighting factors c_j and the integer n of the power [15, 26, 132, 154]. The choice of these parameters is discussed further in [26]. There are still arguments and criticism of the neurological background of this muscle force prediction; however, this approach has been implemented in publicly or commercially available software [27, 31]. The effectiveness of this approach for predicting stereotyped motor performances has been reported in the literature [32, 84, 111].

6.2.3 Individual Muscle Control

Individual muscle control requires solving the inverse problem of the aforementioned muscle force prediction in (45) to control N muscles by adjusting M joint torque inputs. Note that this inverse solution is not straightforward since any induced muscle activation pattern must satisfy the physiology-based optimality criterion. The first condition in (46) represents the balance of joint torques. The second condition means that each muscle can only "pull", exerting positive contracting force limited by its maximum voluntary force. Mathematically, this can be treated as finding an adequate equality constraint for the joint torques such that desired muscle forces are obtained as a result of the cost function minimization. As described earlier, the exoskeleton merely modifies human joint torques, which is equivalent to the modification of the first equality condition in (46).

Let $\boldsymbol{f}_0$ be the nominal muscle forces when a subject is performing a nominal motor task. The human force vector $\boldsymbol{f}_0$ may be permutated according to three groups of muscles: target muscles, which will be controlled to achieve a desired force level; non-target muscles, which are active but not directly controlled; and inactive muscles, which provide no force. Let $\tilde{N} \leq N$ be the number of the active muscles, and $N - \tilde{N}$ be the number of the inactive muscles. The active muscles have elements with nonzero values in $\boldsymbol{f}_0$, and the inactive muscles have zeros. The active muscle group consists of target muscles $\boldsymbol{f}_t \in \Re^{N_t}$ and non-target muscles $\boldsymbol{f}_n \in \Re^{N_n}$ where

$N_t + N_n = \tilde{N}$. Without the loss of generality, the order of the N muscles may be permutated according to these three groups for the simplicity of description.

$$\boldsymbol{f} \triangleq \left[\begin{array}{c} \boldsymbol{f}_t \\ \boldsymbol{f}_n \\ \hline \boldsymbol{0} \end{array}\right] \begin{array}{l} \cdots \text{target muscles} \\ \cdots \text{non-target muscles} \\ \cdots \text{inactive muscles} \end{array} \tag{49}$$

The above permutation for $\boldsymbol{f}$ is also applied to the moment-arm matrix $\boldsymbol{\Psi}$ accordingly:

$$\boldsymbol{\Psi}^\top = \left[\begin{array}{c} \boldsymbol{\Psi}_t \\ \boldsymbol{\Psi}_n \\ \hline \boldsymbol{\Psi}_v \end{array}\right] \begin{array}{l} \cdots \text{target muscles} \\ \cdots \text{non-target muscles} \\ \cdots \text{inactive muscles} \end{array} \tag{50}$$

Hereafter these permutated vectors and matrices will be used.

The desired target muscle forces $\boldsymbol{f}_{td}$ are given as follows by explicitly specifying the ratio of change for each of the target muscles:

$$\boldsymbol{f}_{td} = \mathrm{diag}[\eta_1, \eta_2, \cdots, \eta_{N_t}]\boldsymbol{f}_{t0} \tag{51}$$

where $\eta_j (> 0)$ is the ratio of change of the j-th target muscle. The subscript d denotes the desired muscle forces, and the subscript 0 denotes the nominal muscle forces. Let the total external torque $\boldsymbol{\tau}_{ex} \in \Re^M$ be

$$\boldsymbol{\tau}_{ex} = \boldsymbol{\Omega}^\top \boldsymbol{f}_e - \boldsymbol{\tau}_a. \tag{52}$$

Equation (52) shows how the joint toques can be adjusted by applying $\boldsymbol{\tau}_a$ from the exoskeleton and by exerting $\boldsymbol{f}_e$ at the tip either by performing a motor task or through a robot manipulator. Note that there is a certain freedom in choosing $\boldsymbol{f}_e$ and $\boldsymbol{\tau}_a$ to

achieve a given $\boldsymbol{\tau}_{ex}$. This will be discussed in a later section. The problem to realize $\boldsymbol{f}_{td}$ can be formulated as follows.

Perfect Individual Muscle Control:

Find $\boldsymbol{f}_e$ and $\boldsymbol{\tau}_a$ that will achieve a $\boldsymbol{\tau}_e x$ such that the solution of (45) includes a desired muscle activation pattern for the target muscles, $\boldsymbol{f}_{td}$, i.e.,

$$[\boldsymbol{f}_{td}^{\top}, \boldsymbol{f}_{nd}^{\top}, \mathbf{0}^{\top}]^{\top} = \underset{\boldsymbol{f}(\boldsymbol{\tau}_{ex})}{\operatorname{argmin}} \rho(\boldsymbol{f}) \tag{53}$$

with minimum changes in non-target muscle forces, i.e., $|\boldsymbol{f}_{nd} - \boldsymbol{f}_{n0}| \rightarrow min.$

6.2.4 Solution for Perfect Muscle Force Control

The previous work by Ueda, Ding, et al, [35, 149, 150, 152] provided a solution to exactly realize the desired target muscles forces, which will be referred to as perfect muscle control. Performing the minimization in (53) to find a solution to (44) results in the external torque $\boldsymbol{\tau}_{ex}$ for the perfect control given by

$$\boldsymbol{\tau}_{ex} = \left[\boldsymbol{\Psi}_t^{\top} \ \boldsymbol{\Psi}_n^{\top}\right] w^{-1} \left(\begin{bmatrix} \boldsymbol{\Psi}_t \\ \boldsymbol{\Psi}_n \end{bmatrix} \boldsymbol{\zeta} \right) \tag{54}$$

where $\boldsymbol{\zeta}$ is the control input vector and represents in a moment arm independent manner the change in torques that must be applied to achieve the desired muscle activation pattern. The transformation $w(*)$ is a function that converts the muscle force vector $\boldsymbol{f}$ to a new vector $\boldsymbol{q}$ as $\boldsymbol{q} = w(\boldsymbol{f})$ where the j-th elements of $\boldsymbol{f}$ and $\boldsymbol{q}$ are given as

$$q_j \stackrel{\triangle}{=} \frac{\partial u(\boldsymbol{f})}{\partial f_j} = r c_j {f_j}^{n-1}, (j = 1, \cdots, N), \tag{55}$$

and $w^{-1}(\boldsymbol{q}) = \boldsymbol{f}$ is the inverse function of $w(*)$ and the c_j's are as in (45). $\boldsymbol{q}$ can be permutated in a similar manner to $\boldsymbol{f}$:

$$\boldsymbol{q} = \begin{bmatrix} \boldsymbol{q}_t \\ \boldsymbol{q}_n \\ \hline \boldsymbol{q}_v \end{bmatrix} \begin{matrix} \cdots \text{target muscles} \\ \cdots \text{non-target muscles} \\ \cdots \text{inactive muscles} \end{matrix} \tag{56}$$

The control input vector $\boldsymbol{\zeta}$ is the main element in the solution and is given as

$$\boldsymbol{\zeta} = \boldsymbol{\Psi}_t^+ \left[w(\boldsymbol{f}_{td}) - w(\boldsymbol{f}_{t0}) \right] + (\boldsymbol{I} - \boldsymbol{\Psi}_t^+ \boldsymbol{\Psi}_t)\boldsymbol{\xi}, \tag{57}$$

where $\boldsymbol{I}$ is the identity matrix, and $\boldsymbol{\xi}$ is a free parameter that represents the remaining redundancy for controlling the non-target muscles as the second priority. This solution holds regardless of the choice of the parameter n in (45) and (55), which was verified in [26]. In [149], the existence of this solution relied on three criteria:

1. The target muscles forces must all be linearly independent of one another:

$$\text{rank}\,(\,\boldsymbol{\Psi}_t\,) = \text{rank}\left(\begin{bmatrix} \boldsymbol{\Psi}_t & w(\boldsymbol{f}_{td}) - w(\boldsymbol{f}_{t0}) \end{bmatrix} \right) \tag{58}$$

2. The inactive muscles must be maintained as exactly inactive:

$$-\boldsymbol{\Psi}_v \begin{bmatrix} \boldsymbol{\Psi}_t \\ \boldsymbol{\Psi}_n \end{bmatrix}^+ \begin{bmatrix} \boldsymbol{q}_{t0} \\ \boldsymbol{q}_{n0} \end{bmatrix} - \boldsymbol{\Psi}_v \boldsymbol{\zeta} > 0 \tag{59}$$

3. The non-target active muscles must be maintained as active:

$$\boldsymbol{\Psi}_n \boldsymbol{\zeta} + w(\boldsymbol{f}_{n0}) > 0 \tag{60}$$

The full derivation of these criteria is found in [149]. The method attempted to find a solution by minimizing the change in non-target active muscles while satisfying the three criteria. If this was not possible, then no solution existed that could exactly realize the target muscles forces within physiological constraints. This resulted in a

very narrow range of feasibility that could be practically expanded by relaxing the required assumptions.

In addition, it was assumed that the exoskeleton is ideal, and therefore has means to adjust all of the joints, i.e., $\boldsymbol{\tau}_h$ is *fully* modifiable by $\boldsymbol{\tau}_{ex}$, and a combination of $\boldsymbol{f}_e$ and $\boldsymbol{\tau}_a$ always exists that realizes a given $\boldsymbol{\tau}_{ex}$ via the physical human-robot interaction.

4. The exoskeleton is *ideal*, and therefore $\boldsymbol{\tau}_a$ exists (as well as $\boldsymbol{f}_e$ in the case where a manipulator arm is also used) and can realize $\boldsymbol{\tau}_{ex}$ in (52).

This research shows theoretical results that relax these requirements and reframe the feasibility criteria to achieve the target muscle pattern with as little error as possible.

6.3 Relaxing the Feasibility Conditions

6.3.1 Problem Reformulation

The above limitations on the use of the perfect muscle control solution motivated generalizing the solution to eliminate assumptions and make the control scheme more widely applicable. To do so, it is necessary to examine the three key assumptions, criteria 1-3 discussed in Section 6.2.4.

First, the solution ignores the upper bound on an individual muscle's force. While mathematically sound, this assumption has serious physiological consequences. Should an exoskeleton attempt to apply the resultant torques, and one or more muscles are required to supply more force than physically possible, the wearer of the device could sustain serious injury. Accounting for this limit requires adding the right side of the inequality condition, $f_j \leq f_{\max j} (j = 1, \cdots, N)$, into the Karush-Kuhn-Tucker (KKT) equation, which will result in a second set of λ's. For clarity, the λ's in the initial solution, which correspond to the lower bound $0 \leq f_j$, will be denoted as λ_l, while the λ's corresponding to the upper bound will be denoted as λ_u.

The second assumption is that it is necessary and possible to match the desired target muscle forces exactly. In reality, it is never possible to exactly match all muscle forces, and it is likely not absolutely necessary, either. Therefore, instead of requiring $f_j = f_{jd}$, a small error tolerance e_j is allowed such that $f_j = f_{jd}+e_j$. When performing the transformation $\boldsymbol{q} = w(\boldsymbol{f})$, this becomes $\boldsymbol{q}_t = \boldsymbol{q}_{td} + \boldsymbol{\epsilon}_t$, where $\boldsymbol{\epsilon}_t$ is the allowable error tolerance in $\boldsymbol{q}_t$ and takes the same units as $\boldsymbol{q}$.

Finally, the third assumption states that inactive muscles must stay inactive, and non-target active muscles must stay active. Physically, this may be difficult to realize. Therefore, in the interest of finding a control scheme that is as widely application as possible, it is desired to allow initially active non-target muscles to become inactive, while allowing initially inactive muscles to generate a small amount of force. The former requires including the Lagrange multipliers in the KKT condition as with the generalization applied for the first assumption. The latter requires the introduction of an error tolerance term, $\boldsymbol{\epsilon}_v$, as with the generalization for the second assumption.

6.3.2 New KKT Condition

Combining the generalizations for all three assumptions, a new feasibility equation is obtained from the KKT condition [11, 126]. For convenience, the inequality constraint $0 \leq f_j \leq f_{\max j} (j = 1, \cdots, N)$ was split into two conditions, with the lower and upper bounds corresponding to g_{jl} and g_{ju}, respectively. The updated KKT condition is shown in (61) and is subject to the conditions in (62), (63), and (64).

$$\nabla\rho(\boldsymbol{f}) \quad + \quad \sum_{i=1}^{M} \omega_i \nabla h_i(\boldsymbol{f}) + \sum_{j=1}^{N} \left(\lambda_{jl} \nabla g_{jl}(\boldsymbol{f}) + \lambda_{ju} \nabla g_{ju}(\boldsymbol{f})\right) = 0 \tag{61}$$

$$
\begin{aligned}
h_i(\boldsymbol{f}) &= 0 && (62)\\
\lambda_{jl} g_{jl}(\boldsymbol{f}) &= 0,\ \lambda_{jl} \geq 0,\ g_{jl}(\boldsymbol{f}) \leq 0 && (63)\\
\lambda_{ju} g_{ju}(\boldsymbol{f}) &= 0,\ \lambda_{ju} \geq 0,\ g_{ju}(\boldsymbol{f}) \leq 0 && (64)\\
\text{where} &\quad (i = 1, \ldots, M),\ (j = 1, \ldots, N)
\end{aligned}
$$

The constraints h_i, g_{jl}, and g_{ju} are given by (65), (66), and (67).

$$
\begin{aligned}
h_i(\boldsymbol{f}) &= \tau_i - \boldsymbol{\psi}_i^{\top} \boldsymbol{f} && (65)\\
g_{jl}(\boldsymbol{f}) &= -f_j && (66)\\
g_{ju}(\boldsymbol{f}) &= f_j - f_{\max j} && (67)
\end{aligned}
$$

The derivatives of the three constraints are then given by (68), (69), and (70).

$$
\begin{aligned}
\frac{\partial h_i}{\partial f_j} &= -\psi_{ij} && (68)\\
\frac{\partial g_{j_1 l}}{\partial f_{j_2}} &= \begin{cases} -1, & j_1 = j_2 \\ 0, & j_1 \neq j_2 \end{cases} && (69)\\
\frac{\partial g_{j_1 u}}{\partial f_{j_2}} &= \begin{cases} 1, & j_1 = j_2 \\ 0, & j_1 \neq j_2 \end{cases} && (70)
\end{aligned}
$$

These, combined with the definition of $\boldsymbol{q}$ in (55), which remains unchanged, give the updated equation given by (71).

$$\begin{aligned} \boldsymbol{q} = w(\boldsymbol{f}) &= \boldsymbol{\Psi}^\top \boldsymbol{\omega} + \boldsymbol{\lambda} \\ \text{where} \qquad \boldsymbol{q} &= \begin{bmatrix} q_1 \\ \vdots \\ q_N \end{bmatrix} \quad \boldsymbol{\omega} = \begin{bmatrix} \omega_1 \\ \vdots \\ \omega_M \end{bmatrix} \\ \boldsymbol{\lambda} = \boldsymbol{\lambda}_l - \boldsymbol{\lambda}_u &= \begin{bmatrix} \lambda_{1l} - \lambda_{1u} \\ \vdots \\ \lambda_{Nl} - \lambda_{Nu} \end{bmatrix} \end{aligned} \tag{71}$$

Permutating this equation as done for (56), but without making any simplifications or assumptions, results in (72).

$$\begin{bmatrix} \boldsymbol{q}_t \\ \boldsymbol{q}_n \\ \hline \boldsymbol{q}_v \end{bmatrix} = \begin{bmatrix} \boldsymbol{\Psi}_t \\ \boldsymbol{\Psi}_n \\ \hline \boldsymbol{\Psi}_v \end{bmatrix} \boldsymbol{\omega} + \begin{bmatrix} \boldsymbol{\lambda}_{tl} - \boldsymbol{\lambda}_{tu} \\ \boldsymbol{\lambda}_{nl} - \boldsymbol{\lambda}_{nu} \\ \hline \boldsymbol{\lambda}_{vl} - \boldsymbol{\lambda}_{vu} \end{bmatrix} \tag{72}$$

It is possible to make a few simplifications regarding the inequality constraint multipliers. Target muscles will necessarily always be active, and therefore will supply a non-zero force, so the lower constraint is always satisfied ($\boldsymbol{\lambda}_{tl} = \mathbf{0}$). In addition, inactive muscles by definition supply zero force, so the upper constraint is satisfied ($\boldsymbol{q_v} = 0$ and $\boldsymbol{\lambda}_{vu} = \mathbf{0}$). This yields the result in (73).

$$\begin{bmatrix} \boldsymbol{q}_t \\ \boldsymbol{q}_n \\ \hline \mathbf{0} \end{bmatrix} = \begin{bmatrix} \boldsymbol{\Psi}_t \\ \boldsymbol{\Psi}_n \\ \hline \boldsymbol{\Psi}_v \end{bmatrix} \boldsymbol{\omega} + \begin{bmatrix} -\boldsymbol{\lambda}_{tu} \\ \boldsymbol{\lambda}_{nl} - \boldsymbol{\lambda}_{nu} \\ \hline \boldsymbol{\lambda}_{vl} \end{bmatrix} \tag{73}$$

The result can be evaluated for both the nominal muscle forces, $\boldsymbol{f}_0$, and the desired muscle forces, $\boldsymbol{f}_d$. For the nominal case, by definition, the active non-target muscles will have a positive force, so the lower bound is automatically satisfied ($\boldsymbol{\lambda}_{0nl} = \mathbf{0}$), giving (74). For the desired case, it can be assumed that the desired values of the

target muscles will never be the maximum force for safety reasons, while there is no assumption that the non-target active muscles will stay active. Also, the allowable error tolerance terms, ϵ, are incorporated, which gives (75).

$$\begin{bmatrix} \boldsymbol{q}_{0t} \\ \boldsymbol{q}_{0n} \\ \hline \mathbf{0} \end{bmatrix} = \begin{bmatrix} \boldsymbol{\Psi}_t \\ \boldsymbol{\Psi}_n \\ \hline \boldsymbol{\Psi}_v \end{bmatrix} \boldsymbol{\omega}_0 + \begin{bmatrix} -\boldsymbol{\lambda}_{0tu} \\ -\boldsymbol{\lambda}_{0nu} \\ \hline \boldsymbol{\lambda}_{0vl} \end{bmatrix} \tag{74}$$

$$\begin{bmatrix} \boldsymbol{q}_{dt} + \boldsymbol{\epsilon}_t \\ \boldsymbol{q}_{dn} \\ \hline \boldsymbol{\epsilon}_v \end{bmatrix} = \begin{bmatrix} \boldsymbol{\Psi}_t \\ \boldsymbol{\Psi}_n \\ \hline \boldsymbol{\Psi}_v \end{bmatrix} \boldsymbol{\omega}_d + \begin{bmatrix} \mathbf{0} \\ \boldsymbol{\lambda}_{dnl} - \boldsymbol{\lambda}_{dnu} \\ \hline \boldsymbol{\lambda}_{dvl} \end{bmatrix} \tag{75}$$

6.3.3 Muscle Control

Using the generalized KKT conditions given in (74) and (75), it is possible to derive a control law that can be used to find the value of $\boldsymbol{\tau}_h$ that will induce the desired muscle activation pattern. Since $\boldsymbol{\omega}$ corresponds to the vector of human joint torques, it is the ideal quantity to control, as finding an appropriate value for $\boldsymbol{\omega}_d$ will lead to finding $\boldsymbol{\tau}_{ex}$, and subsequently $\boldsymbol{f}_e$ and $\boldsymbol{\tau}_a$, to realize the desired muscle forces. Therefore, let $\boldsymbol{\omega}_d = \boldsymbol{\omega}_0 + \boldsymbol{\zeta}$, where $\boldsymbol{\zeta}$ is the control input vector, similar to that presented in (57) for the case of perfect muscle control. Through the derivation below, this leads to (76).

$$\begin{aligned} \boldsymbol{q}_d &= \boldsymbol{\Psi}^\top (\boldsymbol{\omega}_0 + \boldsymbol{\zeta}) + \boldsymbol{\lambda}_d \\ &= \boldsymbol{\Psi}^\top \boldsymbol{\omega}_0 + \boldsymbol{\Psi}^\top \boldsymbol{\zeta} + \boldsymbol{\lambda}_d \\ &= \boldsymbol{\Psi}^\top \boldsymbol{\omega}_0 + \boldsymbol{\lambda}_0 + \boldsymbol{\Psi}^\top \boldsymbol{\zeta} + \boldsymbol{\lambda}_d - \boldsymbol{\lambda}_0 \\ &= \boldsymbol{q}_0 + \boldsymbol{\Psi}^\top \boldsymbol{\zeta} + \boldsymbol{\lambda}_d - \boldsymbol{\lambda}_0 \\ \boldsymbol{q}_d - \boldsymbol{q}_0 &= \boldsymbol{\Psi}^\top \boldsymbol{\zeta} + \boldsymbol{\lambda}_d - \boldsymbol{\lambda}_0 \end{aligned}$$

$$\left[\begin{array}{c} \boldsymbol{q}_{dt} + \boldsymbol{\epsilon}_t \\ \boldsymbol{q}_{dn} \\ \hline \boldsymbol{\epsilon}_v \end{array}\right] - \left[\begin{array}{c} \boldsymbol{q}_{0t} \\ \boldsymbol{q}_{0n} \\ \hline \mathbf{0} \end{array}\right] = \left[\begin{array}{c} \boldsymbol{\Psi}_t \\ \boldsymbol{\Psi}_n \\ \hline \boldsymbol{\Psi}_v \end{array}\right] \boldsymbol{\zeta} + \left[\begin{array}{c} \mathbf{0} \\ \boldsymbol{\lambda}_{dnl} - \boldsymbol{\lambda}_{dnu} \\ \hline \boldsymbol{\lambda}_{dvl} \end{array}\right] - \left[\begin{array}{c} -\boldsymbol{\lambda}_{0tu} \\ -\boldsymbol{\lambda}_{0nu} \\ \hline \boldsymbol{\lambda}_{0vl} \end{array}\right] \tag{76}$$

The unknown to be solved for in (76) is the control input for the joint torques, $\boldsymbol{\zeta}$. The $\boldsymbol{q}_0$'s are known from calculating the nominal case and $\boldsymbol{q}_{dt}$ is known from the desired muscle activation pattern, while $\boldsymbol{\Psi}^\top$ is known from the geometry and configuration of the muscles. This leaves $\boldsymbol{q}_{dn}$, both $\boldsymbol{\epsilon}$'s, and all $\boldsymbol{\lambda}$'s as parameters that can be chosen to make the solution feasible. There are so many parameters due to the large difference between the number of muscles, N, and the number of joints, M ($N \gg M$).

Examining (76), it can be seen that each term has a physical meaning. The left hand side, from (55), gives the desired change in muscle forces. The first term on the right hand side provides the effect of the control input on the muscles, since $\boldsymbol{\Psi}^\top$ gives the mapping from joint torques to muscles forces, while the remaining terms account for any muscles which are exactly equal to zero or the muscle's maximum force. It is important to note that the inequality constraint multiplier vectors, $\boldsymbol{\lambda}$'s, will tend to be sparse. The elements of these are only non-zero if that particular muscle is exactly on the constraint multiplied by that $\boldsymbol{\lambda}$. For example, if non-target muscle j is providing maximum force in the nominal case, but is between zero and maximum in the desired case, then $\lambda_{j0nu} > 0$, $\lambda_{jdnu} = 0$, and $\lambda_{jdnl} = 0$. In general, many of the entries in these vectors will be zero.

6.3.4 Solution

The goal of this algorithm is to match the desired target muscle forces as exactly as possible. Since the number of outputs (muscle forces), N, is significantly larger than the number of inputs (joint torques), M, a priority based approach is used to find a solution. Therefore, the solution for $\boldsymbol{\zeta}$ can be found from the first row of (76): $\boldsymbol{q}_{dt} + \boldsymbol{\epsilon}_t - \boldsymbol{q}_{0t} = \boldsymbol{\Psi}_t\boldsymbol{\zeta} + \boldsymbol{\lambda}_{0tu}$. Rearranging slightly, this becomes (77).

$$\boldsymbol{q}_{dt} - \boldsymbol{q}_{0t} + \boldsymbol{\epsilon}_t - \boldsymbol{\lambda}_{0tu} = \boldsymbol{\Psi}_t \boldsymbol{\zeta} \tag{77}$$

Assuming the solution exists (the existence of a solution is discussed in Section 6.3.5), it is given by (78), which is analogous to (57) for the perfect control case.

$$\boldsymbol{\zeta} = \boldsymbol{\Psi}_t^+ \left(\boldsymbol{q}_{dt} - \boldsymbol{q}_{0t} + \boldsymbol{\epsilon}_t - \boldsymbol{\lambda}_{0tu}\right) + (\boldsymbol{I} - \boldsymbol{\Psi}_t^+ \boldsymbol{\Psi}_t)\boldsymbol{\xi} \tag{78}$$

This new solution is applied to (54) to obtain external torques. The free parameter $\boldsymbol{\xi}$ indicates the redundancy of the solution, and has an effect on the values of the remaining non-target (active and inactive) muscles. Increasing $\boldsymbol{\xi}$ has the effect of increasing activation without changing end-point force, which naturally leads to co-contraction. The choice of $\boldsymbol{\xi}$ is generally arbitrary, and will be discussed further with the choice of the other parameters in Section 6.3.5.

6.3.5 Feasibility and Choice of Parameters

Due to the way in which the matrices were permutated, each row of (76) deals with a different set of muscles. The first row is concerned with the target muscles, the second row with the active (in the nominal case) non-target muscles, and the last row with the inactive (again, in the nominal case) non-target muscles. Therefore, each row can be extracted from the matrix equation to determine a set of feasibility criteria for the existence of the solution discussed in Section 6.3.4.

The first row, previously extracted to get (77), is the most important, since it deals with the target muscles. In order to solve (77) using linear algebra, a matrix composed of $\boldsymbol{\Psi}_t$ augmented with the left hand side of the equation must have the same number of linearly independent rows as $\boldsymbol{\Psi}_t$ itself. This is concisely expressed in (79).

$$\text{rank}\left(\ \boldsymbol{\Psi}_t\ \right) = \text{rank}\left(\ \left[\boldsymbol{\Psi}_t \quad (\boldsymbol{q}_{dt} - \boldsymbol{q}_{0t} + \boldsymbol{\epsilon}_t - \boldsymbol{\lambda}_{0tu})\right]\ \right) \tag{79}$$

When this condition is satisfied, it is possible to obtain the desired target muscle forces while also satisfying the bounds on muscle force. The error tolerance $\boldsymbol{\epsilon}_t$ is a parameter that can be chosen to make this condition hold when it is not possible to exactly realize the target forces. In this case, a small value can be given to some or all elements of $\boldsymbol{\epsilon}_t$ to make an approximation of the desired $\boldsymbol{q}_{dt}$ realizable. The multiplier $\boldsymbol{\lambda}_{0tu}$ is known from the nominal muscle distribution, and is only non-zero for muscles that are initially at their maximum force.

The next priority in choosing the solution is to maintain inactive muscles as inactive (or keep them minimally active if this is not possible). The third row of (76), given by (80), provides the necessary condition for this.

$$\boldsymbol{\lambda}_{dvl} - \boldsymbol{\epsilon}_v = \boldsymbol{\lambda}_{0vl} - \boldsymbol{\Psi}_v \boldsymbol{\zeta} \tag{80}$$

For inactive muscles to remain inactive, $\boldsymbol{\lambda}_{dvl}$ must be positive and $\boldsymbol{\epsilon}_v$ will be zero, requiring the right hand side of the equation to be greater than zero. If, however, it is not possible (or not necessary) to meet this exactly, then elements of $\boldsymbol{\epsilon}_v$ can be chosen to be nonzero, leading to the condition given by (81).

$$\boldsymbol{\Psi}_v \boldsymbol{\zeta} + \boldsymbol{\lambda}_{0vl} > -\boldsymbol{\epsilon}_v \tag{81}$$

The final priority is to minimize the change in the forces of the non-target muscles. The second row of (76) can be written as in (82).

$$\boldsymbol{q}_{dn} - \boldsymbol{q}_{0n} = \boldsymbol{\Psi}_n \boldsymbol{\zeta} + \boldsymbol{\lambda}_{dnl} - \boldsymbol{\lambda}_{dnu} + \boldsymbol{\lambda}_{0nu} \tag{82}$$

In the ideal case, none of the non-target muscles are at maximum force, and it is desired to keep them from becoming inactive, so all the λ_n's are zero. For this to be the case, (83) must be true, where $\boldsymbol{q}_{\max} = w(\boldsymbol{f}_{\max})$.

$$0 < \boldsymbol{\Psi}_n \boldsymbol{\zeta} + \boldsymbol{q}_{0n} < \boldsymbol{q}_{\max} \tag{83}$$

Table 10: Desired Muscle Activation Patterns for Testing

#	Muscle 1	Ratio	Muscle 2	Ratio
1	Brachioradialis	x 0.8	Flexor Carpi Ulnaris	x 1.2
2	Brachioradialis	x 1.7	Flexor Carpi Ulnaris	x 0.8
3	Brachioradialis	x 1.5	Extensor Carpi Ulnaris	x 1.5

Table 11: Desired Muscle Activation Pattern Feasibility Results

#	Perfect	Relaxed	Error tolerance
1	Pass	Pass	0.0
2	Fail (Cond. 2, (59))	Pass	0.12
3	Fail (Cond. 3, (60))	Pass	0.05

Substituting the solution for $\boldsymbol{\zeta}$ from (78) into (82), then making the same decisions that lead to (83), the only remaining free parameter is $\boldsymbol{\xi}$. Therefore, a reasonable way to choose $\boldsymbol{\xi}$ is to avoid a change in the non-target muscles, or to minimize $||\boldsymbol{q}_{dn} - \boldsymbol{q}_{0n}||$, where $\boldsymbol{q}_{dn} - \boldsymbol{q}_{0n}$ is given by (84), which assumes that minimal effort is desired. If a non-minimum value of $\boldsymbol{\xi}$ is chosen, this could lead to increased cocontraction among non-target muscles.

$$\begin{aligned} \boldsymbol{q}_{dn} - \boldsymbol{q}_{0n} &= \boldsymbol{\Psi}_n \left[\boldsymbol{\Psi}_t^+ \left(\boldsymbol{q}_{dt} - \boldsymbol{q}_{0t} + \boldsymbol{\epsilon}_t - \boldsymbol{\lambda}_{0tu} \right) + \left(\boldsymbol{I} - \boldsymbol{\Psi}_t^+ \boldsymbol{\Psi}_t \right) \boldsymbol{\xi} \right] \\ &= \boldsymbol{\Psi}_n \boldsymbol{\Psi}_t^+ \left(\boldsymbol{q}_{dt} - \boldsymbol{q}_{0t} + \boldsymbol{\epsilon}_t - \boldsymbol{\lambda}_{0tu} \right) - \left[-\boldsymbol{\Psi}_n (I - \boldsymbol{\Psi}_t^+ \boldsymbol{\Psi}_t) \right] \boldsymbol{\xi} \end{aligned} \quad (84)$$

In general, this is consistent with the condition given by (83). However, due to the need to use the pseudoinverse of $\boldsymbol{\Psi}$ (since $\boldsymbol{\Psi}$ is not square), it is possible for numerical inaccuracies to arise. In this case, if the condition is not satisfied, then one or more non-target muscles is at the upper or lower limit. To maintain feasibility, the appropriate elements of $\boldsymbol{\lambda}_{dnu}$ and $\boldsymbol{\lambda}_{dnl}$ must be chosen such that the condition is again satisfied (Note that $\boldsymbol{\lambda}_{0nu}$ is known from the nominal muscle distribution).

6.3.6 Validation

The relaxed formulation was validated and compared to the perfect muscle control solution using a computer model. The model, developed in prior work by Ueda, Ming,

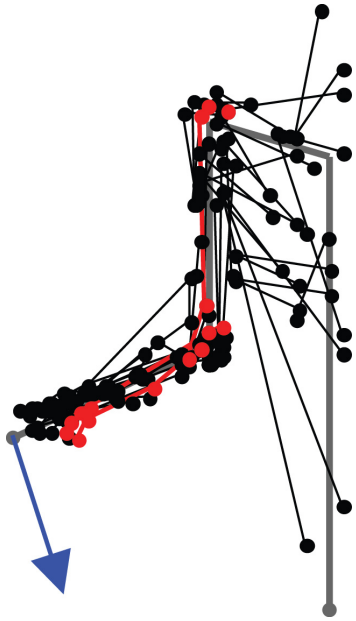

Figure 51: Nominal task, $\boldsymbol{f}_e = [10, 10, 10]$

et al, [149, 150, 152], simulated the muscles of the human upper arm using a total of 9 joints ($M = 9$) from the torso to wrist joint with 51 muscles ($N = 51$), shown in Figures 13 and 14. The Crowninshield's cost function presented in Section 6.2.2 is applied for the optimization criterion in the model. The joint torques an exoskeleton should apply for a variety of target muscle activation patterns, given in Table 10, were calculated using both the perfect control method and the relaxed control method, for comparison. The feasibility of each pattern for both methods is shown in Table 11. For the relaxed method solution, the norm of the error tolerances, $\boldsymbol{\epsilon}_t$ and $\boldsymbol{\epsilon}_v$, are presented normalized by the nominal muscle forces, $\boldsymbol{q}_0$. For all three patterns, the arm is in held straight down at the side of the body with the elbow bent 90° and the forearm held out, as in Figure 51, with an external applied force $\boldsymbol{f}_e = [10, 10, 0]$ for the nominal task.

To demonstrate that the relaxed method includes the solutions the perfect method could find, Figure 52(a) shows the results of both methods for pattern 1. Both solutions are identical, showing that a problem solvable by the perfect control method

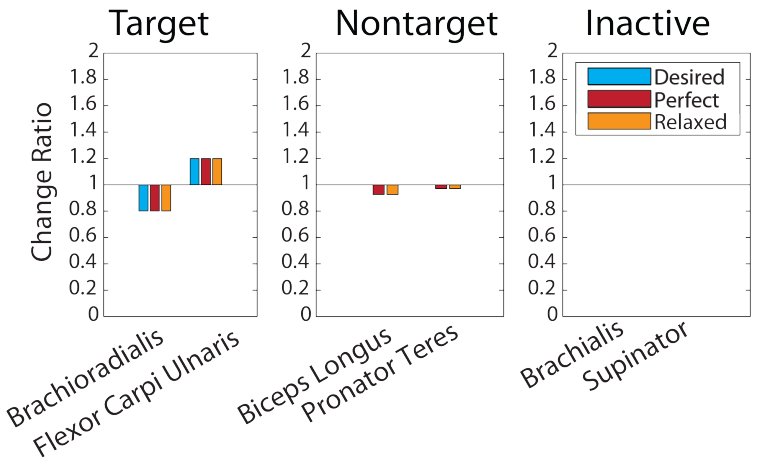

(a) Target pattern 1

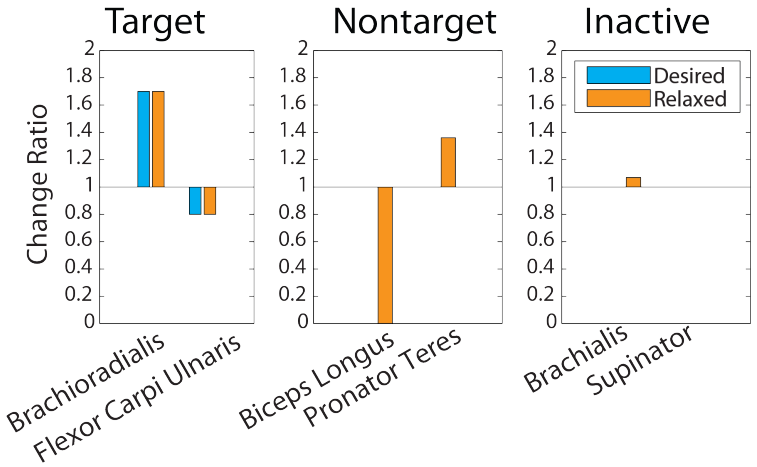

(b) Target pattern 2, error tolerance of 0.12

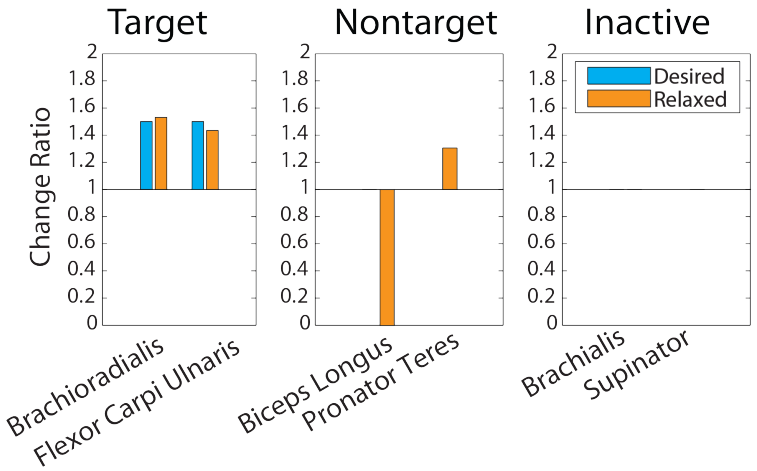

(c) Target pattern 3, error tolerance of 0.05

Figure 52: Simulation results of relaxed method

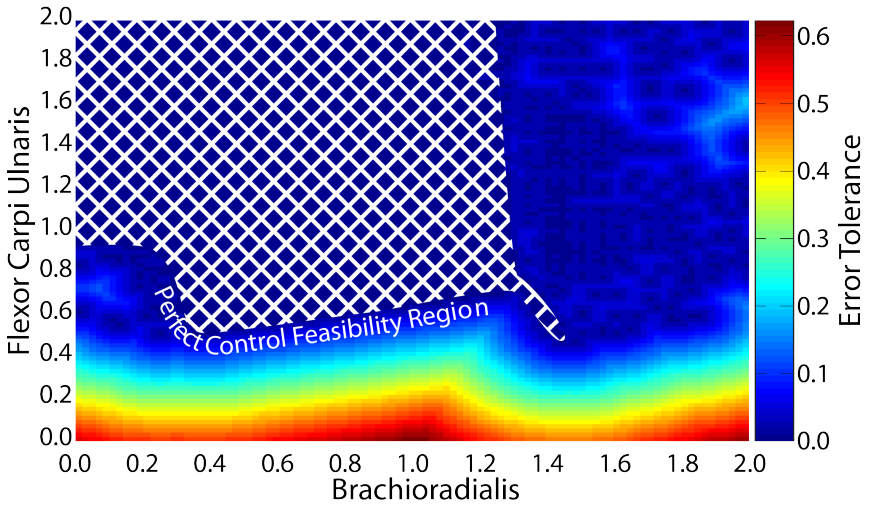

(a) Control of wrist flexor muscle and Brachioradialis

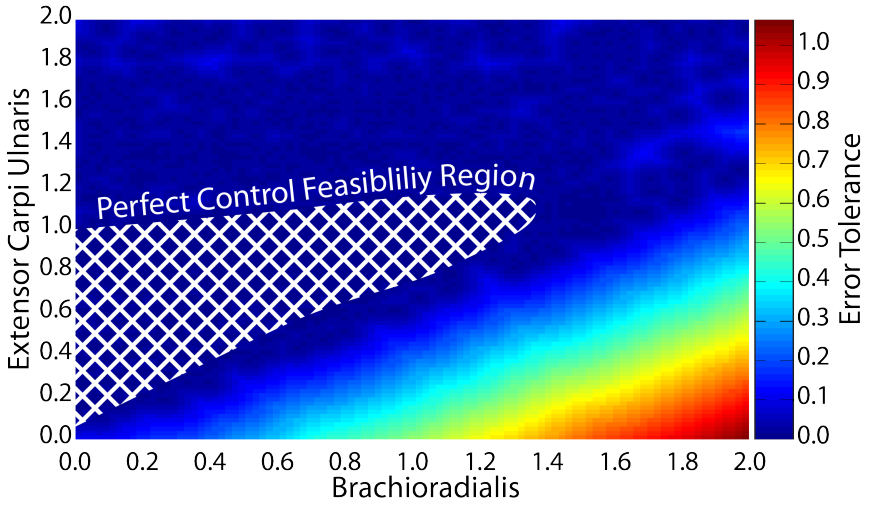

(b) Control of wrist extensor muscle and Brachioradialis

Figure 53: Comparison of feasibility region of both methods: Hatched region shows perfect method feasibility, color indicates required error tolerance to obtain feasible result using relaxed method.

would yield the same solution using the relaxed. For patterns 2 and 3, however, the perfect method could not find a physiologically feasible solution, but the relaxed method could. Figure 52(b) shows the resulting muscle forces for some of the muscles returned by the relaxed method for target pattern 2. The relaxed method was able to find a feasible solution and match the target muscles by allowing inactive muscles to become active. For pattern 3, the results are shown in Figure 52(c). A feasible

solution was found by not matching the target muscles exactly. The muscle forces are presented normalized by $\boldsymbol{q}_0$.

Figure 53 explores the feasibility of combinations between the muscles used in the three patterns for both the perfect and relaxed methods. The hatched areas in both plots represent the feasibility region of the perfect control method. Outside this region, only the relaxed control method was able to find a solution. The shading of the plot indicates the required magnitude of the error tolerance terms, $\boldsymbol{\epsilon}_t$ and $\boldsymbol{\epsilon}_v$, normalized by the nominal muscle force, $\boldsymbol{q}_0$. The relaxed method demonstrated a much larger region in which a feasible solution could be found than the perfect method, with large regions requiring only small allowable errors. In both cases, however, as the limits of the muscle forces were approached, large allowable errors were required to find a feasible solution.

6.4 Applications to Haptic Devices

Such a musculoskeletal model and muscle control scheme has many applications to haptic device control. Designing industrial haptic systems like those discussed in the design of the compensating controller would benefit from a thorough understanding of how the central nervous system modulates muscle activity based on external forces. In addition, such a muscle control routine would be required of any exoskeleton based force amplification system. Exoskeleton systems are worn by the user, and therefore must be carefully designed with the physiology of the user in mind. Combining a system that could adjust to changes in impedance with a system that can actively predict the muscle activity of the user would allow advance control that can ensure the safety of the operator. This would then also be applicable to the design of novel wearable control devices for haptically controller and teleoperated robots, with wide reaching implications from industrial robotics to hazardous environments and space robotics.

CHAPTER VII

CONCLUSION

7.1 Concluding Remarks

Instability of haptic force feedback devices under human contact can lead to undesired oscillations in the combined human and machine system. To improve the performance of haptic force assist devices, a system was designed that could account for changes in the operator's arm stiffness. The discussed compensating controller is a novel design for force amplifying systems that can successfully increase the system's stability on demand, allowing for higher performance than similar systems with low fixed gains but while retaining stability when necessary.

This was accomplished by estimating changes in arm end-point stiffness based on cocontraction levels measured using EMGs. The initial study was completed by measuring muscle activity in antagonistic muscles in the arm using EMG sensors, then calculating the level of cocontraction for each. Pairs which demonstrated a high level of antagonism and were close to the skin were chosen based on a simulation of the upper body musculoskeletal system. The correlation between EMG and stiffness was justified based on experiments. The results demonstrated a statistically significant correlation, which validated the use of EMG signals.

Two different classification systems were designed. The simpler threshold based system demonstrated through experiments that a compensating system could provide better performance without sacrificing stability, but several drawbacks were evident. Most importantely, the system showed excessive chatter between states. A probabilistic model was designed using a Hidden Markov Model (HMM) that could more

accurately classify the operator's intended motion. The designed HMM was effective, but did not show a statistical improvement over the threshold based classifier in experiments.

The gains of the device's impedance controller were adjusted based on the stiffness level estimate. Under low stiffness situations, the parameters were chosen to maintain low damping and allow for fast movement. However, when stiffness increased, the gains were adjusted to increase damping and allow the device to easily be held steady. Experiments showed that the system demonstrated improved stability in stiff situations and improved performance with regards to both speed and accuracy of task completion under real world usage scenarios.

Due to the inherent stochastic nature of the stiffness levels generated by users, the impedance controller's inner position controller was changed from a standard PD controller to one of two stochastically tolerant controllers. A Linear Quadratic Gaussian showed improvement and better modeled the system's parameters, but still required some performance sacrifices with regards to speed. A Linear Quadratic Regulator (LQR) specifically adapted to systems with stochastically varying parameters (SLQR) provided better results than the standard PD controller without the sacrifices of the LQG controller.

Ultimately, the design allowed a haptic controller to be more intelligent, by gathering more information about the operator, therefore enabling it to adjust, decreasing the workload on the operator and increasing overall performance. By allowing such a system to estimate the intentional state of the operator, it can overcome some of the issues with fixed gain systems. This more intelligent controller can simplify the operator's job and allow for performance increase, which in industrial settings could translate into higher productivity. By combining the compensation system with an advance controller capable of predicting, and even controlling, the muscle activity levels of the user, it would be possible to design robots that interact very closely with

people, including wearable exoskeleton systems. This can have useful applications to a wide variety of human-robot interaction situations, not only in industrial robotics, but also in potential personal robotics that must be designed to be safe around unpredictable people or in hazardous environments and space robotics where the situation is unsafe for people.

7.2 Contributions

The research described in the preceding chapters provides several original contributions to the state-of-the-art of HRI:

- pHRI typically requires either a low performance device or very compliant device to ensure the safety of the human, which is difficult to achieve in a force assisting device without comprising its utility. The novel design of a system that adjusts its gains based on an estimate of stiffness from direct muscle activity measurements provides a method for allowing a force assisting device to sense the parameters of the operator and adjust to ensure their safety without compromising performance. This is a new and unique solution to the problem of contact induced instability.

- Hidden Markov Models have been used in some scenarios to estimate human intention in cooperative tasks. This research extended this to the domain of physical human robot interaction, providing an intention model based on physical indicators.

- The standard impedance controller has been extended to be tolerant of stochastically varying systems. By replacing the inner force controller block with a stochastically enhanced version of an LQR controller, the SLQR controller, the impedance controller was made to be much more tolerant to varying system parameters and better able to emulate the desired impedance characteristics.

- The reverse pHRI problem of robot control of human muscles is even more reliant on safe designs. Previous attempts to create a muscle control methodology using exoskeleton robots had some safety concerns and limiting conditions that restricted applicability. A relaxed methodology was developed that ensured safety and provided wide applicability by reframing the control as an optimization problem, allowing errors when necessary.

7.3 Future Enhancements

The system designed showed a significant improvement over fixed gain systems, but still have a variety of drawbacks to be addressed by future research.

7.3.1 Muscle Activity

EMG measurements are only one way of obtaining arm dynamics information. Accelerometer based systems can measure muscle activity through skin vibrations, though they are less common than EMG. Improvements in real time stiffness identification could also benefit this system. Ultrasonic methods can be used to directly measure muscle stiffness, but generally are difficult to implement in real time. Recent work has presented a novel system that uses purposely induced small vibrations combined with system identification techniques to estimate arm parameters [72]. As the accuracy of such methods increases, it could replace surface based muscle activity measurements all together.

Identification of cocontraction is an ongoing research topic, and advances in that regard could be incorporated into this system. While the current method involves simply comparing the magnitude of the activity level of two muscles in time, there are recently identified frequency components to the muscle activity signal that are indicative of cocontraction. A frequency based analysis to identify these components would help provide a better estimation of cocontraction.

7.3.2 Classifiers

The HMM classifier shows promise, but the current implementation was unable to show improvement over the threshold classifier. There are a variety of advancements to the current model that could enhance the systems performance and help eliminate the unwanted chatter. The current HMM was trained based on manually identified states in the EMG cocontraction data. However, the lower than expected real-world accuracy shows that people do not consistently follow directions. In addition, there was likely a delay between the command being shown to the user and the user actually following it, which was unaccounted for by the training routine.

Several approaches can be taked to address these issues. More data should be collected for use in analyzing the model's performance, and potentially providing an expanded body of available training data to generate more accurate models. Also, the current models ran within the controller at the same rate as the controller, which is likely unecessary. The time scale on which the human state changes is orders of magnitude larger than the speed at which the controller runs, updating the model on a more appropriate time scale may provide better results.

The most promising would be to expand the information available to the HMM. Current models relied only on cocontraction data, but future models would likely benfit from the incorporation of other values, since muscle activity is not the only metric indicative of an operator's arm motion. The velocity of the operator's motion would be an excellent indicator of whether they are attempting to hold the device steady or not, and including it in the sensor input to the HMM could improve its accuracy. Similarly, the measured force could provide additional information Additionally, it has been demonstrated the when a person thinks about an object they want to move, they generally look at it [135]. Therefore, studies have used gaze following to estimate the most likely object a person is focusing on. While such research is still on going, future developments may prove useful to the system designed here. In the same way,

metrics such as body pose, grip force, and end point force are indicative to how a person is attempting to move a haptic robot. Therefore, it would be advantageous for the classifier model to be able to take into account more than just muscle activity measurements.

To better represent the complexity of the human's motion, it would be advantageous to allow the training routine to automatically identify the unique states in the system. Different training algorithms than the Viterbi algorithm, such as the Baum Welch technique, have been used with success in gesture and speech recognition problems, and may be applicable here [107, 108]. Also, the current HMM utilizes the simplest structure possible, but a more complex structure, such as a Hierarchical HMM (HHMM), may demonstrate better accuracy. Extending the Baum Welch technique allows the design of HMM that can represent more complex structures with multiple layers of states [45]. An HHMM can automatically identify the states in unlabeled data during training, so those states, once identified, can be associated with the tasks during which they occur to provide the compensation system with the estimates it needs. HHMM's have been used for language and handwriting analysis [7, 16, 19, 45], as well as gesture and motion recognition [119], information and data mining [141, 165], and other more complex models that require more than a simple state model. This makes them a natural next step for the classifier used in this system. Finally, HMM's were chosen for the simplicity and wide applicability to temporal state identification problems, but future work may benefit from a more thorough look at other, non-temporally based techniques, such as Artificial Neural Networks (ANNs) or State Vector Machines (SVMs), both of which are deterministic classifiers.

7.3.3 Controllers

The Stochastic Linear Quadratic Regulator (SLQR) controller provided a significant improvement over the basic PD inner position controller. However, a few advancements could further benefit the system. A standard impedance controller is closed loop with regard to position, but open loop with regard to force. In this research, the force loop was closed by the human contact. A more advanced force based controller that closes the force loop within the controller could help stabilize the system further. In addition, the existing system is a basic switching controller, but moving to something more advanced, such as a sliding mode controller, could help reduce the destabilizing effects of chatter in the classifier. Finally, the SLQR controller does not maintain an online model estimate like the LQG controller does, but the LQG controller only handles noise. By combining the stochastic parameter model with an LQG like real-time model, it might be possible to gain the benefits of both controllers

7.3.4 Testing

Experiments with the 1-degree-of-freedom (1-DOF) device demonstrated the compensating system's effectiveness, but did not promote its generalizability. Therefore, it would be desirable to implement this system on a larger, higher DOF device. Such a device, perhaps similar to that shown in Figure 1, would more accurate simulate the large haptic lifting devices that motivated this research, and would show that the results of this research are easily generalized to other systems.

APPENDIX A

DEVICE DETAILS AND SEPCIFICATIONS

A.1 1-DOF Haptic Feedback Paddle

A.1.1 Hardware

Table 12: Hardware Specifications

	Parameter	Value
Paddle	Radius to Handle	305 mm
	Width	294 mm
	Range of Motion	$\pm 0.325\,\text{rad}\,(\pm 18\,^\circ)$
	Total Travel of Handle	198 mm
Cable Drive	Cable Material	Steel 1x7 Braid
	Cable Strength	$\sim 400\,\text{N}$
	Effective Gear Ratio	27:1
Motor	Manufacturer	Anaheim Automation
	Model	BLWRPG235D-36V-4000-R13
	Type	DC Brushless
	Weight	1.25 kg
	Voltage	36 V
	Rated Torque	1.30 Nm
	Inertia	$2.30 \times 10^{-5}\,\text{kgm}^2$
	Max Force at Handle	138 N
	Gearbox Ratio	13:1
Motor Driver	Manufacturer	Pacific Scientific
	Model	PC833-001-T
	Frequency	16 kHz
	Encoder Decoding	Built In
Encoder	Manufacturer	US Digital
	Model	E2-1000-250-I-H-G-B
	Type	Two Window Quadrature
	Counts per Motor Rotation	$1000\,^{\text{cts}}/_{\text{rot}}$
	Counts per Radian of Handle Motion	$223,677\,^{\text{cts}}/_{\text{rad}}$

Table 13: Hardware Specifications (cont'd)

	Parameter	Value
Force Sensor	Manufacturer	ATI Industrial Automation
	Model	FT3399
	Max Force(X & Y)	$\pm 66.7\,\mathrm{N}$
	Max Force(Z)	$\pm 222\,\mathrm{N}$
	Max Torque(X, Y & Z)	$\pm 66.7\,\mathrm{Nm}$
	Force Resultion (X & Y)	$14\,\mathrm{mN}$
	Force Resultion (Z)	$28\,\mathrm{mN}$
	Torque Resultion (X, Y & Z)	$0.71\,\mathrm{mNm}$
Force Sensor Receiver	Manufacturer	ATI Industrial Automation
	Model	FT04451
	Frequency	$2.5\,\mathrm{kHz}$
	Latency	$800\,\mu\mathrm{s}$
EMG System (Wired)	Manufacturer	RUN Technologies
	Model	Myopac Jr.
	Channels	8
	Analog Output Frequency	$8\,\mathrm{kHz}$
EMG System (Wireless)	Manufacturer	Cometa Systems
	Model	WavePlus
	Channels	8
	Accelermeter Channels	24 (3 per EMG sensor)
	Frequency	$4\,\mathrm{kHz}$
	Latency	$14\,\mathrm{ms}$
CompactRIO	Manufacturer	National Instruments
	Controller Model	cRIO-9024
	Processor Speed	$800\,\mathrm{MHz}$
	RAM	$512\,\mathrm{MB}$
	Memory	$4\,\mathrm{GB}$
	Chassis Model	cRIO-9111
	FPGA	Virtex-5 LX30
	Expansion Slots	4
	C Series Module 1	cRIO-9201 8-channel Analog In
	C Series Module 2	cRIO-9201 4-channel Analog Out
	C Series Module 3	cRIO-9201 8-channel Digital In/Out

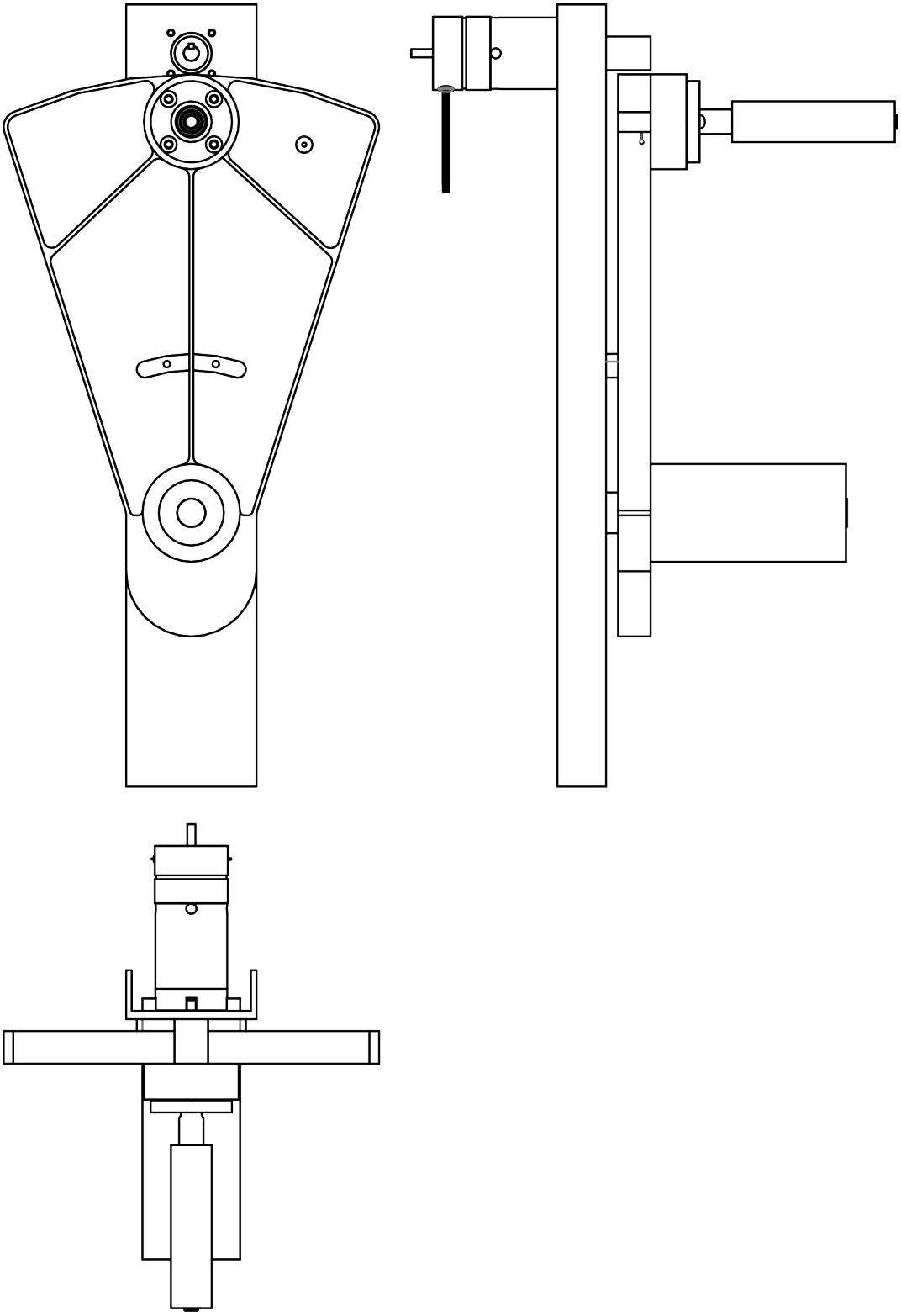

Figure 54: Three view drawing of device

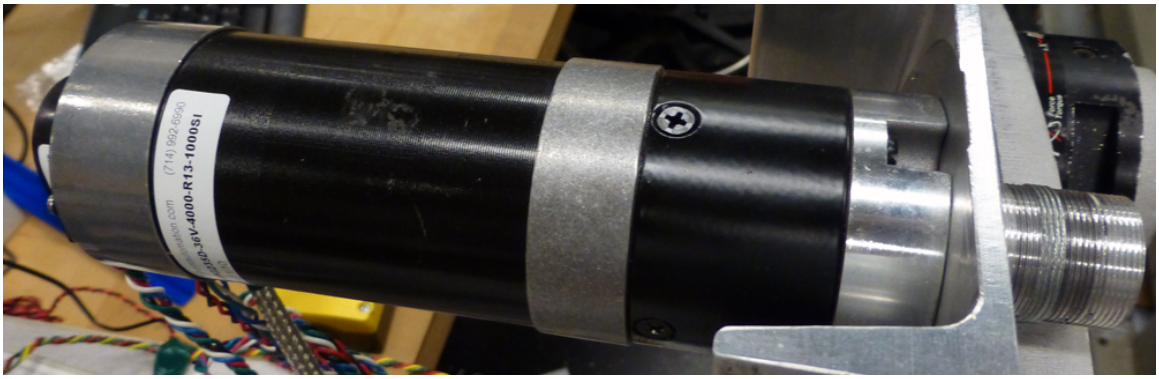

Figure 55: Motor

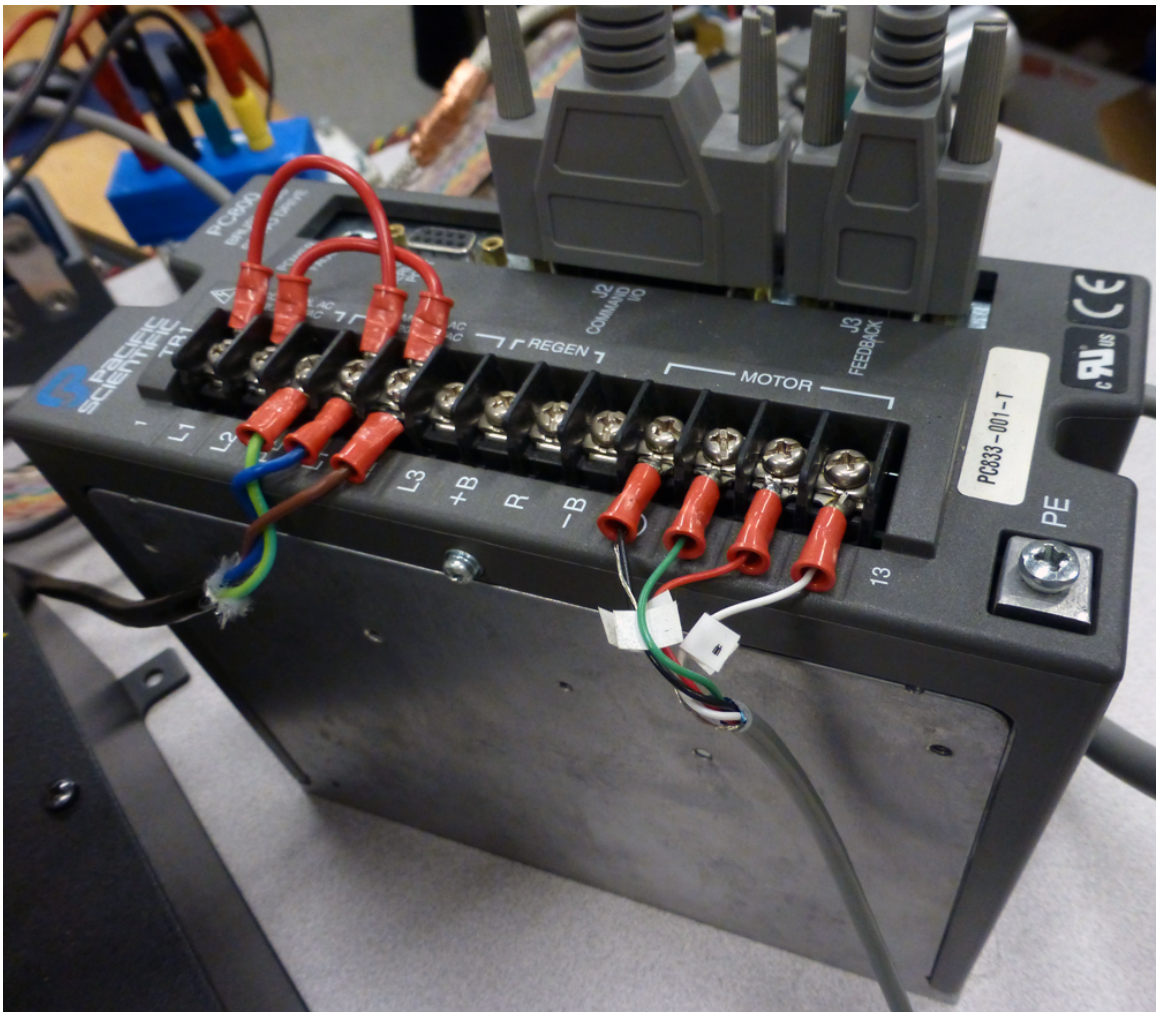

Figure 56: Motor driver

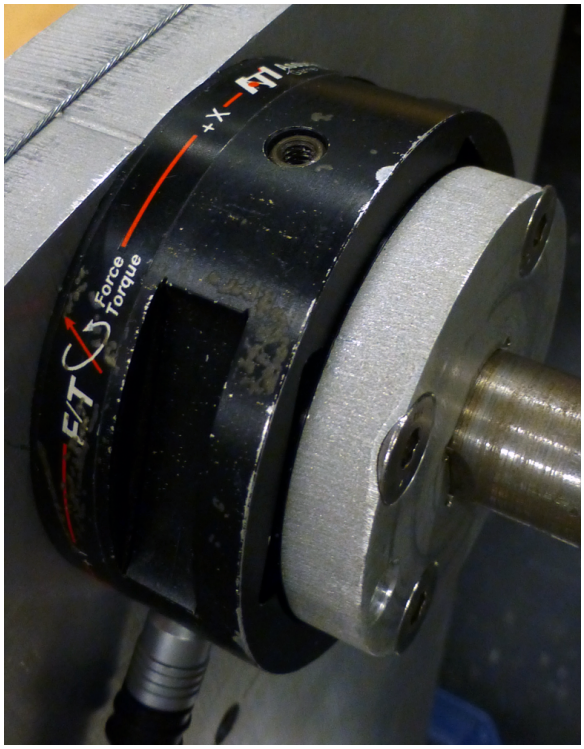

Figure 57: Force sensor

Figure 58: Force sensor reciever

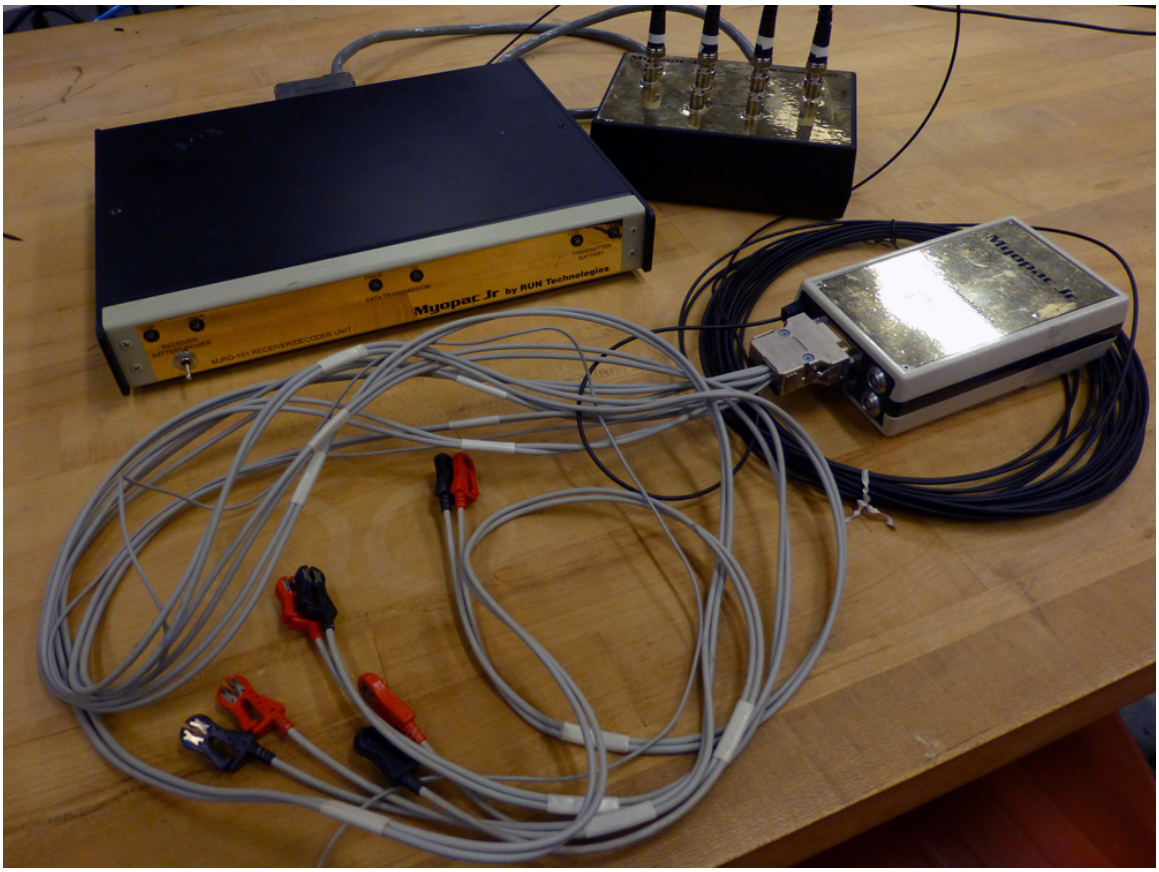

Figure 59: Wired EMG measurement system

Figure 60: Wireless EMG measurement system receiver

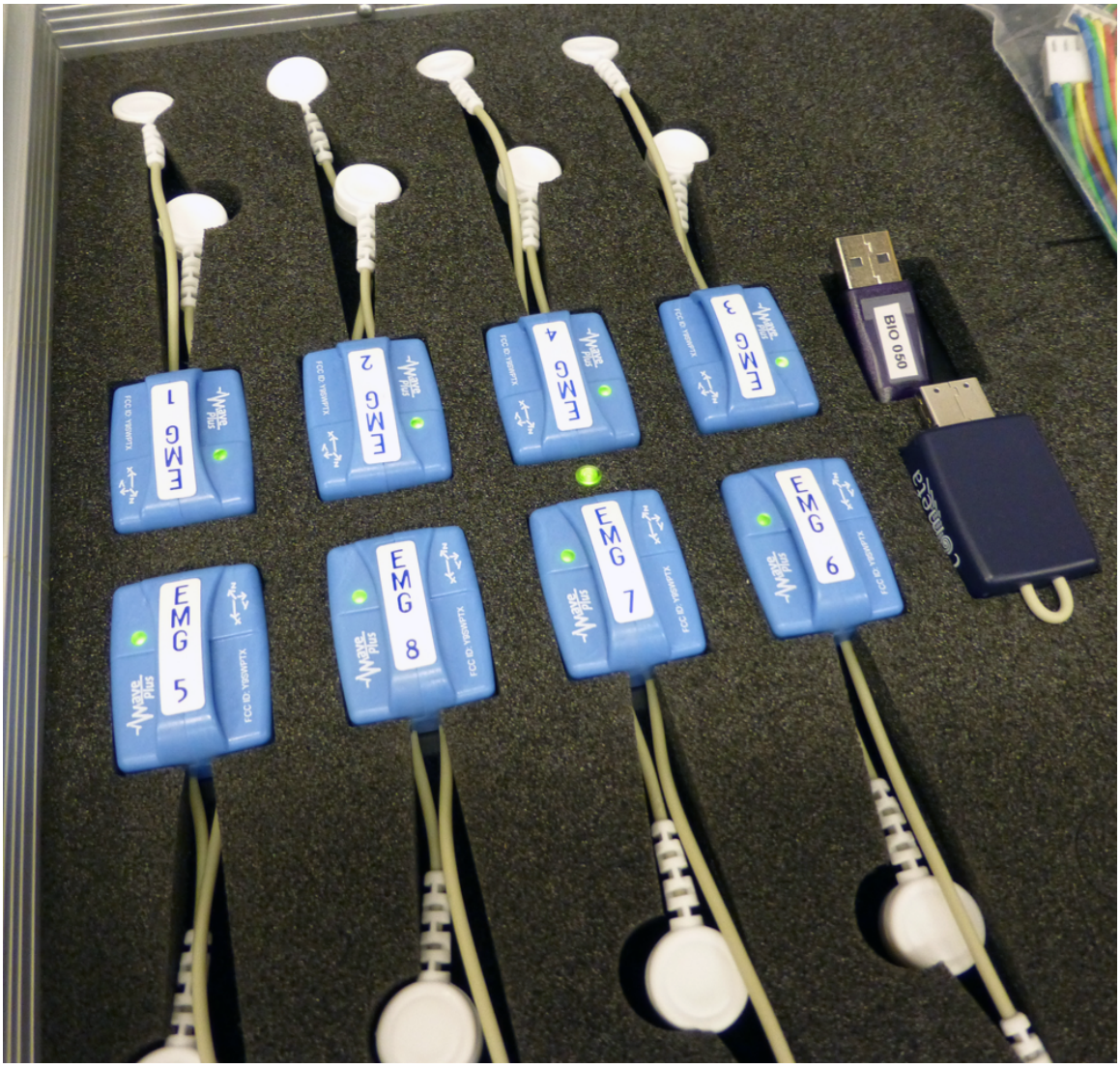

Figure 61: Wireless EMG measurement system electrodes

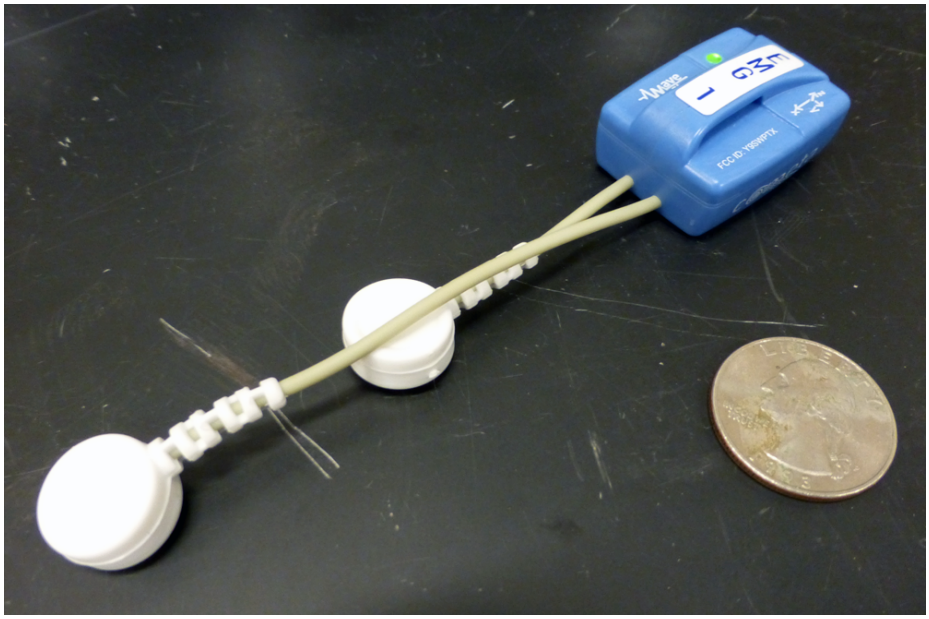

Figure 62: Single wireless EMG measurement system electrode

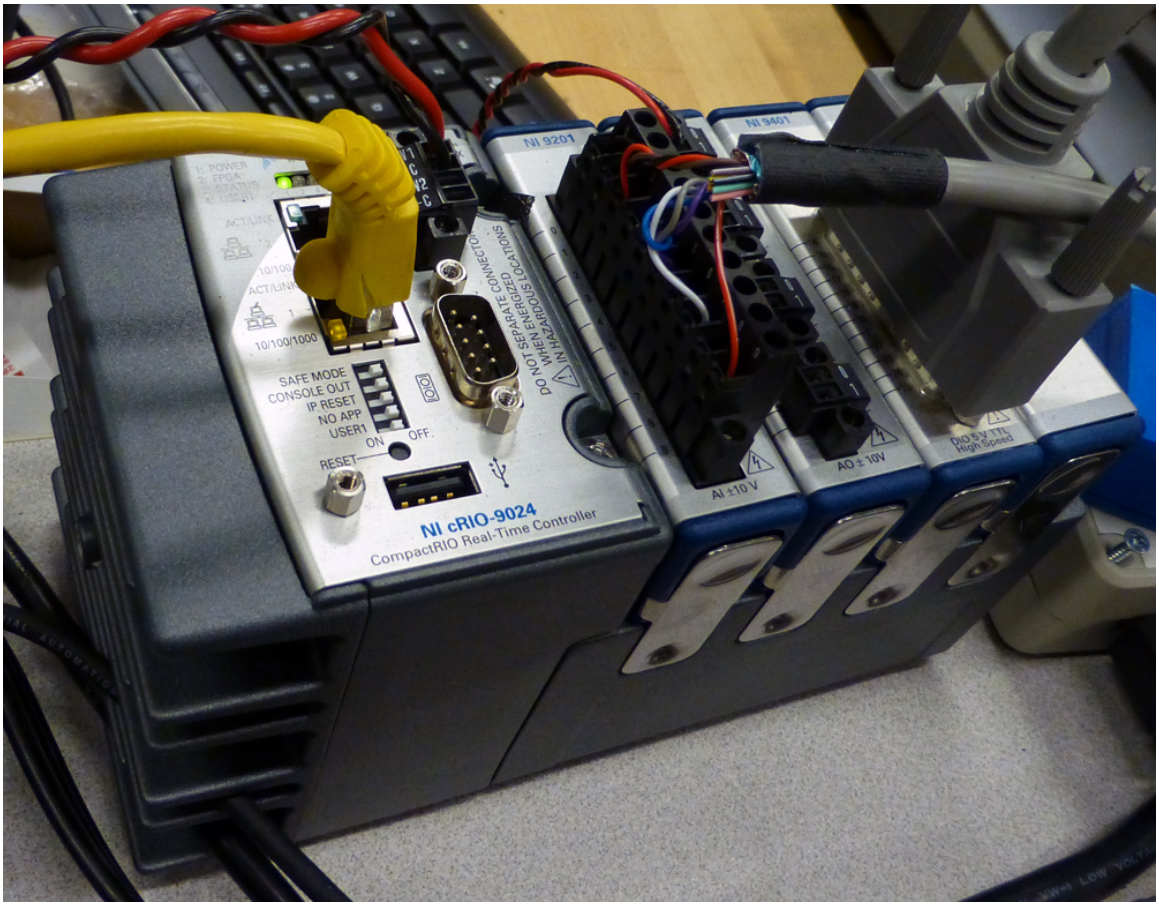

Figure 63: ComapctRIO real-time contoller

A.1.2 Software

Table 14: Software Functionality

Module	Function
FPGA	Encoder position decoding Force sensor reading, removing bias EMG sensor reading Voltage output to motor driver
cRIO Real-Time Processor	Force signal filtering EMG signal processing Percent activity calculation Cocontraction calculation Stiffness classification Impedance and position controllers Controller gain adjustment Data logging to file Telemetry broadcast to client computer(s) Command receive from host computer Idle mode when no host computer connected
Host Computer UI	Data display to user Calibration parameter calculation Control parameter send to cRIO User interface for configuring device Command send to cRIO

FPGA, cRIO Real-Time Processor, and Host Computer UI written in LabView 2012.

Experimental Simulations written in MATLAB 2009a - 2012b.

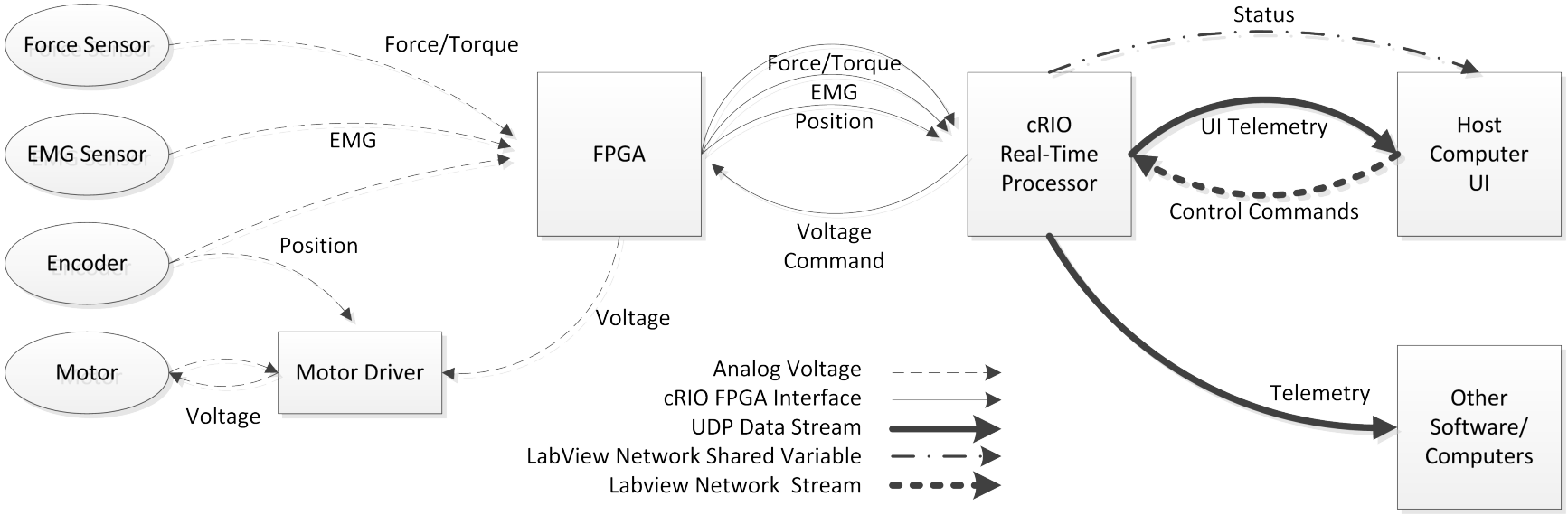

Figure 64: Software data flow diagram

A.2 Wearable Exoskeleton

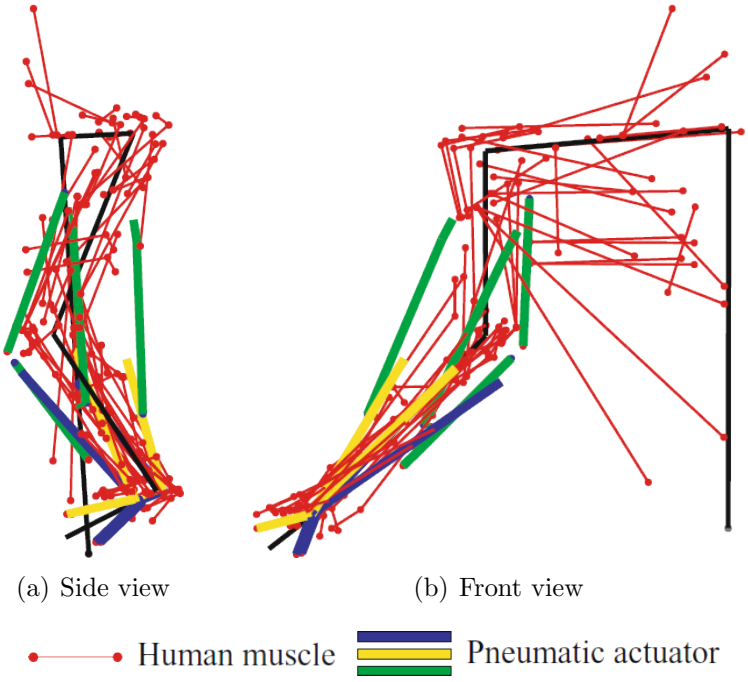

Figure 65: Exoskeleton schematic also showing arm muscles

Figure 66: Exoskeleton device

Figure 67: Outside of the exoskeleton arm

Figure 68: Inside of the exoskeleton arm

APPENDIX B

EXPERIMENTAL DATA AND PLOTS

B.1 Stiffness Correlation Experiment

B.1.1 Participants

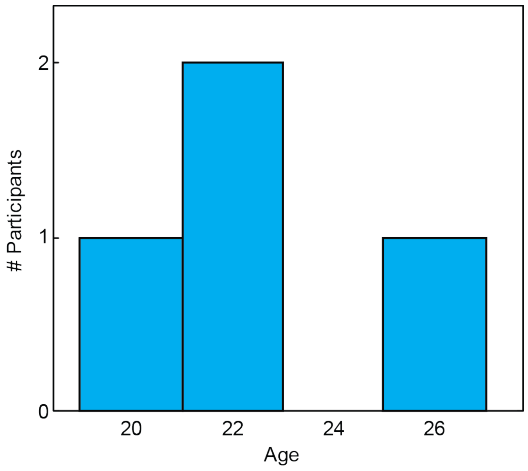

Figure 69: Age of subjects: $n = 4$, $\mu = 22.0$, $\sigma = 2.16$

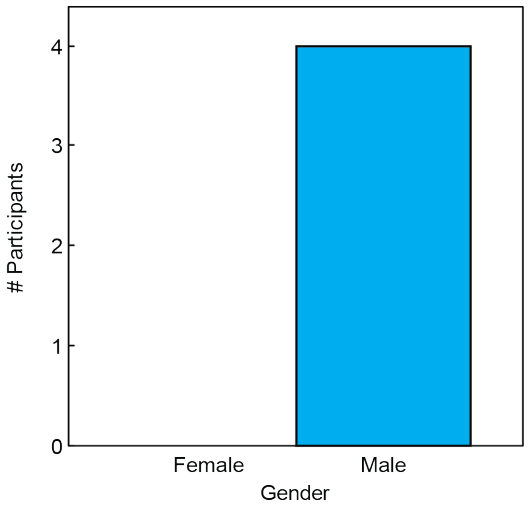

Figure 70: Gender of subjects

Measurement of Human Muscle Stiffness and it Applications to Effective Human-Machine Interface Design

Georgia Institute of Technology
School of Mechanical Engineering
Bio-Robotics and Human-Modeling Lab
Dr. Jun Ueda, Principal Investigator
James D Huggins, Co-Investigator
William Gallagher, Graduate Researcher
Timothy McPherson, Undergraduate Researcher
Dr. Minoru Shinohara, Consultant

Introduction
You are being asked to be a volunteer in a research study conducted by the Bio-Robotics and Human Modeling Lab, directed by Dr. Jun Ueda, a professor in the School of Mechanical Engineering. Participation in this study is entirely your choice.

Purpose
The goal of this study is to examine the relationship between the stiffness of a robot operators arm and the controllability of the system. In addition, it will evaluate the relationship between arm stiffness and muscle activation. You will be asked to perform tasks using a small force-feedback controller. While performing this task, you will be asked to wear an EMG measurement device that will record muscle activation patterns. The findings will be used to design a robot control system that can adjust based on the stiffness of an operators arm. Your results may be combined with those of other volunteers and reported in academic journals. This study plans to enroll 20 healthy adults to participate. You are being asked to be a volunteer in this study.

Procedures
Your participation is only one time and will last approximately 1.5 to 2.0 hours in total, including preparation. During the experiment, you will use a force-feedback haptic control device, known as a Phantom device, in two different tasks. During both tests, you be asked to wear an EMG measurement device on your arm, which will measure muscle activation through the use of small electrodes. This data will be recorded along with the movement of the Phantom device.

Task 1: Controlling an unstable system
You will be asked to control a robotic device using a force feedback enabled haptic controller, known as a Phantom device. The system will be designed with an inherent instability that will induce oscillations that you will have to control. You will be asked to perform simple point-to-point movements using this device. While controlling the device, you will be wearing a device which will measure the activation of muscles in your arm using EMG readings. You will perform approximately 10 trials of this task, which will take between 1 and 2 minutes each, with approximately 1 minute of rest between trials.

Task 2: Measuring arm stiffness
You will be asked to hold the Phantom device in a stationary position. The device will then, unpredictably, apply a force to your hand, during which you will be asked to try to continue holding the device stationary. While performing this task, you will be wearing a device which will measure the activation of muscles in your arm using EMG readings. You will perform approximately 10 trials of this task, which will take between 1 and 2 minutes each, with approximately 1 minute of rest between trials.

Risks/Discomforts
In some rare cases, there may be minor risks or discomfort that may occur as a result of your participation in this study. The contacts for the EMG measurement device may cause minor itchiness or irritation of the skin. This should pass soon after removing the device. Also, the force feedback haptic control device is capable of generating a small force to oppose the motion of the operator. However, the magnitude of this force is small, and is easily overpowered by an adult operator. Therefore, there is little risk of injury due to the force feedback.

Benefits
There are no personal benefits to be derived from participating in this research project. Although there are no direct benefits to you, the information that is obtained will help to learn about the best methods for designing a robotic control system that will be more natural for a human operator.

Compensation to You
You will be paid $10/hour for your time and effort in this study. If you choose to withdraw before the conclusion of this study, you will receive $10 for each hour of participation and the amount will prorated as necessary. For example, you will receive $5 for 30 min of participation.

Confidentiality
The following procedures will be followed to keep your personal information confidential: The data that is collected about you will be kept private to the extent allowed by law. To protect your privacy, your records will be kept under a code number. Your records will be kept in locked files. Only study staff will be allowed to look at them. When results of this study are presented or published, your name and any other fact that might point to you will not appear. To make sure that this research is being carried out in the proper way, the Georgia Institute of Technology Institutional Review Board may review study records. The Office of Human Research Protections may also look at study records. Your privacy will be protected to the extent allowed by law.

Costs to You
There is no cost to you for participation in this study. Expenses for the use of local public transportation (bus or train) to come to the study will be provided. Parking cost will be provided if you come to the study by car. These costs typically are at most $5.

In Case of Injury/Harm
If you are injured as a result of being in this study, please contact Billy Gallagher at 404-385-2763 or bgallagher@gatech.edu, or you may contact Dr. Jun Ueda, Ph.D., at 404-385-3900 or jun.ueda@me.gatech.edu. Neither the Investigators (Principal Investigator or Co-Investigators) nor the Georgia Institute of Technology has made provision for payment of costs associated with any injury resulting from participation in this study.

Subject Rights
Your participation in this study is voluntary. You do not have to be in this study if you do not want to be. You have the right to change your mind and leave the study at any time without giving any reason, and without penalty. Any new information that may make you change your mind about being in this study will be given to you. You will be given a copy of this consent form to keep. You do not waive any of your legal rights by signing this consent form.

Questions about the Study or Your Rights as a Research Subject
If you have any questions about the study, you may contact Billy Gallagher at 404-385-2763 or bgallagher@gatech.edu, or you may contact Dr. Jun Ueda, Ph.D., at 404-385-3900 or jun.ueda@me.gatech.edu. If you have any questions about your rights as a research subject, you may contact Ms. Kelly Winn, Office of Research Compliance at Georgia Institute of Technology, at 404-385-2175.

If you sign below, it means that you have read (or have had read to you) the information given in this consent form, and you would like to be a volunteer in this study.

_____
Subject Name (Print)

_____
Subject Signature **Date**

_____
Signature of Person Obtaining Consent **Date**

Consent Form approved by Georgia Tech IRB from October 29, 2010 to October 28, 2011

Consent Form approved by Georgia Tech IRB from October 29, 2010 to October 28, 2011

Consent Form approved by Georgia Tech IRB from October 29, 2010 to October 28, 2011

Figure 71: Approved adult consent form

B.1.2 Variables

Table 15: Controlled and Measured Variables

Independent	Levels	Dependent	Intermediate
Force (20)	5 N ⋮ 100 N	EMG (4 Muscles)	Stiffness Cocontraction (2 Pair)
Position (3)	−20° 0° 20°		
Total	60 Cases	4 Measured Values	3 Calculated Values

Each participant ran each case 1 time, with each trial giving 10 data points, yielding 2,400 data points. Omitting data due to equipment malfunction reduced this to 1,200 data points.

B.1.3 Data

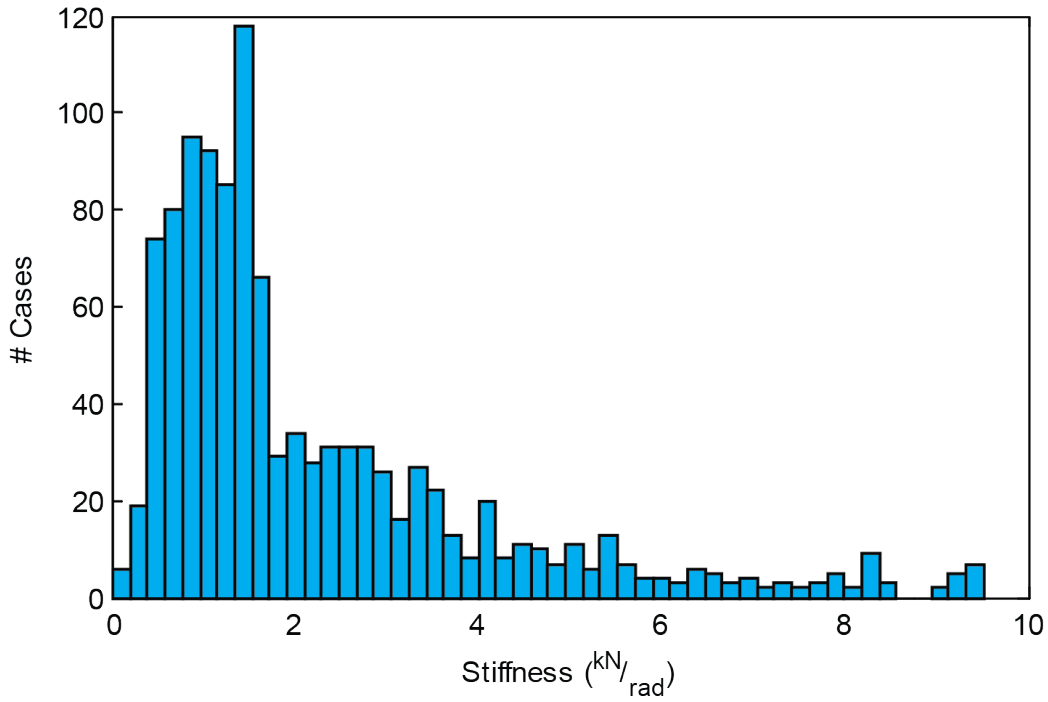

Figure 72: Histogram of stiffness data, $\mu = 2.23 \times 10^3$ kN/rad, $\sigma = 1.90 \times 10^3$ kN/rad

B.1.4 Statistics

Analysis method: Multiple Regression/Correlation (MRC)

Table 16: Regression Results (Force & Position Included as Predictors in All Fits)

Predictors	R^2	df	F	p
4 EMGs	0.201	6	24.884	< 0.001
2 Cocontractions	0.173	4	31.129	< 0.001
4 EMGs - Log transform	0.377	6	59.840	< 0.001
4 Cocontractions - Log transform	0.338	4	75.810	< 0.001

Table 17: Predictor Correlations for EMGs with Log Transform

Predictor	r_n^2	p
Force	0.287	< 0.001
Position	0.002	0.083
EMG - BB	0.116	0.017
EMG - TB	0.160	< 0.001
EMG - ECU	0.080	0.315
EMG - FCU	0.129	< 0.001

Table 18: Predictor Correlations for EMGs with Log Transform

Predictor	r_n^2	p
Force	0.287	< 0.001
Position	0.002	0.226
CC - E	0.117	< 0.001
CC - W	0.111	< 0.001

B.2 Rigid Surface Stability Experiment

B.2.1 Participants

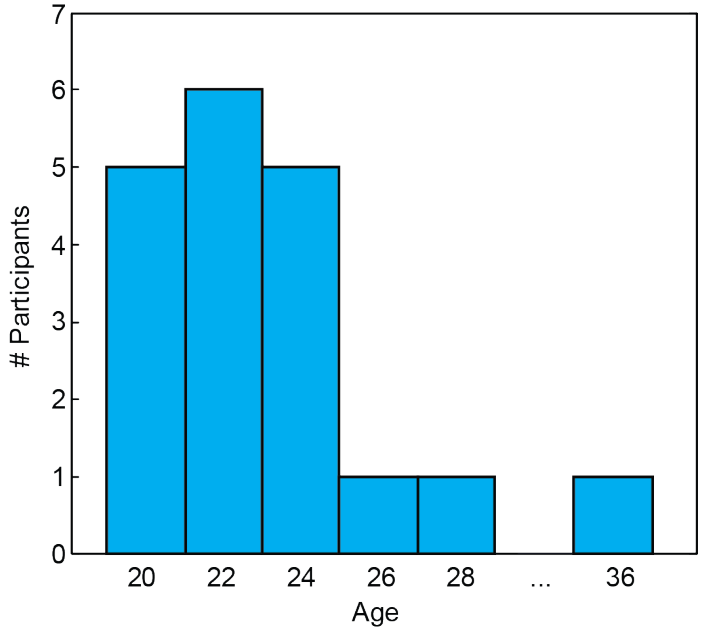

Figure 73: Age of subjects: $n = 20$, $\mu = 23.7$, $\sigma = 4.01$

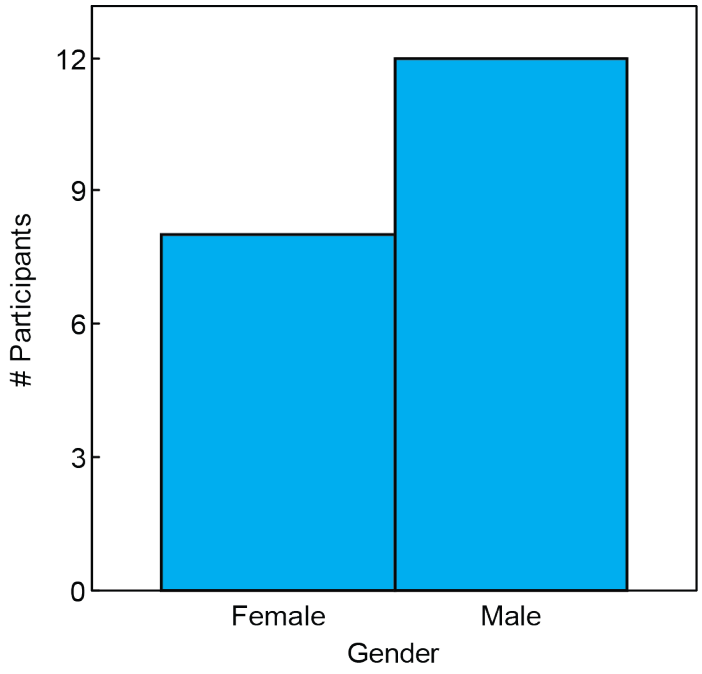

Figure 74: Gender of subjects

Consent form same as stiffness correlation experiment in Appendix B.1.

B.2.2 Variables

Table 19: Controlled and Measured Variables

Independent	Levels	Dependent
Classifier (2)	Fixed Low Damping Threshold	RMSE
Total	2 Cases	1 Measured Value

Each participant ran each case 2 times, yielding 80 data points.

B.2.3 Data

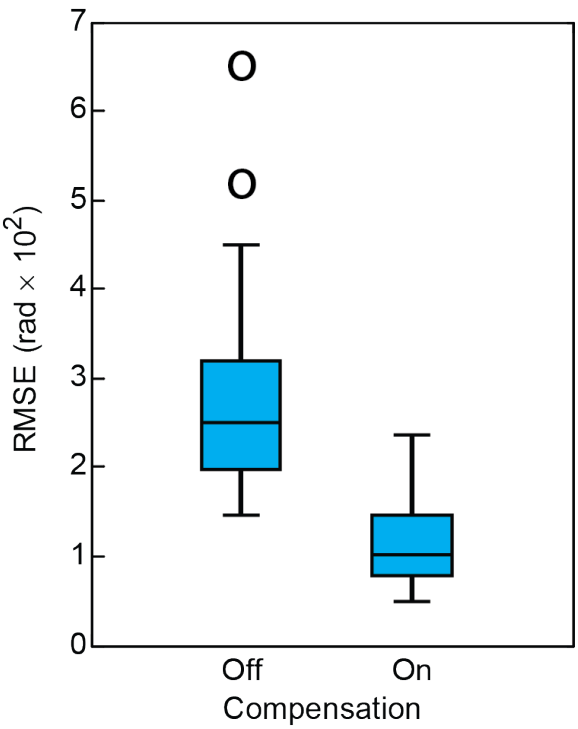

Figure 75: Box plot of RMSE data comparing the two cases

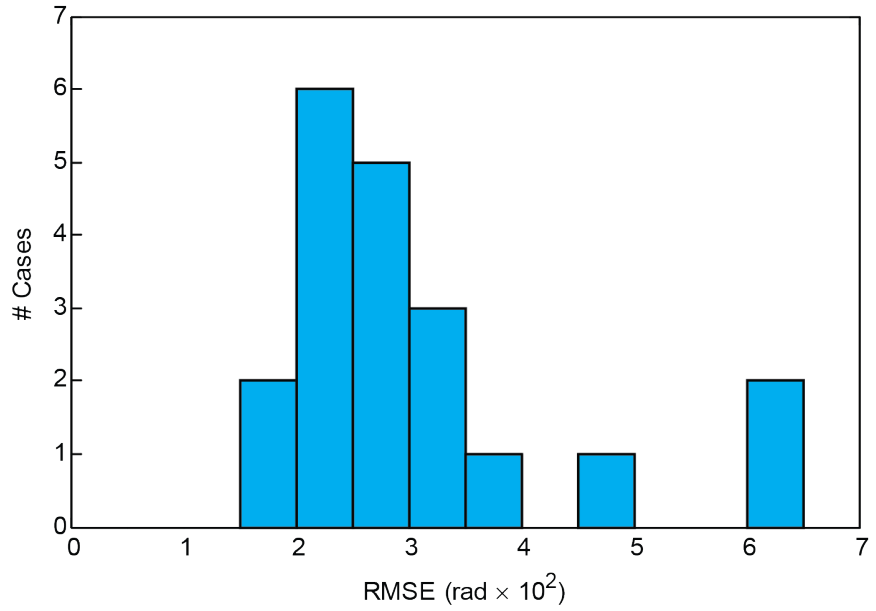

Figure 76: Histogram of RMSE data with compensation off, $\mu = 3.011 \times 10^{-2}$ rad, $\sigma = 1.237 \times 10^{-2}$ rad

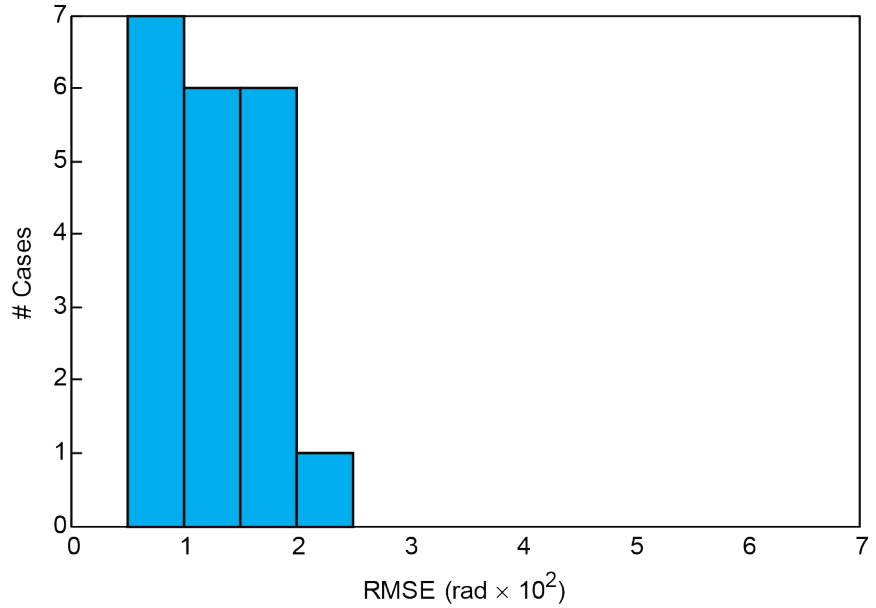

Figure 77: Histogram of RMSE data with compensation on, $\mu = 1.251 \times 10^{-2}$ rad, $\sigma = 0.448 \times 10^{-2}$ rad

B.2.4 Statistics

Analysis method: 1-Way ANOVA

Table 20: ANOVA Results

df	*F*	*p*
1	35.746	< 0.001

Table 21: Means and Confidences of RMSE for Compensation Off and On Cases

Classifier	Mean	Std Dev	95% Interval
Fixed Low Damping	3.011×10^{-2} rad	1.237×10^{-2} rad	2.432×10^{-2} rad - 3.591×10^{-2} rad
Threshold	1.251×10^{-2} rad	0.448×10^{-2} rad	1.042×10^{-2} rad - 1.461×10^{-2} rad

B.3 Simulated Lifting Task Experiment

B.3.1 Participants

Same as rigid surface stability experiment in Appendix B.2. Consent form same as stiffness correlation experiment in Appendix B.1.

B.3.2 Variables

Table 22: Controlled and Measured Variables

Independent	Levels	Dependent
Classifier (2)	Fixed Low Damping Threshold	Placement Speed Placement Accuracy
Total	2 Cases	2 Measured Values

Each participant ran each case 5 times with both speed and accuracy measured from the same set of trials, yielding 100 data points for each.

B.3.3 Data

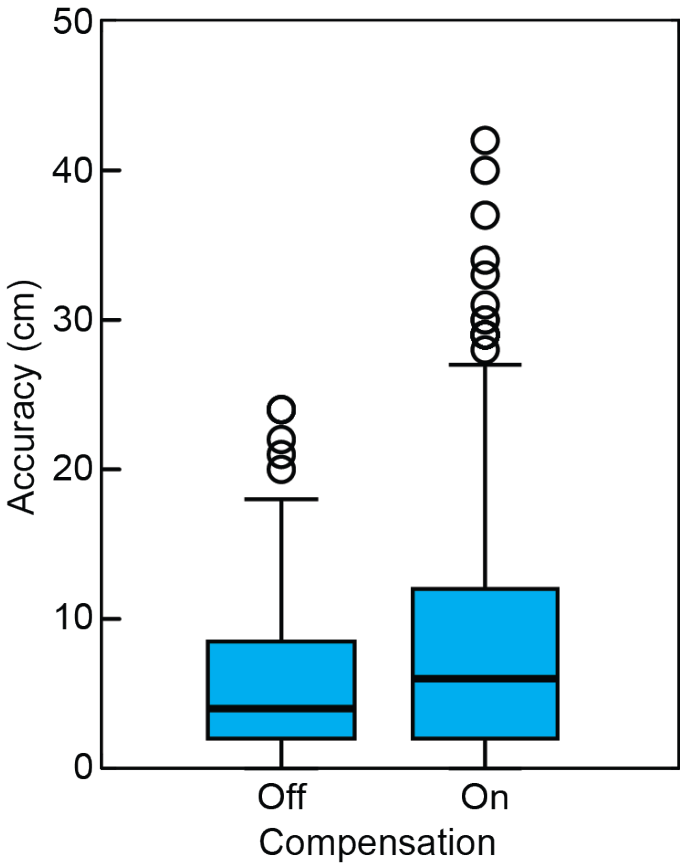

Figure 78: Box plot of accuracy data comparing both cases

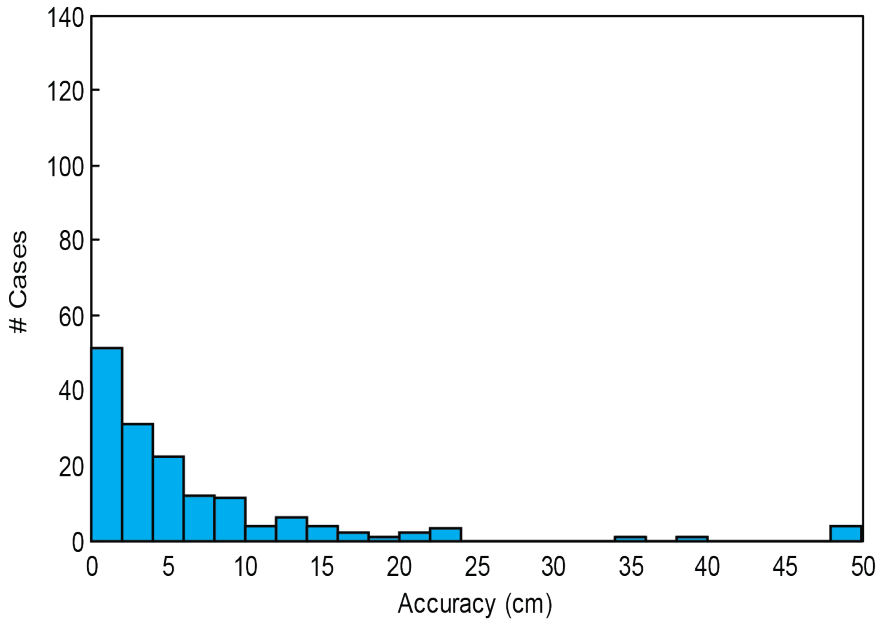

Figure 79: Histogram of accuracy data for compensation off, $\mu = 10.46\,\text{cm}$, $\sigma = 32.79\,\text{cm}$

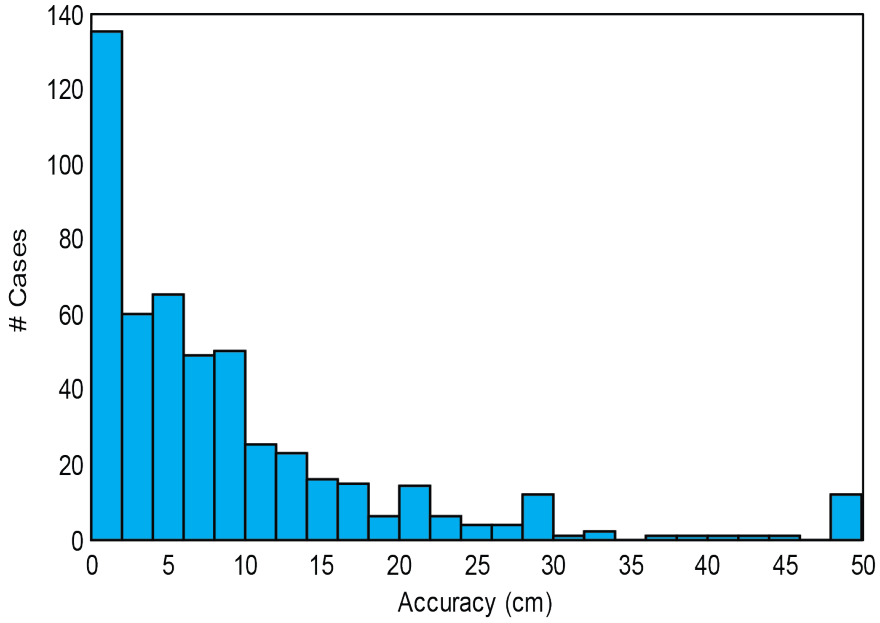

Figure 80: Histogram of accuracy data for compensation on, $\mu = 14.18\,\text{cm}$, $\sigma = 39.99\,\text{cm}$

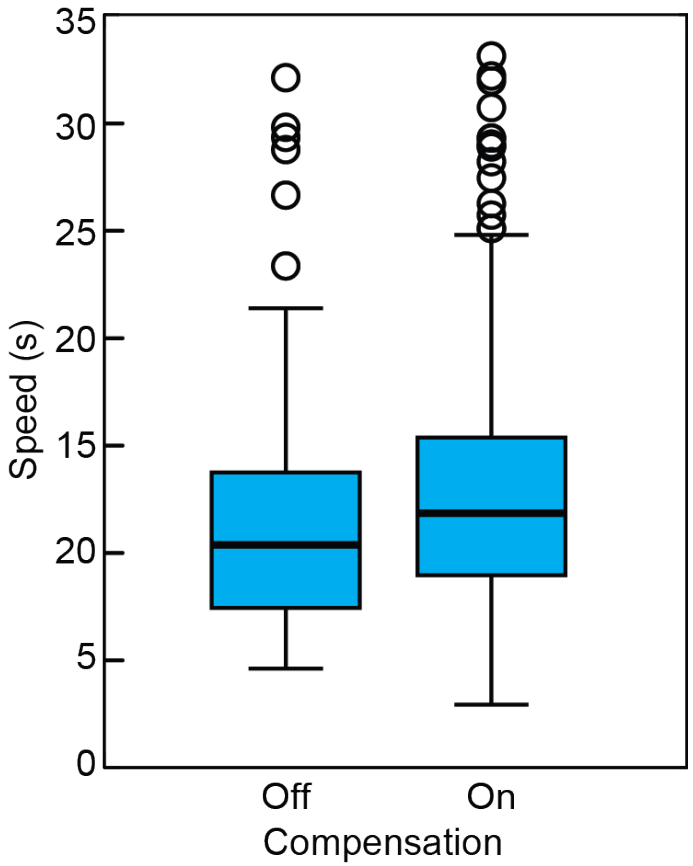

Figure 81: Box plot of speed data comparing both cases

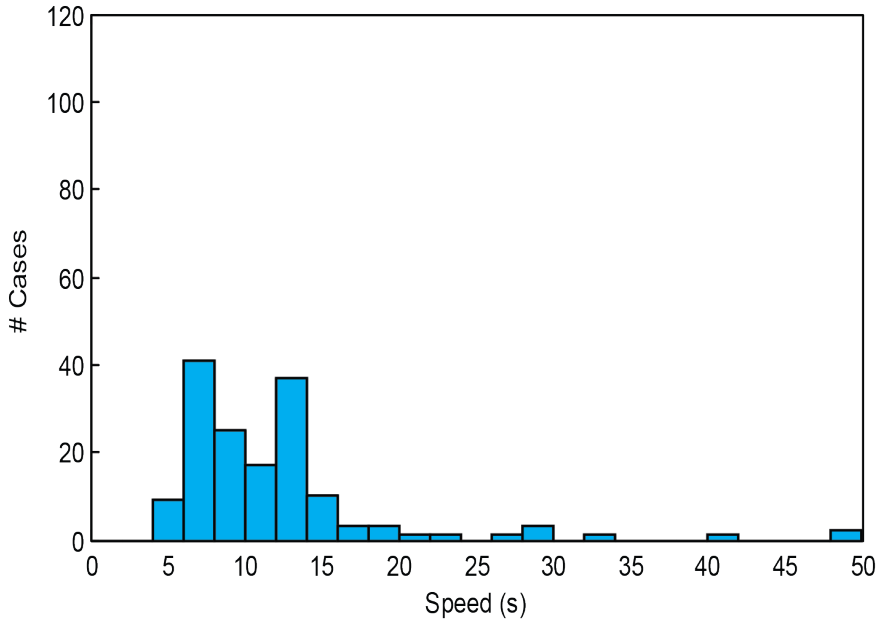

Figure 82: Histogram of speed data for compensation off, $\mu = 11.86\,\mathrm{s}$, $\sigma = 6.994\,\mathrm{s}$

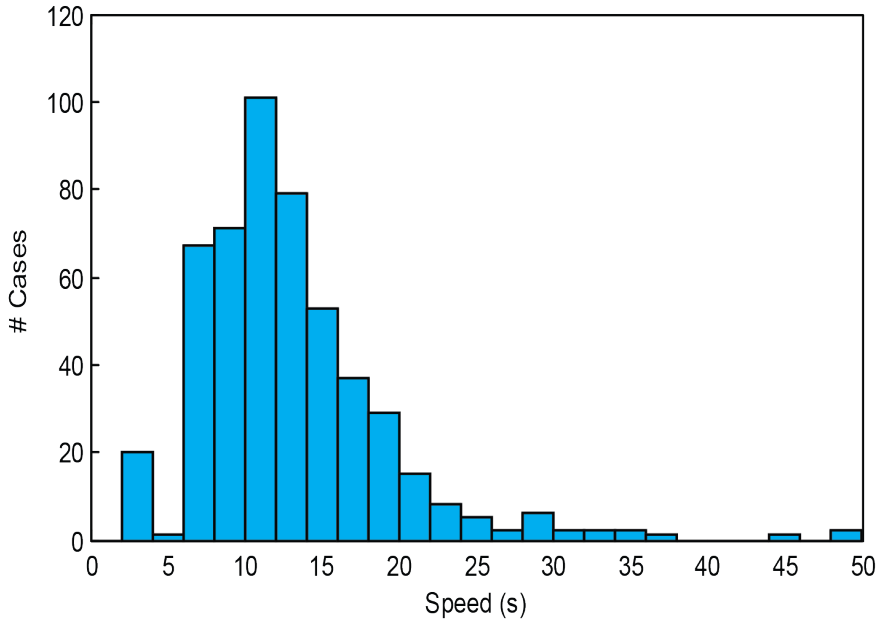

Figure 83: Histogram of speed data for compensation on, $\mu = 12.93\,\mathrm{s}$, $\sigma = 6.301\,\mathrm{s}$

B.3.4 Statistics

Analysis method: 1-Way ANOVA

Table 23: ANOVA Results for Accuracy Data

df	*F*	*p*
1	1.113	0.292

Table 24: Means and Confidences of Accuracy for Compensation Off and On Cases

Classifier	Mean	Std Dev	95% Interval
Fixed Low Damping	10.46 cm	32.79 cm	5.254 cm - 15.66 cm
Threshold	14.18 cm	39.99 cm	10.68 cm - 17.68 cm

Table 25: ANOVA Results for Speed Data

df	*F*	*p*
1	3.269	0.071

Table 26: Means and Confidences of Speed for Compensation Off and On Cases

Classifier	Mean	Std Dev	95% Interval
Fixed Low Damping	11.86 s	6.994 s	10.75 s - 12.97 s
Threshold	12.93 s	6.301 s	12.39 s - 13.48 s

B.4 Performance Comparison Experiment

B.4.1 Participants

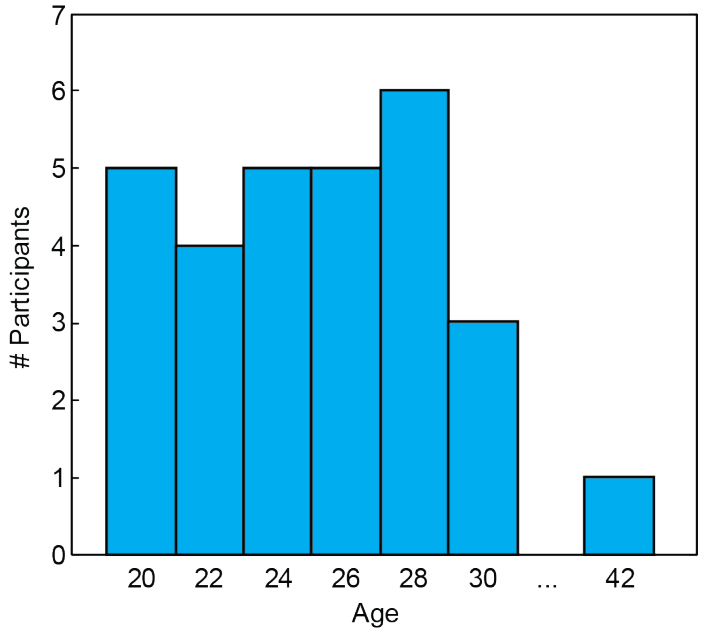

Figure 84: Age of subjects: $n = 24$, $\mu = 25.9$, $\sigma = 4.54$

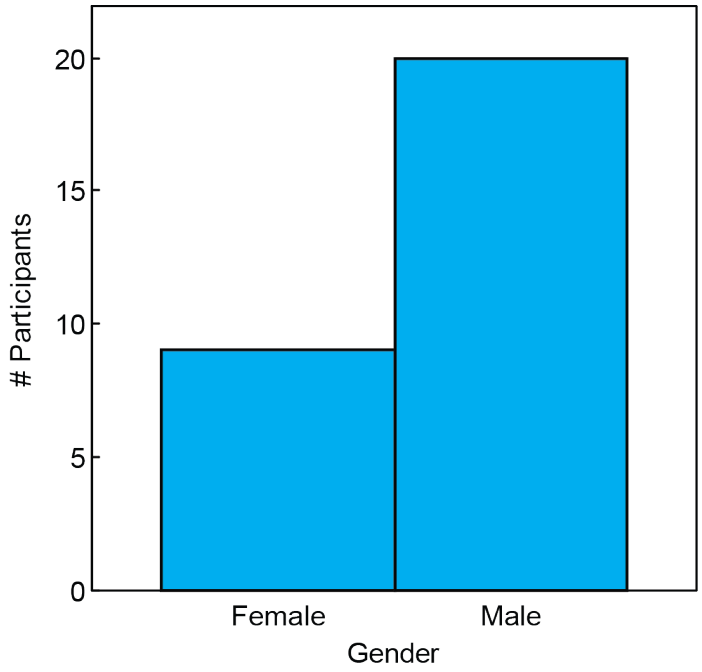

Figure 85: Gender of subjects

Measurement of Human Muscle Stiffness and it Applications to Effective Human-Machine Interface Design

Georgia Institute of Technology
School of Mechanical Engineering
Bio-Robotics and Human-Modeling Lab

William Gallagher, Graduate Researcher
Dr. Jun Ueda, Principal Investigator

Introduction
You are being asked to be a volunteer in a research study conducted by the Bio-Robotics and Human Modeling Lab, directed by Dr. Jun Ueda, a professor in the School of Mechanical Engineering. Participation in this study is entirely your choice.

Purpose
The goal of this study is to examine the relationship between the stiffness of a robot operators arm and the controllability of the system. In addition, it will evaluate the relationship between arm stiffness and muscle activation. You will be asked to perform tasks using a small force-feedback controller. While performing this task, you will be asked to wear an EMG measurement device that will record muscle activation patterns. The findings will be used to design a robot control system that can adjust based on the stiffness of an operators arm. Your results may be combined with those of other volunteers and reported in academic journals. This study plans to enroll up to 60 healthy adults to participate. You are being asked to be a volunteer in this study.

Procedures
Your participation is only one time and will last approximately 1.5 to 2.0 hours in total, including preparation. During the experiment, you will use a force-feedback haptic control device in several different tasks. During the tasks, you be asked to wear an EMG measurement device on your arm, which will measure muscle activation through the use of small electrodes. This data will be recorded along with the movement of the device.

You will be asked to control a robotic device using a force feedback enabled haptic controller. The system will be designed with an inherent instability that will induce oscillations that you will have to control. You will be asked to perform simple movements using this device. You may or may not also be asked to coordinate your movements of the device with a computer display that will provide instructions. While controlling the device, you will be wearing a system which will measure the activation of muscles in your arm using EMG readings. You will be asked to perform multiple trials of this task, which will take between 1 and 2 minutes each, with approximately 1 minute of rest between trials.

Risks/Discomforts
In some rare cases, there may be minor risks or discomfort that may occur as a result of your participation in this study. The contacts for the EMG measurement device may cause minor itchiness or irritation of the skin. This should pass soon after removing the device. Also, the force feedback haptic control device is capable of generating a small force to oppose the motion of the operator. However, the magnitude of this force is small, and is easily overpowered by an adult operator. Therefore, there is little risk of injury due to the force feedback.

Benefits
There are no personal benefits to be derived from participating in this research project. Although there are no direct benefits to you, the information that is obtained will help to learn about the best methods for designing a robotic control system that will be more natural for a human operator.

Compensation to You
You will be paid $10/hour for your time and effort in this study. If you choose to withdraw before the conclusion of this study, you will receive $10 for each hour of participation and the amount will prorated as necessary. For example, you will receive $5 for 30 min of participation.

Confidentiality
The following procedures will be followed to keep your personal information confidential: The data that is collected about you will be kept private to the extent allowed by law. To protect your privacy, your records will be kept under a code number. Your records will be kept in locked files. Only study staff will be allowed to look at them. When results of this study are presented or published, your name and any other fact that might point to you will not appear. To make sure that this research is being carried out in the proper way, the Georgia Institute of Technology Institutional Review Board may review study records. The Office of Human Research Protections may also look at study records. Your privacy will be protected to the extent allowed by law.

Costs to You
There is no cost to you for participation in this study. Expenses for the use of local public transportation (bus or train) to come to the study will be provided. Parking cost will be provided if you come to the study by car. These costs typically are at most $5.

In Case of Injury/Harm
If you are injured as a result of being in this study, please contact Billy Gallagher at 404-385-2763 or bgallagher@gatech.edu, or you may contact Dr. Jun Ueda, Ph.D., at 404-385-3900 or jun.ueda@me.gatech.edu. Neither the Investigators (Principal Investigator or Co-Investigators) nor the Georgia Institute of Technology has made provision for payment of costs associated with any injury resulting from participation in this study.

Subject Rights
Your participation in this study is voluntary. You do not have to be in this study if you do not want to be. You have the right to change your mind and leave the study at any time without giving any reason, and without penalty. Any new information that may make you change your mind about being in this study will be given to you. You will be given a copy of this consent form to keep. You do not waive any of your legal rights by signing this consent form.

Questions about the Study or Your Rights as a Research Subject
If you have any questions about the study, you may contact Billy Gallagher at 404-385-2763 or bgallagher@gatech.edu, or you may contact Dr. Jun Ueda, Ph.D., at 404-385-3900 or jun.ueda@me.gatech.edu. If you have any questions about your rights as a research subject, you may contact Ms. Kelly Winn, Office of Research Compliance at Georgia Institute of Technology, at 404-385-2175.

If you sign below, it means that you have read (or have had read to you) the information given in this consent form, and you would like to be a volunteer in this study.

Subject Name (Print)

Subject Signature **Date**

Signature of Person Obtaining Consent **Date**

APPROVED *Consent Form Approved by Georgia Tech IRB: December 20, 2012 - October 26, 2013*

APPROVED *Consent Form Approved by Georgia Tech IRB: December 20, 2012 - October 26, 2013*

APPROVED *Consent Form Approved by Georgia Tech IRB: December 20, 2012 - October 26, 2013*

Figure 86: Approved adult consent form

Subject: _____

Trial: _____

How much effort did you feel was required to be successful on this trial?
(1 = No effort, 10 = More effort than I am capable of)

1 2 3 4 5 6 7 8 9 10

To what degree did you feel that the device was either helping or fighting your efforts on this trial?
(1 = Helping, 10 = Fighting)

1 2 3 4 5 6 7 8 9 10

Please rate how you felt the stability of the device was on this trial.
(1 = Extremely stable, 10 = Extremely unstable)

1 2 3 4 5 6 7 8 9 10

Figure 87: Survey questions asked after each trial

B.4.2 Variables

Table 27: Controlled and Measured Variables

Independent	Levels	Dependent
Classifier (4)	Fixed Low Damping	Accuracy
	Fixed High Damping	Speed
	Threshold	Survey - Effort
	HMM	Survey - Helping
Controller (3)	PD	Survey - Stability
	LQG	
	SLQR	
Total	12 Cases	5 Measured Values

Each participant ran each case 24 times for the accuracy task and 24 times for the speed task, yielding a total of 6,912 data points each. Each participant filled out 2 surveys for each case, yielding 576 data points for each survey category.

B.4.3 Data

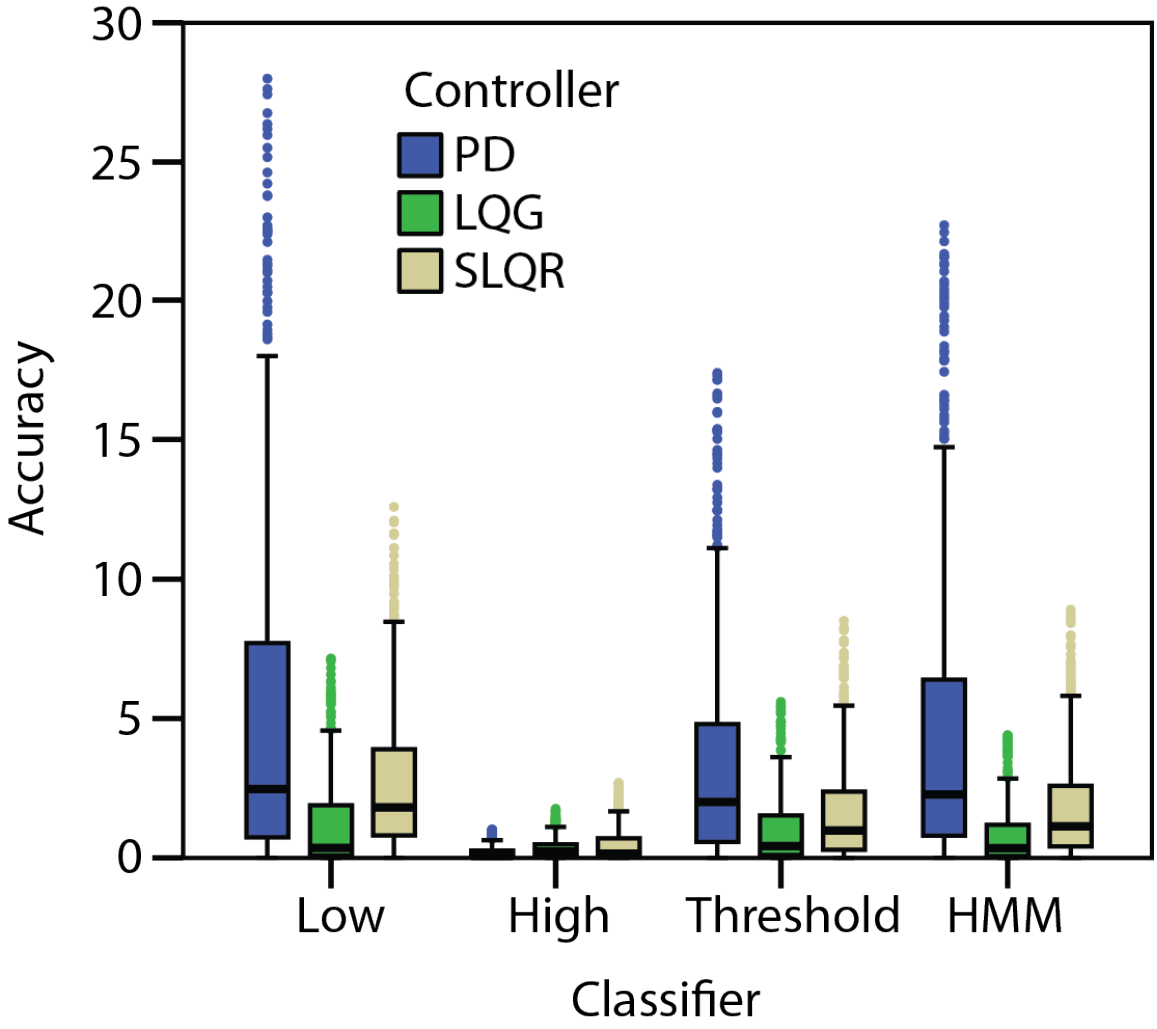

Figure 88: Box plot of accuracy data across all cases

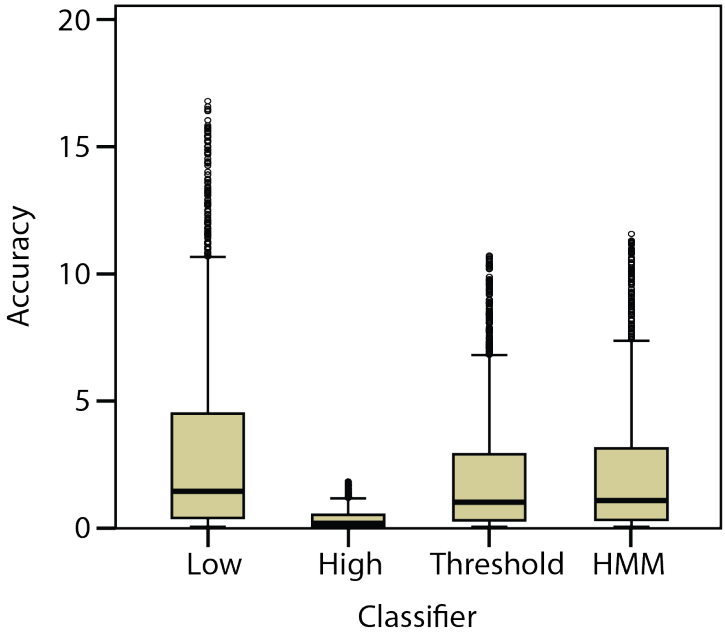

Figure 89: Box plot of accuracy data divided by classifier levels

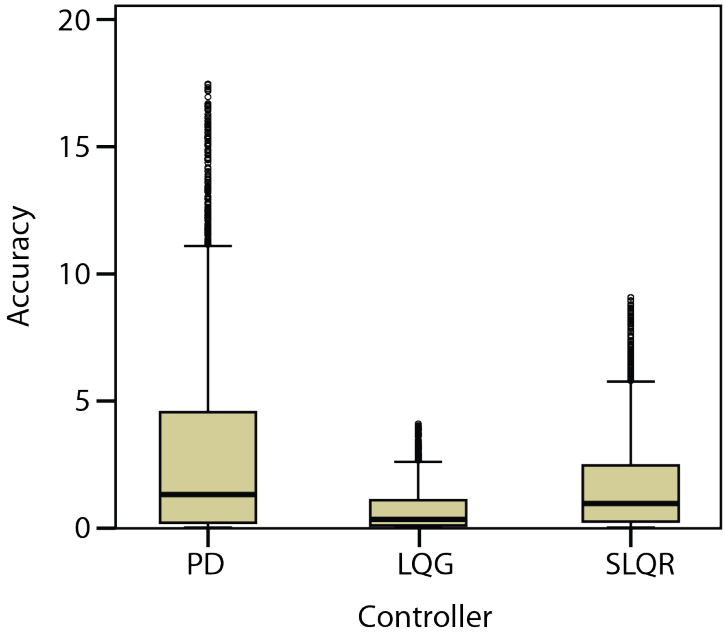

Figure 90: Box plot of accuracy data divided by controller levels

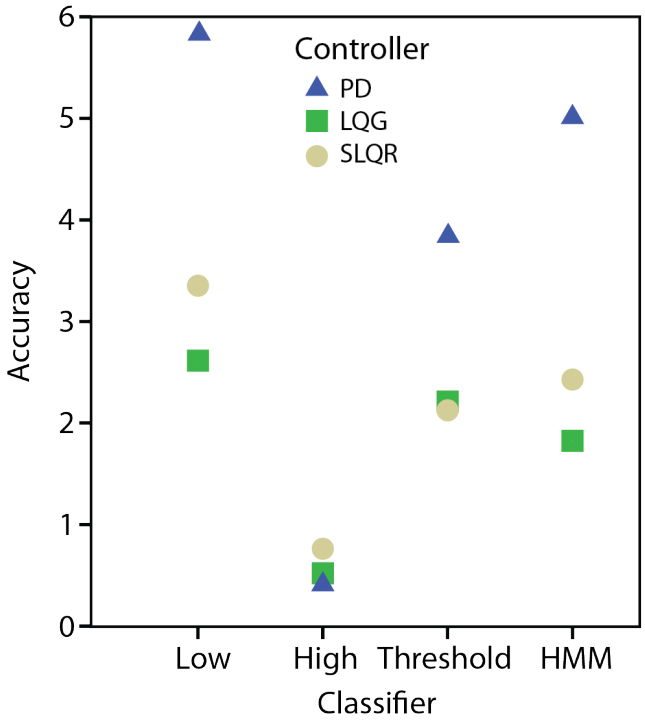

Figure 91: Means of accuracy data divided by classifier levels

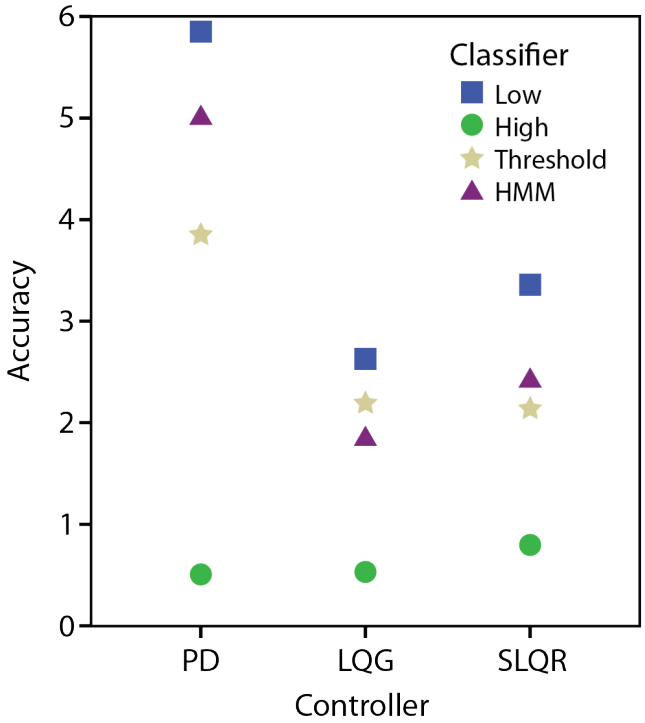

Figure 92: Means of accuracy data divided by controller levels

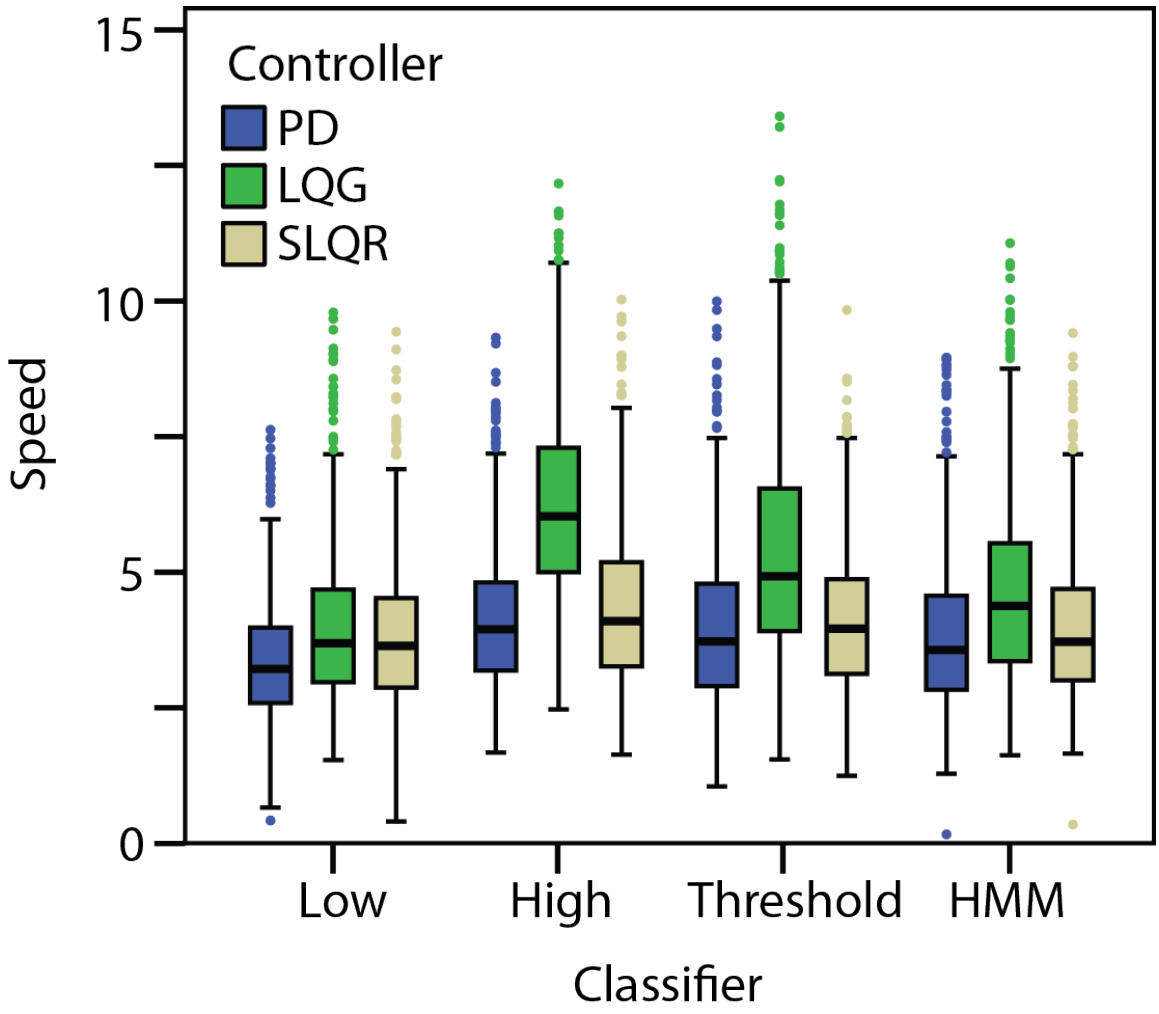

Figure 93: Box plot of speed data across all cases

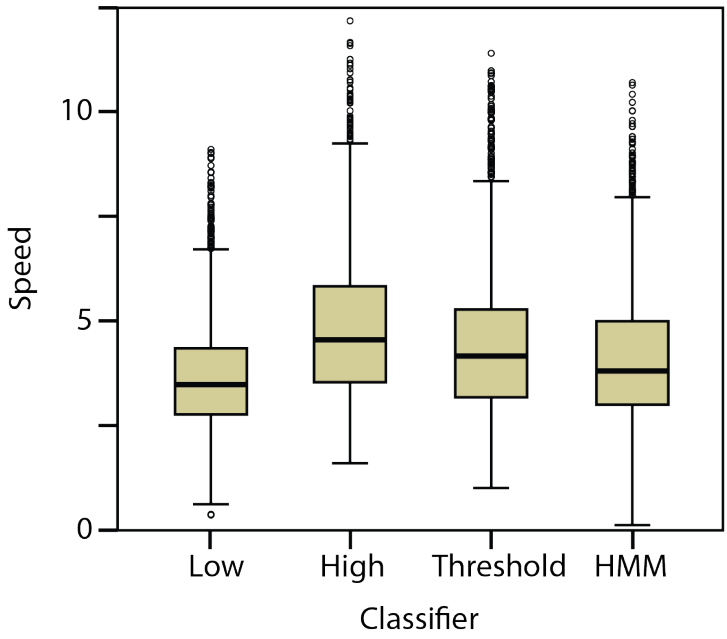

Figure 94: Box plot of speed data divided by classifier levels

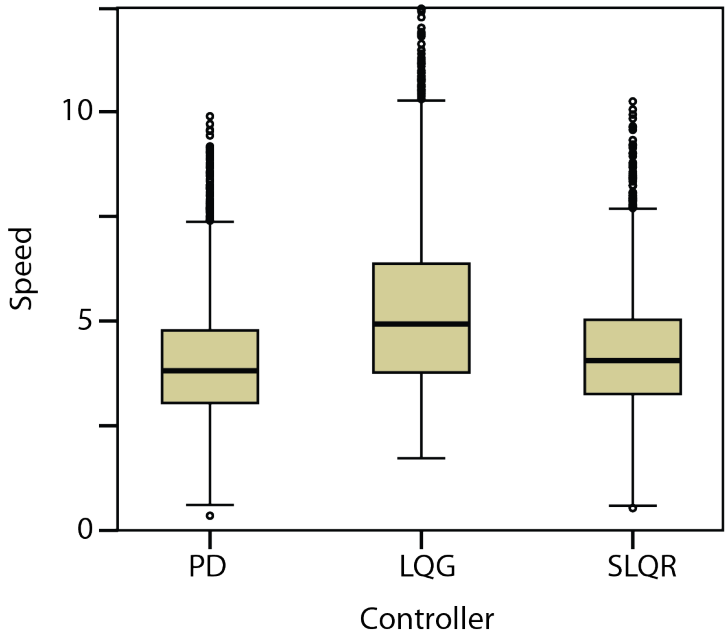

Figure 95: Box plot of speed data divided by controller levels

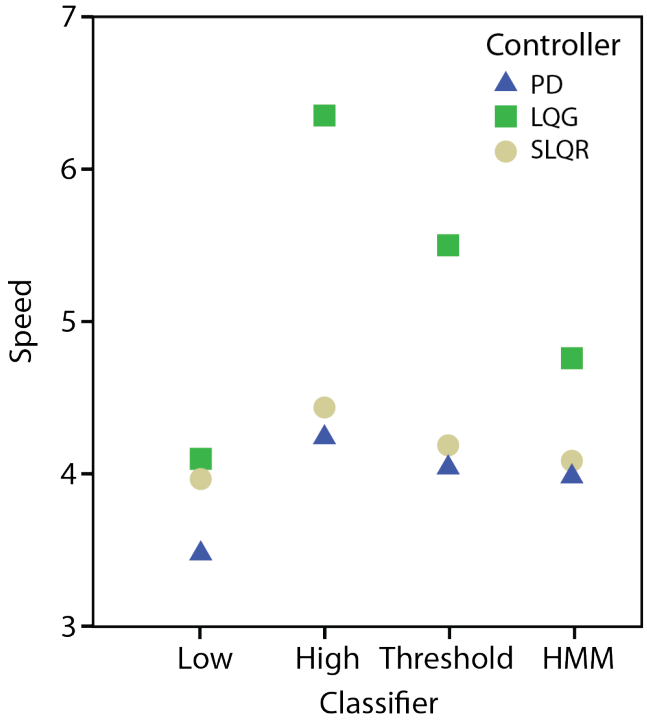

Figure 96: Means of speed data divided by classifier levels

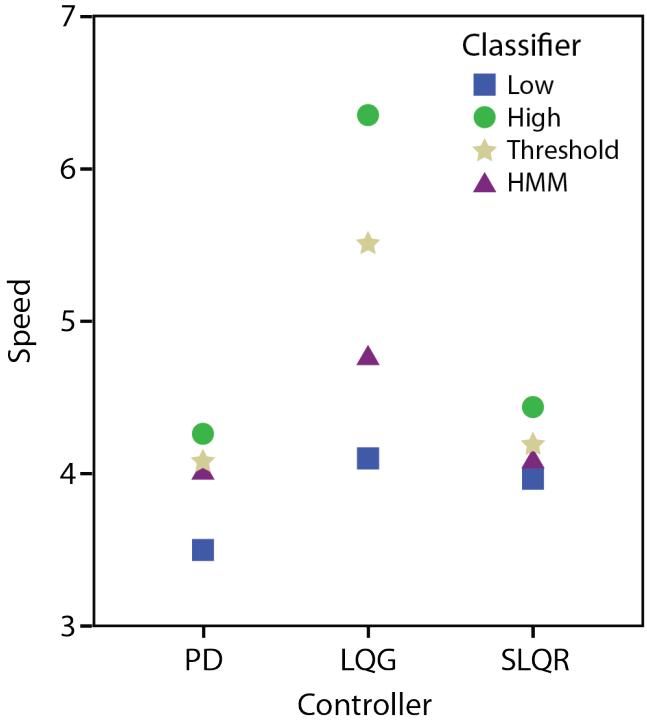

Figure 97: Means of speed data divided by controller levels

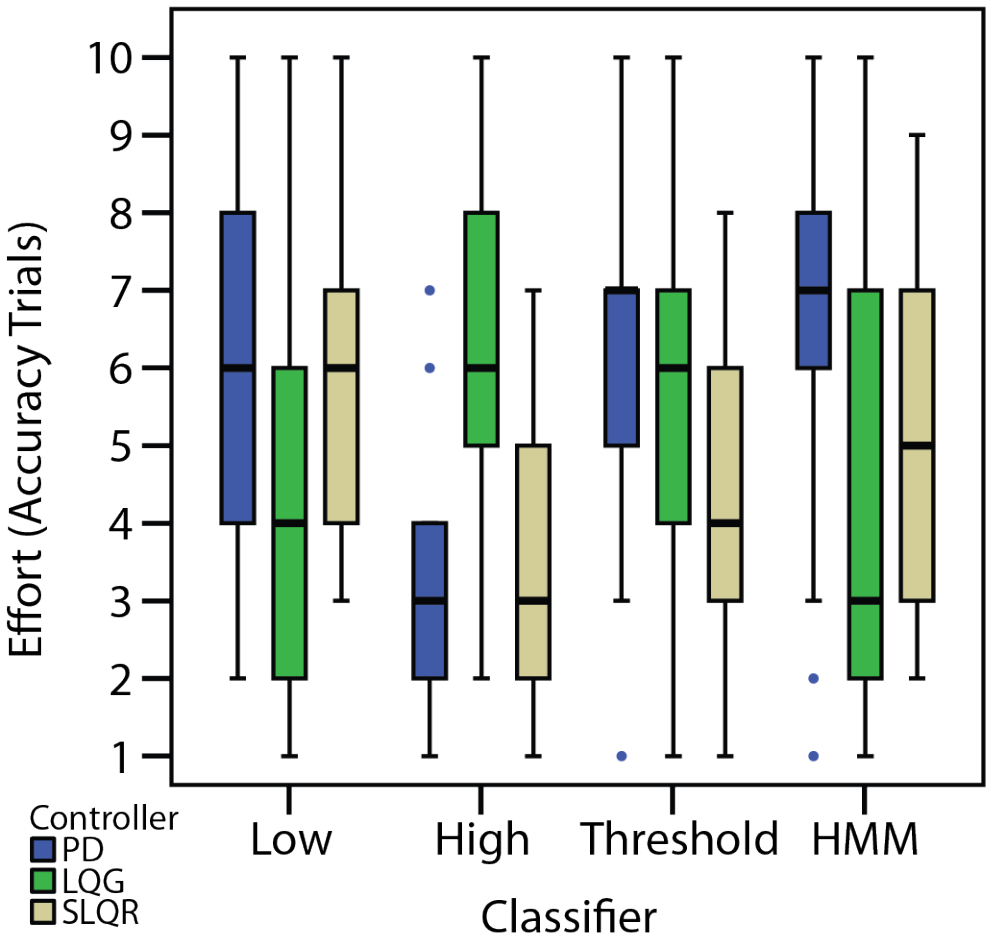

Figure 98: Box plot of effort rating for accuracy trials across all cases

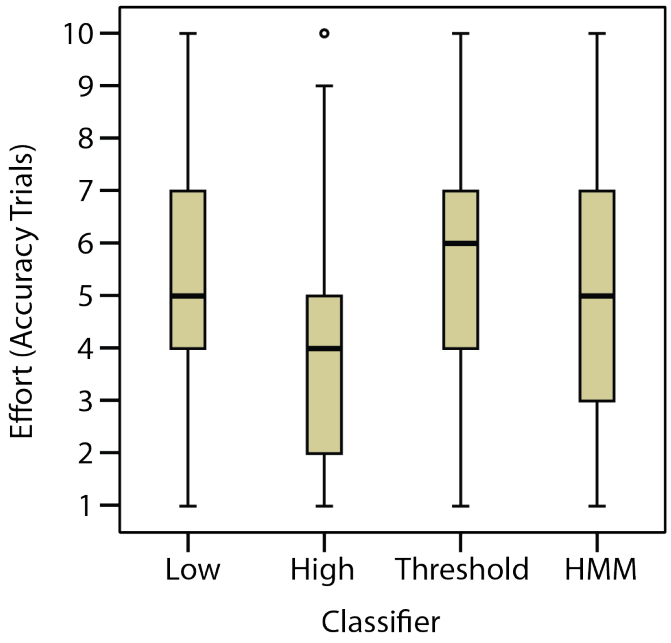

Figure 99: Box plot of effort rating for accuracy trials divided by classifier levels

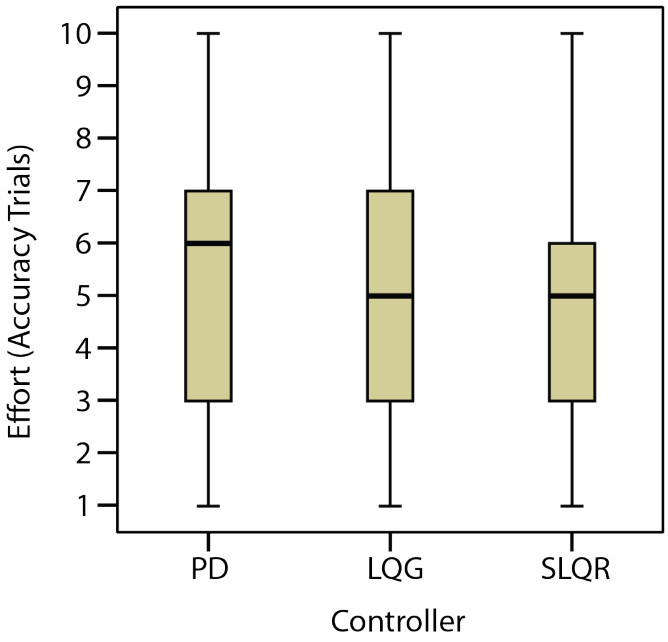

Figure 100: Box plot of effort rating for accuracy trials divided by controller levels

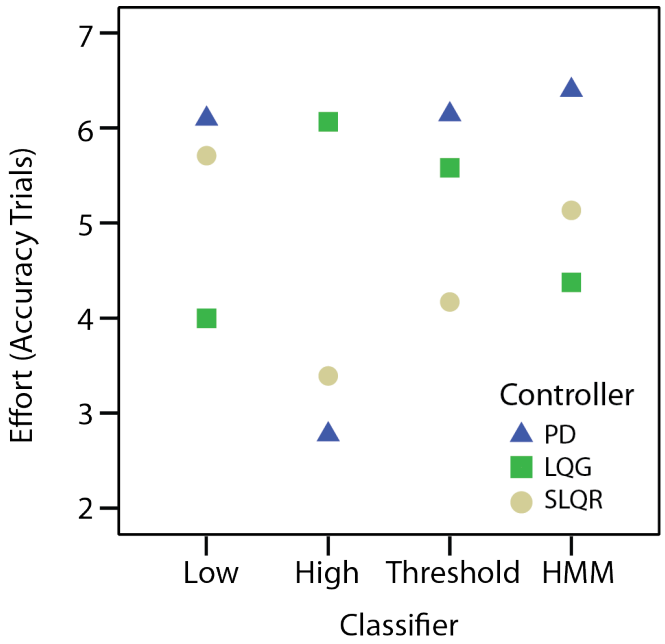

Figure 101: Means of effort rating for accuracy trials divided by classifier levels

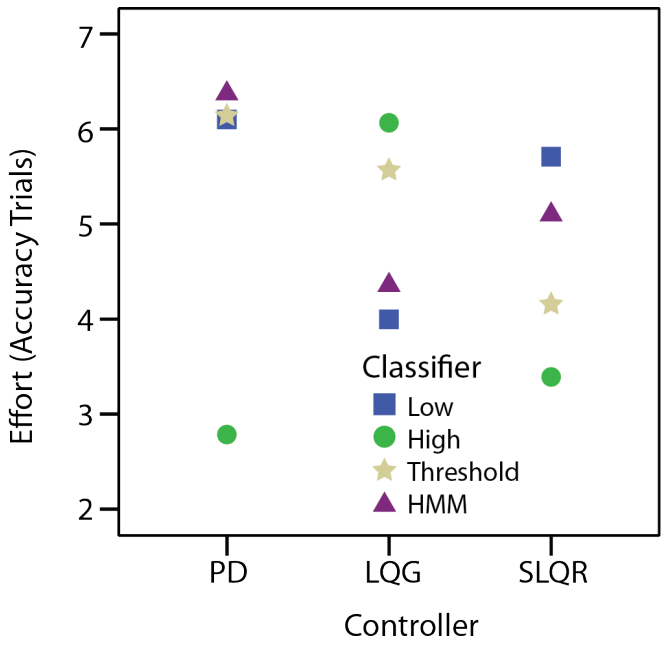

Figure 102: Means of effort rating for accuracy trials divided by controller levels

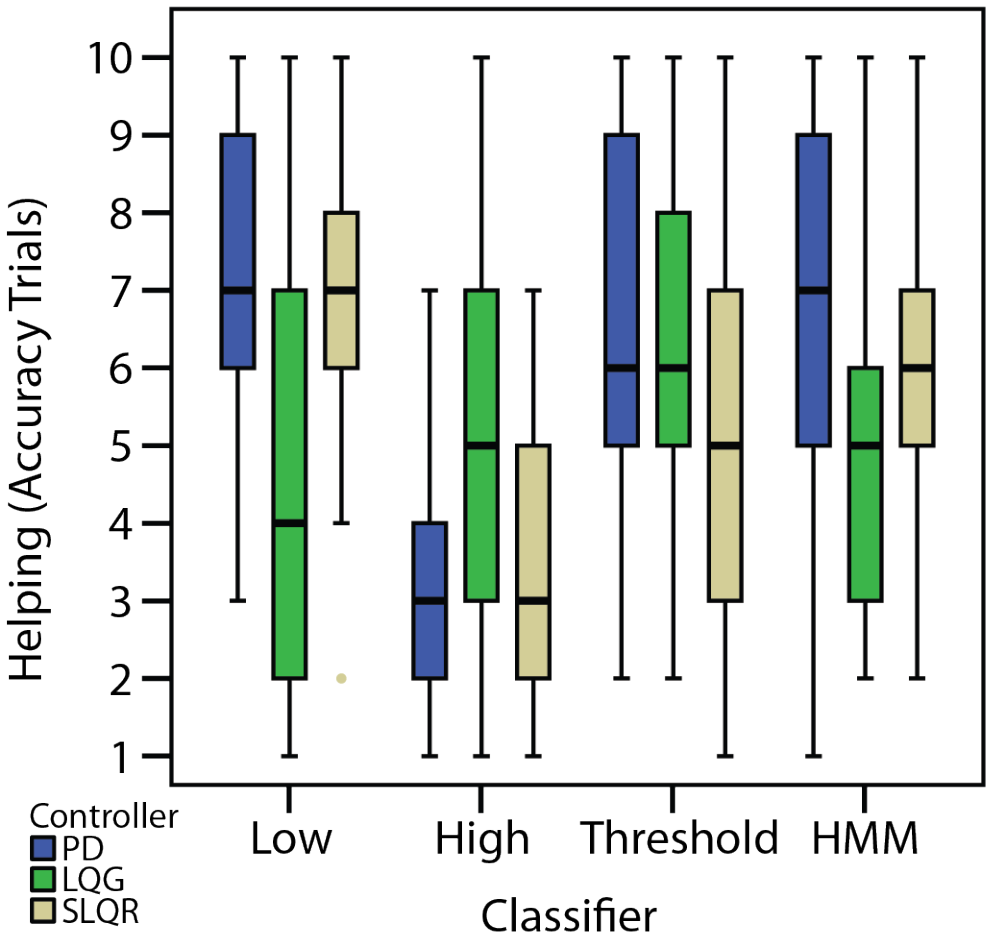

Figure 103: Box plot of helping rating for accuracy trials across all cases

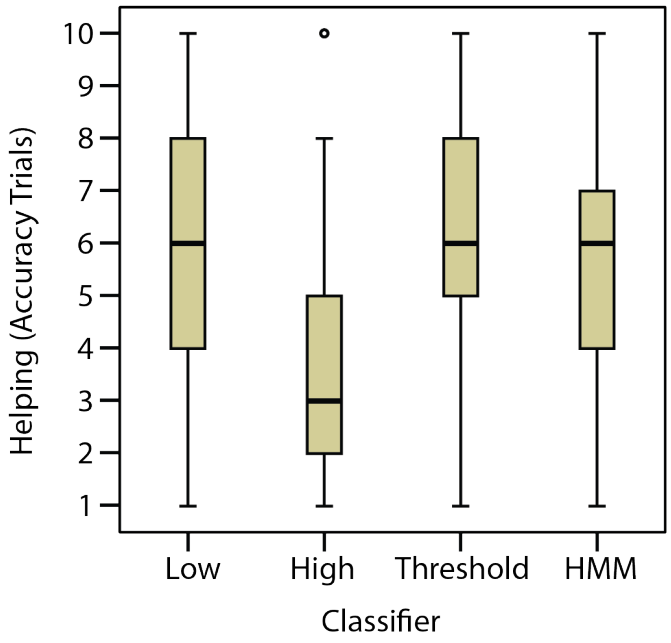

Figure 104: Box plot of helping rating for accuracy trials divided by classifier levels

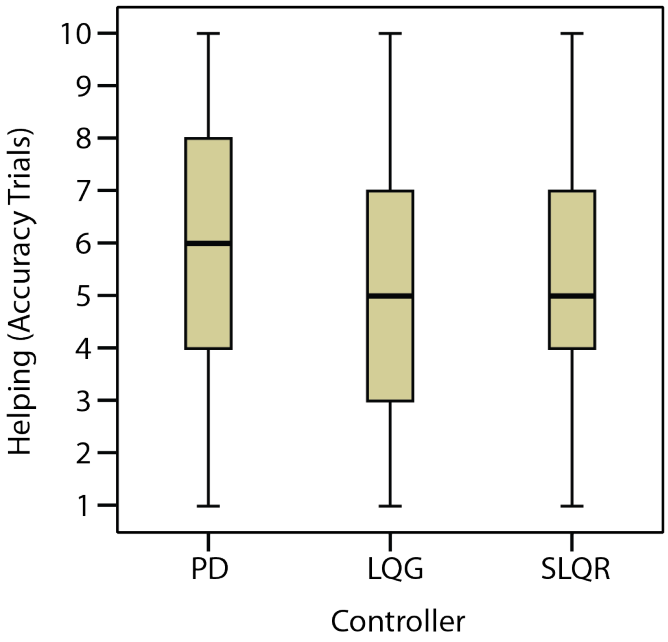

Figure 105: Box plot of helping rating for accuracy trials divided by controller levels

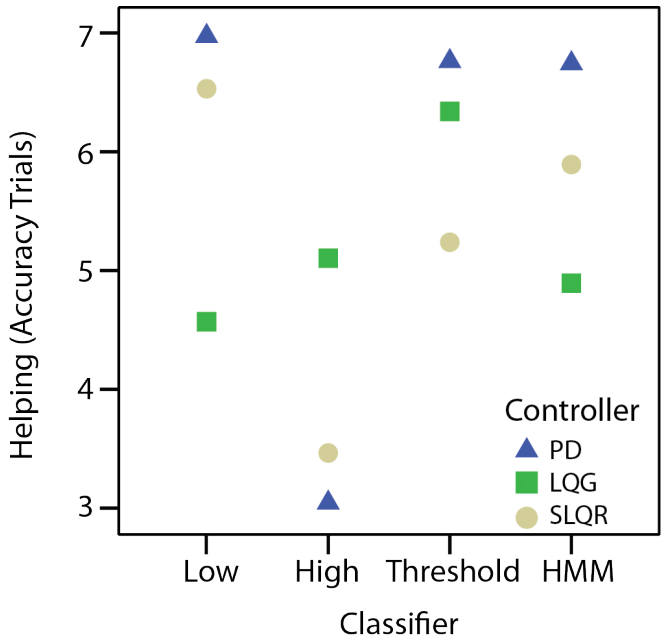

Figure 106: Means of helping rating for accuracy trials divided by classifier levels

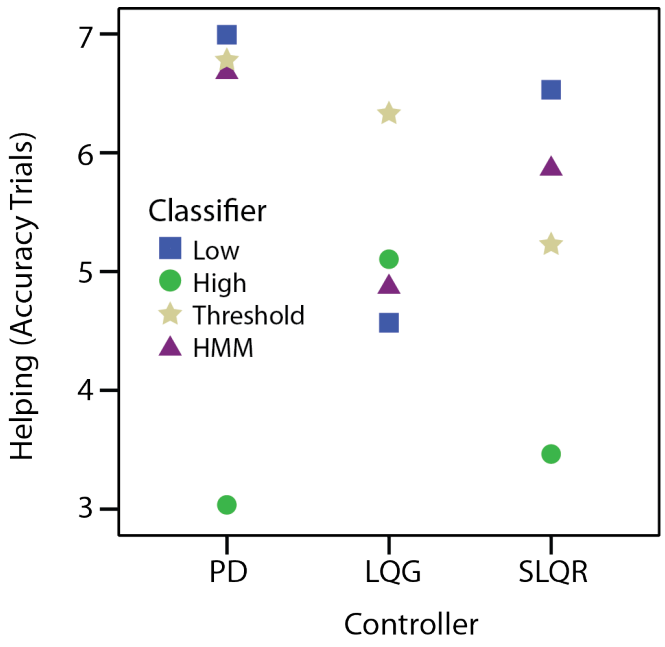

Figure 107: Means of helping rating for accuracy trials divided by controller levels

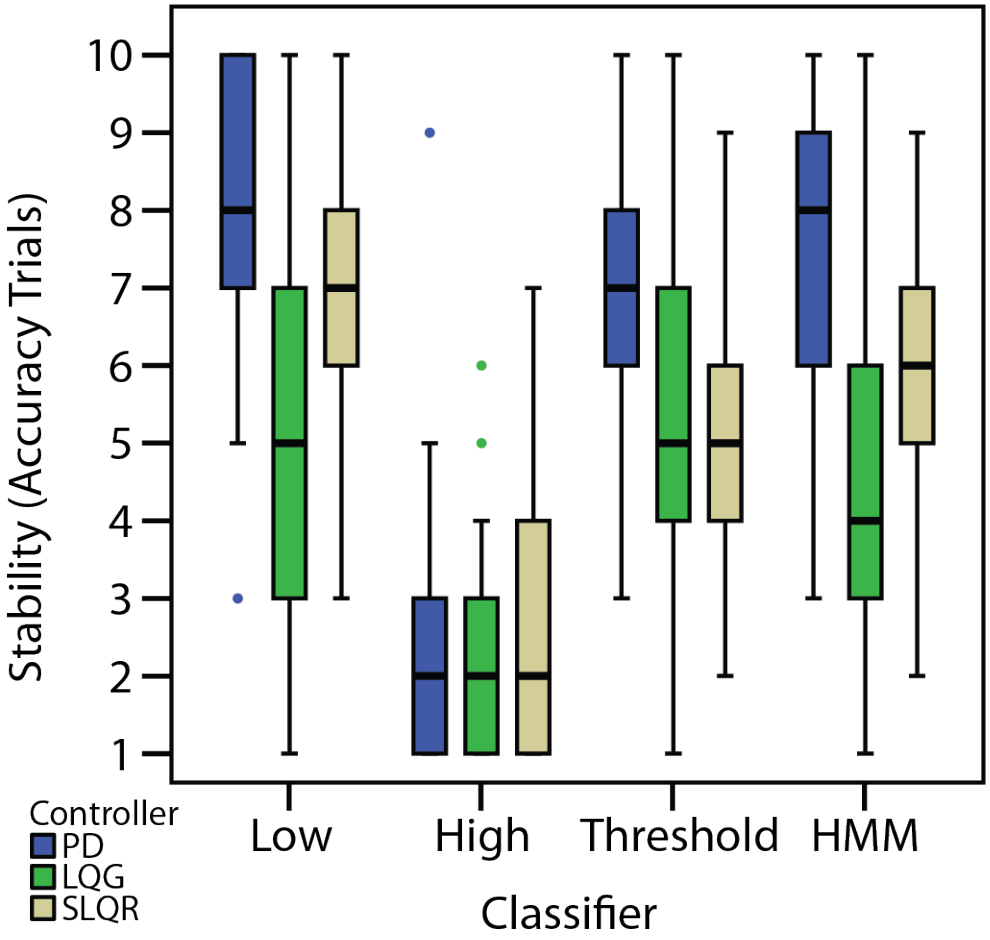

Figure 108: Box plot of stability rating for accuracy trials across all cases

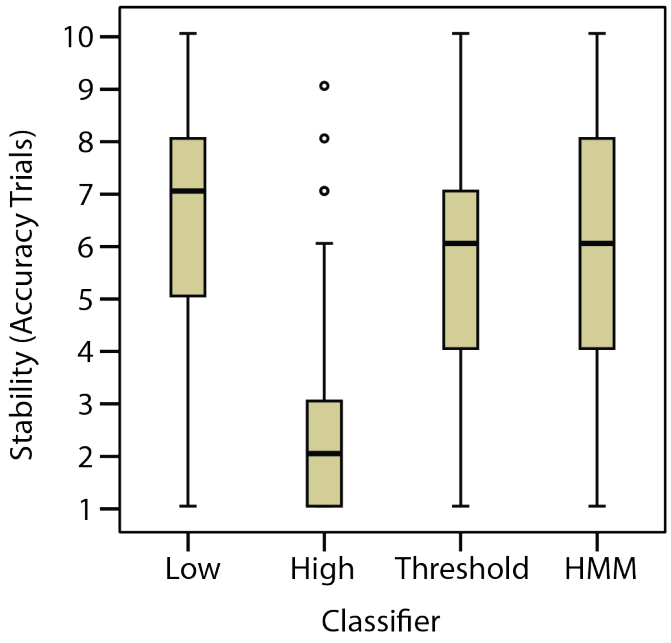

Figure 109: Box plot of stability rating for accuracy trials divided by classifier levels

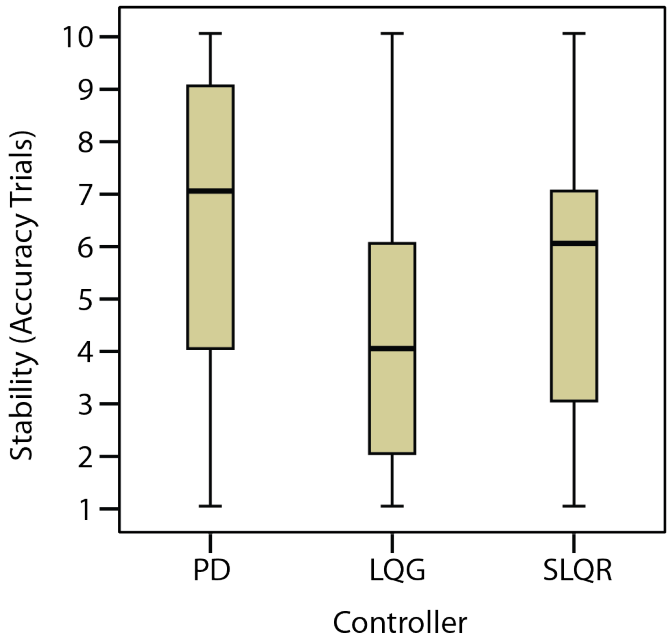

Figure 110: Box plot of stability rating for accuracy trials divided by controller levels

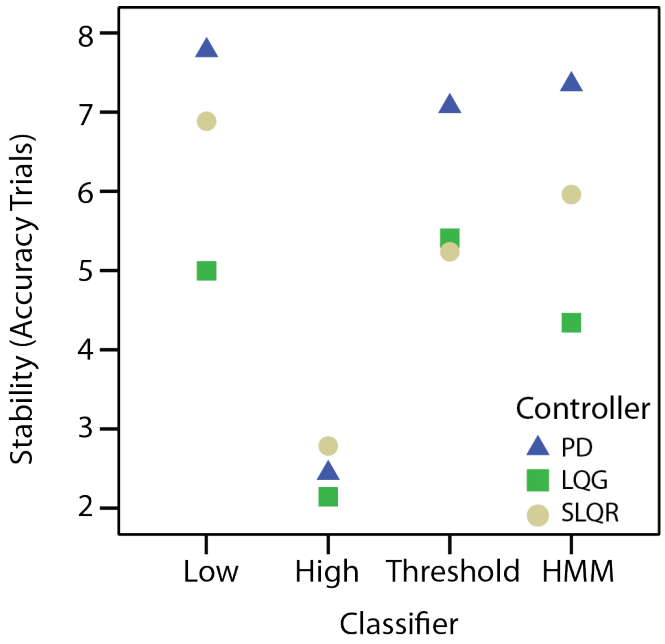

Figure 111: Means of stability rating for accuracy trials divided by classifier levels

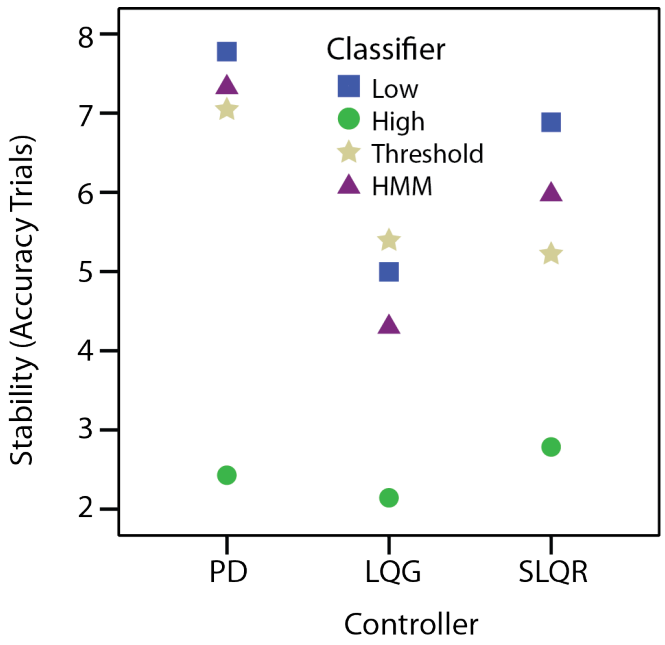

Figure 112: Means of stability rating for accuracy trials divided by controller levels

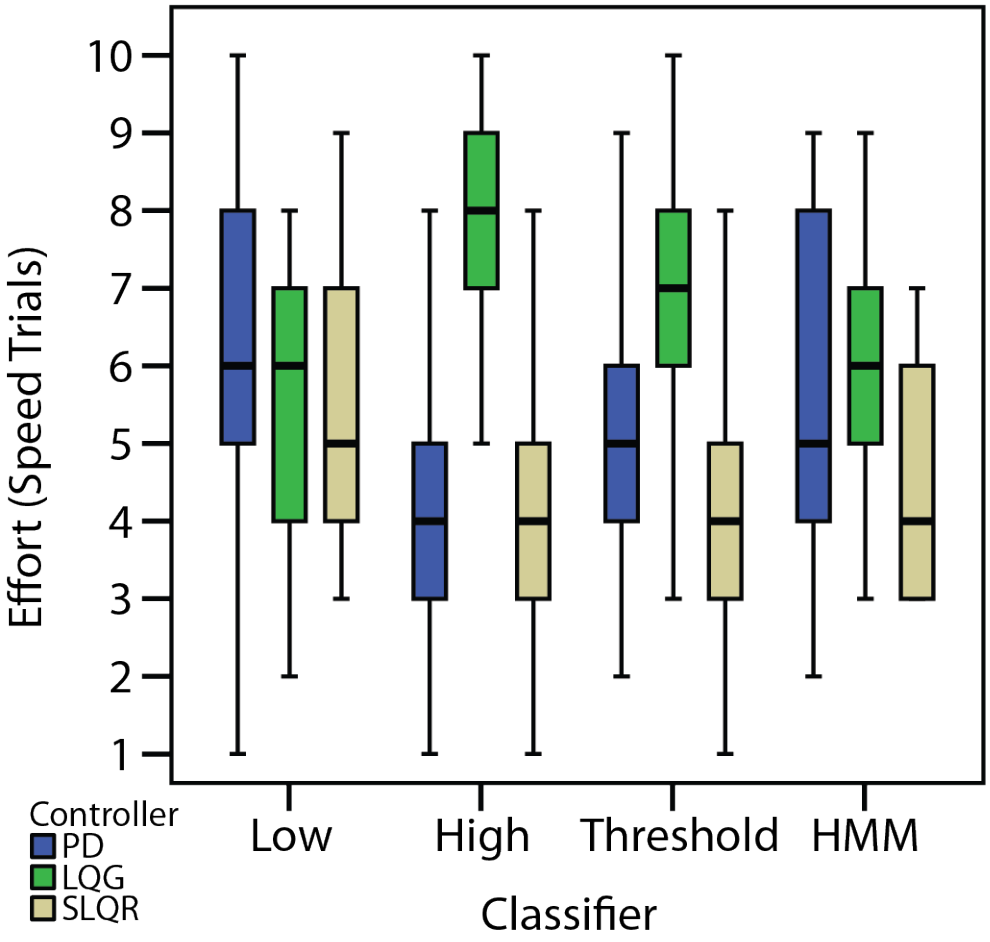

Figure 113: Box plot of effort rating for speed trials across all cases

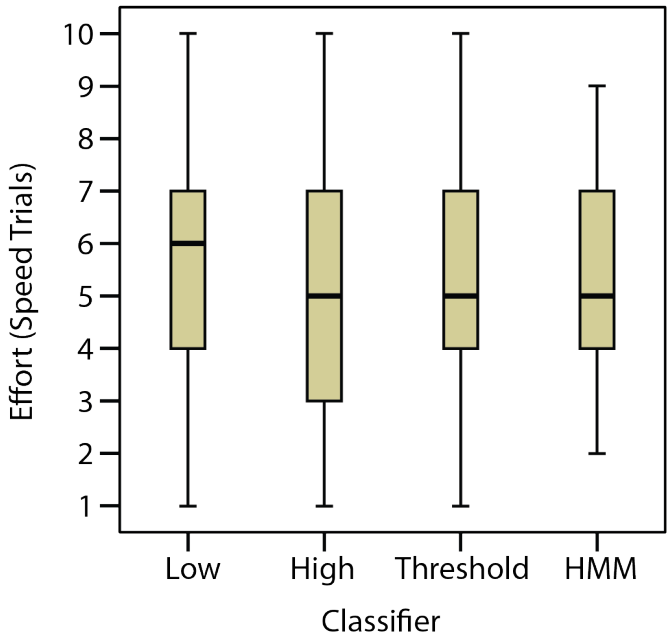

Figure 114: Box plot of effort rating for speed trials divided by classifier levels

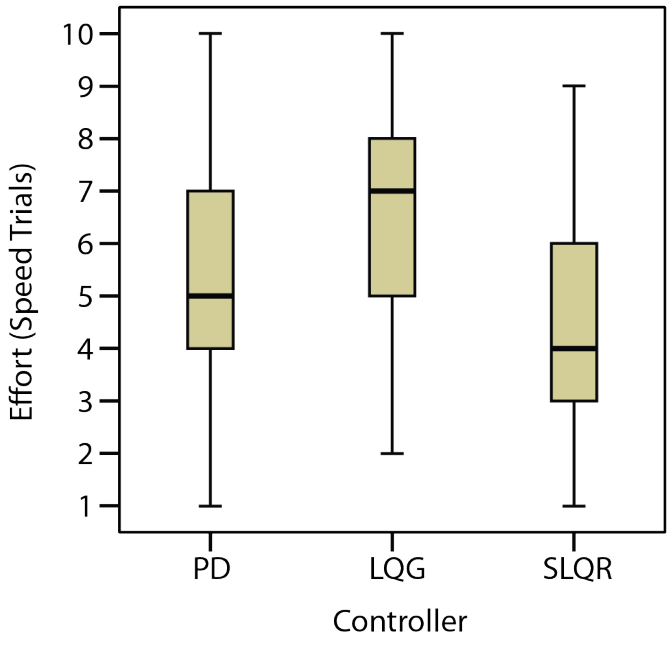

Figure 115: Box plot of effort rating for speed trials divided by controller levels

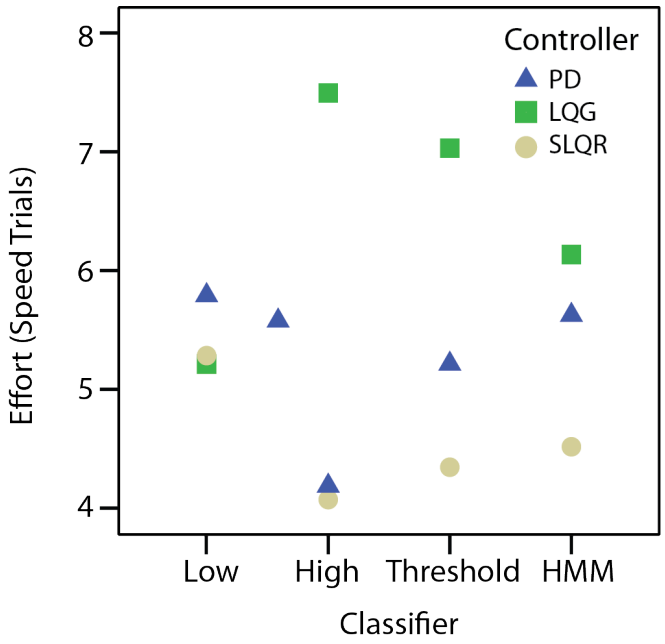

Figure 116: Means of effort rating for speed trials divided by classifier levels

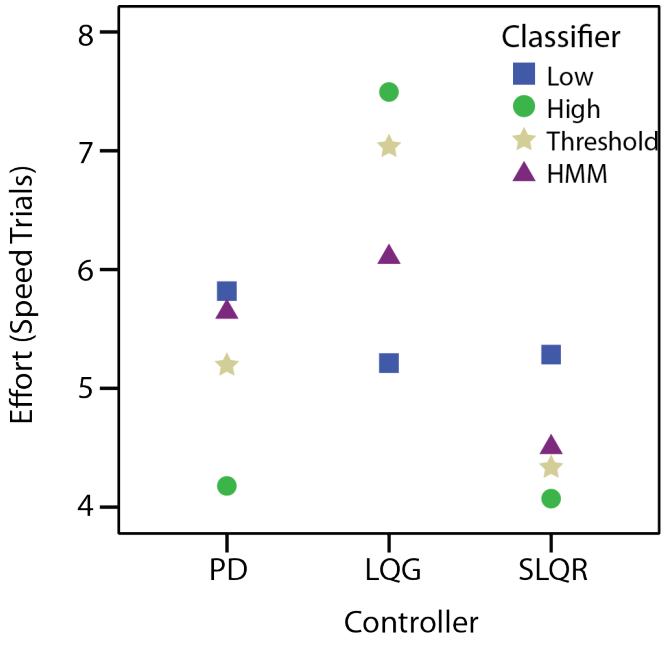

Figure 117: Means of effort rating for speed trials divided by controller levels

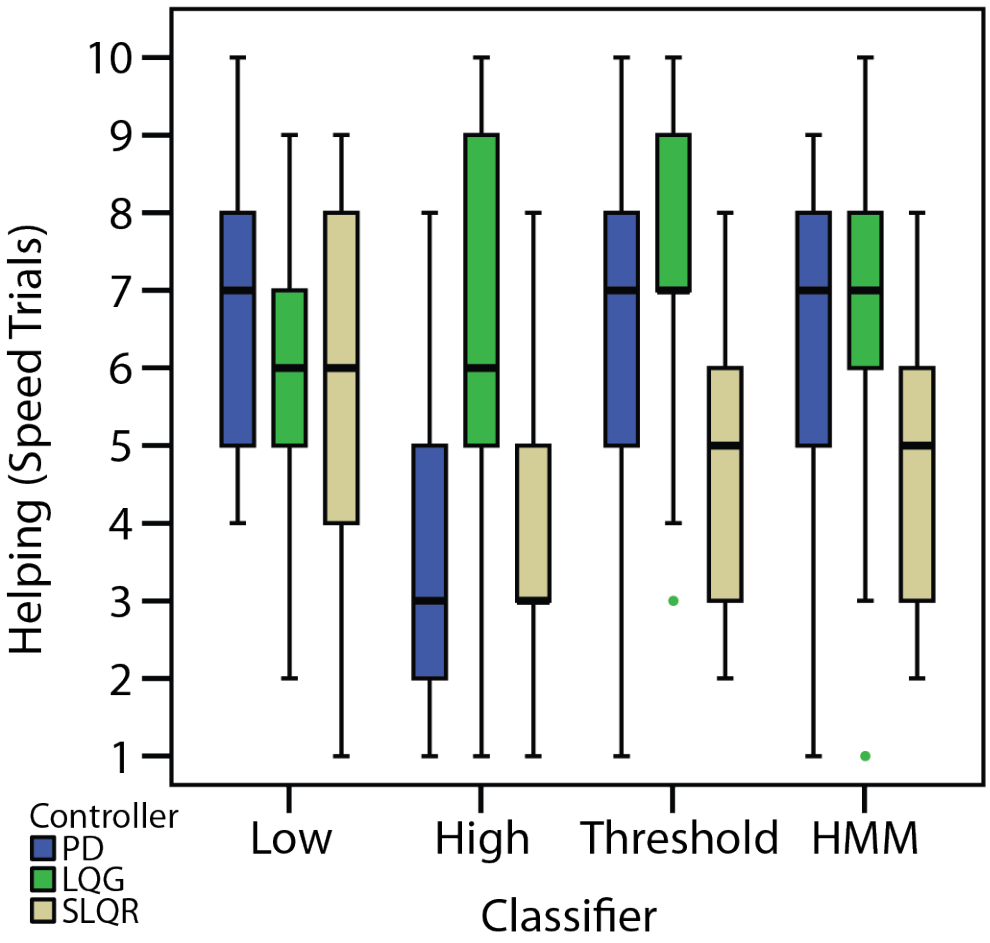

Figure 118: Box plot of helping rating for speed trials across all cases

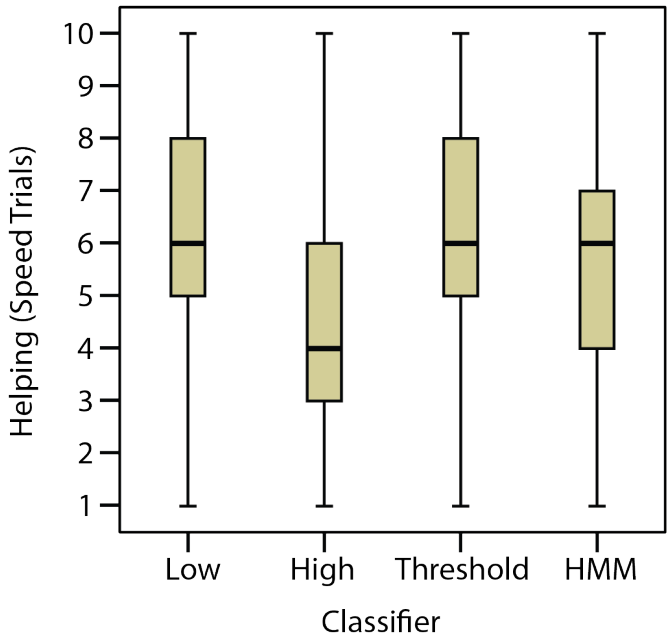

Figure 119: Box plot of helping rating for speed trials divided by classifier levels

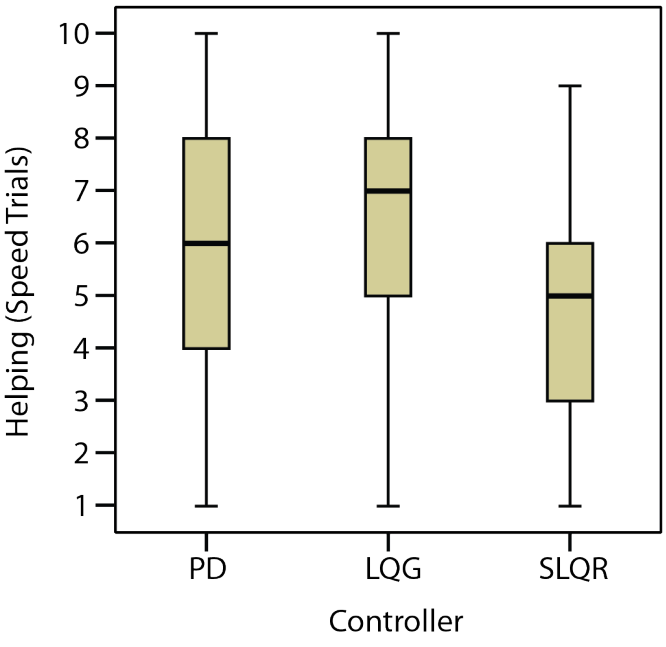

Figure 120: Box plot of helping rating for speed trials divided by controller levels

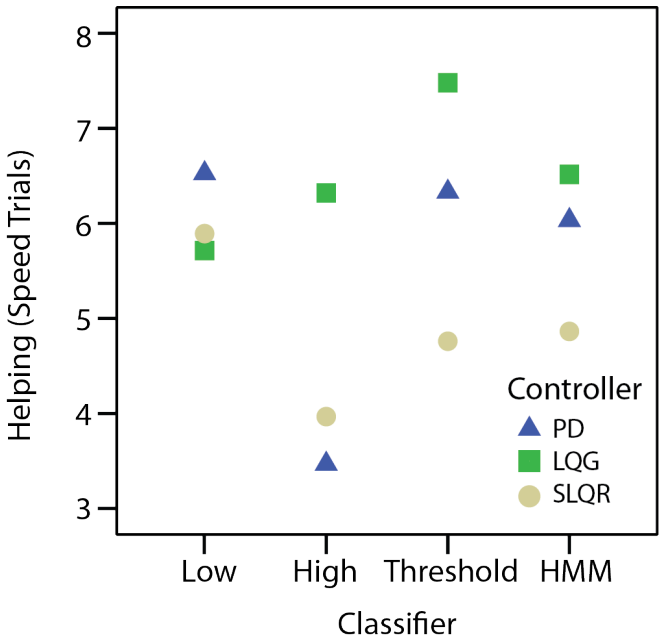

Figure 121: Means of helping rating for speed trials divided by classifier levels

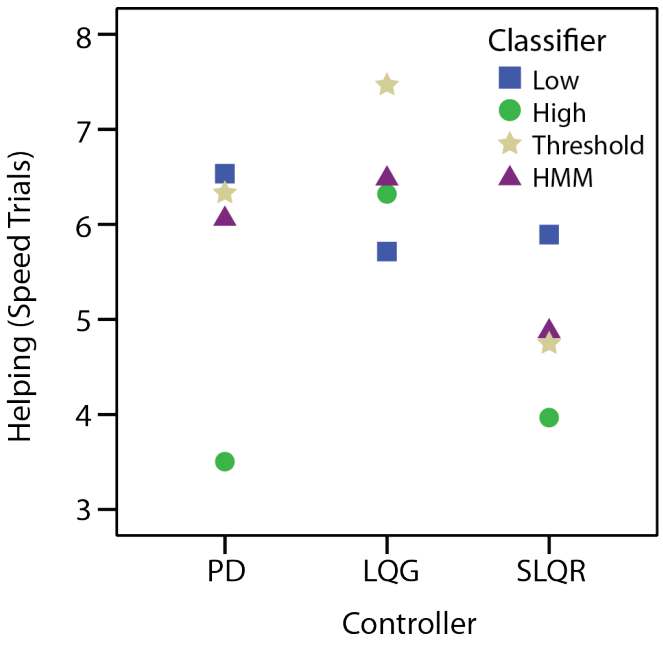

Figure 122: Means of helping rating for speed trials divided by controller levels

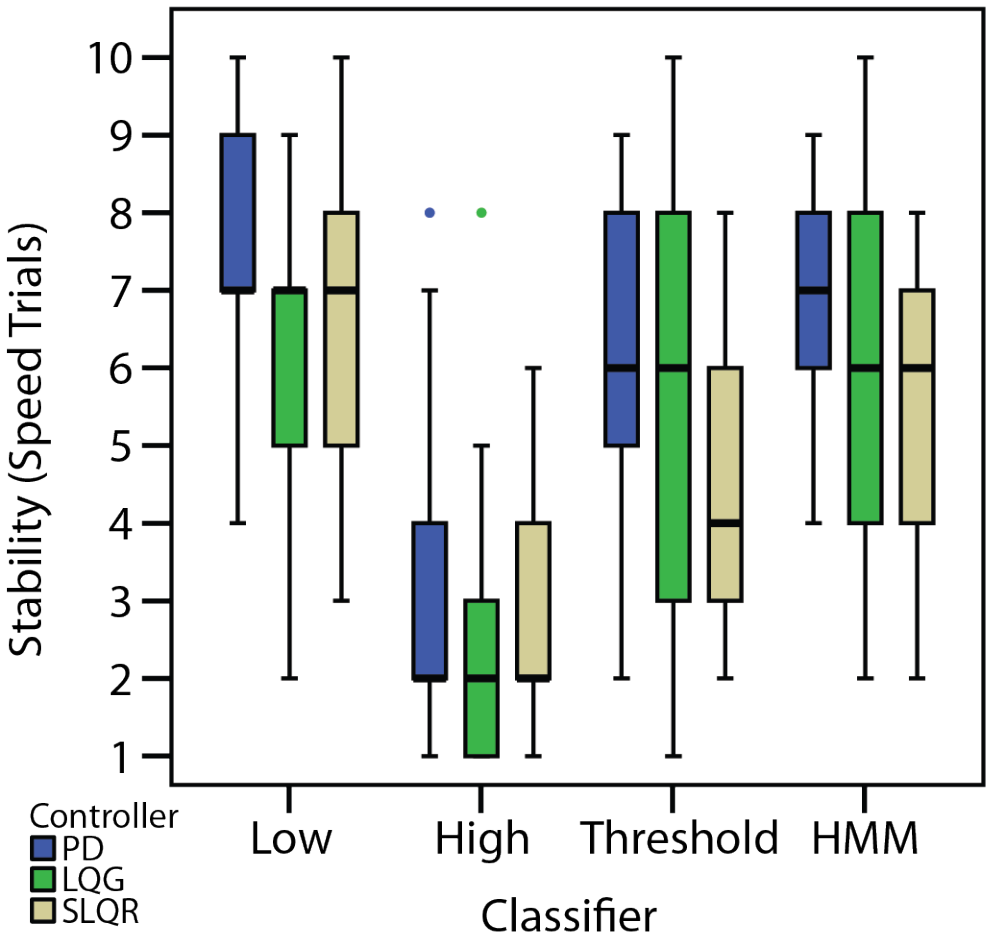

Figure 123: Box plot of stability rating for speed trials across all cases

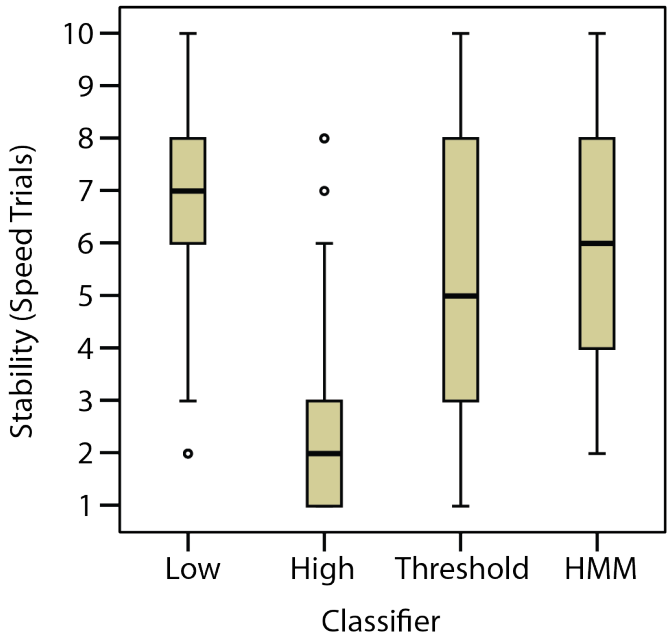

Figure 124: Box plot of stability rating for speed trials divided by classifier levels

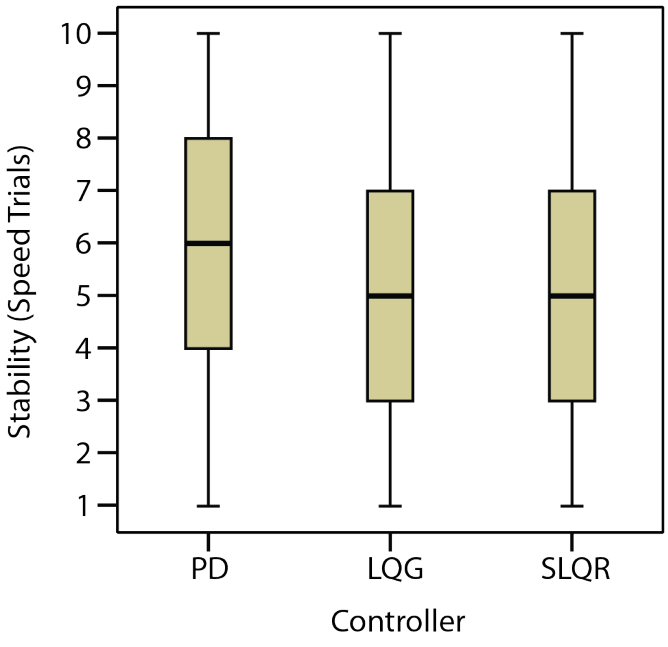

Figure 125: Box plot of stability rating for speed trials divided by controller levels

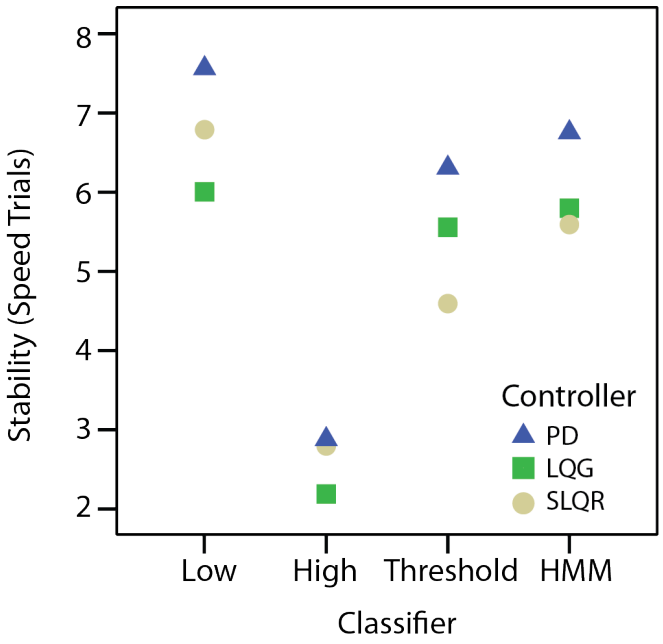

Figure 126: Means of stability rating for speed trials divided by classifier levels

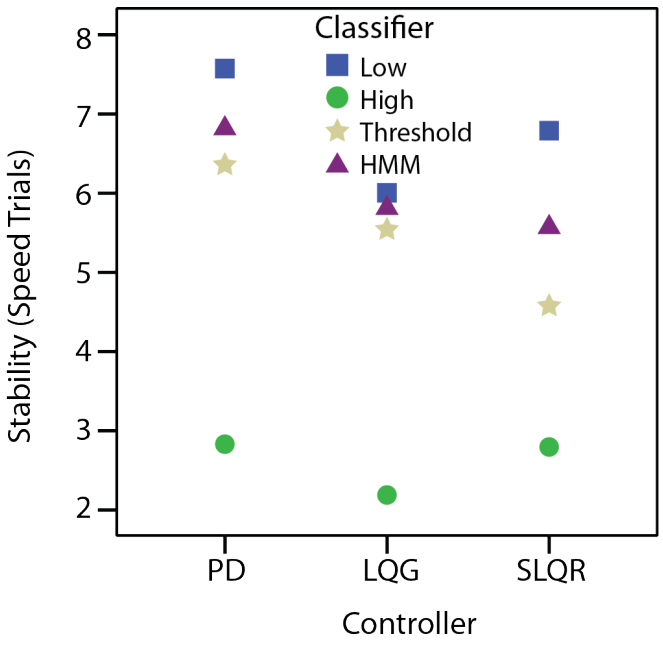

Figure 127: Means of stability rating for speed trials divided by controller levels

B.4.4 Statistics

Analysis method: Multiple ANOVA with Repeated Measures (Equality of variances was not valid, so values reported are corrected metrics using Pillai's Trace)

Table 28: MANOVA Results for Speed and Accuracy

Variable	*PV*	*df*	*F*	*p*
Classifier	0.112	6	161.96	< 0.001
Controller	0.125	4	273.87	< 0.001
Interaction	0.048	12	33.524	< 0.001

Table 29: MANOVA Results for Surveys

Variable	*PV*	*df*	*F*	*p*
Classifier	0.555	18	12.368	< 0.001
Controller	0.391	12	13.191	< 0.001
Interaction	0.300	36	2.890	< 0.001

Table 30: Means and Confidences of Accuracy for Each Case

Classifier	Controller	Mean	Std Dev	95% Interval
Low Damping	PD	5.848	8.507	5.461 - 6.235
	LQG	2.625	5.517	2.238 - 3.013
	SLQR	3.356	4.816	2.968 - 3.743
High Damping	PD	0.503	1.404	0.115 - 0.890
	LQG	0.527	1.165	0.140 - 0.915
	SLQR	0.793	1.726	0.405 - 1.180
Threshold	PD	3.869	5.337	3.479 - 4.240
	LQG	2.201	5.512	1.820 - 2.581
	SLQR	2.142	4.425	1.761 - 2.522
HMM	PD	5.029	7.327	4.649 - 5.410
	LQG	1.844	5.172	1.464 - 2.225
	SLQR	2.442	4.792	2.061 - 2.822

Table 31: Means and Confidences of Speed for Each Case

Classifier	Controller	Mean	Std Dev	95% Interval
Low Damping	PD	3.498	1.068	3.377 - 3.618
	LQG	4.098	1.648	3.978 - 4.218
	SLQR	3.965	1.377	3.845 - 4.085
High Damping	PD	4.259	1.552	4.139 - 4.379
	LQG	6.248	1.908	6.228 - 6.468
	SLQR	4.434	1.410	4.314 - 4.554
Threshold	PD	4.060	1.416	3.942 - 4.178
	LQG	5.498	2.238	5.380 - 5.616
	SLQR	4.186	1.285	4.068 - 4.304
HMM	PD	4.002	1.608	3.884 - 4.120
	LQG	4.757	1.795	4.639 - 4.875
	SLQR	4.085	1.396	3.967 - 4.203

Table 32: Means and Confidences of Effort During Accuracy Trials for Each Case

Classifier	Controller	Mean	Std Dev	95% Interval
Low Damping	PD	6.11	2.21	5.34 - 6.86
	LQG	4.00	2.05	3.24 - 4.75
	SLQR	5.71	1.86	4.95 - 6.47
High Damping	PD	2.79	1.42	2.02 - 3.54
	LQG	6.07	1.96	5.31 - 6.83
	SLQR	3.39	1.77	2.63 - 4.15
Threshold	PD	6.14	1.95	5.39 - 6.88
	LQG	5.59	2.42	4.84 - 6.33
	SLQR	4.17	2.00	3.42 - 4.91
HMM	PD	6.41	2.14	5.66 - 7.15
	LQG	4.38	2.51	3.63 - 5.12
	SLQR	5.14	1.88	4.39 - 5.88

Table 33: Means and Confidences of Helping During Accuracy Trials for Each Case

Classifier	Controller	Mean	Std Dev	95% Interval
Low Damping	PD	7.00	2.19	6.20 - 7.79
	LQG	4.57	2.71	3.77 - 5.36
	SLQR	6.54	1.75	5.74 - 7.33
High Damping	PD	3.04	1.55	2.24 - 3.83
	LQG	5.11	2.31	4.31 - 5.90
	SLQR	3.46	1.68	2.67 - 4.25
Threshold	PD	6.76	2.18	5.97 - 7.53
	LQG	6.34	2.17	5.56 - 7.12
	SLQR	5.24	2.26	4.46 - 6.02
HMM	PD	6.76	2.45	5.97 - 7.53
	LQG	4.90	2.07	4.11 - 5.67
	SLQR	5.90	1.97	5.11 - 6.67

Table 34: Means and Confidences of Stability During Accuracy Trials for Each Case

Classifier	Controller	Mean	Std Dev	95% Interval
Low Damping	PD	7.79	1.81	7.02 - 8.54
	LQG	5.00	1.77	4.23 - 5.76
	SLQR	6.89	2.37	6.13 - 7.65
High Damping	PD	2.43	1.68	1.66 - 3.19
	LQG	2.14	2.02	1.38 - 2.90
	SLQR	2.79	1.82	2.02 - 3.54
Threshold	PD	7.07	1.88	6.32 - 7.81
	LQG	5.41	1.92	4.66 - 6.16
	SLQR	5.24	2.20	4.49 - 5.98
HMM	PD	7.34	2.19	6.59 - 8.09
	LQG	4.34	2.39	3.59 - 5.09
	SLQR	5.97	1.93	5.21 - 6.71

Table 35: Means and Confidences of Effort During Speed Trials for Each Case

Classifier	Controller	Mean	Std Dev	95% Interval
Low Damping	PD	5.82	1.92	5.16 - 6.47
	LQG	5.21	1.72	4.56 - 5.86
	SLQR	5.29	1.71	4.63 - 5.93
High Damping	PD	4.18	1.86	3.52 - 4.83
	LQG	7.50	1.64	6.84 - 8.15
	SLQR	4.07	1.80	3.41 - 4.72
Threshold	PD	5.21	1.78	4.56 - 5.84
	LQG	7.03	1.82	6.39 - 7.67
	SLQR	4.34	1.69	3.70 - 4.98
HMM	PD	5.66	1.95	5.01 - 6.29
	LQG	6.14	1.72	5.49 - 6.77
	SLQR	4.52	1.32	3.87 - 5.15

Table 36: Means and Confidences of Helping During Speed Trials for Each Case

Classifier	Controller	Mean	Std Dev	95% Interval
Low Damping	PD	6.54	1.81	5.80 - 7.27
	LQG	5.71	1.65	4.97 - 6.45
	SLQR	5.89	2.14	5.15 - 6.62
High Damping	PD	3.50	2.00	2.76 - 4.23
	LQG	6.32	2.31	5.58 - 7.05
	SLQR	3.96	1.91	3.22 - 4.70
Threshold	PD	6.34	2.12	5.62 - 7.06
	LQG	7.48	2.02	6.76 - 8.20
	SLQR	4.76	1.52	4.03 - 5.48
HMM	PD	6.07	2.23	5.34 - 6.79
	LQG	6.52	2.08	5.79 - 7.24
	SLQR	4.86	1.74	4.13 - 5.58

Table 37: Means and Confidences of Stability During Speed Trials for Each Case

Classifier	Controller	Mean	Std Dev	95% Interval
Low Damping	PD	7.57	1.42	6.85 - 8.29
	LQG	6.00	1.96	5.28 - 6.71
	SLQR	6.79	1.68	6.06 - 7.50
High Damping	PD	2.82	1.80	2.10 - 3.54
	LQG	2.18	1.61	1.46 - 2.89
	SLQR	2.79	1.61	2.06 - 3.50
Threshold	PD	6.34	2.07	5.63 - 7.05
	LQG	5.55	2.88	4.84 - 6.25
	SLQR	4.59	1.72	3.88 - 5.29
HMM	PD	6.79	1.65	6.08 - 7.49
	LQG	5.79	2.42	5.08 - 6.49
	SLQR	5.59	1.80	4.88 - 6.29

REFERENCES

[1] Anderson, B. D. O. and Moore, J. B., *Optimal Filtering*. Prentice Hall, 1979.

[2] Anderson, R. J. and Spong, M. W., "Bilateral control of teleoperators with time delay," *IEEE Transactions on Automatic Control*, vol. 34, pp. 494–501, May 1989.

[3] Argall, B., Gu, Y., Browning, B., and Veloso, M., "The first segway soccer experience: towards peer-to-peer human-robot teams," in *ACM SIGCHI/SIGART Conference on Human-Robot Interaction (HRI)*, (Salt Lake City, UT, USA), pp. 321–322, ACM, ACM, 2006.

[4] Athans, M., "The role and use of the stochastic linear-quadratic-Gaussian problem in control system design," *IEEE Transactions on Automatic Control*, vol. 16, no. 6, pp. 529–552, 1971.

[5] Athans, M., "The discrete time linear-quadratic-Gaussian stochastic control problem," *Annals of Economic and Social Measurement*, vol. 1, no. 4, pp. 446–488, 1972.

[6] Baird, J. A. and Baldwin, D. A., "Making sense of human behavior: Action parsing and intentional inference," in *Intentions and intentionality: Foundations of social cognition* (Malle, B. F., Moses, L. J., and Baldwin, D. A., eds.), ch. 9, pp. 193–206, MIT Press Cambridge, MA, 2001.

[7] Beal, M. J., Ghahramani, Z., and Rasmussen, C. E., "The infinite hidden Markov model," in *Advances in Neural Information Processing Systems (NIPS)*, (Vancouver, BC, Canada), pp. 577–584, 2001.

[8] Bennett, D. J., Hollerbach, J. M., Xu, Y., and Hunter, I. W., "Time-varying stiffness of human elbow joint during cyclic voluntary movement," *Experimental Brain Research*, vol. 88, no. 2, pp. 433–442, 1992.

[9] Bernhardsson, B., "Robust performance optimization of open loop type problems using models from standard identification," *Systems & control letters*, vol. 25, no. 2, pp. 79–87, 1995.

[10] Bernstein, N. A., *The co-ordination and regulation of movements*. Pergamon Press, 1967.

[11] Bertsekas, D. P., *Nonlinear programming*. Athena Scientific, 1999.

[12] Blackmore, L., "A probabilistic particle control approach to optimal, robust predictive control," in *AIAA Guidance, Navigation, and Control Conference*, (Keystone, CO, USA), 2006.

[13] Blackmore, L., Ono, M., Bektassov, A., and Williams, B. C., "A Probabilistic Particle-Control Approximation of Chance-Constrained Stochastic Predictive Control," *IEEE Transactions on Robotics (T-Ro)*, vol. 26, no. 3, pp. 502–517, 2010.

[14] Bowen, K. and O'Malley, M. K., "Adaptation of Haptic Interfaces for a LabVIEW-based System Dynamics Course," in *ASME Symposium on Haptic Interfaces for Virtual Environment and Teleoperator Systems (Haptics)*, (Arlington, VA, USA), pp. 147–152, 2006.

[15] Buchanan, T. S. and Shreeve, D. A., "An evaluation of optimization techniques for the prediction of muscle activation patterns during isometric tasks.," *Journal of Biomechanical Engineering*, vol. 118, pp. 565–74, Nov. 1996.

[16] Bui, H. H., Phung, D. Q., and Venkatesh, S., "Hierarchical hidden Markov models with general state hierarchy," in *National Conference on Artificial Intelligence*, (San Jose, CA, USA), pp. 324–329, 2004.

[17] Burdet, E., Osu, R., Franklin, D. W., Milner, T. E., and Kawato, M., "The central nervous system stabilizes unstable dynamics by learning optimal impedance.," *Nature*, vol. 414, pp. 446–9, Nov. 2001.

[18] Burdet, E., Osu, R., Franklin, D. W., Toshinori, Y., Milner, T. E., and Kawato, M., "A method for measuring endpoint stiffness during multijoint arm movements," *Journal of biomechanics*, vol. 33, no. 12, pp. 1705–1709, 2000.

[19] Cappé, O., Moulines, E., and Rydén, T., *Inference in Hidden Markov Models*. Springer, 2005.

[20] Chang, S. and Peng, T. K. C., "Adaptive guaranteed cost control of systems with uncertain parameters," *IEEE Transactions on Automatic Control*, vol. 17, pp. 474–483, Aug. 1972.

[21] Cohen, J., Cohen, P., West, S. G., and Aiken, L. S., *Applied multiple regression/correlation analysis for the behavioral sciences*. L. Erlbaum Associates, 3rd ed., 2003.

[22] Colgate, J. E., "Robust impedance shaping telemanipulation," *IEEE Transactions on Robotics and Automation (T-Ro)*, vol. 9, no. 4, pp. 374–384, 1993.

[23] Colgate, J. E. and Hogan, N., "Robust control of dynamically interacting systems," *International Journal of Control*, vol. 48, no. 1, pp. 65–88, 1988.

[24] Colgate, J. E. and Hogan, N., "An analysis of contact instability in terms of passive physical equivalents," in *IEEE International Conference on Robotics and Automation (ICRA)*, (Scottsdale, AZ, USA), pp. 404 –409 vol1, May 1989.

[25] Colgate, J. E. and Schenkel, G. G., "Passivity of a class of sampled-data systems: Application to haptic interfaces," *Journal of Robotic Systems*, vol. 14, pp. 37–47, Jan. 1997.

[26] Crowninshield, R. D. and Brand, R. A., "A physiologically based criterion of muscle force prediction in locomotion.," *Journal of Biomechanics*, vol. 14, pp. 793–801, Jan. 1981.

[27] Damsgaard, M., Rasmussen, J., Christensen, S. r. T. r., Surma, E., and de Zee, M., "Analysis of musculoskeletal systems in the AnyBody Modeling System," *Simulation Modelling Practice and Theory*, vol. 14, pp. 1100–1111, Nov. 2006.

[28] De Koning, W. L., "Infinite horizon optimal control of linear discrete time systems with stochastic parameters," *Automatica*, vol. 18, pp. 443–453, July 1982.

[29] De Koning, W. L., "Optimal estimation of linear discrete-time systems with stochastic parameters," *Automatica*, vol. 20, no. 1, pp. 113–115, 1984.

[30] De Serres, S. J. and Milner, T. E., "Wrist muscle activation patterns and stiffness associated with stable and unstable mechanical loads," *Experimental Brain Research*, vol. 86, no. 2, pp. 451–458, 1991.

[31] Delp, S. L., Anderson, F. C., Arnold, A. S., Loan, P., Habib, A., John, C. T., Guendelman, E., and Thelen, D. G., "OpenSim: open-source software to create and analyze dynamic simulations of movement.," *IEEE Transactions on Biomedical Engineering*, vol. 54, pp. 1940–50, Nov. 2007.

[32] Delp, S. L., Loan, J. P., Hoy, M. G., Zajac, F. E., Topp, E. L., and Rosen, J. M., "An interactive graphics-based model of the lower extremity to study orthopaedic surgical procedures.," *IEEE Transactions on Biomedical Engineering*, vol. 37, pp. 757–67, Aug. 1990.

[33] Demeester, E., Hüntemann, A., Vanhooydonck, D., Vanacker, G., Degeest, A., Van Brussel, H., and Nuttin, M., "Bayesian estimation of wheelchair driver intents: Modeling intents as geometric paths tracked by the driver," in *IEEE/RSJ International Conference on Intelligent Robots and Systems (IROS)*, (Beijing, China), pp. 5775–5780, IEEE, 2006.

[34] Dickinson, M. H., "How Animals Move: An Integrative View," *Science*, vol. 288, pp. 100–106, Apr. 2000.

[35] Ding, M., Kurita, Y., Ueda, J., and Ogasawara, T., "Pinpointed Muscle Force Control Taking Into Account the Control DOF of Power-Assisting Device," *ASME Dynamic Systems and Control Conference (DSCC)*, vol. 2010, no. 44175, pp. 341–348, 2010.

[36] Ding, M., Ueda, J., and Ogasawara, T., "Development of MAS-a system for pin-pointed muscle force control using a power-assisting device," in *IEEE International Conference on Robotics and Biomimetics (ROBIO)*, (Sanya, China), pp. 1463–1469, IEEE, 2007.

[37] Ding, M., Ueda, J., and Ogasawara, T., "Pinpointed muscle force control using a power-assisting device: System configuration and experiment," in *IEEE RAS EMBS International Conference on Biomedical Robotics and Biomechatronics (BioRob)*, (Scottsdale, AZ, USA), pp. 181–186, 2008.

[38] Dombrovsky, V. V. and Lashenko, E. A., "Robust control of linear systems with random parameters and multiplicative disturbances with application to the investment portfolio management," in *SICE Annual Conference*, (Fukui, Japan), 2003.

[39] Doyle, J. C., "Guaranteed margins for LQG regulators," *IEEE Transactions on Automatic Control*, vol. 23, no. 4, pp. 756–757, 1978.

[40] Dreyfus, S., "Some types of optimal control of stochastic systems," *Journal for Industrial & Applied Mathematics, Series A: Control*, vol. 2, no. 1, pp. 120–134, 1962.

[41] Duchaine, V. and Gosselin, C. M., "Investigation of human-robot interaction stability using Lyapunov theory," in *IEEE International Conference on Robotics and Automation (ICRA)*, (Pasadena, CA, USA), pp. 2189–2194, IEEE, May 2008.

[42] Farokhi, F. and Johansson, K. H., "Limited model information control design for linear discrete-time systems with stochastic parameters," in *IEEE Conference on Decision and Control (CDC)*, (Maui, HI, USA), pp. 855–861, Ieee, Dec. 2012.

[43] Faul, F., Erdfelder, E., Lang, A.-G., and Buchner, A., "G*Power 3: a flexible statistical power analysis program for the social, behavioral, and biomedical sciences.," *Behavior Research Methods*, vol. 39, pp. 175–191, May 2007.

[44] Field, A., *Discovering Statistincs Using IBM SPSS Statistics*. Sage, 4 ed., 2013.

[45] Fine, S., Singer, Y., and Tishby, N., "The hierarchical hidden Markov model: Analysis and applications," *Machine learning*, vol. 32, no. 1, pp. 41–62, 1998.

[46] Flash, T. and Mussa-Ivaldi, F., "Human arm stiffness characteristics during the maintenance of posture.," *Experimental Brain Research*, vol. 82, pp. 315–26, Jan. 1990.

[47] Fleming, W. H., "Optimal Continuous-Parameter Stochastic Control," *SIAM Review*, vol. 11, pp. 470–509, Oct. 1969.

[48] Franklin, D. W., Burdet, E., Osu, R., Kawato, M., and Milner, T. E., "Functional significance of stiffness in adaptation of multijoint arm movements to stable and unstable dynamics.," *Experimental Brain Research*, vol. 151, pp. 145–57, July 2003.

[49] Franklin, D. W. and Milner, T. E., "Adaptive control of stiffness to stabilize hand position with large loads.," *Experimental Brain Research*, vol. 152, pp. 211–220, Sept. 2003.

[50] Franklin, D. W., Osu, R., Burdet, E., Kawato, M., and Milner, T. E., "Adaptation to stable and unstable dynamics achieved by combined impedance control and inverse dynamics model.," *Journal of Neurophysiology*, vol. 90, pp. 3270–82, Nov. 2003.

[51] Franklin, G. F., Powell, J. D., and Emami-Naeini, A., *Feedback Control of Dynamic Systems*. Pearson/Prentice Hall, 2006.

[52] Fujimoto, K., Ogawa, S., Ota, Y., and Nakayama, M., "Optimal control of linear systems with stochastic parameters for variance suppression: The finite time horizon case," in *IFAC World Congress*, (Milan, Italy), pp. 12605–12610, 2011.

[53] Fujimoto, K., Ota, Y., and Nakayama, M., "Optimal control of linear systems with stochastic parameters for variance suppression," in *IEEE Conference on Decision and Control and European Control Conference (CDC-ECC)*, (Orlando, FL, USA), pp. 1424–1429, Ieee, Dec. 2011.

[54] Fung, Y. C., *Biomechanics: Mechanical Properties of Living Tissues*. Springer, 2 ed., 1993.

[55] Gallagher, W., Ding, M., and Ueda, J., "Relaxed individual control of skeletal muscle forces via physical human-robot interaction," *Multibody System Dynamics*, vol. 30, pp. 77–99, Mar. 2013.

[56] Gallagher, W., Gao, D., and Ueda, J., "Measurement of muscle stiffness to improve stability of haptic human-robot interfaces," in *ASME Dynamic Systems and Control Conference (DSCC)*, (Ft. Lauderdale, FL, USA), 2012.

[57] Gallagher, W., Gao, D., and Ueda, J., "Improved Stability of Haptic Human-Robot Interfaces using Measurement of Human Arm Stiffness," *Advanced Robotics (Submitted)*, 2013.

[58] Gallagher, W., McPherson, T., Huggins, J. D., Shinohara, M., Gao, D., Menassa, R., and Ueda, J., "An Improved Human-Robot Interface by Measurement of Muscle Stiffness," in *IEEE International Conference on Biomedical Robotics and Biomechatronics (BioRob)*, (Rome, Italy), 2012.

[59] Gardner-Morse, M. G. and Stokes, I. A. F., "Trunk stiffness increases with steady-state effort.," *Journal of Biomechanics*, vol. 34, pp. 457–63, Apr. 2001.

[60] Gershon, E., Limebeer, D. J. N., Shaked, U., and Yaesh, I., "Robust H filtering of stationary continuous-time linear systems with stochastic uncertanties," *IEEE Transactions on Automatic Control*, vol. 46, no. 11, pp. 1788–1793, 2001.

[61] Gershon, E., Shaked, U., and Yaesh, I., "Robust H estimation of stationary discrete-time linear processes with stochastic uncertainties," *Systems & Control Letters*, vol. 45, pp. 257–269, Apr. 2002.

[62] Gil, J. J., Sanchez, E., Hulin, T., Preusche, C., and Hirzinger, G., "Stability Boundary for Haptic Rendering: Influence of Damping and Delay," *Journal of Computing and Information Science in Engineering*, vol. 9, no. 1, p. 011005, 2009.

[63] Gillespie, R. B., Hoffman, M. B., and Freudenberg, J., "Haptic Interface for Hands-On Instruction in System Dynamics and Embedded Control," in *ASME Symposium on Haptic Interfaces for Virtual Environment and Teleoperator Systems (Haptics)*, (Los Angeles, CA, USA), pp. 410–415, 2003.

[64] Granata, K. P. and Orishimo, K. F., "Response of trunk muscle coactivation to changes in spinal stability.," *Journal of Biomechanics*, vol. 34, pp. 1117–23, Sept. 2001.

[65] Grow, D. I., Verner, L. N., and Okamura, A. M., "Educational Haptics," in *AAAI Spring Symposia - Robots and Robot Venues: Resources for AI Education*, (Stanford, CA, USA), 2007.

[66] Hannaford, B., "A design framework for teleoperators with kinesthetic feedback," *IEEE Transactions on Robotics and Automation (T-Ro)*, vol. 5, pp. 426–434, Aug. 1989.

[67] Hansen, L. and Sargent, T., "Robust control and model uncertainty," *American Economic Review*, vol. 91, no. 2, pp. 60–66, 2001.

[68] Hatta, I., Sugi, H., and Tamura, Y., "Stiffness changes in frog skeletal muscle during contraction recorded using ultrasonic waves," *Journal of Physiology*, vol. 403, no. 1, pp. 193–209, 1988.

[69] Hatze, H., "A complete set of control equations for the human musculoskeletal system," *Biomechanics*, vol. 10, pp. 799–805, Jan. 1977.

[70] Hatze, H., "A myocybernetic control model of skeletal muscle," *Biological Cybernetics*, vol. 25, no. 2, pp. 103–119, 1977.

[71] Hill, A. V., "The heat of shortening and the dynamic constants of muscle," *Proceedings of the Royal Society of London. Series B, Biological Sciences*, vol. 126, no. 843, pp. 136–195, 1938.

[72] Hill, M. D. and Niemeyer, G., "Real-time estimation of human impedance for haptic interfaces," in *Joint Eurohaptics Conference and Symposium on Haptic Interfaces for Virtual Environment and Teleoperator Systems (World Haptics)*, (Salt Lake City, UT, USA), pp. 440–445, IEEE, 2009.

[73] Hofbaur, M. and Williams, B. C., "Mode estimation of probabilistic hybrid systems," *Hybrid Systems: Computation and Control*, vol. 2289, no. 1, pp. 253–266, 2002.

[74] Hoffman, G. and Breazeal, C., "Collaboration in human-robot teams," in *AIAA Intelligent Systems Technical Conference*, (Chicago, IL, USA), pp. 1–18, 2004.

[75] Hoffman, G. and Breazeal, C., "Cost-based anticipatory action selection for human–robot fluency," *IEEE Transactions on Robotics (T-Ro)*, vol. 23, no. 5, pp. 952–961, 2007.

[76] Hoffman, G. and Breazeal, C., "Anticipatory perceptual simulation for human-robot joint practice: Theory and application study," in *AAAI Conference on Artificial Intelligence*, vol. 3, (Chicago, IL, USA), pp. 1357–1362 vol 3, AAAI Press, Citeseer, 2008.

[77] Hogan, N., "Adaptive control of mechanical impedance by coactivation of antagonist muscles," *IEEE Transactions on Automatic Control*, vol. 29, pp. 681–690, Aug. 1984.

[78] Hogan, N., "Controlling impedance at the man/machine interface," in *International Conference on Robotics and Automation (ICRA)*, (Scottsdale, AZ, USA), pp. 1626–1631, IEEE Comput. Soc. Press, 1989.

[79] Hulin, T., Preusche, C., and Hirzinger, G., "Stability boundary for haptic rendering: Influence of human operator," in *IEEE/RSJ International Conference on Intelligent Robots and Systems (IROS)*, (Nice, France), pp. 3483–3488, IEEE, Sept. 2008.

[80] Jenkins, O. C., González, G., and Loper, M. M., "Tracking human motion and actions for interactive robots," in *ACM/IEEE International Conference on Human-Robot Interaction (HRI)*, (Washington, DC, USA), pp. 365–372, ACM, 2007.

[81] Julian, F. J. and Sollins, M. R., "Variation of muscle stiffness with force at increasing speeds of shortening.," *The Journal of General Physiology*, vol. 66, pp. 287–302, Sept. 1975.

[82] Kalman, R. E., "A new approach to linear filtering and prediction problems," *Journal of Basic Engineering*, vol. 82, no. 1, pp. 35–45, 1960.

[83] Kalman, R. E. and Bucy, R. S., "New Results in Linear Filtering and Prediction Theory," *Journal of Basic Engineering*, vol. 83, no. 3, p. 95, 1961.

[84] Karlsson, D. and Peterson, B., "Towards a model for force predictions in the human shoulder.," *Journal of Biomechanics*, vol. 25, pp. 189–99, Feb. 1992.

[85] Kárný, M., "Towards fully probabilistic control design," *Automatica*, vol. 32, no. 12, pp. 1719–1722, 1996.

[86] Kárný, M. and Guy, T. V., "Fully probabilistic control design," *Systems & Control Letters*, vol. 55, pp. 259–265, Apr. 2006.

[87] Kasaoka, K. and Sankai, Y., "Predictive control estimating operator's intention for stepping-up motion by exo-skeleton type power assist system HAL," in *IEEE/RSJ International Conference on Intelligent Robots and Systems (IROS)*, vol. 3, (Maui, HI, USA), pp. 1578–1583, IEEE, 2001.

[88] Kazerooni, H., Chu, A., and Steger, R., *That Which Does Not Stabilize, Will Only Make Us Stronger*, vol. 28, pp. 373–395 vol 28. Springer-Verlag, 2006.

[89] Kazerooni, H., Chu, A., and Steger, R., "That Which Does Not Stabilize, Will Only Make Us Stronger," *International Journal of Robotics Research (IJRR)*, vol. 26, pp. 75–89, Jan. 2007.

[90] Kazerooni, H. and Guo, J., "Human Extenders," *Journal of Dynamic Systems, Measurement, and Control*, vol. 115, no. 2B, pp. 281–290, 1993.

[91] Kazerooni, H. and Her, M.-G., "The dynamics and control of a haptic interface device," *IEEE Transactions on Robotics and Automation (T-Ro)*, vol. 10, no. 4, pp. 453–464, 1994.

[92] Kazerooni, H. and Snyder, T. J., "Case study on haptic devices: Human-induced instability in powered hand controllers," *Journal of Guidance, Control, and Dynamics*, vol. 18, pp. 108–113, Jan. 1995.

[93] Kearney, R. E. and Hunter, I. W., "System identification of human joint dynamics," *Critical Reviews in Biomedical Engineering*, vol. 18, no. 1, pp. 55–87, 1990.

[94] Kearney, R. E., Stein, R. B., and Parameswaran, L., "Identification of intrinsic and reflex contributions to human ankle stiffness dynamics.," *IEEE Transactions on Biomedical Engineering*, vol. 44, pp. 493–504, June 1997.

[95] Kobilarov, M., Sukhatme, G., Hyams, J., and Batavia, P., "People tracking and following with mobile robot using an omnidirectional camera and a laser," in *IEEE International Conference on Robotics and Automation (ICRA)*, (Orlando, FL, USA), pp. 557–562, IEEE, 2006.

[96] Kotsalis, G., Megretski, A., and Dahleh, M. A., "Balanced Truncation for a Class of Stochastic Jump Linear Systems and Model Reduction for Hidden Markov Models," *IEEE Transactions on Automatic Control*, vol. 53, pp. 2543–2557, Dec. 2008.

[97] Kuchenbecker, K. J., "Characterizing the human wrist for improved haptic interaction," in *ASME International Mechanical Engineering Congress and Exposition (IMECE)*, (Washington, DC, USA), 2003.

[98] Kullback, S. and Leibler, R. A., "On information and sufficiency," *The Annals of Mathematical Statistics*, vol. 22, no. 1, pp. 79–86, 1951.

[99] Lacquaniti, F., Licata, F., and Soechting, J. F., "The mechanical behavior of the human forearm in response to transient perturbations," *Biological Cybernetics*, vol. 44, no. 1, pp. 35–46, 1982.

[100] Lawrence, D. A., "Stability and transparency in bilateral teleoperation," *IEEE Transactions on Robotics and Automation (T-Ro)*, vol. 9, no. 5, pp. 624–637, 1993.

[101] Lee, D. and Li, P. Y., "Toward Robust Passivity : A Passive Control Implementation Structure for," in *ASME Symposium on Haptic Interfaces for Virtual Environment and Teleoperator Systems (Haptics)*, (Los Angeles, CA, USA), pp. 132–139, 2003.

[102] Lee, P. J., Rogers, E. L., and Granata, K. P., "Active trunk stiffness increases with co-contraction," *Journal of Electromyography and Kinesiology*, vol. 16, pp. 51–57, Feb. 2006.

[103] Li, P. Y., "Passive Control of Bilateral Teleoperated Manipulators," in *American Control Conference*, (Philadelphia, PA, USA), pp. 3838–3842, 1998.

[104] Li, P. Y., "Design and Control of a Hydraulic human power amplifier," in *ASME International Mechanical Engineering Congress and Exposition (IMECE)*, (Anaheim, CA, USA), pp. 385–393, 2004.

[105] Lindstedt, S. L., Reich, T. E., Keim, P., and LaStayo, P. C., "Do muscles function as adaptable locomotor springs?," *Journal of Experimental Biology*, vol. 205, no. 15, p. 2211, 2002.

[106] Liu, L. and Xie, X.-J., "Output-feedback stabilization for stochastic high-order nonlinear systems with time-varying delay," *Automatica*, vol. 47, pp. 2772–2779, Dec. 2011.

[107] Liu, N., Lovell, B. C., and Kootsookos, P. J., "Evaluation of hmm training algorithms for letter hand gesture recognition," in *IEEE International Symposium on Signal Processing and Information Technology (ISSPIT)*, (Darmstadt Germany), pp. 648–651, 2003.

[108] Liu, N., Lovell, B. C., Kootsookos, P. J., and Davis, R. I. A., "Model Structure Selection and Training Algorithms for an HMM Gesture Recognition System," in *International Workshop on Frontiers in Handwriting Recognition*, (Tokyo, Japan), pp. 100–105, Ieee, 2004.

[109] Ma, S.-P. and Zahalak, G. I., "The mechanical response of the active human triceps brachii muscle to very rapid stretch and shortening.," *Journal of Biomechanics*, vol. 18, pp. 585–98, Jan. 1985.

[110] Massie, T. H. and Salisbury, J. K., "The phantom haptic interface: A device for probing virtual objects," in *ASME Symposium on Haptic Interfaces for Virtual Environment and Teleoperator Systems (Haptics)*, vol. 55, (Chicago, IL, USA), pp. 295–300, 1994.

[111] Maurel, W. and Thalmann, D., "A Case Study on Human Upper Limb Modelling for Dynamic Simulation.," *Computer Methods in Biomechanics and Biomedical Engineering*, vol. 2, pp. 65–82, Jan. 1999.

[112] McIntyre, J., Mussa-Ivaldi, F. A., and Bizzi, E., "The control of stable postures in the multijoint arm," *Experimental Brain Research*, vol. 110, pp. 248–264, July 1996.

[113] Milner, T. E. and Cloutier, C., "Compensation for mechanically unstable loading in voluntary wrist movement," *Experimental Brain Research*, vol. 94, no. 3, pp. 522–532, 1993.

[114] Milner, T. E., Cloutier, C., Leger, A. B., and Franklin, D. W., "Inability to activate muscles maximally during cocontraction and the effect on joint stiffness," *Experimental Brain Research*, vol. 107, pp. 293–305, Jan. 1995.

[115] Mobasser, F. and Hashtrudi-Zaad, K., "Adaptive Teleoperation Control using Online Estimate of Operator's Arm Damping," in *IEEE Conference on Decision and Control (CDC)*, (San Diego, CA, USA), pp. 2032–2038, Ieee, 2006.

[116] Monroy, J. A., Lappin, A. K., and Nishikawa, K. C., "Elastic Properties of Active Muscle - On the Rebound?," *Exercise and Sport Sciences Reviews*, vol. 35, no. 4, pp. 174–179, 2007.

[117] Murray, W. M., Delp, S. L., and Buchanan, T. S., "Variation of muscle moment arms with elbow and forearm position," *Journal of Biomechanics*, vol. 28, pp. 513–525, May 1995.

[118] Mussa-Ivaldi, F. A., Hogan, N., and Bizzi, E., "Neural, mechanical, and geometric factors subserving arm posture in humans," *Journal of Neuroscience*, vol. 5, no. 10, pp. 2732–2743, 1985.

[119] Nguyen, N. and Phung, D., "Learning and detecting activities from movement trajectories using the hierarchical hidden Markov model," 2005.

[120] Nielsen, J., Sinkjæ r, T., Toft, E., and Kagamihara, Y., "Segmental reflexes and ankle joint stiffness during co-contraction of antagonistic ankle muscles in man," *Experimental brain research*, vol. 102, no. 2, pp. 350–358, 1994.

[121] Niu, Y., Ho, D. W. C., and Lam, J., "Robust integral sliding mode control for uncertain stochastic systems with time-varying delay," *Automatica*, vol. 41, pp. 873–880, May 2005.

[122] Ogata, K., *System Dynamics*. Prentice Hall, 3 ed., 1998.

[123] Osu, R., Franklin, D. W., Kato, H., Gomi, H., Domen, K., Yoshioka, T., Kawato, M., Hiroaki, G., and Toshinori, Y., "Short-and long-term changes in joint co-contraction associated with motor learning as revealed from surface EMG," *Journal of Neurophysiology*, vol. 88, pp. 991–1004, Aug. 2002.

[124] Osu, R. and Gomi, H., "Multijoint muscle regulation mechanisms examined by measured human arm stiffness and EMG signals," *Journal of Neurophysiology*, vol. 81, no. 4, p. 1458, 1999.

[125] Panossian, H., "Recent Developments in Probabilistic Approaches to Optimal Control Theory," in *American Control Conference*, (Atlanta, GA, USA), pp. 1749–1754, 1988.

[126] Pardalos, P. M. and Rosen, J. B., *Constrained global optimization: algorithms and applications*. Springer-Verlag, 1987.

[127] Perotto, A. and Delagi, E. F., *Anatomical guide for the electromyographer: the limbs and trunk*. Charles C Thomas, 2005.

[128] Perreault, E. J., Kirsch, R. F., and Crago, P. E., "Voluntary Control of Static Endpoint Stiffness During Force Regulation Tasks," *Journal of Neurophysiology*, vol. 87, no. 6, pp. 2808–2816, 2002.

[129] Perreault, E. J., Kirsch, R. F., and Crago, P. E., "Multijoint dynamics and postural stability of the human arm," *Experimental Brain Research*, vol. 157, pp. 507–517, Aug. 2004.

[130] Petersen, I. R., James, M. R., and Dupuis, P., "Minimax optimal control of stochastic uncertain systems with relative entropy constraints," *IEEE Transactions on Automatic Control*, vol. 45, pp. 398–412, Mar. 2000.

[131] Platzer, W. and Kahle, W., *Color Atlas and Textbook of Human Anatomy: Locomotor system*. Color Atlas and Textbook of Human Anatomy: In Three Volumes, Thieme, 1992.

[132] Prilutsky, B. I., "Coordination of two- and one-joint muscles: functional consequences and implications for motor control," *Motor Control*, vol. 4, no. 1, pp. 1—-44, 2000.

[133] Richard, C., Okamura, A. M., and Cutkosky, M. R., "Getting a Feel for Dynamics: using haptic interface kits for teaching dynamics and controls," in *ASME Symposium on Haptic Interfaces for Virtual Environment and Teleoperator Systems (Haptics)*, (Dallas, TX, USA), pp. 15–21, 1997.

[134] Russell, S. J. and Norvig, P., *Artificial Intelligence: a Modern Approach*. Prentice Hall, 2010.

[135] Sakita, K., Ogawara, K., Murakami, S., Kawamura, K., and Ikeuchi, K., "Flexible cooperation between human and robot by interpreting human intention from gaze information," in *IEEE/RSJ International Conference on Intelligent Robots and Systems (IROS)*, vol. 1, (Sendai, Japan), pp. 846–851, IEEE, 2004.

[136] Salisbury, J. K., "Active stiffness control of a manipulator in Cartesian coordinates," in *IEEE Conference on Decision and Control (CDC)*, (Albuquerque, NM, USA), 1980.

[137] Schmid, A. J., Weede, O., and Wörn, H., "Proactive robot task selection given a human intention estimate," in *IEEE International Symposium on Robot and Human Interactive Communication (ROMAN)*, (Jeju Island, South Korea), pp. 726–731, IEEE, 2007.

[138] Siciliano, B. and Villani, L., *Robot force control*. Kluwer international series in engineering and computer science, Kluwer Academic, 1999.

[139] Siljak, D. D., "Parameter space methods for robust control design: a guided tour," *IEEE Transactions on Automatic Control*, vol. 34, no. 7, pp. 674–688, 1989.

[140] Sinkjæ r, T. and Hayashi, R., "Regulation of wrist stiffness by the stretch reflex.," *Journal of Biomechanics*, vol. 22, pp. 1133–40, Jan. 1989.

[141] Skounakis, M., Craven, M., and Ray, S., "Hierarchical hidden markov models for information extraction," in *International Joint Conference on Artificial Intelligence (IJCAI)*, (Acapulco, Mexico), 2003.

[142] Smith, A. M., "The coactivation of antagonist muscles," *Canadian Journal of Physiology and Pharmacology*, vol. 59, no. 7, pp. 733–747, 1981.

[143] Sternad, M. and Ahlén, A., "Robust filtering and feedforward control based on probabilistic descriptions of model errors," *Automatica*, vol. 29, no. 3, pp. 661–679, 1993.

[144] Takeda, T., Hirata, Y., and Kosuge, K., "Dance step estimation method based on HMM for dance partner robot," *IEEE Transactions on Industrial Electronics*, vol. 54, pp. 699–706, Apr. 2007.

[145] Tee, K. P., Burdet, E., Chew, C. M., and Milner, T. E., "A model of force and impedance in human arm movements," *Biological Cybernetics*, vol. 90, no. 5, pp. 368–375, 2004.

[146] Todorov, E., "Cosine tuning minimizes motor errors," *Neural Computation*, vol. 14, pp. 1233–60, June 2002.

[147] Tsuji, T., Morasso, P. G., Goto, K., and Ito, K., "Human hand impedance characteristics during maintained posture," *Biological Cybernetics*, vol. 72, no. 6, pp. 475–485, 1995.

[148] Tsumugiwa, T., Fuchikami, Y., Kamiyoshi, A., Yokogawa, R., and Yoshida, K., "Stability Analysis for Impedance Control of Robot in Human-Robot Cooperative Task System," *Journal of Advanced Mechanical Design, Systems, and Manufacturing*, vol. 1, no. 1, pp. 113–121, 2007.

[149] Ueda, J., Ding, M., Krishnamoorthy, V., Shinohara, M., and Ogasawara, T., "Individual Muscle Control Using an Exoskeleton Robot for Muscle Function Testing," *IEEE Transactions on Neural Systems and Rehabilitation Engineering (TNSRE)*, vol. 18, no. 4, pp. 339–350, 2010.

[150] Ueda, J., Ding, M., Matsugashita, M., Oya, R., and Ogasawara, T., "Pinpointed control of muscles by using power-assisting device," in *IEEE International Conference on Robotics and Automation (ICRA)*, (Rome, Italy), pp. 3621–3626, Apr. 2007.

[151] Ueda, J., Hyderabadwala, M., Ding, M., Ogasawara, T., Krishnamoorthy, V., and Shinohara, M., "Individual Muscle Control Using an Exoskeleton Robot for Muscle Function Testing," in *ASME Dynamic Systems and Control Conference (DSCC)*, (Hollywood, CA, USA), pp. 371–378, ASME, 2009.

[152] Ueda, J., Hyderabadwala, M., Krishnamoorthy, V., and Shinohara, M., "Motor task planning for neuromuscular function tests using an individual muscle control technique," in *IEEE International Conference on Rehabilitation Robotics (ICORR)*, (Kyoto, Japan), pp. 133–138, June 2009.

[153] Ueda, J., Matsugashita, M., Oya, R., and Ogasawara, T., "Control of Muscle Force During Exercise Using a Musculoskeletal-Exoskeletal Integrated Human Model," in *Experimental Robotics* (Khatib, O., Kumar, V., and Rus,

D., eds.), vol. 39 of *Springer Tracts in Advanced Robotics*, pp. 143–152, Springer Berlin / Heidelberg, 2008.

[154] van Bolhuis, B. M. and Gielen, C. C., "A comparison of models explaining muscle activation patterns for isometric contractions.," *Biological Cybernetics*, vol. 81, pp. 249–61, Sept. 1999.

[155] van Dieën, J. H., Kingma, I., and van der Bug, J. C. E., "Evidence for a role of antagonistic cocontraction in controlling trunk stiffness during lifting," *Journal of Biomechanics*, vol. 36, pp. 1829–1836, Dec. 2003.

[156] Vanhooydonck, D., Demeester, E., Nuttin, M., and Van Brussel, H., "Shared control for intelligent wheelchairs: an implicit estimation of the user intention," in *International Workshop on Advances in Service Robotics (ASER)*, (Bardolino, Italy), pp. 176–182, Citeseer, 2003.

[157] Wang, H., "Robust Control of the Output Probability Density Functions for Multivariable Stochastic Systems with Guaranteed Stability," *IEEE Transactions on Automatic Control*, vol. 44, no. 11, pp. 2103–2107, 1999.

[158] Wang, Y., Xie, L., and de Souza, C. E., "Robust control of a class of uncertain nonlinear systems," *Systems & Control Letters*, vol. 19, pp. 139–149, Aug. 1992.

[159] Wang, Z. and Burnhan, K. J., "Discrete-time reduced-order estimator design for bilinear stochastic systems with error covariance assignment," *IMA Journal of Mathematical Control and Information*, vol. 18, no. 1, pp. 99–107, 2001.

[160] Wang, Z., Ho, D. W. C., and Liu, X., "Variance-Constrained Filtering for Uncertain Stochastic Systems with Missing Measurements," *IEEE Transactions on Automatic Control*, vol. 48, no. 7, pp. 1254–1258, 2003.

[161] Wang, Z., Ho, D. W. C., Liu, Y., and Liu, X., "Robust control for a class of nonlinear discrete time-delay stochastic systems with missing measurements," *Automatica*, vol. 45, pp. 684–691, Mar. 2009.

[162] Wang, Z. and Qiao, H., "Robust filtering for bilinear uncertain stochastic discrete-time systems," *IEEE Transactions on Signal Processing*, vol. 50, pp. 560–567, Mar. 2002.

[163] Warner, R. M., *Applied Statistics: From Bivariate Through Multivariate Techniques*. Sage, 1 ed., 2008.

[164] Wong, C. and Okamura, A. M., "The Snaptic Paddle: A Modular Haptic Device," in *Joint Eurohaptics Conference and Symposium on Haptic Interfaces for Virtual Environment and Teleoperator Systems (World Haptics)*, (Pisa, Italy), pp. 537–538, 2005.

[165] Xie, L., Chang, S.-F., Divakaran, A., and Sun, H., "Unsupervised discovery of multilevel statistical video structures using hierarchical hidden Markov models," in *International Conference on Multimedia and Expo (ICME)*, (Baltimore, MD, USA), pp. 29–32, 2003.

[166] Xie, X.-J. and Li, W.-Q., "Output-feedback control of a class of high-order stochastic nonlinear systems," *International Journal of Control*, vol. 82, pp. 1692–1705, Sept. 2009.

[167] Yamada, Y., Umetani, Y., Daitoh, H., and Sakai, T., "Construction of a human/robot coexistence system based on a model of human will-intention and desire," in *IEEE International Conference on Robotics and Automation (ICRA)*, vol. 4, (Detroit, MI, USA), pp. 2861–2867 vol 4, 1999.

[168] Yaz, E., "Minimax control of discrete nonlinear stochastic systems with noise uncertainty," in *Conference on Decision and Control*, (Brighton, England, UK), pp. 1815–1816, 1991.

[169] Yeu, D., Tian, E., Wang, Z., and Lam, J., "Stabilization of Systems With Probabilistic Interval Input Delays and Its Applications to Networked Control Systems," *IEEE Transactions on Systems, Man, and Cybernetics - Part A: Systems and Humans*, vol. 39, pp. 939–945, July 2009.

[170] Yokokohji, Y. and Yoshikawa, T., "Bilateral control of master-slave manipulators for ideal kinesthetic coupling-formulation and experiment," *IEEE Transactions on Robotics and Automation (T-Ro)*, vol. 10, pp. 605–620, Oct. 1994.

[171] Zajac, F. E., "Muscle and tendon: Proporties, models, scaling, and application to biomechanics and motor control," *Critical Reviews in Biomedical Engineering*, vol. 17, no. 4, pp. 359–411, 1989.

[172] Zhang, L.-Q. and Rymer, W. Z., "Simultaneous and nonlinear identification of mechanical and reflex properties of human elbow joint muscles.," *IEEE Transactions on Biomedical Engineering*, vol. 44, pp. 1192–209, Dec. 1997.

[173] Zhou, K. and Doyle, J. C., *Essentials of Robust Control*. Prentice Hall, 1998.

[174] Zhou, K., Doyle, J. C., and Glover, K., *Robust and Optimal Control*. Prentice Hall, 1996.

[175] Zinn, M., Roth, B., Khatib, O., and Salisbury, J. K., "A New Actuation Approach for Human Friendly Robot Design," *The International Journal of Robotics Research*, vol. 23, pp. 379–398, Apr. 2004.